OPEN ACCESS Freely available online

PLoS one

Wnt4 and LAP2alpha as Pacemakers of Thymic Epithelial Senescence

Krisztian Kvell[1], Zoltan Varecza[1], Domokos Bartis[1], Sebastian Hesse[1], Sonia Parnell[2], Graham Anderson[2], Eric J. Jenkinson[2], Judit E. Pongracz[1,2]*

1 Department of Medical Biotechnology, Institute for Immunology and Biotechnology, University of Pecs, Pecs, Hungary, **2** Division of Immunity and Infection, Department of Anatomy, Institute for Biomedical Research, University of Birmingham, Birmingham, United Kingdom

Abstract

Age-associated thymic involution has considerable physiological impact by inhibiting *de novo* T-cell selection. This impaired T-cell production leads to weakened immune responses. Yet the molecular mechanisms of thymic stromal adipose involution are not clear. Age-related alterations also occur in the murine thymus providing an excellent model system. In the present work structural and molecular changes of the murine thymic stroma were investigated during aging. We show that thymic epithelial senescence correlates with significant destruction of epithelial network followed by adipose involution. We also show in purified thymic epithelial cells the age-related down-regulation of Wnt4 (and subsequently FoxN1), and the prominent increase in LAP2α expression. These senescence-related changes of gene expression are strikingly similar to those observed during mesenchymal to pre-adipocyte differentiation of fibroblast cells suggesting similar molecular background in epithelial cells. For molecular level proof-of-principle stable LAP2α and Wnt4-over-expressing thymic epithelial cell lines were established. LAP2α over-expression provoked a surge of PPARγ expression, a transcription factor expressed in pre-adipocytes. In contrast, additional Wnt4 decreased the mRNA level of ADRP, a target gene of PPARγ. Murine embryonic thymic lobes have also been transfected with LAP2α- or Wnt4-encoding lentiviral vectors. As expected LAP2α over-expression increased, while additional Wnt4 secretion suppressed PPARγ expression. Based on these pioneer experiments we propose that decreased Wnt activity and increased LAP2α expression provide the molecular basis during thymic senescence. We suggest that these molecular changes trigger thymic epithelial senescence accompanied by adipose involution. This process may either occur directly where epithelium can trans-differentiate into pre-adipocytes; or indirectly where first epithelial to mesenchymal transition (EMT) occurs followed by subsequent pre-adipocyte differentiation. The latter version fits better with literature data and is supported by the observed histological and molecular level changes.

Citation: Kvell K, Varecza Z, Bartis D, Hesse S, Parnell S, et al. (2010) Wnt4 and LAP2alpha as Pacemakers of Thymic Epithelial Senescence. PLoS ONE 5(5): e10701. doi:10.1371/journal.pone.0010701

Editor: Immo A. Hansen, New Mexico State University, United States of America

Received February 4, 2010; **Accepted** April 27, 2010; **Published** May 18, 2010

Funding: Research was supported by the following grants: The Wellcome Trust grant No.: 079415 (grant-holders: J.E.P., G.A. and E.J.J.), 'Science Please' Research Team on Innovation grant No.: SROP-4.2.2/08/1/2008-0011 (grant holder: J.E.P.) and OTKA (Hungarian Scientific Research Fund) type: PD (post-doctoral) grant No.: 78310 (grant-holder: K.K.). The funders had no role in study design, data collection and analysis, decision to publish, or preparation of the manuscript.

Competing Interests: The authors have declared that no competing interests exist.

* E-mail: judit.e.pongracz@aok.pte.hu

Introduction

Thymic senescence

Thymic senescence begins early, around late puberty. This process is called adipose involution, as the thymus is invaded by adipose tissue [1]. Due to decrease in thymic epithelial tissue mass, the thymus can no longer support the same output of T-cell production [2]. Therefore peripheral blood T lymphocyte composition exhibits the dominance of memory T lymphocytes resulting in impaired responses towards novel, particularly viral infections [3,4,5]. Since the thymic epithelium has a key role in deleting auto-reactive T-cell clones, functional impairment increases the chances of developing auto-immune disease [6]. If we were able to slow down or even stop the loss of thymic epithelium the elderly would have a better chance to address late-onset autoimmune diseases and viral infections. However, despite studies of thymic senescence, the molecular mechanism of thymic aging remains elusive.

Signaling pathways of thymic epithelial cell development and maintenance

Understanding signaling mechanisms that regulate tissue development and maintenance of thymic epithelial cells might reveal the process of adipose involution. Certainly, maintenance and functional integrity of the thymic stroma requires stimuli through Notch, BMP, and Wnt signaling pathways [7,8,9,10,11]. Undoubtedly, the Wnt family of secreted glycoproteins is one of the best analyzed among the required ligands [12]. Most members of the nineteen known Wnt glycoproteins have been implicated in both the development of embryonic thymus and the maintenance of adult thymic epithelium [13]. In the thymus, Wnt ligands originate primarily from thymic epithelial cells and activate a highly complex signaling network via ten G-protein dependent receptors called Frizzleds (Fz), and their co-receptors of low-density lipoprotein receptor-related proteins 5/6 called LRP5/6 [14,15]. The actual constellation of ligands, receptors, co-receptors and further regulatory molecules define Wnt-mediated effects.

Recent studies have highlighted Wnt4 as responsible for the direct up-regulation of FoxN1, a key transcription factor responsible for the differentiation of thymic epithelial cells and the subsequent maintenance of thymic epithelial identity [13]. Interestingly, the Wnt/β-catenin pathway is known to efficiently block the adipocyte differentiation program in mesenchymal elements like fibroblasts [16,17,18,19].

Trans-differentiation of fibroblasts into adipocytes

Studies with fibroblast cells have also revealed that fibroblast to pre-adipocyte transformation is strongly connected to LAP2α, the member of the LAP2 protein family [17]. To date there are 7 classified intranuclear LAP2 polypeptides marked by the Greek alphabet. They are all splice variants of the same LAP2 gene previously called thymopoietin. While most splice variants associate with the nuclear envelope, LAP2α is involved in several nucleoplasmic activities including cell-cycle control and differentiation [20,21]. LAP2α is synthesized in the cytoplasm and is then transported into the nucleus by a PKC-dependent mechanism [22]. The mere over-expression of LAP2α in fibroblasts is known to directly up-regulate PPARγ expression, an acknowledged marker and key transcription factor of pre-adipocyte differentiation [17]. In pre-adipocytes PPARγ expression is followed by an increase of ADRP expression (adipose differentiation-related protein) a known direct target gene of PPARγ. Although LAP2α over-expression alone initiates pre-adipocyte differentiation in fibroblasts, it is not sufficient to complete the adipocyte differentiation program in the absence of additional stimuli [17].

Results and Discussion

Disintegration of epithelial network

Senescence exhibits characteristic histological changes in both the human and mouse thymus [1,23]. In order to demonstrate this process the thymic lobes of 1 month and 1 year old BALB/c mice were analyzed (see Figures 1A and 1B). In young adult mice, histology revealed strict segregation of epithelial cell compartments by staining for medullary ($EpCAM1^{++}$, $Ly51^{-}$) and cortical ($EpCAM1^{+}$, $Ly51^{++}$) epithelial cellular subsets (Figure 1A). This shows high level of morphological integrity just preceding puberty/early adulthood. However, the highly organized structure disintegrates and becomes chaotic by the age of 1 year (Figure 1B). By this age the previously shown strict cortico-medullary delineation becomes disintegrated, degenerative vacuoles appear surrounded by areas showing strong co-staining with both epithelial markers. There are also other large cellular areas that lack staining with either epithelial marker, a pattern completely absent at the young adult age.

Staining of extracellular matrix components of fibroblast origin ($ER\text{-}TR7^{++}$) was also performed on cryostate thymic sections of 2

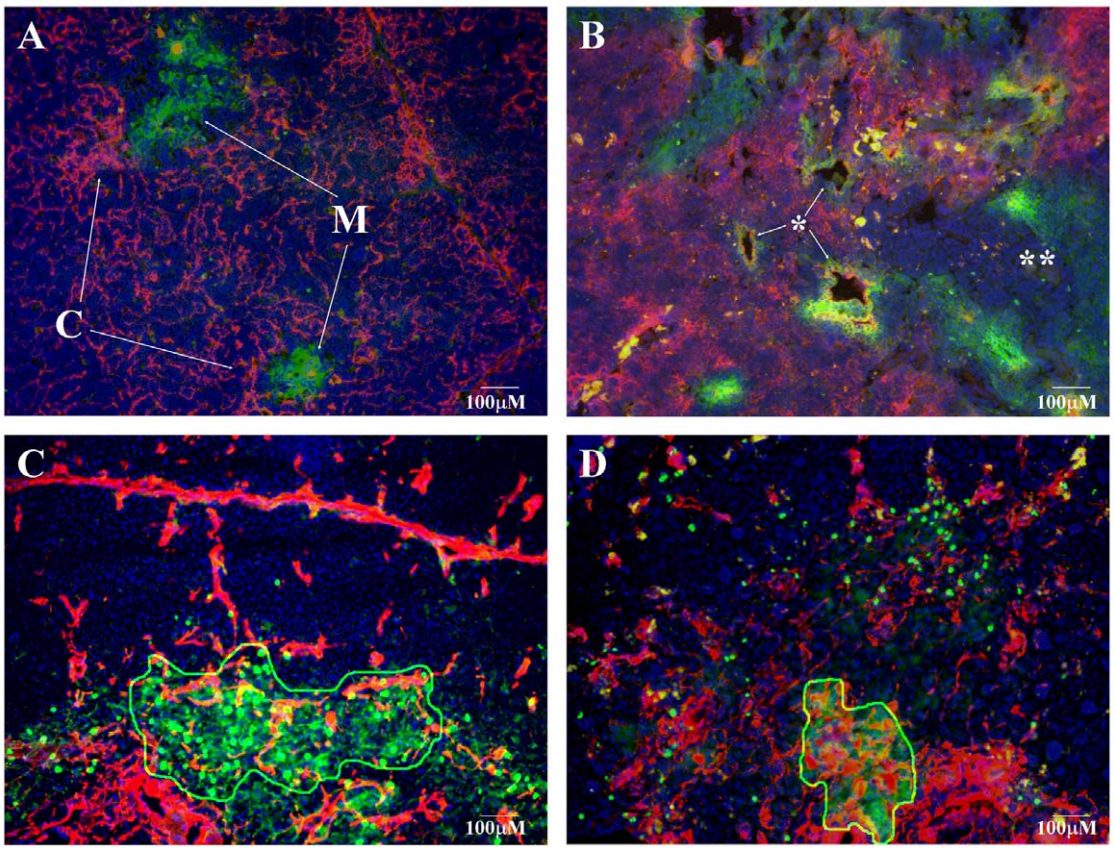

Figure 1. Disintegration of epithelial network. Figure 1A demonstrates cryostat section of 1 month, whereas figure 1B presents cryostat section of 1 year old BALB/c mouse thymus. Staining pattern: anti-EpCAM1-FITC (green), anti-Ly51-PE (red), DAPI (blue). 'M' marks medullary ($EpCAM1^{++}$, $Ly51^{-}$), while 'C' marks cortical ($EpCAM1^{+}$, $Ly51^{++}$) epithelial compartments on Figure 1A. Single asterisk (*) marks degenerative vacuoles, while double asterisk (**) mark the loss of epithelial staining on Figure 1B. Figure 1C (lower left) shows cryostate section of 2 month, whereas figure 1D (lower right) demonstrates cryostate section of 9 month old BALB/c mouse thymus. Staining pattern: anti-EpCAM1-FITC, ER-TR7-PE, DAPI (blue). The $EpCAM1^{++}$ thymic medulla is outlined by continuous line on Figures 1C and 1D for easier visualization.
doi:10.1371/journal.pone.0010701.g001

month and 9 month old BALB/c mice to identify epithelial and mesenchymal elements in young adult and aging thymic lobes. The above ages were selected to check additional time points and more precisely map the timeframe of thymic physiological senescence (see Figures 1C and 1D). The staining patterns are strikingly different at the two ages examined. In the 2 month old thymic tissue section a-EpCAM1 and ER-TR7-staining show little tendency for co-localization. In stark contrast, by the age of 9 months a-EpCAM1 and ER-TR7-staining show significant overlap within the thymic medulla, a phenomenon completely absent at earlier ages.

Adipose involution

To demonstrate how the disorganization of thymic epithelial network is followed by the emergence of adipocytes, thymic sections of 1.5 year old GFP-transgenic BALB/c mice were analyzed. This mouse strain develops and reproduces exactly like control BALB/c mice, and the thymic epithelial function and thymocyte maturation is indistinguishable from wild type controls [24]. However, due to the ubiquitous and strong EF1 promoter-driven transgene transcription, bright GFP expression offers a native, green-colored, cytoplasmic staining for all the cells in these mice. Thymic sections of senescent GFP-transgenic mice were co-stained with LipidTox Red to identify adipocytes. Histology shows the presence of relatively large, inflated cells in which the green-colored (GFP-containing) cytoplasm is pushed to the periphery by red-staining neutral lipid deposits, a pattern characteristic of adipose cells (see Figure 2).

Molecular changes of thymic epithelium

Having presented structural changes of thymic epithelial senescence, we set out to investigate the underlying molecular events. In order to detect gene expression changes, thymic epithelial cells were purified from 1 month and 1 year old BALB/c mice based on EpCAM1 expression (MACS separation). Following cDNA synthesis, quantitative RT-PCR analysis was performed. Several genes including Wnt4, FoxN1, PPARγ, ADRP, lamin1 and LAP2α were tested (Table 1 lists primer sequences and characteristics, see Figures 3A–D for changes in gene expression). Figure 3A shows that the expression of both Wnt4 and FoxN1 decreases in thymic epithelial cells. Highly decreased level (or total absence in some cases) of FoxN1 could be the consequence of strong Wnt4 down-regulation by the age of 1 year, indicating that thymic epithelial cells can down-regulate FoxN1 expression while maintaining that of epithelial cell surface markers like EpCAM1 [13]. At the same time, mRNA levels of pre-adipocyte differentiation markers PPARγ and ADRP rise with age in the same, EpCAM1-positive cell population (Figure 3C). This finding is in harmony with histological data demonstrating the emergence of adipocytes in the thymic lobes of senescent mice (Figure 2). The expression of lamin1, a key component of the nuclear lamina remains unaffected during senescence in thymic epithelial cells; whereas, the expression of LAP2α increases significantly (see Figure 3B). This degree of dissociation between lamin1 and LAP2α expression is of note and suggests functional differences despite conventionally anticipated association of lamin1 and LAP2 molecular family members. The measured LAP2α up-regulation associated with age-related adipose involution is, however, in perfect agreement with other literature data suggesting the pre-adipocyte differentiation-promoting effect of LAP2α in fibroblasts [17]. This is the first report to show that such, normally fibroblast associated molecular changes occur in purified thymic epithelial cells. In the literature, epithelial-mesenchymal transition is associated with differential expression of E- and N-cadherin [25]. While E-cadherin decreases, N-cadherin normally compensates for the loss of E-cadherin expression. To investigate whether the first step towards pre-adipocyte differentiation is the epithelial-mesenchymal transition of epithelial cells, gene expression changes of E-cadherin and N-cadherin were measured (Figure 3D). While E-cadherin mRNA levels significantly decreased, N-cadherin gene expression showed a slight increase, indicating that EMT might be the initial step in epithelial cell transition to become pre-adipocytes.

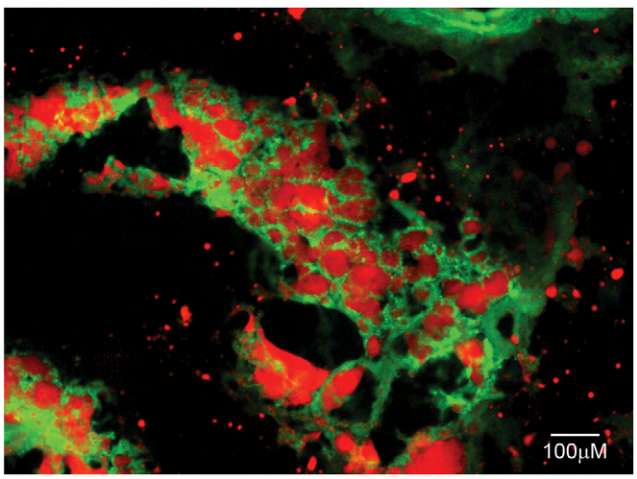

Figure 2. Adipose involution. Figure 2 shows adipose involution over cryostat section of 1.5 year old GFP-transgenic BALB/c mouse thymus. Staining pattern: GFP (green), LipidTox Red (red).
doi:10.1371/journal.pone.0010701.g002

Transgenic cell lines

Stable LAP2α over-expressing or Wnt4-secreting transgenic TEP1 cell lines were established using lentiviral transgenesis. The use of a primary-derived model cell line provides the advantage of absolute purity, the complete lack of other cell types that could potentially affect the gene expression profile of epithelial cells [26]. The established transgenic cell lines proliferated normally and did not show obvious signs of phenotypic changes (data not shown). In contrast to morphology, quantitative RT-PCR analysis revealed that LAP2α over-expression triggers an immense surge of PPARγ expression (Figure 4). Such an increase in mRNA level suggests that this is not a plain quantitative, but rather a qualitative change. ADRP a direct target gene of PPARγ was also up-regulated albeit to a lesser extent (Figure 4). On the other hand in Wnt4-secreting TEP1 cells the mRNA level of both PPARγ and ADRP was decreased (Figure 4). In the TEP1 cell line the expression of FoxN1 could not be addressed as it is very low/undetectable and remains as such with all the tested treatments (data not shown).

Transfected embryonic thymic organ cultures

To confirm the involvement of LAP2α and Wnt4 during adipogenesis through their direct effect on PPARγ expression in primary cells, murine thymic lobes were isolated from timed pregnancies at E12. Thymic lobes at the age of E12 provide an excellent experimental setting where the thymus has just been formed and there is no sign of aging. Furthermore, thymic lobes at this stage are also small enough to be both cultured and transfected as a whole, nutrients and virions have free access to most of the cells in the lobe without the need of disrupting any intercellular connection or tissue matrix [8,27]. The isolated lobes were therefore transfected with lentiviral vectors encoding GFP (mock), Wnt4 or LAP2α and were cultured for 4 days *in vitro*. Q-PCR was

Table 1. List of gene specific PCR primers.

Gene	Forward primer	Reverse primer
β-actin	5′-TGG CGC TTT TGA CTC AGG A -3′	5′-GGG AGG GTG AGG GAC TTC C - 3′
Wnt4	5′-CTC AAA GGC CTG ATC CAG AG - 3′	5′-TCA CAG CCA CAC TTC TCC AG - 3′
LAP2α	5′-TGA ACT GCA GGC AGC TAA GA-3′	5′-TCA TAG CTA GAC TCT GAG G-3′
Lamin1	5′ - TGA GTA CAA CCT GCG CTC AC -3′	5′ - TGA CTA GGT TGT CCC CGA AG -3′
PPARγ	5′ - CCC AAT GGT TGC TGA TTA CAA A -3′	5′ - AAT AAT AAG GTG GAG ATG CAG GTT CT -3′
ADRP	5′ - CGC CAT CGG ACA CTT CCT TA -3′	5′ - GTG ATG GCA GGC GAC ATC T -3′
E-cadherin	5′- AAG TGA CCG ATG ATG ATG CC -3′	5′- CTT CAT TCA CGT CTA CCA CGT -3′
N-cadherin	5′ - GTG GAG GCT TCT GGT GAA AT - 3′	5′ - CTG CTG GCT CGC TGC TT - 3′
FoxN1	Applied Biosystems TaqMan probe PN4351272 (Mm00477457_m1)	

doi:10.1371/journal.pone.0010701.t001

performed to confirm over-expression of LAP2α and Wnt4 in the embryonic thymic lobes as a result of lentiviral transgenesis (Figure 5A) and their effect on PPARγ expression was also analyzed (Figure 5B). The level of over-expression was confirmed following transfection with both LAP2α- and Wnt4-encoding viral vectors. Q-PCR analysis revealed that LAP2α over-expression triggers an increase of PPARγ expression, whereas additional Wnt4 secretion suppresses PPARγ level (Figure 5B). The latter Wnt4-mediated suppression of PPARγ expression in cultures of E12 thymic embryonic lobes was also confirmed by treatment with Wnt4-containing supernatants of Wnt4 over-expressing TEP1 cell line (data not shown). Interestingly, the expression of FoxN1 did not decrease in LAP2α over-expressing thymic lobes (data not shown), possibly due to high levels of Wnt4 in the embryonic thymic tissue preserving FoxN1 status. Our molecular studies using E12 thymic lobes confirmed our data obtained with the TEP1 cell lines, that even in embryonic thymic tissue pre-adipocyte differentiation markers can be up-regulated in the presence of LAP2α, indicating that the process can be dissected and controlled at a molecular level.

Conclusion

Here we show that with senescence, thymic epithelial Wnt4 secretion decreases, possibly below a threshold level that is required to maintain the identity of established thymic epithelial cells. This is measured by the loss of FoxN1 expression, a key transcription factor defining thymic epithelial cell identity. However, these epithelial cells still express cell surface markers

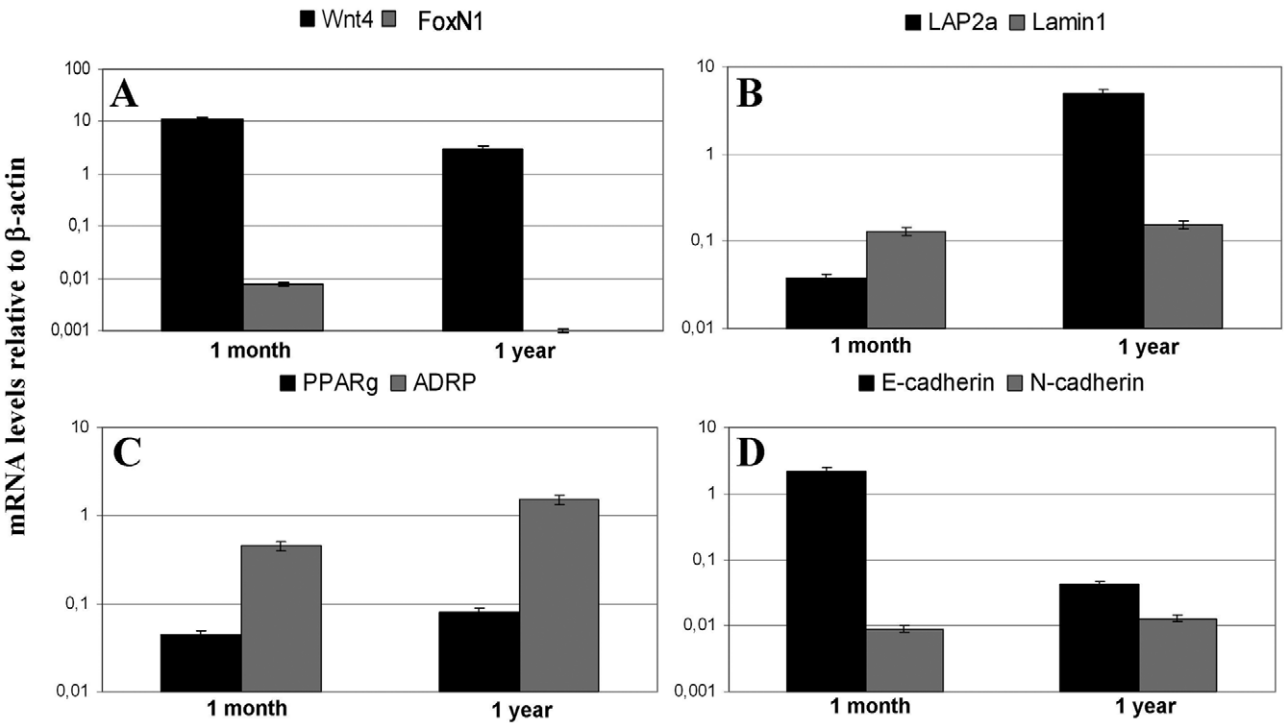

Figure 3. Molecular changes in thymic epithelium. Figures 3A–D demonstrate gene expression changes of MACS purified thymic epithelial cells measured by Q-PCR. Please note that the Y-axis scale is logarithmic. Error bars show ±1 SD.
doi:10.1371/journal.pone.0010701.g003

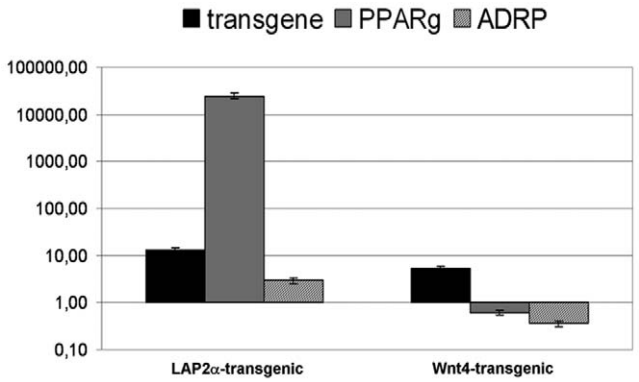

Figure 4. Confirmation in transgenic thymic cell lines. Figure 4 shows gene expression changes of LAP2α and Wnt4 over-expressing transgenic TEP1 cells measured by Q-PCR. Please note that Y-axis scale is logarithmic. Error bars show ±1 SD.
doi:10.1371/journal.pone.0010701.g004

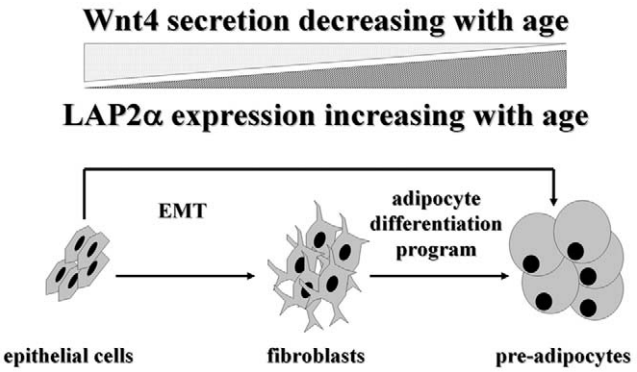

Figure 6. Model for thymic epithelial senescence. Figure 6 demonstrates our molecular level model of thymic adipose involution. Decreasing Wnt4 and increasing LAP2α levels promote epithelial cells to differentiate into pre-adipocytes either directly or indirectly via EMT.
doi:10.1371/journal.pone.0010701.g006

characteristic for thymic epithelial cells – i.e. EpCAM1. Wnt4 deprivation opens up an opportunity for trans-differentiation into pre-adipocytes. The simultaneous increase in LAP2α expression provides the necessary signal that pushes de-differentiated thymic epithelial cells to differentiate into pre-adipocytes, as detected by increased mRNA levels of PPARγ and ADRP.

We propose two different mechanisms for the process of adipose involution (see Figure 6). The first allows for the direct initiation of pre-adipocyte differentiation from de-differentiated thymic epithelial cells due to the down-regulation of Wnt4 and up-regulation of LAP2α. Although we cannot rule out this first model, we favor the second model where the process occurs indirectly: de-differentiation of thymic epithelial cells triggers EMT first, and then the resulting fibroblasts undergo the conventional route of differentiation program towards adipocyte-lineage commitment. The latter model certainly fits better with current literature of EMT [28] and is also supported by our histological and molecular results. Co-localization of a-EpCAM1 and ER-TR7-staining in the aging thymic medulla (Figure 1D) confirms that in the 9 month old thymus there are cells expressing the EpCAM1 marker as a legacy of their primary origin, and also secreting ER-TR7-positive extracellular matrix components, a function conventionally attributed to fibroblast cells. Moreover, Q-PCR data obtained with cDNA samples of MACS-purified thymic epithelial cells also demonstrate an age-related shift in cadherin expression levels characteristic for EMT (Figure 3D) providing additional evidence for the active process of EMT during thymic epithelial senescence.

Our model of thymic epithelial senescence is based on data obtained with mice undergoing physiological senescence. This is the first model for the molecular basis of the thymic epithelium to undergo adipose involution. This model withstands molecular level proof-of-principle using both a model cell line and primary embryonic thymic organ cultures rendered transgenic by lentiviral transgenesis.

Perspectives

Further experiments, however, are required. We plan using inducible, LAP2α-transgenic mice to allow us precise temporal-spatial over-expression of LAP2α in adult thymic epithelium to model and decisively verify the role of LAP2α in pre-adipocyte trans-differentiation *in vivo* exploiting our experience in establishing transgenic animals [24,29]. If LAP2α proves to be a master regulator of thymic adipose involution *in vivo* too, this knowledge appoints LAP2α as target molecule for directed rejuvenation of the thymic epithelial structure and function. This rejuvenation process could theoretically reinforce naïve T-cell output to reach young adult levels that could ameliorate senescence-related immunological disorders like impaired antiviral defense and late-onset autoimmune diseases.

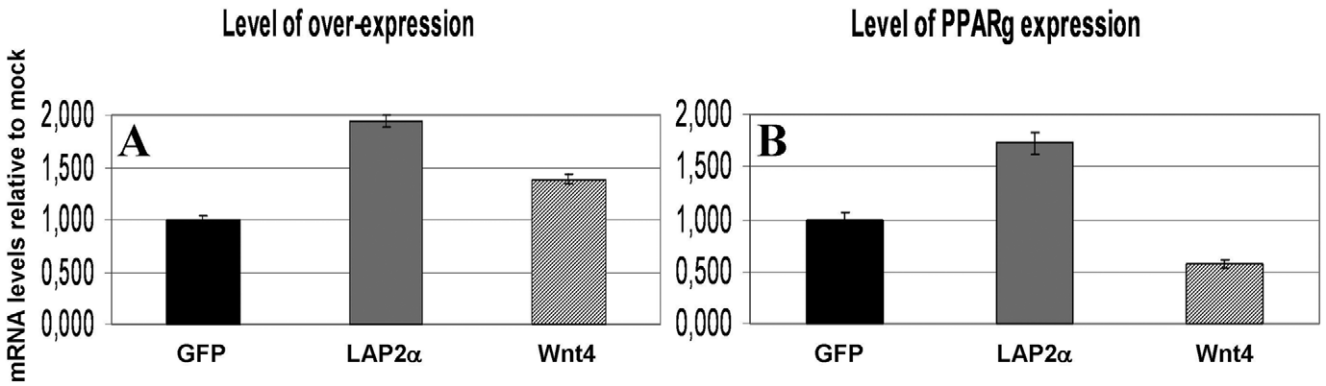

Figure 5. Confirmation in transfected thymic lobes. Figures 5A–B present gene expression changes measured by Q-PCR from cDNA of murine thymic lobes transfected at E12 and cultured for 4 days *in vitro*. Please note that Y-axis scale is linear. Error bars show ±1 SD.
doi:10.1371/journal.pone.0010701.g005

Methods

Cell lines and mice

The 293T (ATCC: CRL-11268) and TEP1 [26] cell lines were cultured in DMEM supplemented with 10% FCS, penicillin, streptomycin and β-mercapto-ethanol (Lonza Walkersville). For the experiments we used thymic lobes from timed pregnancies at E12, and also from adult BALB/c mice at 4 week and 1 year of age, and from 1.5 year old GFP-transgenic BALB/c-mice. Mice were bred in our animal facility; all animal work has been conducted according to relevant national and international guidelines following approval of ethics committee of the University of Pecs. Senescent animals developed and aged normally, without any treatment.

Transgenic cell, organ and animal models

The GFP-transgenic BALB/c model was created using lentiviral transgenesis as published by our group [24]. The Wnt4 sequence was purchased and subcloned from an Origene (Origene) vector containing human full-length Wnt4 cDNA. The full-length murine LAP2α cDNA containing plasmid was a kind gift of Dr. Simon Amos. The GFP (mock), LAP2α or Wnt4 over-expressing TEP1 cell lines or E12 thymic lobes were generated using lentiviral vectors that were prepared as described previously [30]. Following overnight lentiviral transfection the thymic lobes were transferred over Nucleopore Track-Etch Membranes (Whatman) and were cultured in DMEM supplemented with 20% FCS, penicillin, streptomycin, ciprofloxacin, amphotericin-B and β-mercapto-ethanol (Lonza Walkersville).

Histology using fluorescent antibodies, proteins and dyes

Sections (9 μm) of frozen thymic lobes of BALB/c mice were fixed in cold acetone, then dried and blocked using 5% BSA in PBS for 20 min before staining with a-Ly51-PE (clone 6C3), a-EpCAM-FITC (clone G8.8), ER-TR7-PE antibodies and DAPI. Thymic sections of GFP-transgenic mice were fixed in 4% paraformaldehyde before staining with LipidTOX Red following the manufacturer's instructions (Invitrogen). The sections were analyzed using an Olympus BX61 microscope equipped with a CCD camera and AnalySIS software.

Separation and enrichment of thymic epithelial cells

Thymic lobes were digested with type F collagenase from *C. hystolyticum* (Sigma) for 30 min, then washed with DMEM 10% FCS. Cell suspensions were then labeled with anti-EpCAM1-FITC (clone G8.8) and washed with MACS-buffer followed by incubation with anti-FITC micro-beads (Miltenyi Biotec), the $EpCAM^{+}$-cells were used for total RNA isolation and subsequent quantitative PCR analysis. The cells were purified using MACS LS separation columns (Miltenyi Biotec).

RNA isolation, preparation of cDNA, Q-PCR analysis

Total RNA was isolated the RNAII kit (Macherey-Nagel), including an on column DNA digestion step. cDNA was constructed using the high capacity RNA to cDNA kit (Applied Biosystems). For Q- PCR analysis, we used an AB7500 platform and either SYBR green or TaqMan PCR master mix (Applied Biosystems). Gene expression was normalized to β-actin. The sequences and data of primers are listed in Table 1.

Statistical analysis

All experiments were performed on three occasions, representative experiments are shown. Measures were obtained in triplicates; data are presented as mean ±1 SD by error bars.

Acknowledgments

The supernatant of ER-TR7 hybridoma clone was originally donated by Dr. Willem van Ewijk to Dr. Peter Balogh, who provided it for the authors. The authors are grateful to Prof. S. Amos (Institute of Hematology, Chaim Sheba Medical Center, Tel-Hashomer, Israel) for providing the murine LAP2α construct and Prof. E. L. Cooper (Laboratory of Comparative Neuroimmunology, Department of Neurobiology, David Geffen School of Medicine at UCLA, University of California, Los Angeles, USA) for critically and carefully reading the manuscript.

Author Contributions

Conceived and designed the experiments: KK GA EJJ JEP. Performed the experiments: KK ZV DB SH SP. Analyzed the data: KK ZV DB SH SP GA EJJ JEP. Contributed reagents/materials/analysis tools: KK GA EJJ JEP. Wrote the paper: KK JEP.

References

1. Marinova TT (2005) Epithelial framework reorganization during human thymus involution. Gerontology 51: 14–18.
2. Ribeiro RM, Perelson AS (2007) Determining thymic output quantitatively: using models to interpret experimental T-cell receptor excision circle (TREC) data. Immunol Rev 216: 21–34.
3. Grubeck-Loebenstein B (2009) Fading Immune Protection in Old Age: Vaccination in the Elderly. J Comp Pathol.
4. Chidgey A, Dudakov J, Seach N, Boyd R (2007) Impact of niche aging on thymic regeneration and immune reconstitution. Semin Immunol 19: 331–340.
5. Gui J, Zhu X, Dohkan J, Cheng L, Barnes PF, et al. (2007) The aged thymus shows normal recruitment of lymphohematopoietic progenitors but has defects in thymic epithelial cells. Int Immunol 19: 1201–1211.
6. Hsu HC, Mountz JD (2003) Origin of late-onset autoimmune disease. Immunol Allergy Clin North Am 23: 65–82, vi.
7. Bleul C, Boehm T (2005) BMP signaling is required for normal thymus development. J Immunol 175: 5213–5221.
8. Pongracz J, Hare K, Harman B, Anderson G, Jenkinson E (2003) Thymic epithelial cells provide Wnt signals. Eur J Immunol 33: 1949–1956.
9. Osada M, Ito E, Fermin HA, Vazquez-Cintron E, Venkatesh T, et al. (2006) The Wnt signaling antagonist Kremen1 is required for development of thymic architecture. Clin Dev Immunol 13: 299–319.
10. Kuraguchi M, Wang XP, Bronson RT, Rothenberg R, Ohene-Baah NY, et al. (2006) Adenomatous polyposis coli (APC) is required for normal development of skin and thymus. PLoS Genet 2: e146.
11. Anderson G, Pongracz J, Parnell S, Jenkinson EJ (2001) Notch ligand-bearing thymic epithelial cells initiate and sustain Notch signaling in thymocytes independently of T cell receptor signaling. Eur J Immunol 31: 3349–3354.
12. Mikels AJ, Nusse R (2006) Wnts as ligands: processing, secretion and reception. Oncogene 25: 7461–7468.
13. Balciunaite G, Keller M, Balciunaite E, Piali L, Zuklys S, et al. (2002) Wnt glycoproteins regulate the expression of FoxN1, the gene defective in nude mice. Nat Immunol 3: 1102–1108.
14. Gordon MD, Nusse R (2006) Wnt signaling: multiple pathways, multiple receptors, and multiple transcription factors. J Biol Chem 281: 22429–22433.
15. Schweizer L, Varmus H (2003) Wnt/Wingless signaling through beta-catenin requires the function of both LRP/Arrow and frizzled classes of receptors. BMC Cell Biol 4: 4.
16. Torday JS, Rehan VK (2006) Up-regulation of fetal rat lung parathyroid hormone-related protein gene regulatory network down-regulates the Sonic Hedgehog/Wnt/betacatenin gene regulatory network. Pediatr Res 60: 382–388.
17. Dorner D, Vlcek S, Foeger N, Gajewski A, Makolm C, et al. (2006) Lamina-associated polypeptide 2alpha regulates cell cycle progression and differentiation via the retinoblastoma-E2F pathway. J Cell Biol 173: 83–93.
18. Christodoulides C, Lagathu C, Sethi JK, Vidal-Puig A (2009) Adipogenesis and WNT signalling. Trends Endocrinol Metab 20: 16–24.
19. Moldes M, Zuo Y, Morrison RF, Silva D, Park BH, et al. (2003) Peroxisome-proliferator-activated receptor gamma suppresses Wnt/beta-catenin signalling during adipogenesis. Biochem J 376: 607–613.
20. Berger R, Theodor L, Shoham J, Gokkel E, Brok-Simoni F, et al. (1996) The characterization and localization of the mouse thymopoietin/lamina-associated polypeptide 2 gene and its alternatively spliced products. Genome Res 6: 361–370.
21. Hutchison CJ, Alvarez-Reyes M, Vaughan OA (2001) Lamins in disease: why do ubiquitously expressed nuclear envelope proteins give rise to tissue-specific disease phenotypes? J Cell Sci 114: 9–19.

22. Dreger M, Otto H, Neubauer G, Mann M, Hucho F (1999) Identification of phosphorylation sites in native lamina-associated polypeptide 2 beta. Biochemistry 38: 9426–9434.
23. Oksanen A (1971) Multilocular fat in thymuses of rats and mice associated with thymus involution: a light- and electron-microscope and histochemical study. J Pathol 105: 223–226.
24. Kvell K, Czompoly T, Hiripi L, Balogh P, Kobor J, et al. Characterisation of eGFP-transgenic BALB/c mouse strain established by lentiviral transgenesis. Transgenic Res 19: 105–112.
25. Seike M, Mizutani H, Sudoh J, Gemma A (2009) Epithelial to mesenchymal transition of lung cancer cells. J Nippon Med Sch 76: 181.
26. Beardsley TR, Pierschbacher M, Wetzel GD, Hays EF (1983) Induction of T-Cell Maturation by a Cloned Line of Thymic Epithelium (TEPI) 10.1073/pnas.80.19.6005. Proceedings of the National Academy of Sciences 80: 6005–6009.
27. Pongracz JE, Parnell SM, Jones T, Anderson G, EJ. J (2006) Overexpression of ICAT highlights a role for catenin-mediated canonical Wnt signalling in early T cell development. Eur J Immunol 36: 2376–2383.
28. Friedl P, Gilmour D (2009) Collective cell migration in morphogenesis, regeneration and cancer. Nat Rev Mol Cell Biol 10: 445–457.
29. Hiripi L, Negre D, Cosset FL, Kvell K, Czompoly T, et al. Transgenic rabbit production with simian immunodeficiency virus-derived lentiviral vector. Transgenic Res.
30. Kvell K, Nguyen TH, Salmon P, Glauser F, Werner-Favre C, et al. (2005) Transduction of CpG DNA-stimulated primary human B cells with bicistronic lentivectors. Mol Ther 12: 892–899.

PLOS ONE

RESEARCH ARTICLE

Thymic Atrophy and Apoptosis of $CD4^+CD8^+$ Thymocytes in the Cuprizone Model of Multiple Sclerosis

Izabella Solti[1☯], Krisztian Kvell[2☯], Gergely Talaber[3], Sara Veto[1], Peter Acs[4], Ferenc Gallyas, Jr.[1,5,6], Zsolt Illes[7], Katalin Fekete[1], Petra Zalan[1], Arpad Szanto[8], Zita Bognar[1]*

1 Department of Biochemistry and Medical Chemistry, University of Pecs, Pecs, Hungary, **2** Department of Pharmaceutical Biotechnology, University of Pecs, Pecs, Hungary, **3** Karolinska Institutet, Department of Biosciences and Nutrition, NOVUM, Huddinge, Sweden, **4** Department of Neurology, University of Pecs, Pecs, Hungary, **5** MTA-PTE Nuclear-Mitochondrial Research Group, Pecs, Hungary, **6** Szentagothai Research Center, University of Pecs, Pecs, Hungary, **7** Department of Neurology, Odense University Hospital, Institute of Clinical Research, University of Southern Denmark, Odense, Denmark, **8** Department of Urology, University of Pecs, Pecs, Hungary

☯ These authors contributed equally to this work.
* zita.bognar@aok.pte.hu

Citation: Solti I, Kvell K, Talaber G, Veto S, Acs P, Gallyas F, Jr., et al. (2015) Thymic Atrophy and Apoptosis of $CD4^+CD8^+$ Thymocytes in the Cuprizone Model of Multiple Sclerosis. PLoS ONE 10(6): e0129217. doi:10.1371/journal.pone.0129217

Academic Editor: Arun Rishi, Wayne State University, UNITED STATES

Received: February 24, 2015

Accepted: May 6, 2015

Published: June 8, 2015

Data Availability Statement: All relevant data are within the paper.

Funding: This work was supported by Hungarian grants OTKA NN109841 (FG) and PTE AOK KA 2013/4 (ZB). The funders had no role in study design, data collection and analysis, decision to publish, or preparation of the manuscript.

Competing Interests: The authors have declared that no competing interests exist.

Abstract

Previous studies on the degenerative animal model of multiple sclerosis suggested that the copper-chelator cuprizone might directly suppress T-cell functions. Peripheral T-cell function in the cuprizone model has already been explored; therefore, in the present study, we investigated, for the first time, how cuprizone feeding affects the thymus, the organ of T-cell maturation and selection. We found that even one week of cuprizone treatment induced significant thymic atrophy, affecting the cortex over the medulla. Fluorescent microscopy and flow-cytometric analyses of thymi from cuprizone- and vehicle-treated mice indicated that eradication of the cluster of the differentiation-4 (CD4)-CD8 double-positive T-cell subset was behind the substantial cell loss. This result was confirmed with CD3-CD4-CD8 triple-staining experiments. Ultrastructurally, we observed degraded as well as enlarged mitochondria, myelin-bodies, large lipid droplets, and large lysosomes in the thymi of cuprizone-treated mice. Some of these features were similar to those in physiological and steroid-induced accelerated aging. According to our results, apoptosis was mainly of mitochondrial origin mediated by both caspase-3- and apoptosis inducing factor-mediated mechanisms. Additionally, mitogen activated protein kinase activation and increased pro-apoptotic B cell lymphoma-2 family protein expression were the major underlying processes. Our results do not indicate a functional relationship between cuprizone-induced thymus involution and the absence of inflammatory responses or the selective demyelination observed in the cuprizone model. On the other hand, due to the reversible nature of cuprizone's deleterious effects, the cuprizone model could be valuable in studying thymus regeneration as well as remyelination processes.

Introduction

Administration of the copper chelator cuprizone to young adult C57BL/6 mice induces multifocal demyelination mainly in the corpus callosum and superior cerebellar peduncle [1] without significant T-cell activation in the affected areas [2]. According to histopathological studies [3], the pattern of cuprizone-induced demyelination resembles that of type III multiple sclerosis (MS) lesions characterised by oligodendrocyte degeneration and minor inflammation [4]. Therefore, the cuprizone model was extensively used for studying the degenerative aspects of MS [5]. The mechanism of the oligodendrocyte loss and demyelination in the cuprizone model is not well understood. Mature oligodendrocytes seem to be the primary targets, which are eliminated by apoptosis inducing factor (AIF)-mediated apoptosis [6]. Cuprizone-induced early formation of mega-mitoachondria in the liver [7] and oligodendrocytes [8], and expressional and functional changes of mitochondrial enzymes [9,10] indicate mitochondrial dysfunction behind the oligodendrocyte loss. However, there is no explanation for the preferential regional distribution of cuprizone-induced demyelination, and the exclusivity of the cell death toward oligodendrocytes.

Unlike the cuprizone model, experimental allergic encephalomyelitis (EAE) reflects the autoimmune feature of MS [11,12]. In this model, after immunising the animals with myelin antigens, myelin-specific $CD4^+$ T-cells are initially activated in the peripheral immune organs and migrate to the central nervous system (CNS) [13] where they encounter their cognate antigen on CNS antigen presenting cells and produce immune mediators such as pro-inflammatory cytokines and chemokines. These immune mediators locally activate the second cascade of the autoimmune response involving microglia, the resident macrophage [14,15]. In contrast, demyelinating areas in the cuprizone model, were reported to lack B and T-cells, and the blood brain barrier was found to be intact [2,16]. Additionally, with respect to the cuprizone model, RAG-1(1/1) mice, which lack mature B and T lymphocytes are indistinguishable from controls, indicating that T-cells may not play a role in cuprizone-induced demyelination [16]. The major difference between type III MS lesions and cuprizone-induced demyelination is the presence of perivascular inflammation and $CD3^+$ T-cells in the former [4]. This difference, along with the down-regulation of EAE by cuprizone-treatment [16–18] suggests that cuprizone may directly suppress T-cell functions [19]. A previous study [17] has already explored peripheral T-cell function in the cuprizone model. However there is no data regarding the thymus, the organ of T-cell maturation and selection. To elaborate on the suggested suppressive effect of cuprizone on T-cell function, in the present study, we investigated how cuprizone feeding affects the thymus.

Materials and Methods

Ethics Statement

The investigation conforms to the Guide for the Care and Use of Laboratory Animals published by the U.S. National Institutes of Health (NIH Publication No. 85–23, revised 1996), and was approved by the Animal Research Review Committee of the University of Pecs, Medical School.

Animals and cuprizone administration

C57BL/6 male mice were purchased from Charles River Laboratories Hungary Ltd (Isaszeg, Hungary) and kept under standardised, specific pathogen free circumstances. Starting at four weeks of age, mice received a diet of powdered rodent chow containing 0.2% cuprizone (bis-cyclohexanone oxaldihydrazone) (Sigma, Steinheim, Germany) by weight for three or seven days *ad libitum*. Age and gender matched littermates receiving powdered rodent chow served as the control group.

Acquisition of thymus samples

The weight of the mice was measured at the beginning and at the end of the treatment period. Then, animals were euthanised with an overdose of ketamine hydrochloride intraperitoneally, and their chest was opened. The thymi were photographed, carefully dissected and their wet weight was measured. They were freshly processed for RNA isolation, fixed for electron microscopy, frozen for histochemistry and immunohistochemistry, or homogenised in phosphate buffered saline (PBS) with a glass/glass homogeniser. Alternatively, thymic cell suspension was prepared by gentle mechanic agitation followed by filtering through a nylon mesh. The suspension was washed once and the cells were resuspended in PBS. An aliquot of cells was diluted 1:100, the cells were counted using the Trypan blue method with a hemocytometer, and the cell number was set to $5x10^5$ or 10^6 per sample.

Thymic epithelial cell (TEC) enrichment

TECs were enriched as previously described [20]. Briefly, the thymic lobes were digested using a collagenase-based solution. Then TECs were labelled with anti-epithelial cell adhesion molecule- (EpCAM1) antibody followed by their direct enrichment using magnetic beads (Dynabeads). TEC purity was repeatedly found to be approx. 90% based on qRT-PCR measurements as published previously.

Apoptosis detection

For apoptosis detection, double staining with Annexin V-fluorescein isothyocyanate (FITC; BD Pharmingen, CA) and propidium-iodide (Sigma-Aldrich) was performed according to Vermes et al. [21]. Briefly, $5x10^5$ thymocytes were resuspended in 100 μl Annexin binding buffer (10mM HEPES/NaOH, pH 7.4, 140mM NaCl and 2.5mM $CaCl_2$) and incubated for 20 minutes at room temperature with Annexin V-FITC in the dark, before then being diluted with 400 μl Annexin binding puffer. Propidium-iodide was given to the cells immediately before the flow-cytometric analysis. Two-parameter dot-plots showing Annexin V/propidium-iodide staining (FL1/FL3 channels) were created to determine the ratio of apoptotic cells in the thymus glands.

Flow-cytometry

For the simultaneous detection of cell surface expressed CD4, CD8 and CD3, a triple labelling technique was used. Thymocyte samples were incubated with monoclonal antibody cocktails for 30 min in 100 ml binding buffer on ice (PBS containing 0.1% NaN_3 and 0.1% BSA), then washed twice in PBS, and finally resuspended in 500 ml 0.1% buffered PFA (paraformaldehyde) in PBS. For staining the following monoclonal antibodies were used: phycoerythrin (PE) conjugated rat anti-mouse CD4, CyChrome (CyC) conjugated rat anti-mouse CD8 and FITC conjugated rat anti-mouse CD3, all purchased from BD Pharmingen, CA. Samples were measured and analysed in a FACSCalibur flow-cytometer (Becton Dickinson, San Jose, CA), using the CellQuest software. Generally 10.000 events were recorded. Thymocytes were gated according to their size and granularity on forward and side scatter dot plots. The gate set on untreated control living thymocytes was used for the analysis of all samples. We used fluorescent dot plots for both comparing the different samples and for calculating the ratio of positively stained cells.

Immunofluorescence

Frozen thymic sections (7–10 μm thick) were fixed in cold acetone, then air-dried and blocked using 5% bovine serum albumin (BSA) in PBS for 20 min before staining with a-Ly51-PE (clone

6C3, BD Biosciences) and a-EpCAM1-FITC (clone G8.8, hybridoma from the Dept. Immunology and Biotechnology, University of Pecs) antibodies for at least 30 minutes to visualise the thymic epithelial network (EpCAM-1 is a marker for all TECs, but stains the medullar area stronger than the cortical area, while Ly51 stains only cortical TECs). The remaining sections were stained under the same conditions with a-CD4-FITC (YTS191.1, hybridoma from the Dept. Immunology and Biotechnology, University of Pecs) and a-CD8-Alexa fluor 647 (clone 53–6.7, BD Biosciences) to analyse the staining pattern of the thymocytes. The sections were analysed using an Olympus BX61 microscope equipped with CCD-camera and AnalySIS software.

Electron microscopy

In order to investigate ultra-structural changes of the thymic lobes, mice were sacrificed after three days of treatment and their thymi were fixed in buffered 2.5% formaldehyde—2.5% glutaraldehyde solution for 24 hours at 4°C. After washing in phosphate buffer, the samples were fixed in 1% osmium tetroxide in 0.1 M PBS for 35 minutes. After that, the samples were washed in buffer several times for 10 minutes and dehydrated in an ascending ethanol series, including a step of uranyl acetate (1%) solution in 70% ethanol to increase contrast. Dehydrated blocks were transferred to propylene oxide before being placed into aluminium-foil boats containing Durcupan resin (Sigma) and then embedded in gelatine capsules containing Durcupan. The blocks were placed in thermostate for 48 hours at 56°C. From the embedded blocks 1 μm semithin and serial ultrathin sections (70 nanometer) were cut with Leica ultramicrotome, and mounted either on mesh, or on Collodion-coated (Parlodion, Electron Microscopy Sciences, Fort Washington, PA) single-slot copper grids. Additional contrast was provided to these sections with uranyl acetate and lead citrate solutions, and they were examined with JEOL 1200EX-II electron microscope.

Immunoblot analysis

Tissue samples were taken from animals sacrificed after three or seven days of treatment. The thymi of the mice were carefully dissected and 25 mg tissues were homogenised in ice-cold 10 mM Tris buffer, pH 7.4 (containing 0.5 mM sodium metavanadate, 1mM EDTA and protease inhibitor cocktail (1:200); all purchased from Sigma-Aldrich, Steinheim, Germany). Homogenates (10 μg each) were boiled and subjected to 10% sodium dodecyl sulphate polyacrylamide gel electrophoresis then were transferred to nitrocellulose membranes. The membranes were blocked in 5% low fat milk for 1.5 h at room temperature before then being exposed to primary antibodies at 4°C overnight in a blocking solution. The following antibodies were used: Polyclonal caspase 3 (1:500, clone H-277), monoclonal Histone H1(1:200), polyclonal Cytochrome c, polyclonal AIF, monoclonal phospho-p38 MAPK (Thr180/Tyr182), polyclonal phospho-extracellular signal-regulated kinase (ERK)1/2 (Thr202/Tyr204), polyclonal phospho-specific c-Jun N-terminal kinase (JNK) Thr183-Tyr185, polyclonal Bad (D24A9), polyclonal phospho-Bad (Ser112), polyclonal BIM and polyclonal Bax antibodies (each 1:500 dilution), monoclonal Glyceraldehyde-3-phosphate dehydrogenase (1:2000, clone 6C5). Antibodies were purchased from Cell Signaling Technology (Beverly, MA, USA) except from caspase 3, Histone H1 that were bought from Santa Cruz Biotechnology (Wembley, UK), Glyceraldehyde-3-phosphate dehydrogenase antibody was obtained from Merck Millipore. Appropriate horseradish peroxidase-conjugated secondary antibodies were used at a 1:5.000 dilution (anti-mouse and anti-rabbit IgGs; Sigma-Aldrich, Steinheim, Germany) and visualised by enhanced chemiluminescence (Amersham Biosciences, Piscataway, New Jersey, USA). The films were scanned, and the pixel volumes of the bands were determined using NIH Image J software (Bethesda, Maryland, USA). For membrane stripping and re-probing, the membranes were washed in a stripping

buffer (0.1 M glycine, 5 M $MgCl_2$, pH 2.8) for an hour at room temperature. After washing and blocking, the membranes were incubated with primary antibodies for non-phosphorylated or loading control proteins.

RNA isolation and quantitative polymerase chain reaction (qPCR) analysis

To investigate the relative expression of thymic epithelial cell markers major histocompatibility complex (MHC)II and autoimmune regulator (AIRE), we used a real-time qPCR approach after seven days of treatment. From carefully dissected thymi, the total RNA was extracted and DNase digestion was performed using the NucleoSpin RNA isolation kit (Macherey-Nagel, Düren, Germany) as described in the manufacturer's manual. For quality control, RNA purity was verified using the optical density $(OD)_{260/280}$ ratio and was found to be between 1.8 and 2.0. The total RNA (1.0μg) was reverse-transcribed to cDNA using the High-Capacity cDNA reverse transcription kit (Applied Biosystems). Subsequent qPCR reactions for MHCII and AIRE were performed in duplicate on the Applied Biosystems HT7500 system using the Absolute QPCR SYBR Green low ROX Mix (Abgene, Epsom, UK) with specific primers (MHC II forward primer: 5′ -CTA GCC AAG TCC CTC CTA AGG-3′ , reverse primer: 5′ - ATC TCA GAC TGA TCC TGG CAT -3′ ; AIRE forward primer: 5′ -ACC TAA ACC AGT CCC GGA AAG-3 ', reverse primer: 5′ -CGA GGC TCC AGT GCT T-3′). The three step qPCR was performed using 58°C annealing temperature and 30sec elongation period. Analysing melting curves validated the specificity of products from each primer set. All experimental samples were analysed and normalised with the internal control gene, 18 S rRNA (forward primer: 5′ -GGG TCG GGA GTG GGT AAT TT-3′ , reverse primer: 5′ -AGA AAC GGC TAC CAC ATC CAA-3′). Relative quantification of the fold-change was performed comparing *Ct* values from individual mice, applying the $2^{-\Delta\Delta Ct}$ method [22,23].

Statistical analysis

All experiments were repeated at least three times, including at least three animals in each group, for each experiment. Accordingly, the mean + the standard error of the mean (SEM) values of the individual animals ($n \geq 9$) were presented in the figures and throughout the text. On the other hand, for comparing groups, we utilised data of the experiments repeated at least three times, including at least three animals in each groups. We used one-way or two-way analysis of variance, followed by Tukey's post-hoc test. When the F-test indicated unequal variances, the Kruskal-Wallis test was performed. Differences were considered significant at values of $p<0.05$ or lower.

Results

Cuprizone induced acute thymic atrophy

In order to investigate the effect of cuprizone on the thymus, four-week-old male C57BL/6 mice were fed with pulverised chow containing 0.2% of the drug. As early as after one week of cuprizone administration, severe thymic atrophy was observed (Fig 1) that was accompanied by significant thymic tissue mass loss when compared to the control (Fig 1B). Since cuprizone treatment resulted in a significant weight loss for the animals as well (Fig 1C), we normalised their thymic mass to their body mass, and found this relative thymus mass still reduced in the cuprizone-treated mice (Fig 1D), indicating a disproportional thymus involution in these animals. The absolute thymocyte number was also found to be lowered from $1.7\pm0.2 \times 10^8$ to $7.8 \pm 2.3 \times 10^6$ upon cuprizone treatment.

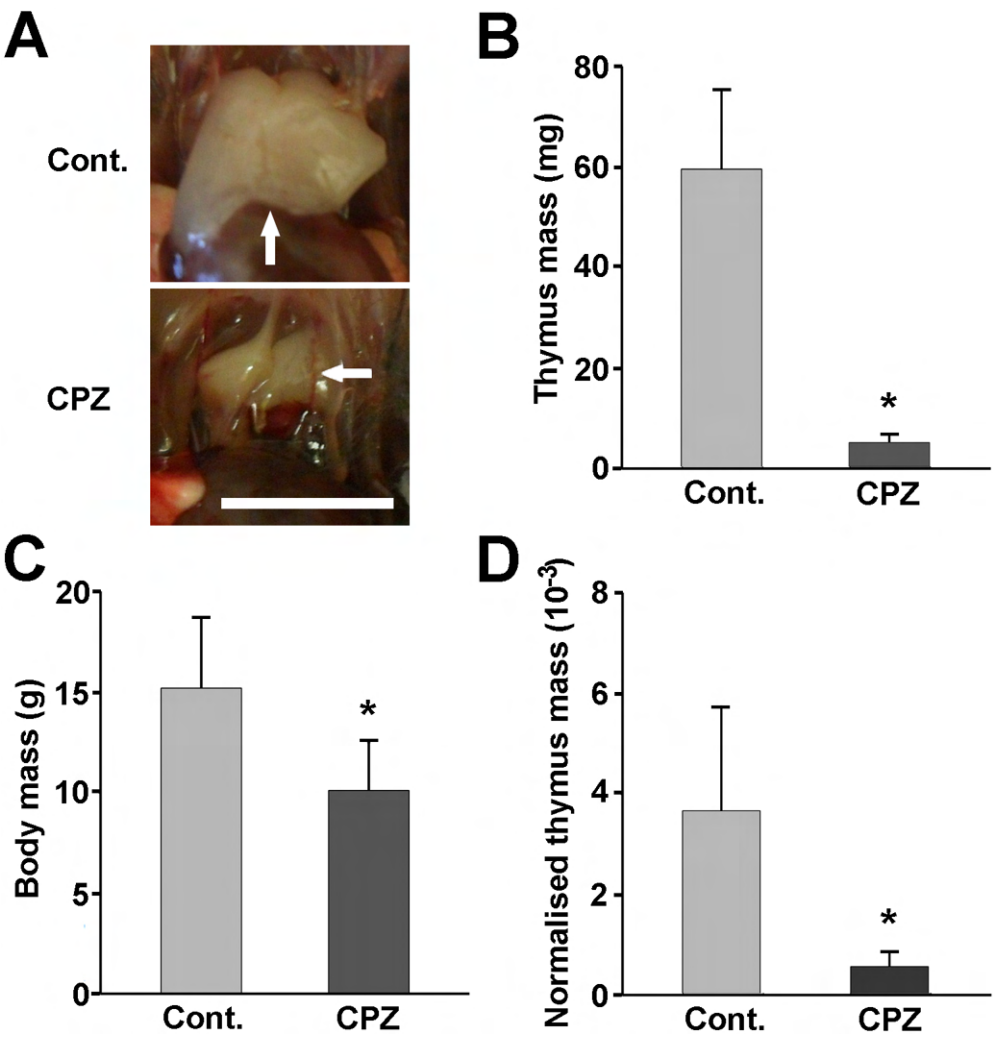

Fig 1. Macroscopic changes of the thymi upon cuprizone treatment. Four week-old male mice were treated with cuprizone for one week. Representative photographs (A) of the open chest of a control (Cont.) and a cuprizone-treated (CPZ) animal are demonstrated. Arrows point to the thymi of the mice. The scale bar indicates 5 mm. Thymus mass (B), body mass (C) and relative thymus mass (thymus tissue mass/ body mass) (E) of control (grey bars) and cuprizone-treated (black bars) animals are presented as bar diagrams, mean + SEM ($n \geq 9$). * denotes a significant difference from control $p<0.05$.

doi:10.1371/journal.pone.0129217.g001

Cuprizone-induced cell death was predominantly apoptotic

We investigated the type of cell death responsible for the substantial cuprizone-induced thymic involution by performing flow-cytometry on the thymic cell suspension following double staining the cells with FITC-conjugated Annexin V and propidium iodide. Propidium iodide is excluded by viable cells. On the other hand, it can penetrate cell membranes of dying or dead cells, and intercalate into double-stranded nucleic acids, thereby increasing the intensity of its fluorescence manyfold. Annexin V binds to phosphatidylserine exposed on the surface of apoptotic cells only, and therefore, this staining technique can differentiate between living (double negative), early apoptotic (Annexin V single positive), and late apoptotic/necrotic (AnnexinV and propidium iodide double positive) cells. As we found, in the untreated control mice, most of the cells were double negative (83.9 ± 4.1%), which was substantially decreased in cuprizone treated animals (22.8 ± 13.2%, $p<0.001$, Fig 2). In these mice, the decrease in the living cells

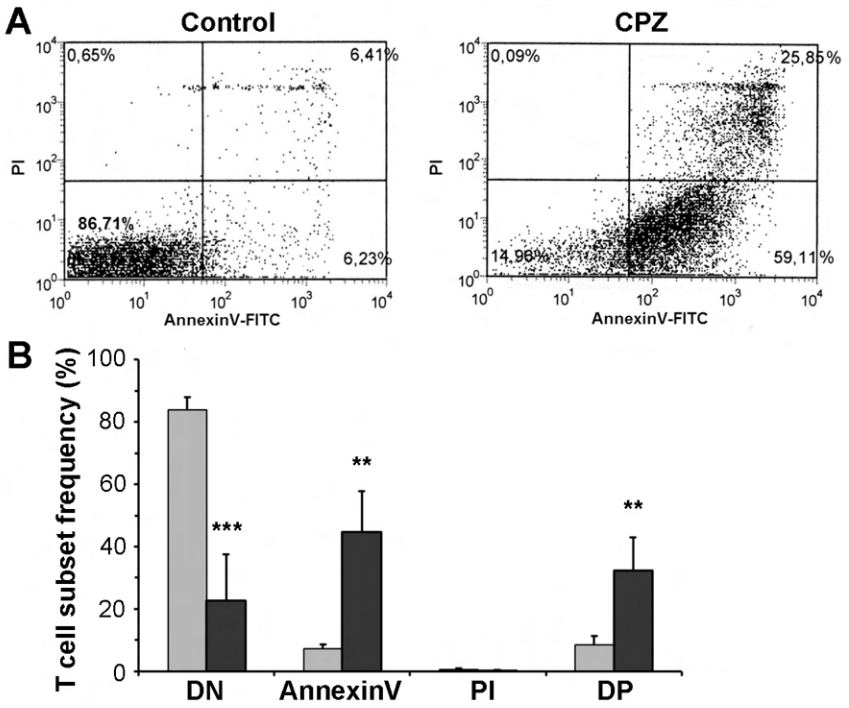

Fig 2. Characterisation of cuprizone-induced cell death. Four week-old male mice were treated with cuprizone for one week. Type of cell death was determined using flow cytometry following double staining with FITC-labelled AnnexinV and propidium iodide thymus suspensions of untreated (Control, grey bars) and cuprizone-treated (CPZ, black bars) mice. Results are presented as representative dot-plots (A) and bar diagrams (B), mean + SEM ($n \geq 9$). Significant difference from control; **p<0.01, *** p<0.001. DN: live cells (lower left quadrant); AnnexinV: early apoptotic cells (lower right quadrant); PI: necrotic cells (upper left quadrant); DP: late apoptotic cells (upper right quadrant).

doi:10.1371/journal.pone.0129217.g002

was accompanied by a significant increase of the early apoptotic (44.6 ± 13.2%, $p<0.001$) and late apoptotic/necrotic cells (32.4 ± 10.5%, $p<0.01$, respectively Fig 2). We could not observe propidium iodide single positivity among the animals regardless of the treatment. All these data indicate that the cuprizone-induced death was preponderantly apoptotic.

Cuprizone-induced cell loss in the cortex was more severe than in the medulla

We determined macroscopic morphological characteristics of the cuprizone-induced thymus involution by fluorescent microscopy after double staining thymus sections with FITC-labelled anti-EpCAM1 and PE-labelled anti-Ly-51 antibodies. The former antibody stains mostly the medulla while the latter stains the cortex of the thymus. We observed more substantial cell loss in the cortex than in the medulla (Fig 3A). To support these findings, we determined the MHCII and AIRE mRNA levels in the thymi of the control and cuprizone treated mice. We found a significant abundance of both of these medulla-associated markers in the cuprizone treated animals (Fig 3B), indicating that cuprizone preferentially affected cortical cells.

Cuprizone eliminated mostly the CD4-CD8 double positive immature thymocytes

To further analyse cuprizone's effect on the thymus, we performed anti-CD4 (green) and anti-CD8 (red) immunofluorescence microscopies. On merged images of the control thymi, the

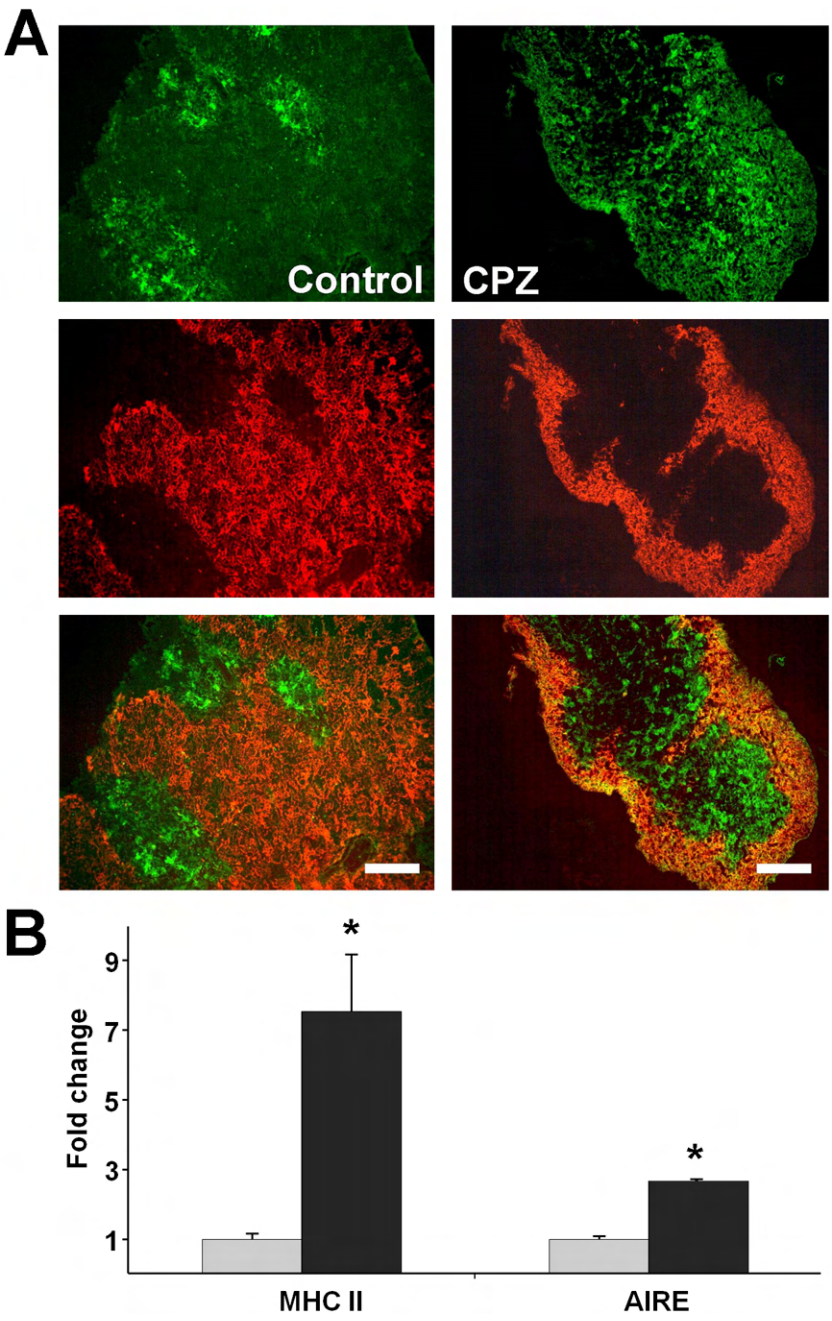

Fig 3. Effect of cuprizone on thymic epithelial cells. Four week-old male mice were treated with cuprizone for one week, then immune-staining (A) with FITC-labelled anti-EpCAM1 (green) and PE-labelled anti-Ly-51 (red) antibodies was performed on thymic sections of untreated (Control) and cuprizone-treated (CPZ) mice. Representative images (A) are presented of the green channel (top panels), the red channel (middle panels) and the merged channels (bottom panels) of three independent experiments, including at least three animals in each group for each experiment. Fluorescent photographs were taken using a 10x objective. The scale bar indicates 200 μm. In a parallel experiment, thymic MHC II and AIRE mRNA expression (B) was determined by using qPCR analysis in untreated (grey bars) and cuprizone-treated (black bars) mice. Results are presented as fold change, mean + SEM ($n \geq 9$). Significant difference from control; *$p<0.05$.

doi:10.1371/journal.pone.0129217.g003

cortex appeared yellow as it is mainly occupied by $CD4^+CD8^+$ thymocytes while the medulla appeared green because of the predominance of $CD4^+$ cells (Fig 4A). Cuprizone-treatment resulted in an almost complete disappearance of the double positive and a relative increase of the $CD4^+$ areas, as well as an overall less dense staining of the shrunken thymi (Fig 4A). To ensure that the double positivity of the control cortices indeed resulted mainly from the presence of the $CD4^+CD8^+$ thymocytes, we performed anti-CD4 and anti-CD8 flow-cytometry on the thymic suspensions. To exclude dead or apoptotic cells, the gate was set on untreated control thymocytes and was fixed for the whole analysis. In the case of the four week-old male C57BL/6 control mice, we found that the most considerable population was that of $CD4^+CD8^+$ thymocytes (73.4 ± 2.6%, Fig 4B and 4C). The most immature $CD4^-CD8^-$ thymocytes made up 9.8 ± 5.3%, while the most mature $CD4^+$ and $CD8^+$ thymocytes represented 11.6 ± 2.2 and 5.3 ± 1.7% of the total population, respectively (Fig 4B and 4C). One week of cuprizone treatment completely eradicated $CD4^+CD8^+$ thymocytes (1.0 ± 0.1%, $p<0.001$, Fig 4B and 4C). If we consider the total cell numbers of the thymi, this decrease was from $1.3 \pm 0.2 \times 10^8$ to $8.1 \pm 3.5 \times 10^4$ double positive thymocytes suggesting a complete disappearance of this cell population. This finding is reflected by a decrease of the double positive/double negative thymocyte ratio from 7.5 ± 4.5 to 0.04 ± 0.02 ($p<0.001$) upon cuprizone treatment, while all other ratios ($CD4^+/CD8^+$ and $CD4^+$/double negative) remained practically unchanged (Fig 4C).

CD3 expression increases along thymocyte maturation. Accordingly, we stained thymus suspensions for CD3, performed flow-cytometry, and assessed the ratio of immature ($CD3^{low}$) and mature ($CD3^{high}$) thymocytes in the untreated and cuprizone-treated groups. In four week-old male C57BL/6 control mice, we found that the $CD3^{low}$ and $CD3^{high}$ thymocytes comprised about 76 and 19%, respectively, of the whole thymocyte population. One week of cuprizone treatment resulted in a significantly lower proportion of immature thymocytes (28.2 ± 8.8, $p<0.001$) and a corresponding increase in the ratios of mature (67.5 ± 8.5, $p<0.001$) thymocytes (Fig 5A and 5B). Thereby, cuprizone treatment increased the $CD3^{high}/CD3^{low}$ ratio from about 0.25 to 2.4 ($p<0.001$, Fig 5B) indicating that cuprizone eliminated immature thymocytes preferentially. Additionally, we triple stained thymocytes of control and cuprizone-treated animals for CD3, CD4 and CD8, and performed flow cytometry on them. When we filtered the results for the $CD3^{low}$ (Fig 5C and 5D) and $CD3^{high}$ (Fig 5E and 5F) subpopulations, we found changes in the T-cell subset frequencies upon cuprizone treatment that were completely consistent with those we found on the unfiltered population, as well as being consistent with our present knowledge of CD3, CD4 and CD8 expression during thymocyte maturation. Namely, almost all CD4-CD8 double positive cells were $CD3^{low}$ and were almost completely depleted by cuprizone (Fig 5C and 5D). Additionally, there was CD8 and CD4 dominance in the $CD3^{low}$ and $CD3^{high}$ subset, respectively that was augmented by the cuprizone treatment (Fig 5C–5F).

Cuprizone induces subcellular structural alterations in thymic cells

Cuprizone was reported to induce giant mitochondria formation and mitochondrial malfunctioning in mouse liver [24]. Since mitochondria are major regulators of the cell death process [25], we assessed cuprizone's effect on thymic mitochondria by using electron microscopy. As demonstrated in Fig 6, cuprizone-treated thymic cells contained both enlarged and medium-sized mitochondria (Fig 6B); the latter are similar to those observed in untreated animals (Fig 6A). The diameter of the enlarged mitochondria did not reach 1 μm, the conventional threshold to be categorised as mega-mitochondria [26]. In addition to enlarged mitochondria, cuprozine treatment resulted in the degradation of cellular organelles, such as mitochondria (Fig 6C). Myelin-bodies (Fig 6C), large lipid droplets (Fig 6D) and large lysosomes packed with dark-staining material (Fig 6E) were also frequently observed.

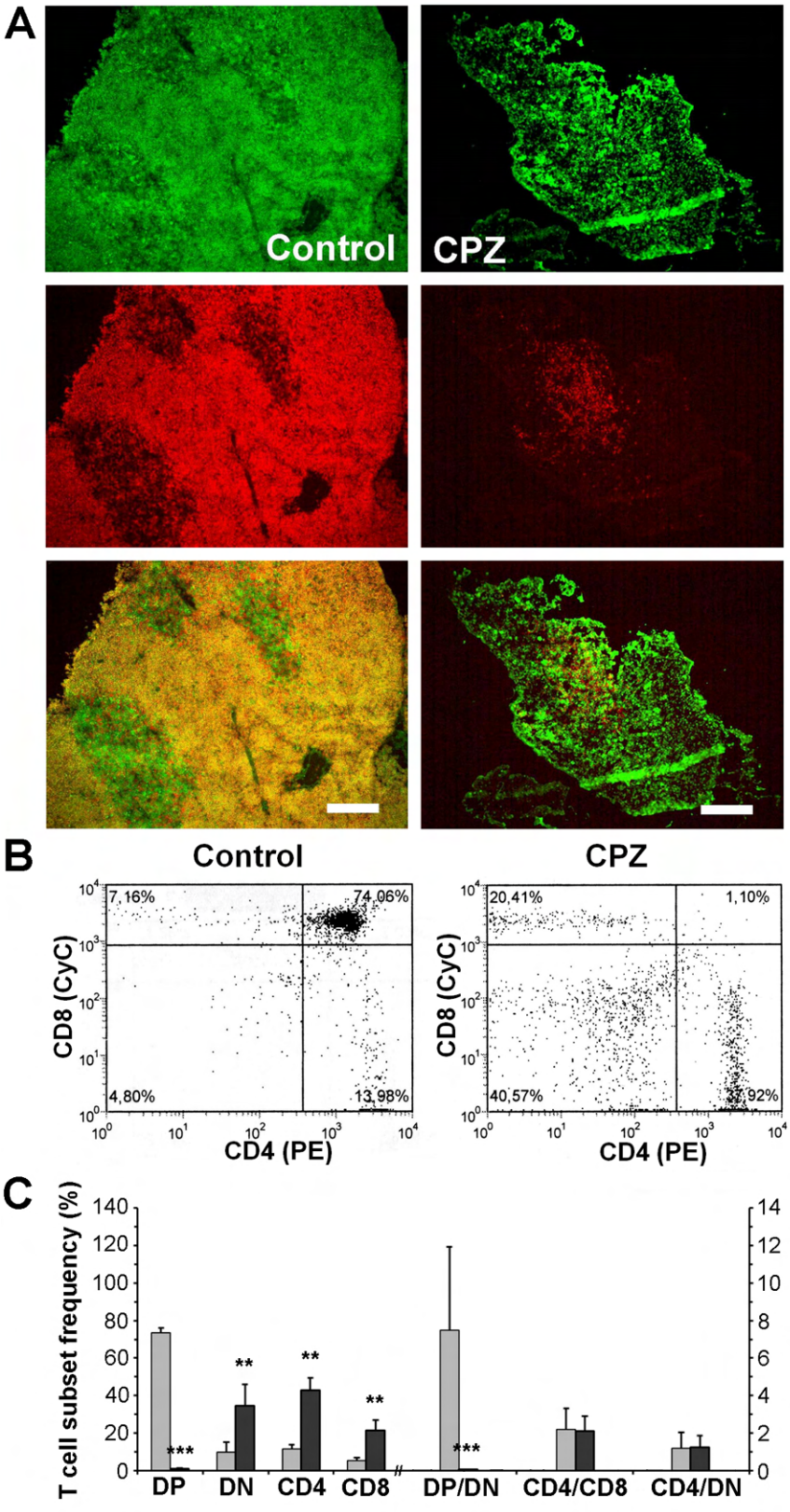

Fig 4. Effect of cuprizone treatment on thymocytes. Four week-old male mice were treated with cuprizone for one week, then immune-staining (A) with FITC-labelled anti-CD4 (green) and Alexa647-labelled anti-CD8

(red) antibodies was performed on thymic sections of untreated (Control) and cuprizone-treated (CPZ) mice. Representative images (A) are presented of the green channel (top panels), the red channel (middle panels) and the merged channels (bottom panels) of three independent experiments including at least three animals in each group for each experiment. Fluorescent photographs were taken using a 10x objective. The scale bar indicates 200 μm. In a parallel experiment, flow cytometry was performed on thymus suspensions of untreated (Control, grey bars) and cuprizone-treated (CPZ. black bars) mice following double staining with PE-labelled CD4 and CyChrome (CyC)-labelled CD8 antibodies. Results are presented as representative dot-plots (B) and bar diagrams (C), mean + SEM ($n \geq 9$). Significant difference from control; **$p<0.01$, ***$p<0.001$. DN: $CD4^-/CD8^-$ cells (lower left quadrant); CD4: $CD4^+$ cells (lower right quadrant); CD8: $CD8^+$ cells (upper left quadrant); DP: $CD4^+/CD8^+$ cells (upper right quadrant); DP/DN: ratio of DP and DN cells; CD4/CD8: ratio of $CD4^+$ and $CD8^+$ cells; CD4/DN: ratio of $CD4^+$ and DN cells. Please note that the x-axis is broken, and the ratios are measured on the right y-axis.

doi:10.1371/journal.pone.0129217.g004

Cuprizone-treatment activated mitochondrial death pathways

To investigate which death pathways were involved in cuprizone-induced thymic atrophy, we examined caspase activation, pro-apoptotic mitochondrial inter-membrane protein release, and major pro- and anti-apoptotic B cell lymphoma (BCL) proteins by using immunoblot analysis of thymus homogenates of untreated and cuprizone-treated animals. We used thymi after only three days of cuprizone-feeding since we were interested in the processes leading to the massive thymocyte loss.

We detected a substantial release to the cytoplasm of cytochrome C, in addition to a resulting increased cleavage i.e. activation of caspase 3 (Fig 7A), but not of caspase 8 (data not shown). We also observed nuclear translocation of AIF (Fig 7A), indicating that the cuprizone-induced apoptosis was of mainly mitochondrial origin. We found that the pro-apoptotic Bcl-2 family members Bim, Bax and Bad had overlapping functions in cuprizone-induced killing of CD4-CD8 double-positive thymocytes. The expression level of all three proteins was increased significantly after three days of cuprizone-treatment, although, Bax expression was augmented at least 10 times over the other two (Fig 7B). Additionally, increased Bad expression was accompanied by decreased phosphorylation of the protein (Fig 7B) that emphasises its pro-apoptotic role in cuprizone-induced thymocyte loss.

Cuprizone-treatment activated all three MAP kinases

A number of reports implicate MAPK activation as a causative factor of mitochondrial damage and apoptotic cell death [27,28]. Therefore, we assessed phosphorylation i.e. activation of JNK, ERK and p38 in thymus homogenates by using phosphorylation-specific primary antibodies and immunoblotting. After three days of cuprizone-feeding we found increased activation of all three MAP kinases. JNK and p38 phosphorylation were increased upon cuprizone treatment by over 600% while ERK phosphorylation increased by only about 30% (Fig 7C).

Discussion

To enhance our knowledge of the degenerative animal model of MS, we investigated the effect of cuprizone on the thymus, the site of T-cell maturation and selection. Although, thymus involution in the cuprizone model is extremely apparent (Fig 1A), we could not find any previous report mentioning it. Cuprizone-treatment results in reduced thriving of the animals [29]; however, thymus retardation upon cuprizone-treatment was more pronounced than that of the rest of the body (Fig 1D), resulting mainly from apoptotic death (Fig 2).

By using immunostaining and fluorescent microscopy, we demonstrated that cuprizone-treatment affected the cortex over the medulla (Fig 3A), supported by the relatively higher expression level (Fig 3B) of AIRE, a gene expressed by the thymic medullary epithelial cells [30],

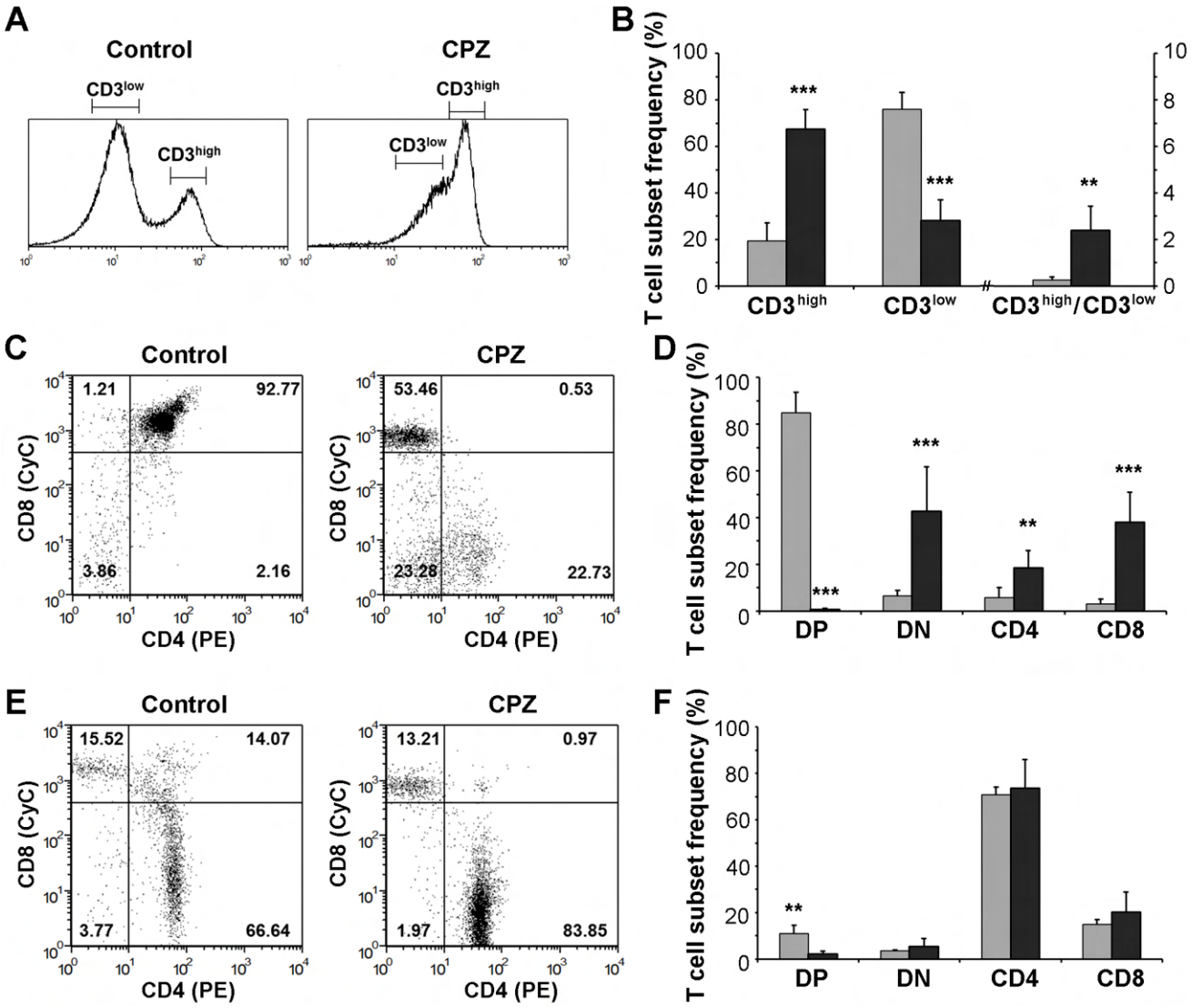

Fig 5. Effect of cuprizone treatment on thymocyte subpopulations. Four week-old male mice were treated with cuprizone for one week, then flow cytometry was performed on thymus suspensions on thymus suspensions of untreated (Control, grey bars) and cuprizone-treated (CPZ, black bars) mice following triple staining with FITC-labelled CD3, PE-labelled CD4 and CyChrome (CyC)-labelled CD8 antibodies. Based on CD3 positivity (A, B) the data on CD4 and CD8 were allocated to low ($CD3^{low}$; C, D) and high ($CD3^{high}$; E, F) CD3 positivity subgroups (the ranges are indicated in A). Results are presented as representative line charts (A), dot-plots (C, E) and bar diagrams (B, D, F), mean + SEM ($n \geq 9$). Significant difference from control; **p<0.01, *** p<0.001. DN: $CD4^-/CD8^-$ cells (lower left quadrant); CD4: $CD4^+$ cells (lower right quadrant); CD8: $CD8^+$ cells (upper left quadrant); DP: $CD4^+/CD8^+$ cells (upper right quadrant); $CD3^{high}/CD3^{low}$: ratio of $CD3^{high}$ and $CD3^{low}$ cells. Please note that the x-axis in B is broken, and the ratio is measured on the right y-axis.

doi:10.1371/journal.pone.0129217.g005

in the thymi of cuprizone-treated mice. Since the cortex is associated mostly with the positive selection of T-cells while the medulla is the location of the negative selection of auto-reactive T-cells from the mature repertoire, this result indicated that cuprizone affected immature T-cells more severely than it affected the mature ones. Accordingly, the observed relatively higher expression level of MHCII (Fig 3B) in the thymi of cuprizone-treated mice resulted mainly from the preservation of mature T-cells residing dominantly in the medulla.

We intended to identify the T-cell subpopulation that was most sensitive to cuprizone. Immunofluorescence and flow-cytometry analysis revealed that cuprizone eradicated $CD4^+CD8^+$ T-cells while practically did not affect ratios of other T cell subpopulations (Fig 4).

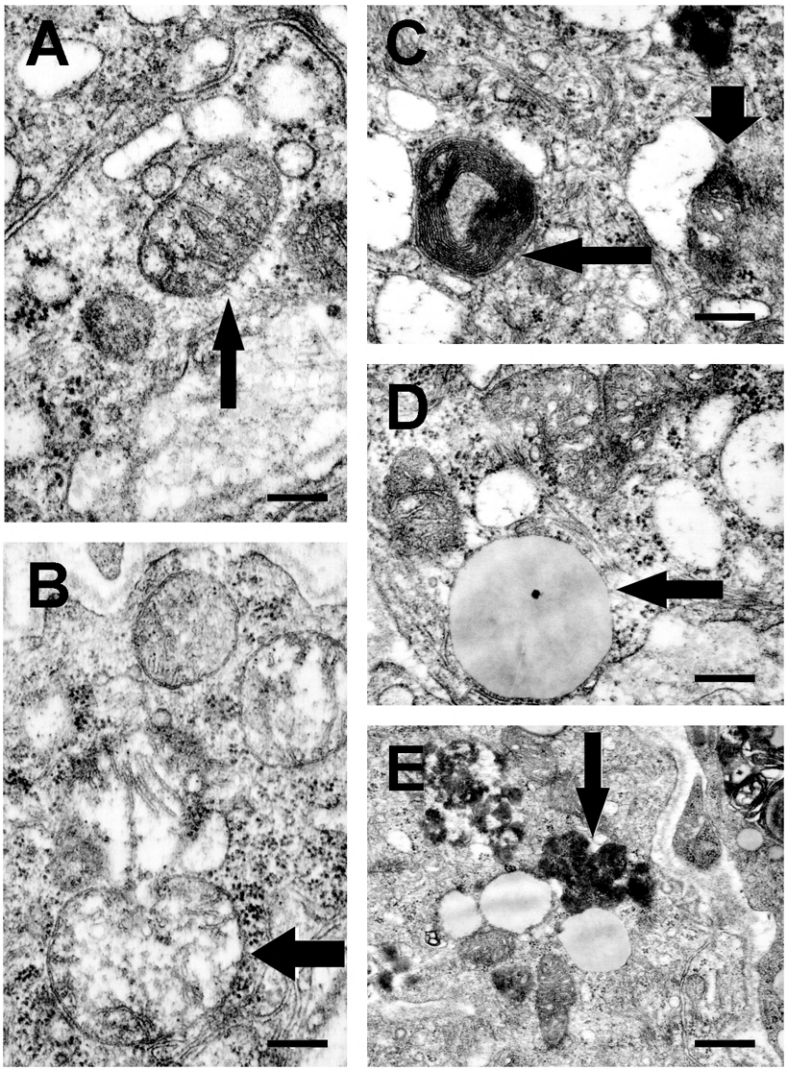

Fig 6. Effect of cuprizone treatment on subcellular morphology. Four week-old male mice were treated with cuprizone for one week. Subcellular morphology was assessed in ultrathin thymic sections of control (A) and cuprizone-treated (B-E) mice. Representative images are presented of three independent experiments including at least three animals in each group for each experiment. Arrows indicate normal (A) and enlarged (B) mitochondria, a large lipid droplet (D), and large lysosomes packed with darkly stained material (E). Horizontal thin and vertical thick arrows in (C) point to myelin body and a degraded mitochondrion, respectively. Scale bars indicate 200 nm.

doi:10.1371/journal.pone.0129217.g006

These results were confirmed when we filtered the results of CD4 and CD8 positivity of the cells according to their CD3 status. The double positive subset of T-cells of low CD3 status was abolished by cuprizone while there was $CD8^+$ dominance among the surviving cells, and a corresponding $CD4^+$ dominance was observed among the cuprizone-resistant T-cells of high CD3 status (Fig 5). These data are in accord with our aforementioned findings and the present view of T-cell maturation. Namely, immature double negative T-cells first express CD8 before becoming double positive, which cells undergo positive and negative selection to reach their mature $CD4^+$ or $CD8^+$ phenotype, while CD3 positivity increases along the maturation process.

By chelating copper, cuprizone may interfere with cellular energy metabolism. Supporting this notion, megamitochondrion formation was observed as early as after three days of

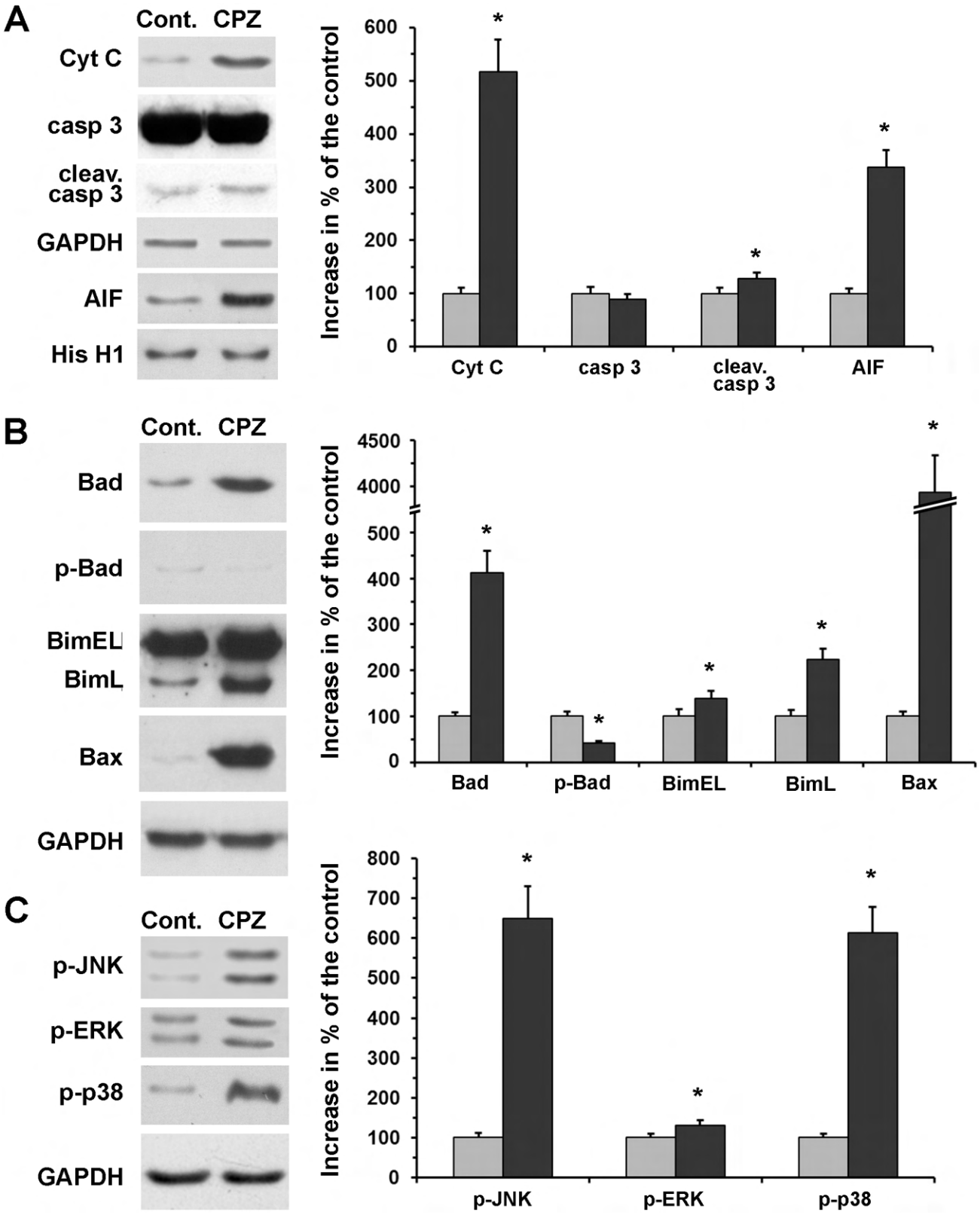

Fig 7. Effect of cuprizone treatment on death pathway and signalling proteins in the thymus. Four week-old male mice were treated with cuprizone for three days. Steady-state cytoplasmic levels of cytochrome C (Cyt C) (A), caspase 3 (casp 3) (A), cleaved caspase 3 (cleav. casp 3) (A) and nuclear

apoptosis inducing factor (AIF) content (A), as well as cellular levels of Bad (B), BimEL (B), BimL (B) and Bax (B) were assessed in the thymi of untreated (Cont., grey bars) and cuprizone-treated (CPZ, black bars) mice by using specific primary antibodies and immunoblotting. The activation state of Bad (p-Bad) (B), JNK (p-JNK) (C), ERK (p-ERK) (C) and p38 MAPK (p-p38) (C) was also determined by using phosphorylation-specific primary antibodies and immunoblotting. GAPDH (A-C) and histone H1 (His H1) (A) were used as loading controls for cytoplasmic/cellular and nuclear fractions, respectively. Results are presented as representative immunoblots and bar diagrams, mean + SEM ($n \geq 9$). Significant difference from control; *$p<0.05$. Please note that the y-axis in B is broken to accommodate the very high Bax value.

doi:10.1371/journal.pone.0129217.g007

cuprizone-feeding in mouse liver [24,29], and the oligodendrocytes of the corpus callosum [31]. Furthermore, increased ROS production, and decreased activities of the various complexes of the respiratory chain were found in the mitochondria of cuprizone-treated oligodendroglia cells [32,33]. We found degraded, as well as enlarged, although not giant, mitochondria in the thymi of cuprizone-treated mice (Fig 6). Additionally, myelin-bodies, large lipid droplets, and large lysosomes were also frequently present in these cells (Fig 6). The observed large lysosomes could result from lysosome membrane permeabilisation, which contributes to thymocyte apoptosis by releasing lysosomal proteases, thereby causing the degradation of vital cytosolic proteins and the activation of additional hydrolases, including caspases [34]. This scenario is consistent with the finding that, unlike in the case of oligodendrocytes [6], both AIF- and caspase-mediated apoptosis was observed in the thymi of cuprizone-treated mice (Fig 7A). On the other hand, cytoplasmic translocation of mitochondrial cytochrome C (Fig 7A) may entirely account for the observed caspase-3 activation.

Both nuclear translocation of AIF and cytoplasmic translocation of cytochrome C could result from mitochondrial outer membrane permeability, which is regulated by pro-apoptotic members of the BCL-2 family [35]. Bad forms heterodimers with other family members or BH3-only proteins such as Bax and Bim, attach to the outer mitochondrial membrane, and destabilize it [35]. Bim, an essential mediator of apoptosis in thymocytes, has three isoforms (BimS, BimL and BimEL), which promote intrinsic apoptosis to different extents [36]. Accordingly, we detected enhanced expression of Bad, Bax and Bim upon cuprizone treatment (Fig 7B). Activation of ERK1/2 was reported to promote phosphorylation of BimEL targeting it to proteosomal degradation [37]. ERK1/2 was also indicated in Bad phosphorylation, preventing its association with other pro-apoptotic BCL-2 proteins [38]. In contrast, JNK and p38 MAPK activation was found to trigger Bad and Bim expression, labilise mitochondrial integrity, induce ROS production and promote apoptosis [39]. Accordingly, we found that all three MAPK families become activated upon cuprizone treatment; however, JNK and p38 activation was overwhelmingly more pronounced than was that of ERK1/2 (Fig 7C).

During development, thymocytes undergo positive and negative selection, eliminating roughly 98% of $CD4^+CD8^+$ cells before they maturate along the $CD4^+$ or $CD8^+$ phenotype. Additionally, when the thymus undergoes physiologic or pathologic involution during aging, infectious diseases, sepsis, malnutrition, physical or emotional stress, chemotherapeutics, glucocorticoids or radiation injury, cortical double positive cells, primarily, suffer apoptosis, while $CD4^+$ or $CD8^+$ cells are less affected [40–43], indicating that cortical double positive cells represent the most vulnerable cell population in the thymus. In this respect, cuprizone-induced thymus involution is similar to all aforementioned conditions. In other respects, the cuprizone model shows both similarities and differences compared to physiological or steroid-induced thymic aging.

The thymus undergoes adiposeous involution during aging. We observed large lipid droplets (Fig 6D) similar to those found in physiological and steroid-induced accelerated aging [41]. However, the thymic epithelium is affected differently by these conditions. The medullary region suffers less damage compared to the cortical region in the cuprizone model, which is in marked contrast to physiological or steroid-induced aging [44,45]. The observed enlarged lysosomes (Fig 6E) could be involved not only in apoptosis but also in other types of cell death.

There is increasing evidence that the lysosome is also involved in the pathogenesis of a variety of neurodegenerative diseases, including Alzheimer's disease, Parkinson's disease, Huntington's disease, and amyotrophic lateral sclerosis [34].

The thymus can have dual functions in MS. It can be the organ, where potentially self-reactive T-cells mature and differentiate inducing or exacerbating the disease. However, it is also the cradle of regulatory T-cells that can potentially suppress self-reactive immune responses, locally [46,47] Our results do not indicate a functional relationship between cuprizone-induced thymus involution and the absence of inflammatory responses or the selective demyelination observed in the cuprizone model. Rather, cuprizone-induced thymocyte and oligodendrocyte apoptosis seems to occur parallel to each other, and in both cases the toxin affects the most vulnerable cells in the given organ. It raises the possibility that similar selective elimination of the most vulnerable cell type in other organs is responsible for the absence of thriving that is characteristic of the cuprizone model. An important feature of the cuprizone model is that after termination of the toxin feeding, an accelerated thriving and regeneration occurs. Therefore, the cuprizone model could be valuable in studying thymus regeneration as well as the remyelination processes.

Author Contributions

Conceived and designed the experiments: IS KK ZB FG. Performed the experiments: IS KK GT SV PA KF PZ. Analyzed the data: IS KK AS ZB. Contributed reagents/materials/analysis tools: IS KK SV PA KF PZ ZB. Wrote the paper: FG ZI AS ZB FG.

References

1. Matsushima GK, Morell P. The neurotoxicant, cuprizone, as a model to study demyelination and remyelination in the central nervous system. Brain Pathol. 2001; 11(1):107–16. PMID: 11145196
2. Remington LT, Babcock AA, Zehntner SP, Owens T. Microglial recruitment, activation, and proliferation in response to primary demyelination. Am J Pathol. 2007; 170(5): 1713–24. PMID: 17456776
3. Torkildsen O, Brunborg LA, Myhr KM, Bø L. The cuprizone model for demyelination. Acta Neurol Scand Suppl. 2008; 188: 72–6. doi: 10.1111/j.1600-0404.2008.01036.x PMID: 18439226
4. Lucchinetti C, Brück W, Parisi J, Scheithauer B, Rodriguez M, Lassmann H. Heterogeneity of multiple sclerosis lesions: implications for the pathogenesis of demyelination. Ann Neurol. 2000; 47(6): 707–17. PMID: 10852536
5. van der Star BJ, Vogel DY, Kipp M, Puentes F, Baker D, Amor S. In vitro and in vivo models of multiple sclerosis. CNS Neurol Disord Drug Targets. 2012; 11(5): 570–88. PMID: 22583443
6. Veto S, Acs P, Bauer J, Lassmann H, Berente Z, Setalo G Jr, et al. Inhibiting poly(ADP-ribose) polymerase: a potential therapy against oligodendrocyte death. Brain. 2010; 133(Pt 3): 822–34 doi: 10.1093/brain/awp337 PMID: 20157013
7. Tandler B, Hoppel CL. Division of giant mitochondria during recovery from cuprizone intoxication. J Cell Biol. 1973; 56(1): 266–72. PMID: 4118453
8. Komoly S. Experimental demyelination caused by primary oligodendrocyte dystrophy. Regional distribution of the lesions in the nervous system of mice [corrected]. Ideggyogy Sz. 2005; 58(1–2): 40–3. PMID: 16252890
9. Venturini G. Enzymic activities and sodium, potassium and copper concentrations in mouse brain and liver after cuprizone treatment in vivo. J Neurochem. 1973; 21(5): 1147–51. PMID: 4357499
10. Russanov EM, Ljutakova SG. Effect of cuprizone on copper exchange and superoxide dismutase activity in rat liver. Gen Pharmacol. 1980; 11(6): 535–8. PMID: 7461431
11. Baxter AG. The origin and application of experimental autoimmune encephalomyelitis. Nat Rev Immunol. 2007; 7(11): 904–12. PMID: 17917672
12. Lassmann H. Experimental models of multiple sclerosis. Rev Neurol (Paris). 2007; 163(6–7): 651–5.
13. Utz U, McFarland HF. The role of T cells in multiple sclerosis: implications for therapies targeting the T cell receptor. J Neuropathol Exp Neurol. 1994; 53(4): 351–8. PMID: 8021708

14. Benveniste EN. Role of macrophages/microglia in multiple sclerosis and experimental allergic encephalomyelitis. J Mol Med (Berl). 1997; 75(3): 165–73. PMID: 9106073

15. Smith ME. Phagocytic properties of microglia in vitro: implications for a role in multiple sclerosis and EAE. Microsc Res Tech. 2001; 54(2):81–94 PMID: 11455615

16. Hiremath MM, Chen VS, Suzuki K, Ting JP, Matsushima GK. MHC class II exacerbates demyelination in vivo independently of T cells. J Neuroimmunol. 2008; 203(1): 23–32. doi: 10.1016/j.jneuroim.2008.06.034 PMID: 18805594

17. Emerson MR, Biswas S, LeVine SM. Cuprizone and piperonyl butoxide, proposed inhibitors of T-cell function, attenuate experimental allergic encephalomyelitis in SJL mice. J Neuroimmunol. 2001; 119 (2): 205–13. PMID: 11585623

18. Maña P, Fordham SA, Staykova MA, Correcha M, Silva D, Willenborg DO, et al. Demyelination caused by the copper chelator cuprizone halts T cell mediated autoimmune neuroinflammation. J Neuroimmunol. 2009; 210(1–2): 13–21 doi: 10.1016/j.jneuroim.2009.03.008 PMID: 19345424

19. Herder V, Hansmann F, Stangel M, Schaudien D, Rohn K, Baumgärtner W, et al. Cuprizone inhibits demyelinating leukomyelitis by reducing immune responses without virus exacerbation in an infectious model of multiple sclerosis. J Neuroimmunol. 2012 Mar; 244(1–2): 84–93. doi: 10.1016/j.jneuroim.2012.01.004 PMID: 22306300

20. Kutlesa S, Wessels JT, Speiser A, Steiert I, Müller CA, Klein G. E-cadherin-mediated interactions of thymic epithelial cells with CD103+ thymocytes lead to enhanced thymocyte cell proliferation. J Cell Sci. 2002; 115(Pt 23): 4505–15. PMID: 12414996

21. Vermes I, Haanen C, Steffens-Nakken H, Reutelingsperger C. A novel assay for apoptosis. Flow cytometric detection of phosphatidylserine expression on early apoptotic cells using fluorescein labelled Annexin V. J Immunol Methods. 1995; 184(1): 39–51. PMID: 7622868

22. Winer J, Jung CK, Shackel I, Williams PM. Development and validation of real-time quantitative reverse transcriptase-polymerase chain reaction for monitoring gene expression in cardiac myocytes in vitro. Anal Biochem. 1999; 270(1): 41–9. PMID: 10328763

23. Schmittgen TD, Zakrajsek BA, Mills AG, Gorn V, Singer MJ, Reed MW. Quantitative reverse transcription-polymerase chain reaction to study mRNA decay: comparison of endpoint and real-time methods. Anal Biochem. 2000; 285(2): 194–204. PMID: 11017702

24. Suzuki K. Giant hepatic mitochondria: production in mice fed with cuprizone. Science. 1969; 163 (3862): 81–2. PMID: 5763494

25. Green DR, Galluzzi L, Kroemer G. Metabolic control of cell death. Science. 2014; 345(6203): 1250256. doi: 10.1126/science.1250256 PMID: 25237106

26. Ghadially FN. Case for the panel. Mitochondrial inclusions in prostate adenocarcinoma. Ultrastruct Pathol. 1997; 21(5): 475–7. PMID: 9273979

27. Racz B, Hanto K, Tapodi A, Solti I, Kalman N, Jakus P,et al. Regulation of MKP-1 expression and MAPK activation by PARP-1 in oxidative stress: a new mechanism for the cytoplasmic effect of PARP-1 activation. Free Radic Biol Med. 2010; 49(12): 1978–88. doi: 10.1016/j.freeradbiomed.2010.09.026 PMID: 20920579

28. Procaccio V, Bris C, Chao de la Barca JM, Oca F, Chevrollier A, Amati-Bonneau P, et al. Perspectives of drug-based neuroprotection targeting mitochondria. Rev Neurol (Paris). 2014; 170(5): 390–400. doi: 10.1016/j.neurol.2014.03.005 PMID: 24792485

29. Suzuki K, Kikkawa Y. Status spongiosus of CNS and hepatic changes induced by cuprizone (biscyclohexanone oxalyldihydrazone). Am J Pathol. 1969; 54(2): 307–25. PMID: 5765567

30. Peterson P, Org T, Rebane A. Transcriptional regulation by AIRE: molecular mechanisms of central tolerance. Nat Rev Immunol. 2008; 8(12): 948–57. doi: 10.1038/nri2450 PMID: 19008896

31. Acs P, Komoly S. Selective ultrastructural vulnerability in the cuprizone-induced experimental demyelination. Ideggyogy Sz. 2012; 65(7–8): 266–70. PMID: 23126218

32. Pasquini LA, Calatayud CA, Bertone Uña AL, Millet V, Pasquini JM, Soto EF. The neurotoxic effect of cuprizone on oligodendrocytes depends on the presence of pro-inflammatory cytokines secreted by microglia. Neurochem Res. 2007; 32(2): 279–92. PMID: 17063394

33. Acs P, Selak MA, Komoly S, Kalman B. Distribution of oligodendrocyte loss and mitochondrial toxicity in the cuprizone-induced experimental demyelination model. J Neuroimmunol. 2013; 262(1–2): 128–31. doi: 10.1016/j.jneuroim.2013.06.014 PMID: 23890808

34. Zhang L, Sheng R, Qin Z. The lysosome and neurodegenerative diseases. Acta Biochim Biophys Sin (Shanghai). 2009; 41(6): 437–45. PMID: 19499146

35. Ryan JA, Brunelle JK, Letai A. Heightened mitochondrial priming is the basis for apoptotic hypersensitivity of CD4(+) CD8(+) thymocytes. Proceedings of the Proc Natl Acad Sci U S A. 2010; 107(29): 12895–900. doi: 10.1073/pnas.0914878107 PMID: 20615979

36. Ruppert SM, Li W, Zhang G, Carlson AL, Limaye A, Durum SK, Khaled AR. The major isoforms of Bim contribute to distinct biological activities that govern the processes of autophagy and apoptosis in interleukin-7 dependent lymphocytes. Biochim Biophys Acta. 2012; 1823(10): 1877–93. doi: 10.1016/j.bbamcr.2012.06.017 PMID: 22728771

37. Ley R, Balmanno K, Hadfield K, Weston C, Cook SJ. Activation of the ERK1/2 signaling pathway promotes phosphorylation and proteasome-dependent degradation of the BH3-only protein, Bim. J Biol Chem. 2003; 278(21): 18811–6. PMID: 12646560

38. Park HJ, Park KH, Shin KS, Lee MK. The roles of cyclic AMP-ERK-Bad signaling pathways on 6-hydroxydopamine-induced cell survival and death in PC12 cells. Toxicol In Vitro. 2013; 27(8): 2233–41. doi: 10.1016/j.tiv.2013.09.014 PMID: 24055892

39. Miloso M, Scuteri A, Foudah D, Tredici G. MAPKs as mediators of cell fate determination: an approach to neurodegenerative diseases. Curr Med Chem. 2008; 15(6): 538–48. PMID: 18336268

40. Grillot DA, Merino R, Núñez G. Bcl-XL displays restricted distribution during T cell development and inhibits multiple forms of apoptosis but not clonal deletion in transgenic mice. J Exp Med. 1995; 182(6): 1973–83. PMID: 7500043

41. Pearse G. Normal structure, function and histology of the thymus. Toxicol Pathol. 2006; 34(5): 504–14. PMID: 17067941

42. Savino W, Dardenne M, Velloso LA, Dayse Silva-Barbosa S. The thymus is a common target in malnutrition and infection. Br J Nutr. 2007; 98 Suppl 1:S11–6. PMID: 17922946

43. Strasser A, Harris AW, Cory S. Bcl-2 transgene inhibits T cell death and perturbs thymic self-censorship. Cell. 1991; 67(5): 889–99. PMID: 1959134

44. Kvell K, Varecza Z, Bartis D, Hesse S, Parnell S, Anderson G, et al. Wnt4 and LAP2alpha as pacemakers of thymic epithelial senescence. PLoS One. 2010; 5(5): e10701. doi: 10.1371/journal.pone.0010701 PMID: 20502698

45. Talaber G, Kvell K, Varecza Z, Boldizsar F, Parnell SM, Jenkinson EJ, et al. Wnt-4 protects thymic epithelial cells against dexamethasone-induced senescence. Rejuvenation Res. 2011; 14(3): 241–8. doi: 10.1089/rej.2010.1110 PMID: 21453014

46. Costantino CM, Baecher-Allan C, Hafler DA. Multiple sclerosis and regulatory T cells. J Clin Immunol. 2008; 28(6): 697–706. doi: 10.1007/s10875-008-9236-x PMID: 18763026

47. Venken K, Hellings N, Liblau R, Stinissen P. Disturbed regulatory T cell homeostasis in multiple sclerosis. Trends Mol Med. 2010; 16(2): 58–68. doi: 10.1016/j.molmed.2009.12.003 PMID: 20159585

frontiers in Immunology

ORIGINAL RESEARCH
published: 24 April 2019
doi: 10.3389/fimmu.2019.00862

Transgenic Exosomes for Thymus Regeneration

Krisztina Banfai[1,2], *Kitti Garai*[1,2], *David Ernszt*[2,3], *Judit E. Pongracz*[1,2] *and Krisztian Kvell*[1,2]*

[1] Department of Pharmaceutical Biotechnology, Faculty of Pharmacy, University of Pécs, Pécs, Hungary, [2] Szentagothai Research Center, University of Pécs, Pécs, Hungary, [3] Faculty of Medicine, Institute of Physiology, University of Pécs, Pécs, Hungary

During senescence, Wnt4 expression is down-regulated (unlike their Frizzled receptors), while PPARgamma expression increases in the thymus. Together, these changes allow for thymic degeneration to occur, observed as adipose involution. However, when restored, Wnt4 can efficiently counteract PPARgamma and prevent thymic senescence from developing. The Wnt-pathway activator miR27b has also been reported to inhibit PPARgamma. Our goal was to evaluate the Wnt4 and miR27b levels of Wnt4-transgenic thymic epithelial cell (TEC)-derived exosomes, show their regenerative potential against age-related thymic degeneration, and visualize their binding and distribution both *in vitro* and *in vivo*. First, transgenic exosomes were harvested from Wnt4 over-expressing TECs and analyzed by transmission electron microscopy. This unveiled exosomes ranging from 50 to 100 nm in size. Exosomal Wnt4 protein content was assayed by ELISA, while miR27b levels were measured by TaqMan qPCR, both showing elevated levels in transgenic exosomes relative to controls. Of note, kit-purified TEI (total exosome isolate) outperformed UC (ultracentrifugation)-purified exosomes in these parameters. In addition, a significant portion of exosomal Wnt4 proved to be displayed on exosomal surfaces. For functional studies, steroid (Dexamethasone or DX)-induced TECs were used as cellular aging models in which DX-triggered cellular aging was efficiently prevented by transgenic exosomes. Finally, DiI lipid-stained exosomes were applied on the mouse thymus sections and also iv-injected into mice, for *in vitro* binding and *in vivo* tracking, respectively. We have observed distinct staining patterns using DiI lipid-stained transgenic exosomes on sections of young and aging murine thymus samples. Moreover, *in vivo* injected DiI lipid-stained transgenic exosomes showed detectable homing to the thymus. Of note, Wnt4-transgenic exosome homing outperformed control (Wnt5a-transgenic) exosome homing. In summary, our findings indicate that exosomal Wnt4 and miR27b can efficiently counteract thymic adipose involution. Although extrapolation of mouse results to the human setting needs caution, our results appoint transgenic TEC exosomes as promising tools of immune rejuvenation and contribute to the characterization of the immune-modulatory effects of extracellular vesicles in the context of regenerative medicine.

Keywords: aging, thymus, exosome, Wnt4, miR27b

OPEN ACCESS

Edited by:
Denise Doolan,
James Cook University, Australia

Reviewed by:
Axel T. Lehrer,
University of Hawaii at Manoa, United States
Csaba Vizler,
Hungarian Academy of Sciences, Hungary

***Correspondence:**
Krisztian Kvell
kvell.krisztian@pte.hu

Specialty section:
This article was submitted to Vaccines and Molecular Therapeutics, a section of the journal Frontiers in Immunology

Received: *06 July 2018*
Accepted: *04 April 2019*
Published: *24 April 2019*

Citation:
Banfai K, Garai K, Ernszt D, Pongracz JE and Kvell K (2019) Transgenic Exosomes for Thymus Regeneration. Front. Immunol. 10:862. doi: 10.3389/fimmu.2019.00862

INTRODUCTION

Transcription factor FoxN1 is the mastermind of thymus organogenesis and identity (1), and is also an acknowledged direct molecular target of the glycolipoprotein Wnt4 (2). As a consequence, Wnt4 plays a key role during embryonic thymus development (3, 4) and the maintenance of its identity in adulthood (5–7). Thymic epithelial cells secrete less Wnt4, while their Frizzled receptors (Fz4 and Fz6) become up-regulated indicating a potential compensatory mechanism and possibly enhanced Wnt4-binding (8). This loss of Wnt4 expression weakens thymic epithelial identity and allows for thymic adipose involution to occur (9). This latter process leads to the expansion of thymic adipose tissue orchestrated by transcription factor PPARgamma (10). The Wnt/b-catenin pathway and PPARgamma have been reported to act as mutual inhibitors of one another in several tissue contexts, including the thymus (11–13). We have previously shown that the addition of exogenous Wnt4 reinforces thymic epithelial identity and confers resistance in a steroid-induced model of senescence through suppressing PPARgamma (2, 14).

Previous records reported that Wnt4 loses its activity when purified as a sole compound, but retains activity as supernatant fraction (15). In harmony, recent publications of various tissue contexts have suggested that Wnt molecules (including Wnt4) travel in conjunction with extracellular vesicles (EVs), more specifically exosomes (12, 16). It has also been reported that a significant portion of the Wnts—including Wnt4—may actually be displayed on exosomal surfaces. Along with Wnt4, the Wnt-pathway activator miR27b has also been shown to specifically inhibit PPARgamma activity via binding to its promoter region (17, 18). Similar to the Wnts above, miRNA species have also been suggested to preferentially reside and travel in EVs, especially in exosomes (19, 20).

EVs are released by most cell types of all phyla and mediate various biological effects. EVs are classified by their size where exosomes represent the smallest vesicles with a diameter of between 30 and 200 nm. Exosomes are produced by a multi-step process where multi-vesicular bodies (MVBs) are formed first by cell-membrane invaginations, followed by the extracellular release of exosomes (21). Biological functions attributed with exosomes encompass several physiological and pathological conditions, including cell and tissue regeneration (22, 23). The thymus epithelium has also been reported to be a rich source of exosomes with key immunological relevance (24–26) e.g., in thymocyte selection (25, 27), Yet to date, TEC (thymic epithelial cell) exosomes have not been linked with thymus tissue regeneration. Thymus tissue regeneration is not only relevant for aging studies, but also in conditions that accelerate thymus degeneration due to environmental stimuli including specific toxins, viruses, or heavy metals (28).Due to the reasons above, we have set out to characterize transgenic exosomes produced by Wnt4 over-expressing TECs for their Wnt4 and miR27b content, to test their biological activity in the context of tissue regeneration, and distribution properties both *in vitro* and *in vivo*.

MATERIALS AND METHODS

Cell Cultures

In vitro experiments were performed using the TEP1 primary-derived (BALB/c) thymic epithelial cell lines or the A549 human lung epithelial cell line (A549 served as control producer cell compared to TEP1). The Wnt4 over-expressing version of TEP1 and the Wnt5a over-expressing version of A549 were generated via lentiviral transfection linked to the green fluorescent protein (GFP) as published previously (Wnt5a served as control compared to Wnt4) (29, 30). Cells were maintained in DMEM (Dulbecco's Modified Eagle's medium, Lonza) supplemented with 10% FBS (EuroClone), Penicillin-Streptomycin, L-glutamine, Hepes buffer, non-essential amino acids (Lonza), and β-mercapto-ethanol (Sigma). In order to differentiate thymic epithelial cells (TECs) toward adipose, lineage steroid treatment was used. Dexamethasone (DX) was diluted from a stock solution of 4 mg/mL to a final concentration of 1 μM as formerly described (10). To counteract the aging effect of steroid treatment, isolated Wnt4 exosomes were added to the cell cultures.

Flow-Cytometry

Cell suspensions were prepared from both TEP1 and Wnt4 over-expressing TEP1 cell lines in order to check the presence of Wnt4 over-expression via analyzing the GFP-positive cells. A total of 150,000 cells were collected and washed with 1x PBS (Fisher BioReagents) then fixed using paraformaldehyde containing PBS solution. BD FACSCanto™ II flow-cytometer (Becton Dickinson) was used for data acquisition at a medium flow rate and stopped at 10,000 events. Measurements were performed and analyzed with BD FACSDiva Software version 6.1.3.

Exosome Staining, Collection and Isolation

Control mouse TECs(thymic epithelial cells), Wnt4 over-expressing mouse TECs and Wnt5a over-expressing human A549 cells were cultured in Stemline® T Cell Expansion Medium (Merck) and serum-free DMEM (Lonza) until they reached 80–90% confluence. Serum-free media were used to eliminate the effect of serum-derived exosomes. Equal volume of FBS-free cell culture media were collected from T75 tissue culture flasks (TPP) and centrifuged at 2,000 g for 30 min to completely remove cell debris and apoptotic bodies. Supernatants were filtered through a 0.45 μm filter (Merck Millipore) and incubated overnight at 4°C having added Total Exosome Isolation Reagent (Invitrogen). Following a 1 h centrifugation at 10,000 g, pellets were collected and re-suspended in sterile PBS (GE Healthcare Life Sciences) for further use. Exosomes were fluorescently-stained using DiI lipid stain (Invitrogen). DiI lipid-stain was added to the cell culture medium the day before collecting cell supernatant. DiI lipid-stain stock solution (50 mg/mL dissolved in DMSO) was diluted 10,000-fold (31).

Transmission Electron Microscopy

Pelleted exosomes were added in 50 μl of PBS onto mesh grids and dried overnight without the use of any fixative (32). Contrast staining was performed using uranyl-acetate and lead-citrate. Exosomes were examined using a Morgagni

268D transmission electron microscope. Images were acquired using an integrated MegaView III digital camera (Olympus Soft Imaging Solutions GmbH).

Immune-Fluorescent Staining

Immune-fluorescent staining was performed on 2-month-old and 21-month-old mouse thymus cryosections. Seven micrometer thick tissue sections were mounted onto glass slides and dried overnight. Tissue samples were fixed with cold acetone then unspecific protein-protein interactions were blocked with 5% BSA in PBS solution before applying fluorochrome-conjugated primary antibodies. FITC-conjugated a-mouse CD326 (EpCAM) (Clone G8.8, BioLegend) was used at 1:100 dilution and DAPI (1:1,000, Life Technologies) was added as a nuclear counterstain. Slides were also incubated overnight with previously DiI-stained Wnt4 exosomes. Following washing steps with 1x PBS, samples were imaged using Nikon Eclipse Ti-U microscope equipped with a CCD camera (Andor 4Zyla 5.5) and

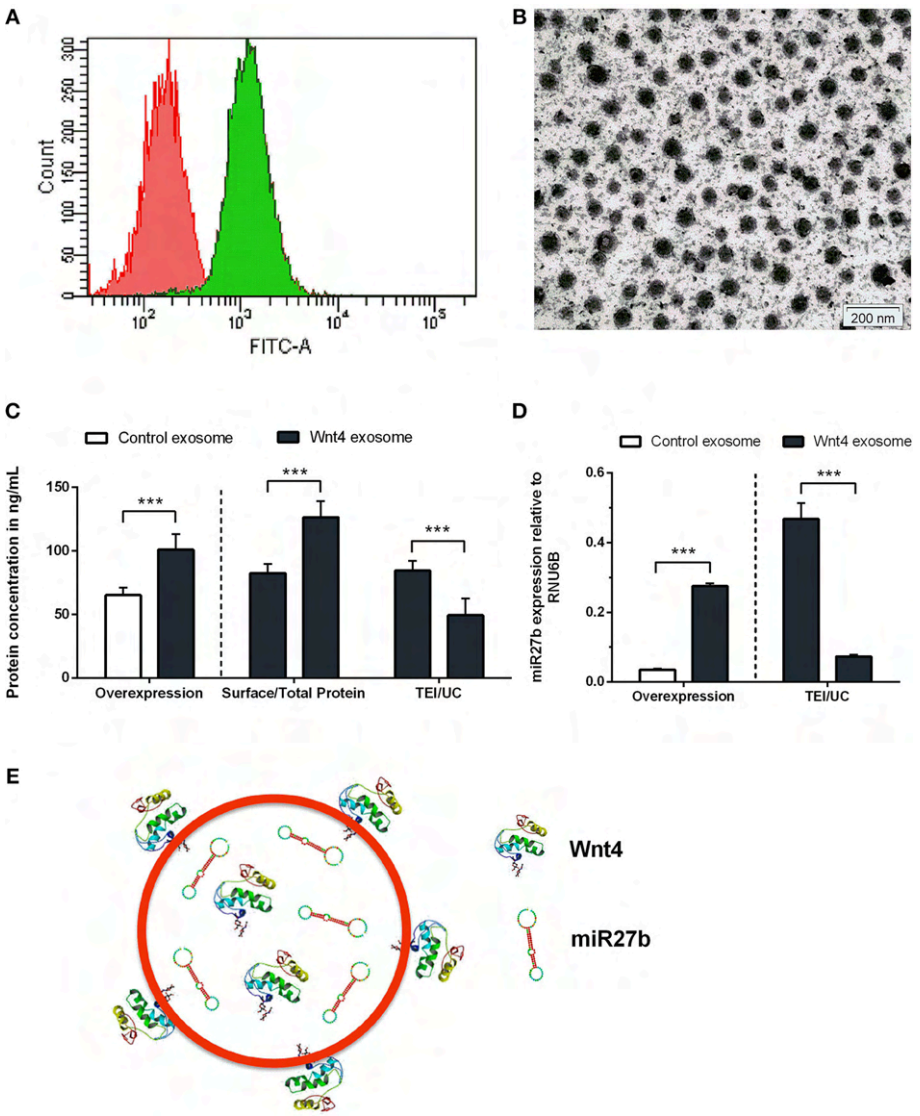

FIGURE 1 | Characterization of transgenic exosomes. Flow-cytometric analysis of control (shown in red) and GFP+ Wnt4 over-expressing TECs (thymic epithelial cells) (shown in green) is presented **(A)**. FITC-A corresponds to FL1 channel where GFP-emitted fluorescence is detected. Please note that FITC-A scale is logarithmic. Transmission electron micrograph shows TEI exosomes of approx. 50–100 nm in size **(B)**. Wnt4 protein **(C)** and miR27b RNA **(D)** levels of TEI (total exosome isolate) and UC (ultracentrifuged) exosomes are shown as obtained by ELISA and TaqMan qPCR, respectively. From left to right column pairs show level of over-expression, surface/total content, and TEI/UC content, as applicable. Absolute concentration is shown in ng/ml for Wnt4 **(C)** and absolute copy number is shown for miR27b relative to rnu6b **(D)**. Eight **(C)** and three **(D)** replicates were used for statistical analysis. Significant differences are shown by asterisks (n/a for not applicable, ns for not significant, $^{*}p \leq 0.05$, $^{**}p \leq 0.01$, $^{***}p \leq 0.001$) and were calculated using independent samples *t*-test. For exact numerical values and statistical analysis please refer to **Supplementary Material**. Representative drawing of a DiI lipid-stained (red) Wnt4-transgenic exosome showing Wnt4 (surface and internal) content and miR27b (internal) cargo **(E)**.

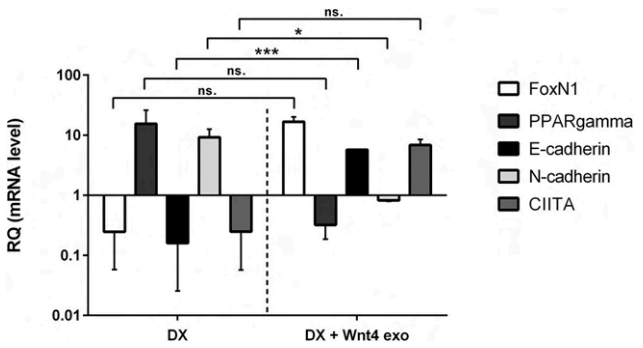

FIGURE 2 | *In vitro* biological effect of transgenic exosomes. Gene expression changes of FoxN1, PPARgamma, E-cadherin, N-cadherin, and CIITA are shown as measured by SYBR-green qPCR following steroid (DX)-treatment alone (DX, left half of figure), or in combination with transgenic exosomes (DX + Wnt4 exo, right half of figure). Three samples of each were used for statistical analysis. Fold change (relative quantity or RQ) expression is shown, where RQ = 1 represents baseline control. RQ is relative to control level (left half of figure), or relative to DX-treatment (right half of figure). Please note that Y-axis is logarithmic. Significant differences are shown by asterisks (n/a for not applicable, ns for not significant, $^{*}p \leq 0.05$, $^{**}p \leq 0.01$, $^{***}p \leq 0.001$) and were calculated using independent samples *t*-test. For exact numerical values and statistical analysis please refer to **Supplementary Material**.

images were captured using NIS-Elements Software. Images were analyzed using ImageJ Software. Thymus lobes of iv-injected mice were sectioned to 5 μm thickness and the same staining procedure was used as described above. Staining procedures were optimized using previous literature data (33–36).

RNA Isolation, cDNA Preparation, qRT-PCR, TaqMan Array

Total RNA was isolated using NucleoSpin RNA II Kit (Macherey-Nagel). High Capacity cDNA Reverse Transcription Kit (Applied Biosystems) was used for preparation of cDNA to a final concentration of 1 μg/μL. For qPCR analysis, PikoReal™ Real-Time PCR System (Thermo Fisher Scientific) was used adding Luminaris Color HiGreen qPCR Master Mix (Thermo Fisher Scientific) to the samples. Gene expression was normalized to mouse β-actin and HPRT housekeeping genes (See **Figures 1**, **2** for detailed primer list). To detect miR27b levels in exosomes, Total Exosome RNA & Protein Isolation Kit (Invitrogen) was used for miRNA isolation. cDNA synthesis was carried out using High Capacity cDNA Reverse Transcription Kit (Applied Biosystems) and specific primers for U6B as endogenous control and miR27b as target gene. Quantification of miR27b was performed using specific gene targeted TaqMan™ MicroRNA Assay adding TaqMan Universal PCR Master Mix (Applied Biosystems). Measurements were run on a PikoReal™ Real-Time PCR System as well using FAM as a fluorophore. Data evaluation was accomplished using Microsoft Excel.

ELISA

Human Wnt4 ELISA Kit (Merck) was used to measure the Wnt4 protein levels of isolated exosomes. Exosomes isolated from TEP1 cell culture media were used as controls. We aimed to quantify surface and total exosome protein levels separately. To detect surface proteins, pelleted exosomes were dissolved in PBS (for intact exosomes), while to determine total protein concentration, exosomes were diluted in Exosome Resuspension Buffer (for disintegrated exosomes) as suggested by Total Exosome RNA & Protein Isolation Kit Manual (Invitrogen). Plates were measured immediately at 450 nm using EnSpire® Multimode Plate Reader (PerkinElmer) with its integrated data analysis software. Using OD values mean absorbance of standards and samples were calculated and results were analyzed with the help of Microsoft Excel. Standard curve was plotted and protein concentrations were calculated in ng/ml. The obtained R^2 values showed >0.91 alignment to the standard curve in all cases.

Ultracentrifugation

In order to compare TEI efficiency (37) with standard ultracentrifugation methods confirming previous literature data (38, 39), 1 ml serum-free medium containing exosomes was centrifuged at 100,000 g for 3 h at 4°C (40) using Sorvall™ MTX 150 Micro-Ultracentrifuge (Thermo Scientific™). Pelleted exosomes were re-suspended in PBS and used for further experiments. Protein concentration of ultracentrifuged exosomes were determined with ELISA and following miRNA isolation, miR27b levels were assessed by TaqMan™ MicroRNA Assay.

In vivo Exosome Homing

Eight week-old BALB/c mice were used for intravenous introduction of DiI lipid-stained exosomes in a pilot study (41, 42). For control purpose a mouse received 2 doses of DiI lipid-stained Wnt5a exosomes diluted in 200 μL of sterile PBS. Another mouse was injected with the same dosage of DiI lipid-stained Wnt4 exosomes diluted in 200 μL of sterile PBS. After 24 h, mice were sacrificed and organs were analyzed for fluorescent intensity with the help of IVIS Lumina III *in vivo* Imaging System. Imaging of the thymus, lungs, liver, and spleen was performed at 520 nm using Living Image Software. Thymus lobes were embedded into cryomold and sectioned to confirm tissue homing. Mice were housed under minimal disease (MD) conditions and kept in the Laboratory Animal Core Facility of the University. Experimental procedures were carried out according to the "1988/XXVIII act of the Hungarian Parliament on Animal Protection (243/1988)" which complies with recommendations of the Helsinki Declaration. All animal experiments were performed with the consent of the Ethics Committee on Animal Research of the University (ref. no.: #BA02/2000-46/2016).

Statistical Analysis

Statistical analyses were conducted using SPSS version 22. Descriptive statistics (mean ± SD) were calculated for all data. Normality was assessed using the Shapiro-Wilk test ($n < 50$). Comparisons were performed using one sample *t*-test and independent samples *t*-test. The level of significance was set at $P \leq 0.05$.

RESULTS

Characterization of Transgenic Exosomes

Stable Wnt over-expressing BALB/c TEC (thymic epithelial cell) lines have been generated using lentiviral vectors as described previously (30). In the current setting, we focused on the characterization of exosomes secreted by the transgenic cell lines. Purity and transgenic status of cell lines was confirmed by GFP expression provided by the same bicistronic construct that also drives Wnt secretion. Flow-cytometric analysis verified that the transgenic cells express GFP and hence secrete Wnt4 at a uniform level (see **Figure 1A**). TECs have been reported to be rich EV and exosome sources. Using a commercially available PEG-based kit (40) we then enriched transgenic exosomes (TEI: total exosome isolate) from TEC line supernatant. The enriched supernatant fraction was confirmed by transmission electron microscopy to contain of uniform-sized exosomes of approx. 50–100 nm in diameter (see **Figure 1B**). Along with Wnt4, the Wnt-pathway activator miR27b has also been reported to suppress PPARgamma (17, 18, 43, 44). For this reason, we have measured both Wnt4 protein and miR27b RNA quantities in transgenic exosomes relative to their control counterparts, using ELISA and TaqMan qPCR methods, respectively. As expected, both Wnt4 and miR27b showed elevated and statistically significant levels in exosomes of transgenic TECs compared to their control counterparts (see **Figures 1C,D**). Furthermore, we have measured total Wnt4 concentration (via lysis of exosomes) and surface Wnt4 concentration (using intact exosomes) showing that a significant portion of Wnt4 is surface-displayed, in harmony with literature (8, 19) (**Figure 1C**). Of note, UC (ultracentrifugation) has repeatedly provided poor exosomal protein and miRNA yield as compared to TEI (see **Figures 1C,D**). **Figure 1E** shows schematic drawing of DiI lipid-stained transgenic exosome with Wnt4 content and miR27b cargo.

Biological Effect of Transgenic Exosomes

We have previously reported that the supernatant of the Wnt4 over-expressing BALB/c TEC (thymic epithelial cell) line confers resistance to steroid (Dexamethasone or DX)-induced accelerated aging in our cellular model system (2). In short, DX-treatment triggers adipose transformation of TECs via epithelial-to-mesenchymal transition (EMT) (10). We have used the same experimental setting using enriched transgenic exosomes instead of transgenic supernatant. As expected and shown by SYBR-green qPCR (see **Figure 2**), the applied DX-treatment triggers loss of TEC identity (decreased FoxN1 and MHCII or CIITA expression), promotes EMT (cadherin switch or decreased E-cadherin and increased N-cadherin expression), and initiates adipose transformation (increased PPARgamma expression). In perfect conformity with our previous reports using transgenic supernatant (2, 4), the transgenic exosomes

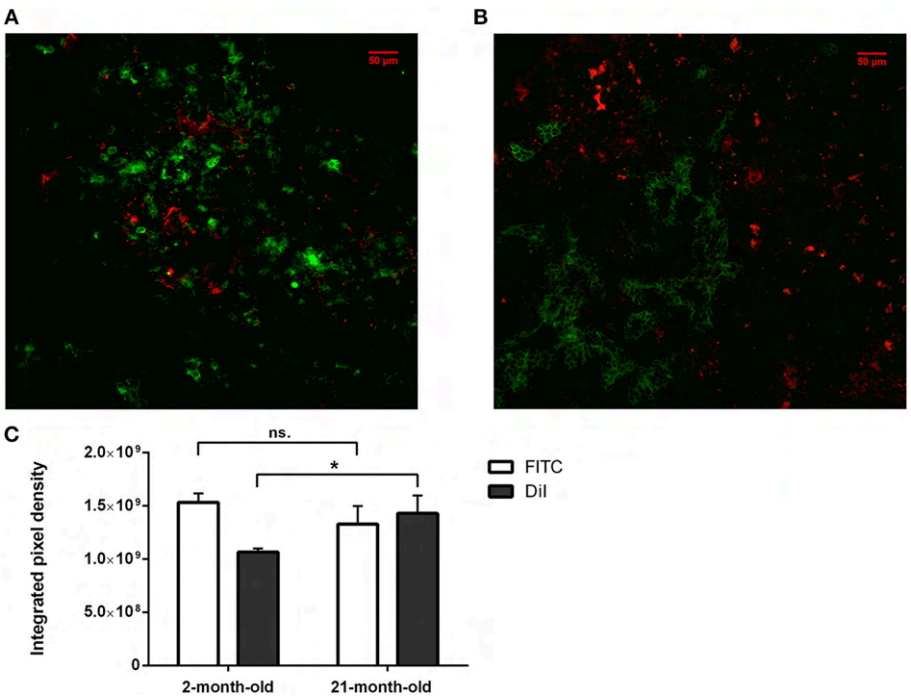

FIGURE 3 | *In vitro* binding and distribution of transgenic exosomes. Frozen mouse thymic sections from young adult (2 months, **A**) and senior adult (21 months, **B**) are shown. Sections were labeled using EpCAM1-FITC (shown in green). Transgenic exosomes were pre-stained using DiI lipid stain (shown in red). Representative slide is presented. Data were calculated using five slides each. Integrated pixel density values are shown for EpCAM1 (shown in green) and DiI lipid stain (shown in red) **(C)**. Significant differences are shown by asterisks (n/a for not applicable, ns for not significant, $*p \leq 0.05$, $**p \leq 0.01$, $***p \leq 0.001$) as obtained using independent sample *t*-test. Data were calculated using five slides each. For exact numerical values and standard deviation please refer to **Supplementary Material**.

also efficiently counteract all of the above gene expressional changes, preserving TEC identity, blocking EMT, and adipose transformation from developing.

In vitro Binding and Distribution of Transgenic Exosomes

We have shown above that our transgenic exosomes harbor elevated amounts of Wnt4 of which a significant portion is surface-displayed. Previously we have reported that Wnt4-binding Frizzled receptors (Fz4 and Fz6) are up-regulated in aged TECs (thymic epithelial cells) as compared to young TECs (8). Next, we have tested whether thymic histological sections can bind transgenic exosomes using standard immune-fluorescent staining protocol. We were also interested to see if histological *in vitro* binding shows a particular pattern and furthermore, if this pattern changes with the age of the epithelium as suggested by Frizzled up-regulation (2, 8). For this reason, DiI lipid-stained transgenic exosomes have been applied on thymic sections of mice of 2-month-old (young) and 21-month-old (aged) for histological staining. As anticipated, both young and old mouse thymic sections efficiently bind transgenic exosomes (see **Figures 3A,B**, respectively). Relative to the histological presentation of the EpCAM-1^{++} medullary epithelium, the transgenic exosomes showed preferential binding to medullary regions at a young age (see **Figure 3A**), while a more profound cortical binding pattern was observed at an old age (see **Figure 3B**). Not only does the binding pattern change with age (shifting from medullary at a young age to cortical at an old age), but binding efficiency also increases with age (observed as increased, statistically significant DiI/fluorescent integrated pixel density at old age compared to young age, see **Figure 3C**). Please also note that the medullary area shrinks with age relative to other areas, in harmony with our previous records (4) observed here as mild indicative decrease of FITC integrated pixel density at old age compared to young age (see **Figure 3C**).

In vivo Binding and Distribution of Transgenic Exosomes

The thymic epithelium has been reported to be highly active in exosome trafficking (24, 25, 45). We have shown above that our Wnt4-transgenic exosomes readily bind to the thymic epithelium *in vitro* on histological sections. However, we were interested to see if *in vivo* binding of transgenic exosomes also occurs in the thymic epithelium. For this reason, DiI lipid-stained Wnt5a-transgenic (serving as control) human (A549), and Wn4-transgenic (serving as sample) BALB/c (TEP1) exosomes have been injected into tail veins of young adult BALB/c mice to check their *in vivo* topological distribution after 24 h. It has been reported that certain organs (e.g., liver, lungs, and spleen) capture a significant portion of exosomes rapidly and non-specifically following systemic administration (46). Using IVIS Lumina III imaging and performing topological reconstruction of murine organs over standard mouse contour, we were able to record detectable homing of transgenic exosomes to the thymus despite significant non-specific capture by other organs (e.g., liver, lungs, and spleen) (see **Figure 4A**). Fluorescent signals of DiI lipid-stained sample Wnt4-transgenic TEC (thymic epithelial cell) exosomes exceeded control values of Wnt5a-transgenic exosomes (see **Figure 4B**). It is worthy of note that thymic signals exceed pulmonary and splenic signals, despite significant size differences. Furthermore, immune-fluorescently labeled sections of the *in vivo* Wnt4-transgenic exosome-infiltrated thymus revealed the histological level homing pattern observed after 24 h (see **Figures 5A,B**) that allows for the quantitative evaluation of transgenic exosome homing (see **Figure 5C**).

DISCUSSION

In harmony with literature data, our results confirm that the thymic epithelium is a particularly rich source of EVs and exosomes (24, 25, 45). The Wnt4 over-expressing transgenic TEC (thymic epithelial cell) line proves to be a reliable source of transgenic exosomes that are easy to visualize, enrich to high purity, characterize, and apply in experiments. As anticipated, the transgenic exosomes contain elevated levels of Wnt4 protein, as well as the Wnt-pathway activator miR27b, which potentially synergizes with Wnt4 to counteract PPARgamma.

Based on our current results obtained with our thymus aging cellular model system the transgenic exosomes transmit the biological activity that was previously attributed to supernatant transfer (2, 4). The applied transgenic exosomes efficiently prevent steroid-triggered adipose transformation as supported by reinforced epithelial identity (increased FoxN1 and CIITA expression), lack of EMT (sustained E-cadherin and low N-cadherin expression) and resistance to adipose differentiation (low PPARgamma expression) in line with our previous reports using transgenic supernatants.

Histological level analysis of *in vitro* transgenic exosome binding provides information in more depth. At a young age (2-month-), transgenic exosomes readily bind to the thymic epithelium with slight medullary preference. In contrast, at an old age (21-month-), transgenic exosomes show a moderate cortical preference. Furthermore, transgenic exosomes show significantly higher overall binding frequency at an old age, suggesting that the senescent thymic epithelium readily adsorbs Wnt4-transgenic exosomes. This is supported by literature data and our own results showing that a significant portion of exosomal Wnt4 is surface-displayed and that Wnt4-binding Frizzled receptors (Fz4 and Fz6) are up-regulated in senescent TECs (8). Combined, our previous and current results suggest that as Wnt4 secretion decreases with age and since cortical areas show preferential binding of the remaining Wnt4 (a key factor of TEC identity) at an old age, age-related medullary involution may precede cortical involution due to the medullary lack of Wnt4-effect (10, 14, 47). To our knowledge, this is a novel molecular level explanation of accelerated medullary involution. Highlighting the relevance of our *in vitro* binding assay, our *in vivo* transgenic exosome homing assay shows detectable homing to the thymus when using mouse TEC-derived Wnt4-transgenic exosomes as opposed to control exosomes (human A549-derived Wnt5a-transgenic exosomes). Histological

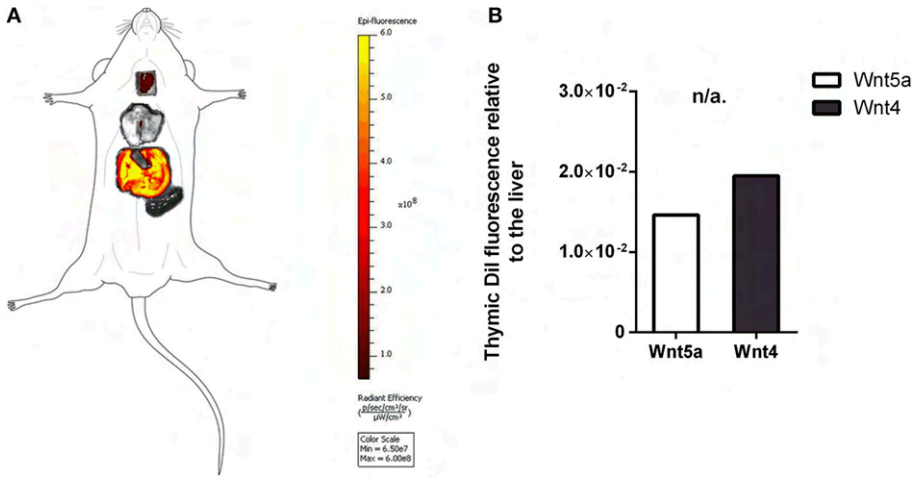

FIGURE 4 | *In vivo* binding and distribution of transgenic exosomes. DiI lipid-stained and iv-injected exosomes show differential topological distribution patterns (radiant efficiency) after 24 h. Organotopic distribution was reconstructed using standard mouse contour. The thymus, lungs, spleen, and liver were analyzed using IVIS Lumina imaging **(A)**. Radiant efficiency of thymus relative to liver (RQ) is shown for of DiI lipid-stained and iv-injected transgenic exosomes after 24 h for Wnt5a (control) and Wnt4 (sample) **(B)**. Significant differences are shown by asterisks (n/a for not applicable, ns for not significant, $^{*}p \leq 0.05$, $^{**}p \leq 0.01$, $^{***}p \leq 0.001$) as obtained using independent samples *t*-test. Pilot study is shown. For exact numerical values please refer to **Supplementary Material**.

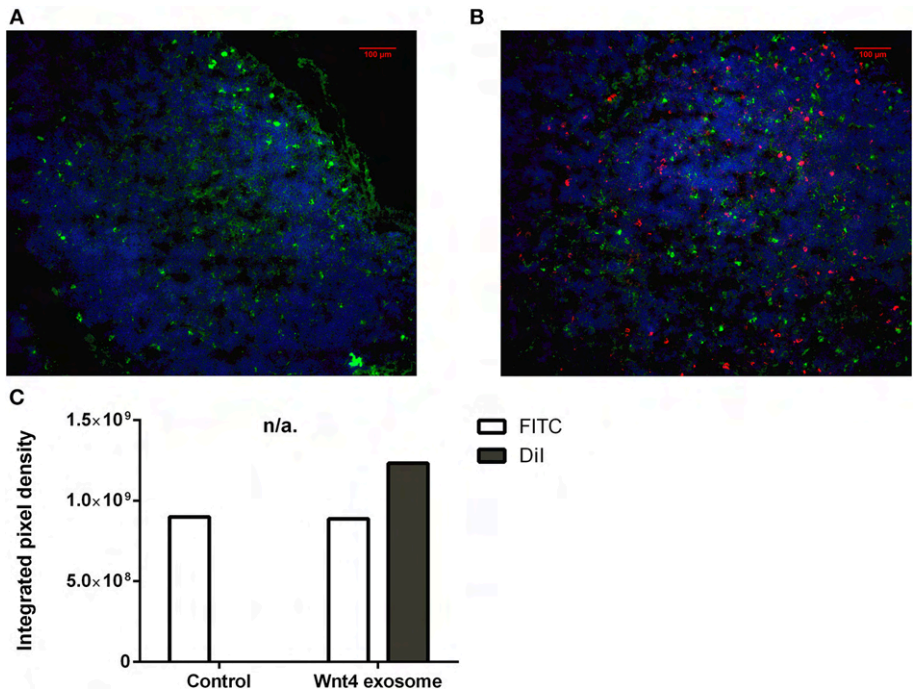

FIGURE 5 | *Ex vivo* binding and distribution of transgenic exosomes. Frozen mouse thymic sections from control **(A)** and DiI lipid-stained Wnt4-transgenic exosome iv-injected mouse **(B)** are shown 24 h after administration. Sections were stained for EpCAM1-FITC (shown in green). Transgenic exosomes were pre-stained using DiI lipid stain (shown in red). DAPI was used as nuclear counter-stain (shown in blue). Integrated pixel density values are shown for EpCAM1 (shown in green) and DiI lipid stain (shown in red) **(C)**. Significant differences are shown by asterisks (n/a for not applicable, ns for not significant, $^{*}p \leq 0.05$, $^{**}p \leq 0.01$, $^{***}p \leq 0.001$) as obtained using independent samples *t*-test. Pilot study is shown. For exact numerical values please refer to **Supplementary Material**.

analysis of Wnt4-transgenic exosome-infiltrated thymus sections confirms their presence also showing distribution pattern and binding frequency.

In summary, based on our cellular aging model system, along with *in vitro* and *in vivo* binding and homing studies, respectively; our results confirm that transgenic exosomes

readily and efficiently provide a permissive niche for immune regeneration in the mouse setting and hold promise for human application as well.

ETHICS STATEMENT

Experimental procedures were carried out according to the 1988/XXVIII act of the Hungarian Parliament on Animal Protection (243/1988) which complies with recommendations of the Helsinki Declaration. All animal experiments were performed with the consent of the Ethics Committee on Animal Research of the University (ref. no.: #BA02/2000-46/2016).

AUTHOR CONTRIBUTIONS

KB performed histological, cellular- and molecular biology work in the project and was involved in manuscript preparation. KG prepared exosome fractions and performed statistical analysis. DE executed *in vivo* tracking. JP was involved in planning experiments, manuscript preparation and also supervised the host department. KK planned experiments, prepared the manuscript and supervised the project.

FUNDING

Scientific research support was provided by the Hungarian National Science Foundation (No. 78310) and PTE AOK KA-2016-16 to KK. The project was also supported by the University of Pecs in the frame of Pharmaceutical Talent Center program and the Viral Pathogenesis Talent Center program via KK. The Janos Bolyai Scholarship of the Hungarian Academy of Sciences and ÚNKP-18-4 (Bolyai+) also supported KK. JP was supported by the European Union and he State of Hungary, co-financed by the European Social Fund in the framework of GINOP 2.3.2–15–2016-00022 TAMOP-4.2.2. A-11/1/KON-2012-0024, TAMOP-4.2.4.A/2-11/1-2012-0001 National Excellence Program, PTE AOK-KA-2013/22 and EFOP-3.6.1-16-2016-00004.

ACKNOWLEDGMENTS

We are grateful to Prof. Graham Anderson (Institute of Immunology and Immunotherapy, University of Birmingham, UK) for providing us the TEP1 mouse thymic epithelial cell line. The authors wish to thank Prof. Hajnalka Abraham MD, Ph.D. (Central Electron Microscope Laboratory, University of Pecs, Hungary) for the technical aid in taking transmission electron microscope images, Prof. Peter Balogh MD Ph.D. (Department of Immunology and Biotechnology, University of Pecs, Hungary) for providing professional help during *in vivo* administration of exosomes, and also Tamas Kiss diagnostic assistant (*in vivo* Imaging Core Facility, Szentagothai Research Center, University of Pecs, Hungary). The authors wish to thank Ricky Odedra (Humeltis Ltd) and prof. Mary Keen (University of Birmingham, UK) for improving the manuscript using their native speaker skills.

SUPPLEMENTARY MATERIAL

The Supplementary Material for this article can be found online at: https://www.frontiersin.org/articles/10.3389/fimmu.2019.00862/full#supplementary-material

REFERENCES

1. Romano R, Palamaro L, Fusco A, Giardino G, Gallo V, Del Vecchio L, et al. FOXN1: a master regulator gene of thymic epithelial development program. *Front Immunol.* (2013) 4:187. doi: 10.3389/fimmu.2013.00187
2. Kvell K, Varecza Z, Bartis D, Hesse S, Parnell S, Anderson G, et al. Wnt4 and LAP2alpha as pacemakers of thymic epithelial senescence. *PLoS ONE.* (2010) 5:e10701. doi: 10.1371/journal.pone.0010701
3. Pongracz JE, Parnell SM, Jones T, Anderson G, Jenkinson EJ. Overexpression of ICAT highlights a role for catenin-mediated canonical Wnt signalling in early T cell development. *Eur J Immunol.* (2006) 36:2376–83. doi: 10.1002/eji.200535721
4. Kvell K, Fejes A V, Parnell SM, Pongracz JE. Active Wnt/beta-catenin signaling is required for embryonic thymic epithelial development and functionality *ex vivo*. *Immunobiology.* (2014) 219:644–52. doi: 10.1016/j.imbio.2014.03.017
5. Heinonen KM, Vanegas JR, Brochu S, Shan J, Vainio SJ, Perreault C. Wnt4 regulates thymic cellularity through the expansion of thymic epithelial cells and early thymic progenitors. *Blood.* (2011) 118:5163–73. doi: 10.1182/blood-2011-04-350553
6. Taub DD, Longo DL. Insights into thymic aging and regeneration. *Immunol Rev.* (2005) 205:72–93. doi: 10.1111/j.0105-2896.2005.00275.x
7. Pongracz J, Hare K, Harman B, Anderson G, Jenkinson EJ. Thymic epithelial cells provide Wnt signals to developing thymocytes. *Eur J Immunol.* (2003) 33:1949–56. doi: 10.1002/eji.200323564
8. Varecza Z, Kvell K, Talabér G, Miskei G, Csongei V, Bartis D, et al. Multiple suppression pathways of canonical Wnt signalling control thymic epithelial senescence. *Mech Ageing Dev.* (2011) 132:249–56. doi: 10.1016/j.mad.2011.04.007
9. Marinova TT. Epithelial framework reorganization during human thymus involution. *Gerontology.* (2005) 51:14–18. doi: 10.1159/000081429
10. Talaber G, Kvell K, Varecza Z, Boldizsar F, Parnell SM, Jenkinson EJ, et al. Wnt-4 protects thymic epithelial cells against dexamethasone-induced senescence. *Rejuvenation Res.* (2011) 14:241–8. doi: 10.1089/rej.2010.1110
11. Gustafson B, Smith U. The WNT inhibitor Dickkopf 1 and bone morphogenetic protein 4 rescue adipogenesis in hypertrophic obesity in humans. *Diabetes.* (2012) 61:1217–24. doi: 10.2337/db11-1419
12. Lecarpentier Y, Claes V, Vallée A, Hébert J-L. Thermodynamics in cancers: opposing interactions between PPAR gamma and the canonical WNT/beta-catenin pathway. *Clin Transl Med.* (2017) 6:14. doi: 10.1186/s40169-017-0144-7
13. Lecarpentier Y, Vallée A. Opposite Interplay between PPAR gamma and canonical Wnt/Beta-catenin pathway in amyotrophic lateral sclerosis. *Front Neurol.* (2016) 7:100. doi: 10.3389/fneur.2016.00100
14. Kvell K, Pongracz JE. *Central Immune Senescence, Reversal Potentials*. InTech (2012). Available online at: http://www.ncbi.nlm.nih.gov/pubmed/28045481 (accessed July 4, 2018).
15. Willert K, Brown JD, Danenberg E, Duncan AW, Weissman IL, Reya T, et al. Wnt proteins are lipid-modified and can act as stem cell growth factors. *Nature.* (2003) 423:448–52. doi: 10.1038/nature01611
16. Zhang L, Wrana JL. The emerging role of exosomes in Wnt secretion and transport. *Curr Opin Genet Dev.* (2014) 27:14–9. doi: 10.1016/j.gde.2014.03.006

17. Wang T, Xu Z. miR-27 promotes osteoblast differentiation by modulating Wnt signaling. *Biochem Biophys Res Commun.* (2010) 402:186–9. doi: 10.1016/j.bbrc.2010.08.031
18. Jennewein C, von Knethen A, Schmid T, Brüne B. MicroRNA-27b contributes to lipopolysaccharide-mediated peroxisome proliferator-activated receptor gamma (PPARgamma) mRNA destabilization. *J Biol Chem.* (2010) 285:11846–53. doi: 10.1074/jbc.M109.066399
19. Gross JC, Chaudhary V, Bartscherer K, Boutros M. Active Wnt proteins are secreted on exosomes. *Nat Cell Biol.* (2012) 14:1036–45. doi: 10.1038/ncb2574
20. Xu D, Tahara H. The role of exosomes and microRNAs in senescence and aging. *Adv Drug Deliv Rev.* (2013) 65:368–75. doi: 10.1016/j.addr.2012.07.010
21. Théry C, Zitvogel L, Amigorena S. Exosomes: composition, biogenesis and function. *Nat Rev Immunol.* (2002) 2:569–79. doi: 10.1038/nri855
22. Wu Y, Deng W, Klinke DJ. II. Exosomes: improved methods to characterize their morphology, RNA content, and surface protein biomarkers. *Analyst.* (2015) 140:6631–42. doi: 10.1039/c5an00688k
23. Prattichizzo F, Micolucci L, Cricca M, De Carolis S, Mensà E, Ceriello A, et al. Exosome-based immunomodulation during aging: a nano-perspective on inflamm-aging. *Mech Ageing Dev.* (2017) 168:44–53. doi: 10.1016/j.mad.2017.02.008
24. Skogberg G, Telemo E, Ekwall O. Exosomes in the thymus: antigen transfer and vesicles. *Front Immunol.* (2015) 6:366. doi: 10.3389/fimmu.2015.00366
25. Turiák L, Misják P, Szabó TG, Aradi B, Pálóczi K, Ozohanics O, et al. Proteomic characterization of thymocyte-derived microvesicles and apoptotic bodies in BALB/c mice. *J Proteomics.* (2011) 74:2025–33. doi: 10.1016/j.jprot.2011.05.023
26. Skogberg G, Gudmundsdottir J, van der Post S, Sandström K, Bruhn S, Benson M, et al. Characterization of human thymic exosomes. *PLoS ONE.* (2013) 8:e67554. doi: 10.1371/journal.pone.0067554
27. Lundberg V, Berglund M, Skogberg G, Lindgren S, Lundqvist C, Gudmundsdottir J, et al. Thymic exosomes promote the final maturation of thymocytes. *Sci Rep.* (2016) 6:36479. doi: 10.1038/srep36479
28. Solti I, Kvell K, Talaber G, Veto S, Acs P, Gallyas F, et al. Thymic atrophy and apoptosis of CD4+CD8+ thymocytes in the cuprizone model of multiple sclerosis. *PLoS ONE.* (2015) 10:e0129217. doi: 10.1371/journal.pone.0129217
29. Feller D, Kun J, Ruzsics I, Rapp J, Sarosi V, Kvell K, et al. Cigarette smoke-induced pulmonary inflammation becomes systemic by circulating extracellular vesicles containing Wnt5a and inflammatory cytokines. *Front Immunol.* (2018) 9:1724. doi: 10.3389/fimmu.2018.01724
30. Kvell K, Nguyen TH, Salmon P, Glauser F, Werner-Favre C, Barnet M, et al. Transduction of CpG DNA-stimulated primary human B cells with bicistronic lentivectors. *Mol Ther.* (2005) 12:892–9. doi: 10.1016/j.ymthe.2005.05.010
31. Ragnarson B, Bengtsson L, Haegerstrand A. Labeling with fluorescent carbocyanine dyes of cultured endothelial and smooth muscle cells by growth in dye-containing medium. *Histochemistry.* (1992) 97:329–33.
32. Wei M, Yang T, Chen X, Wu Y, Deng X, He W, et al. Malignant ascites-derived exosomes promote proliferation and induce carcinoma-associated fibroblasts transition in peritoneal mesothelial cells. *Oncotarget.* (2017) 8:42262–71. doi: 10.18632/oncotarget.15040
33. Ter-Ovanesyan D, Kowal EJK, Regev A, Church GM, Cocucci E. Imaging of isolated extracellular vesicles using fluorescence microscopy. *Methods Mol Biol.* (2017) 1660:233–41. doi: 10.1007/978-1-4939-7253-1_19
34. Rana S, Yue S, Stadel D, Zöller M. Toward tailored exosomes: the exosomal tetraspanin web contributes to target cell selection. *Int J Biochem Cell Biol.* (2012) 44:1574–84. doi: 10.1016/J.BIOCEL.2012.06.018
35. Lankford KL, Arroyo EJ, Nazimek K, Bryniarski K, Askenase PW, Kocsis JD. Intravenously delivered mesenchymal stem cell-derived exosomes target M2-type macrophages in the injured spinal cord. *PLoS ONE.* (2018) 13:e0190358. doi: 10.1371/journal.pone.0190358
36. Mineo M, Garfield SH, Taverna S, Flugy A, De Leo G, Alessandro R, et al. Exosomes released by K562 chronic myeloid leukemia cells promote angiogenesis in a src-dependent fashion. *Angiogenesis.* (2012) 15:33–45. doi: 10.1007/s10456-011-9241-1
37. Ludwig A-K, De Miroschedji K, Doeppner TR, Börger V, Ruesing J, Rebmann V, et al. Precipitation with polyethylene glycol followed by washing and pelleting by ultracentrifugation enriches extracellular vesicles from tissue culture supernatants in small and large scales. *J Extracell Vesicles.* (2018) 7:1528109. doi: 10.1080/20013078.2018.1528109
38. Phan J, Kumar P, Hao D, Gao K, Farmer D, Wang A. Engineering mesenchymal stem cells to improve their exosome efficacy and yield for cell-free therapy. *J Extracell Vesicles.* (2018) 7:1522236. doi: 10.1080/20013078.2018.1522236
39. Ramirez MI, Amorim MG, Gadelha C, Milic I, Welsh JA, Freitas VM, et al. Technical challenges of working with extracellular vesicles. *Nanoscale.* (2018) 10:881–906. doi: 10.1039/C7NR08360B
40. Van Deun J, Mestdagh P, Sormunen R, Cocquyt V, Vermaelen K, Vandesompele J, et al. The impact of disparate isolation methods for extracellular vesicles on downstream RNA profiling. *J Extracell Vesicles.* (2014) 3:24858. doi: 10.3402/jev.v3.24858
41. Takahashi Y, Nishikawa M, Shinotsuka H, Matsui Y, Ohara S, Imai T, et al. Visualization and *in vivo* tracking of the exosomes of murine melanoma B16-BL6 cells in mice after intravenous injection. *J Biotechnol.* (2013) 165:77–84. doi: 10.1016/j.jbiotec.2013.03.013
42. Wei G, Jie Y, Haibo L, Chaoneng W, Dong H, Jianbing Z, et al. Dendritic cells derived exosomes migration to spleen and induction of inflammation are regulated by CCR7. *Sci Rep.* (2017) 7:42996. doi: 10.1038/srep42996
43. Karbiener M, Fischer C, Nowitsch S, Opriessnig P, Papak C, Ailhaud G, et al. microRNA miR-27b impairs human adipocyte differentiation and targets PPARgamma. *Biochem Biophys Res Commun.* (2009) 390:247–51. doi: 10.1016/j.bbrc.2009.09.098
44. Lin Q, Gao Z, Alarcon RM, Ye J, Yun Z. A role of miR-27 in the regulation of adipogenesis. *FEBS J.* (2009) 276:2348–58. doi: 10.1111/j.1742-4658.2009.06967.x
45. Skogberg G, Lundberg V, Berglund M, Gudmundsdottir J, Telemo E, Lindgren S, et al. Human thymic epithelial primary cells produce exosomes carrying tissue-restricted antigens. *Immunol Cell Biol.* (2015) 93:727–34. doi: 10.1038/icb.2015.33
46. Wen SW, Sceneay J, Lima LG, Wong CSF, Becker M, Krumeich S, et al. The biodistribution and immune suppressive effects of breast cancer-derived exosomes. *Cancer Res.* (2016) 76:6816–27. doi: 10.1158/0008-5472.CAN-16-0868
47. Ernszt D, Banfai K, Kellermayer Z, Pap A, Lord JM, Pongracz JE, et al. PPARgamma deficiency counteracts thymic senescence. *Front Immunol.* (2017) 8:1515. doi: 10.3389/fimmu.2017.01515

Conflict of Interest Statement: The authors declare that the research was conducted in the absence of any commercial or financial relationships that could be construed as a potential conflict of interest.

Immunobiology 219 (2014) 644–652

Contents lists available at ScienceDirect

Immunobiology

journal homepage: www.elsevier.com/locate/imbio

Active Wnt/beta-catenin signaling is required for embryonic thymic epithelial development and functionality *ex vivo*

Krisztian Kvell[a,*], Aniko V. Fejes[a], Sonia M. Parnell[b], Judit E. Pongracz[a,b]

[a] Department of Pharmacological Biotechnology, University of Pecs, Hungary
[b] Department of Anatomy, Division of Immunity and Infection, Institute for Biomedical Research, University of Birmingham, UK

ARTICLE INFO

Article history:
Received 13 July 2013
Accepted 25 March 2014
Available online 2 April 2014

Keywords:
Embryonic development
FoxN1
ICAT
Thymic epithelium
Wnt

ABSTRACT

The Wnt/beta-catenin signaling pathway plays an important role in the commitment and development of thymic epithelial precursors. Here we document similarities of thymic epithelial development during embryogenesis in human and mouse. We stained for thymic epithelial surface markers (EpCAM1, Ly51, K8) and ligand/receptor pair (Wnt4, Fz4). Our results confirm the relevance of using murine test systems to model human embryonic thymic epithelial cell development.

We have efficiently transduced murine embryonic epithelial cells using mock (GFP) and Wnt/beta-catenin-inhibiting (ICAT-encoding) recombinant adenoviral vectors. The effect of Wnt4 was assayed in the form of Wnt4-containing supernatant. Gene expressional changes were assessed by Q-PCR and also morphology using conventional and confocal fluorescent microscopy. Functional aberration caused by ICAT was assessed through evaluation of thymocyte maturation.

Our results demonstrate that ICAT and Wnt4 have reciprocal effects during embryonic thymic epithelial cell development. While Wnt4 is capable of increasing the expression level of characteristic intracellular (FoxN1), surface (MHCII) and secreted (IL7) molecules, Wnt/beta-catenin inhibition through ICAT can moderately decrease their expression. Morphological changes induced by ICAT resulted in the development of hollow, inflated thymic lobes with reduced epithelial cell numbers. The ICAT-treated thymic lobes also showed significant impairment in supporting thymocyte development and maturation.

Introduction

Along with Notch and BMP, the abundantly secreted Wnt (wingless-related MMTV integration site) glycoproteins have been proposed to play an elementary role in the development, maintenance and functional integrity of the thymic stroma (Bleul and Boehm 2005; Pongracz et al. 2003; Osada et al. 2006; Anderson et al. 2001). The current article focuses on the evolutionarily conserved molecular family of secreted Wnt glycoproteins. The nineteen known Wnt glycoproteins signal through ten G-protein dependent receptors, called Frizzled receptors. For active signal transduction, Frizzled receptors need to form a complex with low density lipoprotein receptor-related proteins (LRP), as co-receptors. The actual constellation of the ligand, receptor and co-receptor defines Wnt-mediated effects in a context-dependent manner (Mikels and Nusse 2006; Gordon and Nusse 2006; Schweizer and Varmus 2003). Wnt4 is in spotlight of the current work being one of the most abundantly expressed non-canonical Wnt molecule secreted by the thymic epithelium during embryonic development, with expression levels progressively decreasing during postnatal development and aging (Kvell et al. 2010; Kvell and Pongracz 2011; Varecza et al. 2011). It is of note that FoxN1 (a key transcription factor that defines thymic epithelial identity) is an acknowledged target gene of Wnt4 in the thymic epithelial context (Balciunaite et al. 2002). ICAT (inhibitor of beta-catenin and TCF-4) is a polypeptide that inhibits Wnt/beta-catenin nuclear signaling by binding and competing its interaction with the transcription factor TCF (T cell factor) in the nucleus. Therefore ICAT is an intracellular negative regulator of the Wnt/beta-catenin pathway (Pongracz et al. 2006). Since the Wnt glycoproteins and Wnt4 in particular are key players of embryonic thymic epithelial development we examined the effect of both increased Wnt-effect (additional Wnt4 in the form of supernatant)

Abbreviations: BMP, bone morphogenic protein; EpCAM, epithelial cell adhesion molecule; FoxN1, forkhead box N1; Fz, frizzled; GFP, green fluorescent protein; ICAT, inhibitor of beta-catenin; IL7, interleukin 7; K, keratin; LRP, low density lipoprotein receptor-related proteins; MHCII, major histocompatibility complex II; TCF, T-cell factor; rAd, recombinant adeno-viruses; Wnt, wingless-related MMTV integration site.

* Corresponding author at: Department of Pharmacological Biotechnology, University of Pecs, 20 Ifjusag Street, H-7624 Pecs, Hungary. Tel.: +36 72 536 000/29250.
E-mail address: kvell.krisztian@pte.hu (K. Kvell).

http://dx.doi.org/10.1016/j.imbio.2014.03.017
0171-2985/

and decreased Wnt-effect (ICAT over-expression through adenoviral vectors) in embryonic thymic lobes *ex vivo*. In the mouse the thymus appears on day eleven (E11) of the total 21 days of embryonic development. The epithelial progenitors appear first followed by the quick colonization by T-cell progenitors from E12 onwards. By E15 the thymic epithelial medulla and cortex begin to form separate compartments required for the selection steps of developing thymocytes (Rezzani et al. 2008). In the human embryo the thymus appears on week 5 (W5) of the total 40 weeks of embryonic development. T-cell progenitors colonize the stromal niche from W7 (Hayward and Ezer 1974; Lobach and Haynes 1987). Despite obvious differences between murine and human embryonic thymic development concerning timing, numerous inter-species similarities exist in terms of function and immunological competence. The current article includes histological comparison of human and mouse embryonic thymic sections to identify similarities in staining patterns of cell surface and secreted proteins. Such similarities would highlight the utility of murine embryonic thymic test systems for their relevance in the context of human embryonic thymic epithelial development.

Materials and methods

Mouse and human thymic samples

Mice were bred in our animal facility. All animal work has been conducted according to relevant national and international guidelines following approval of ethics committee of the University of Pecs (ref. no. BA02/2000-3/2006). For *ex vivo* experiments we used thymic lobes from timed pregnancies at E12 and E15.

Human thymic sample originates from W15 aborted fetus. Abortion was initiated due to diagnosis of Patau-syndrome (chromosome 13 trisomy) that does not interfere with embryonic thymic development. The procedures were conducted according to relevant national and international guidelines following approval of ethics committee of the University of Pecs (ref. no. ad.8-2/2009-1018EKU).

Ex vivo experiments

Murine embryonic E12 and E15 thymic lobes were cultured in DMEM supplemented with 10% FCS, penicillin, streptomycin and beta-mercapto-ethanol (Lonza Walkersville). Recombinant adenoviral (rAd) preparations (prepared as published previously) that specifically transfect epithelial cells were added to the culture medium of murine thymic lobes that were further cultured for up to seven days (Hare et al. 2003). Flow-cytometric analysis of E12 murine thymic epithelial cells was performed 48 h following rAd transfection (E12 murine thymic lobes are devoid of thymocytes). E15 murine thymocytes were selectively liberated by mechanic dispersion then stained 168 h after rAd transfection (E15 murine thymic epithelial cells would require prolonged collagenase digestion for liberation). Murine thymocytes were stained with CD4-PE (clone H129.19 from BD Pharminden) and CD8-FITC (clone 53-6.7 from BioLegend) labeled antibodies. FACS Calibur cytometer and Cell Quest software were used for analysis (Becton Dickinson, USA).

The supernatant of mock and Wnt4-secreting transgenic TEP1 cells (murine thymic epithelial cell line model) were prepared as published previously (Kvell et al. 2010). (Recombinant Wnt proteins become inactivated during the process of purification, hence the use of supernatants instead). In order to exclude the thymocyte-mediated effects of secreted Wnt4 either E12 tmurine hymic lobes were used (practically devoid of thymocyte progenitors) or E15 murine thymic lobes were pre-treated with deoxiguanosine (at 2 mM final, Sigma) for five days prior to the ten-day supernatant treatment.

Histology

Cryostate sections (9 μm) of murine and human thymic lobes were fixed in cold acetone, then dried and blocked using 5% BSA in PBS for 20 min before staining with a-Ly51-PE (clone 6C3 from BD Pharmingen), a-EpCAM-FITC (clone G8.8, monoclonal antibody prepared in our lab), a-K8 (clone Ks8.7 from Santa Cruz Biotechnology), a-Wn4 (clone C-14 from Santa Cruz Biotechnology) or a-Fz4 (clone C-18 from Santa Cruz Biotechnology). Unlabeled antibodies were visualized using secondary antibodies of the Northern Light secondary antibody family (NL557 family, NL001: anti-goat, NL007: anti-mouse from R&D Systems). The sections were analyzed using Olympus BX61 system.

Cultured E12 murine thymic lobes were fixed in paraformaldehyde and stained in whole using the same reagents as above, but applying extended incubation period for fixation, wash and staining (~60 min each) to allow for antibodies to penetrate the miniature embryonic thymic lobes. Confocal fluorescent images were captured using the Olympus Fluoview-1000 system.

RNA isolation, cDNA preparation, Q-PCR analysis

Total RNA was isolated from the cultured murine thymic lobes using the RNAII kit (Macherey-Nagel), including a DNase digestion step. Then cDNA was synthesized using the high capacity RNA to cDNA kit (Life Technologies). For Q-PCR analysis, we used an AB7500 platform and SYBR green I chemistry (Life Technologies). Gene expression was normalized to beta-actin. The sequences/catalog numbers of mouse-specific primers are listed in Table 1. Primers were not designed to be exon-spanning, however, on column DNase digestion during RNA preparation eliminated genomic DNA residues.

Statistical analysis

All experiments were performed on three occasions, representative experiments are shown. Measures were obtained in triplicates; data are presented as mean ± 1 SD by error bars.

Results

Histological characterization of human embryonic thymus

Human embryonic thymic sections from W15 were stained for characteristic cell surface and secreted markers. Fig. 1A shows staining for EpCAM-1 and Ly-51 surface antigens. As expected EpCAM-1 is moderately expressed by all thymic epithelial cells with areas showing increased EpCAM-1 staining that correspond to epithelial cells of the medulla. Parallel Ly-51 staining identifies cortical epithelial cells. It appears that by W15 the thymic epithelial cells show distinct patterning to regions of the medulla and cortex, based on staining with these two markers. Fig. 1B shows co-localization of EpCAM-1 and cytokeratin8 following histological staining. Cytokeratin8 appears to stain broad epithelial areas of the human thymus, largely overlapping with EpCAM-1 staining. The staining patterns of the secreted Wnt4 molecule as well as its ligand Fz4 have also been assayed as demonstrated by Fig. 1C and D. As expected, Wnt4 is primarily expressed by the thymic epithelium as shown by the significantly overlapping staining pattern of Wnt4 and EpCAM-1. On the other hand, Fz4 expression shows only moderate co-localization with EpCAM-1, and indeed

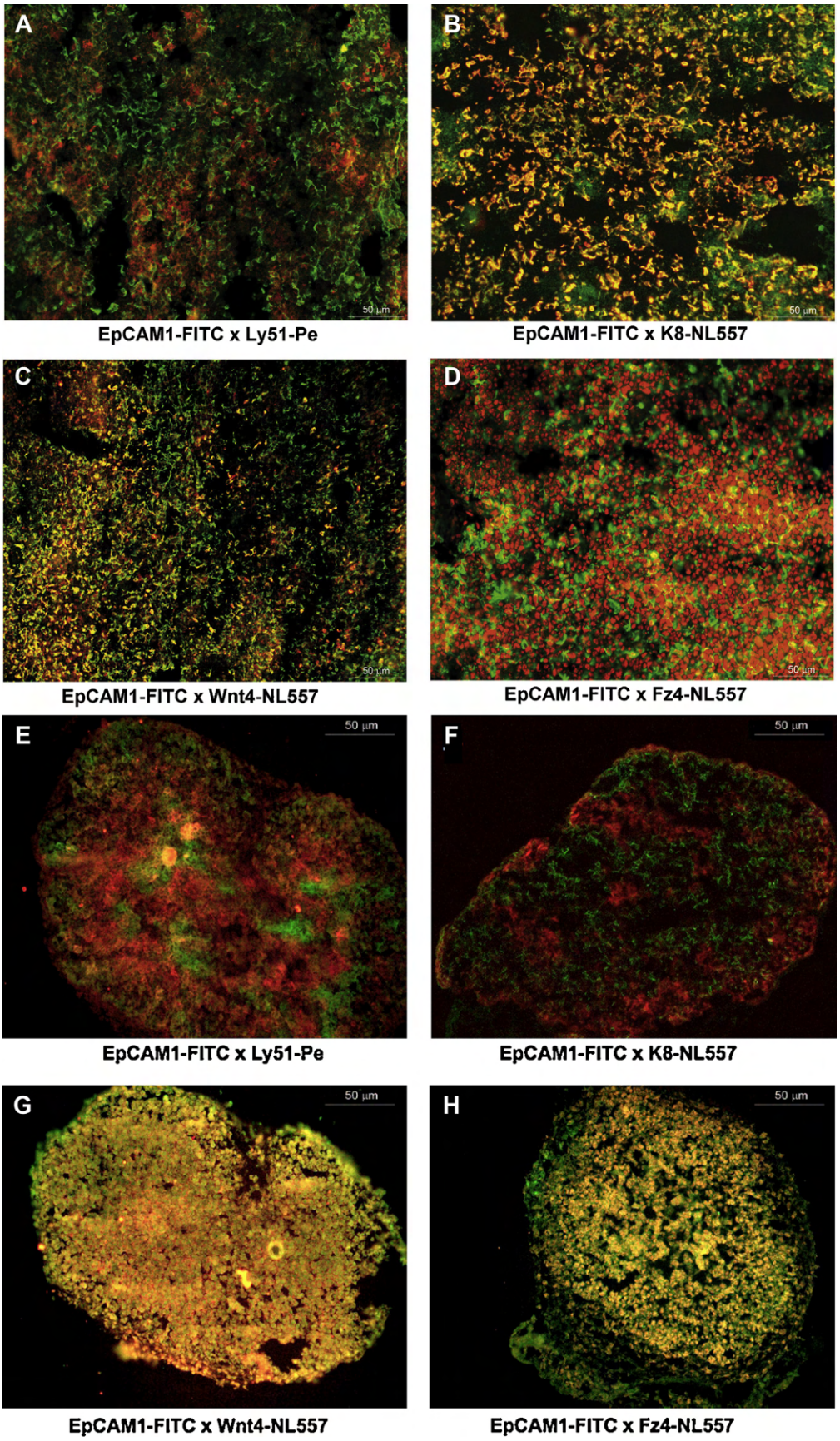

Fig. 1. Figure shows the histological characterization of the human embryonic thymus at 15w of age at 20× magnification using fluorescent microscopy. The figures portray co-localization patterns with EpCAM1 epithelial surface antigen. (A) Shows Ly51, (B) demonstrates cytokeratin8, (C) portrays Wnt4, while (D) depicts Fz4 staining pattern with respect to the thymic epithelial context. (A) Shows segregation of medullary (EpCAM1++) and cortical (Ly51+) epithelial cells. (B, C) Identify epithelial cells as the major source of K8 expression and Wnt4 secretion in this setting. As expected, (D) shows a distinct pattern as epithelial cells are not the only Fz4-bearing cells in thymus.

Table 1
List of gene specific PCR primers.

Gene	Forward primer	Reverse primer
Beta-actin	5′-TGG CGC TTT TGA CTC AGG A-3′	5′-GGG AGG GTG AGG GAC TTC C-3′
ICAT	5′-CGG AGG AGA TGT ACA TTC AAC AGA-3′	5′-TCA CTG GCG GTC AGG TTT G-3′
MHCII	5′-CTA GCC AAG TCC CTC CTA AGG-3′	5′-ATC TCA GAC TGA TCC TGG CAT-3′
IL7	5′-ACT ACA CCC ACC TCC CGC A-3′	5′-TCT CAG TAG TCT CTT TAG G-3′
FoxN1	Applied Biosystems TaqMan probe PN4351272 (Mm00477457_m1)	–

the vast population of non-epithelial cells including thymocytes are also known to be among Wnt4-binding cells.

Histological characterization of mouse embryonic thymus

Mouse embryonic thymic sections from E15 were also stained for the same, characteristic cell surface and secreted markers used above. Fig. 1E portrays staining for EpCAM-1 and Ly-51 surface antigens. As observed with the human sections, EpCAM-1 is expressed by all thymic epithelial cells with certain areas showing increased EpCAM-1 expression identifying epithelial cells of the medulla, while Ly-51 staining defines cortical epithelial cells. It seems that by the embryonic age E15 the thymic epithelial cells show differentiation toward either medullary or cortical phenotype, based on staining patterns. Fig. 1F shows staining with EpCAM-1 and cytokeratin8. The murine section shows expression with both surface markers, although the staining pattern is different from that of the human section showing significantly less overlap. The expression and staining pattern of the secreted Wnt4 molecule as well as its ligand Fz4 have also been tested as shown by Fig. 1G and H. Both Wnt4 and Fz4 are rather ubiquitously expressed in the mouse thymus and both show significant overlap with EpCAM-1. This co-localization is more significant in the mouse compared to the human section for both Wnt4 and Fz4.

Adenoviral transgene delivery to thymic epithelial cells

E12 murine thymic epithelial cells were transfected with recombinant adenoviral (rAd) vectors that specifically transfect epithelial cells and leave other cells unaffected. The vectors encoded either GFP marker gene alone (mock) or in combination with ICAT. Transfection efficiency was assayed by flow cytometry 48 h later and was found to be very high with the mock vector (91.49%) and high with the ICAT-encoding rAd vector (69.36%) based on GFP expression of transected cells (see Fig. 2A and B). Transgene expression was also verified at the mRNA level for ICAT by Q-PCR and was found to be efficiently over-expressed (∼10,000× or four magnitudes, see Fig. 2C) in the case of ICAT-encoding rAd compared to mock-transfection baseline, proving that rAd vectors are highly suitable vehicles for gene delivery into thymic epithelial cells.

Mouse E15 embryonic thymic lobes were transfected with rAd vectors encoding either GFP marker gene alone (mock) or combined with ICAT. In parallel, following thymocyte-depletion achieved by deoxiguanosine-treatment, further E15 murine thymic lobes were incubated in the presence of supernatants of either control or Wnt4-secreting transgenic TEP1 cells (thymic epithelial cell line model, method published previously (Beardsley et al. 1983). The effect of ICAT over-expression and additional Wnt4-treatment on gene expression was tested at the level mRNA by Q-PCR after seven days of incubation following treatment as shown on Fig. 3. Both treatments had their own controls (control supernatant for Wnt4-treatment and mock (GFP)-transfection for ICAT-transfection). Values corresponding to these controls were set as starting levels represented by value 1 of the vertical axis hence called relative gene expression. The assayed genes included surface (MHCII), intracellular (FoxN1) and secreted (IL7) molecules, conventionally associated with epithelial phenotype and function in the context of the thymus. Our results indicate that all the three assayed genes were up-regulated following increased Wnt4 exposure provided by Wnt4-containing supernatant compared to treatment with mock supernatant (MHCII: >2×, FoxN1: >3×, IL7: ∼6×). In parallel, the same read-out genes showed moderate, but consequent down-regulation following the over-expression of ICAT compared to mock-transfection baseline. Thus our data summarized by Fig. 3 indicate that increased Wnt4-exposure and the inhibition of the Wnt/beta-catenin pathway through ICAT have reciprocal effects on characteristic surface (MHCII), intracellular (FoxN1) and secreted (IL7) molecules conventionally associated with epithelial phenotype and function in the context of the thymus.

Morphological changes at the level of histology

Mouse embryonic thymic lobes from E12 (predominantly containing thymic epithelial progenitors) have been transfected with the above mock (GFP) and ICAT-encoding adenoviral vectors. Following an incubation period of seven days the thymic lobes were visualized in whole by conventional and confocal fluorescent microscopy following staining for EpCAM-1 to show thymic epithelial cells. Fig. 4A and B show mock-transfected and ICAT-transfected stained whole thymic lobes, respectively, by conventional fluorescent microscopy. The thymic lobe transfected with rAd ICAT appears to be larger in diameter compared to the mock-transfected thymic lobe (∼0.85 mm *vs.* ∼1.35 mm based on scale bar). However, if the same lobes are visualized using a confocal microscope combined with trans-white imaging, it becomes evident that the ICAT-transfected lobe is hollow compared to the mock-transfected thymic lobe (see Fig. 4C and D, respectively) harboring a large cavity without cells. It is also of note that the remaining epithelial cells reside adjacent to the inner lining of the internal cavity. (These phenomena are shown by the combination of confocal single-plane and conventional trans-white imaging used on Fig. 4C and D). Occasional thymic cysts were also observed with this combined imaging technique following ICAT-transfection (see Fig. 4D). Decreased cellularity despite increased lobe size was also supported by significantly lower RNA yield (∼0.3×) obtained with ICAT-transfected lobes compared to mock-transfected lobes (data not shown).

Figure portrays the histological characterization of the mouse embryonic thymus at E15 of age at 10× magnification using fluorescent microscopy. The figures show co-localization patterns with EpCAM1 epithelial surface antigen. (E) Demonstrates Ly51, (F) shows cytokeratin8, (G) depicts Wnt4, while (H) portrays Fz4 staining pattern with respect to the thymic epithelial context. According to (E) the medullary (EPCAM1++) and cortical (Ly51+) thymic epithelial regions show distinct patterns by E15. (F) Shows that K8 expression is different in the mouse as in the human, there is no significant overlap with EpCAM1-expression. (G) Shows similar ubiquitous expression of Wnt4 as seen in the human section. (H) Demonstrates that Fz4 expression is rather ubiquitous in the mouse setting compared to the human section.

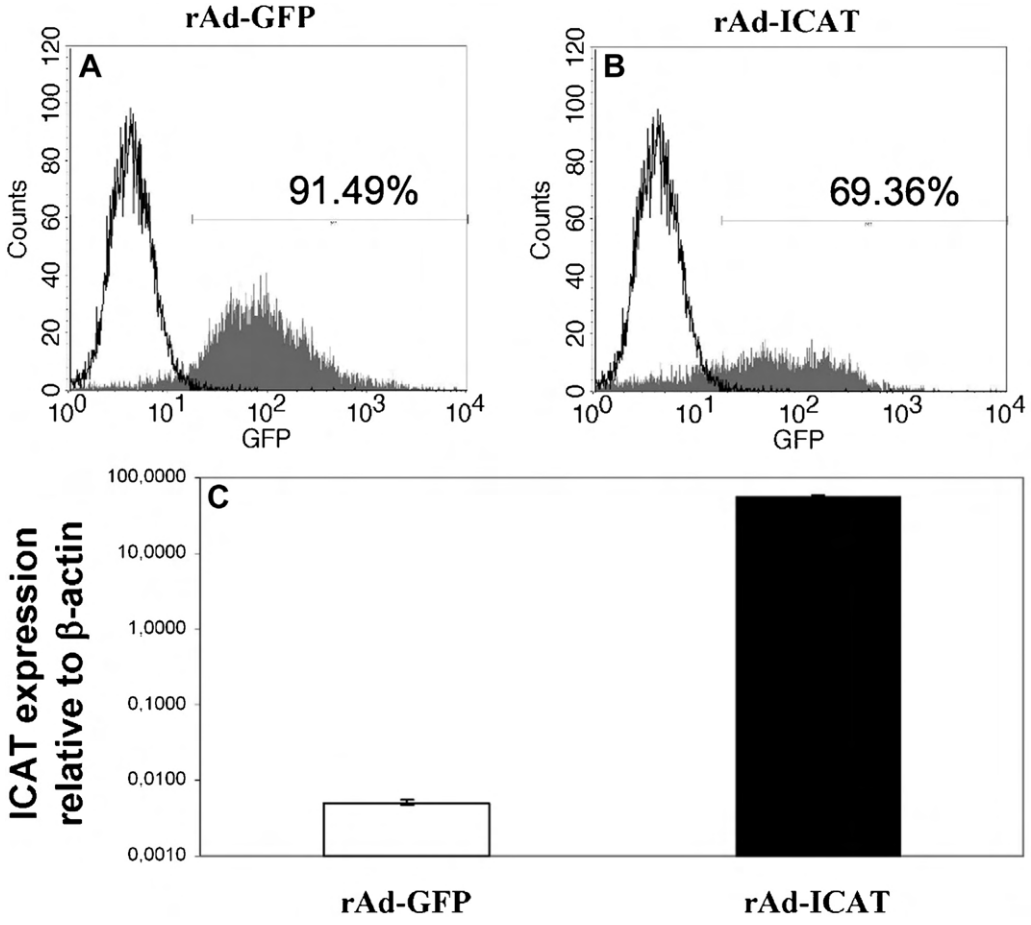

Fig. 2. Figure shows the flow-cytometric and Q-PCR characterization of transfection efficiency using recombinant adenoviral vectors to transfect E12 embryonic thymix epithelial cells. (A, B) Demonstrate GFP marker gene expression 48 h following GFP or ICAT transfection (shown by gray fill) compared to control cells (shown by black line). Transfection efficiencies were 91.49% for GFP(mock)- and 69.36% for ICAT-transfection, respectively. (C) Shows the increase of ICAT mRNA level obtained following transfection with ICAT-encoding recombinant adenoviral vector compared to vector encoding GFP alone. Please note that scale is exponential and hence shows increase of four magnitudes.

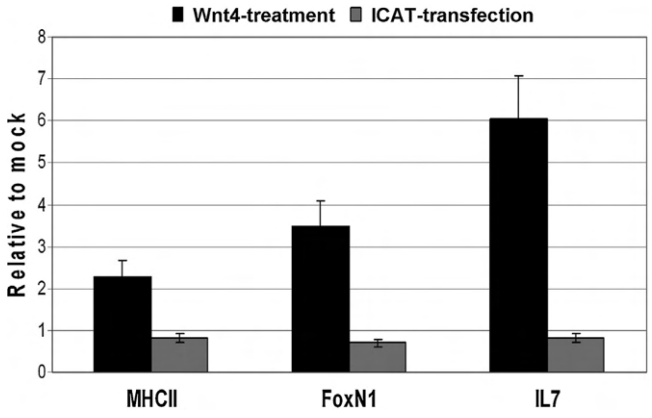

Fig. 3. Figure demonstrates gene expressional changes of characteristic epithelial cell surface (MHCII), intracellular (FoxN1) and secreted (IL7) in the embryonic thymic context measured by Q-PCR. The figure shows the effects of Wnt4-treatment (black boxes) and ICAT-transfection (gray boxes) on the mRNA levels of the assessed genes in E15 thymic lobes, error bars show ±1 S.D. Both Wnt4-treatment and ICAT-transfection had their own controls in the form of control-treatment and GFP(mock)-transfection, respectively. These provide control values represented by value 1 on the vertical axis (hence relative expression). Please note that Wnt4-treatment can reach all cells, whereas ICAT-transfection cannot.

Functional changes indicated by thymocyte maturation

Mouse embryonic thymic lobes from E15 (already colonized by thymocyte precursors) have also been transfected with the above mock (GFP)- and ICAT-encoding adenoviral vectors. Following an incubation period of seven days thymocytes were selectively liberated by mechanic dispersion then stained for CD4 and CD8 expression (E15 murine thymic epithelial cells would require prolonged collagenase digestion for liberation). During flow-cytometric evaluation viable cells (using morphological R1 gate, see Fig. 5A) were statistically analyzed for CD4/CD8 ratio (see Fig. 5B–D). A young adult (1 month old) female BALB/c mouse was sacrificed and the thymocytes were likewise liberated and stained for CD4/CD8 expression and ratio, serving as control (see Fig. 5B). The young adult thymus contains plenty of double positive thymocytes (46.6% CD4+, CD8+) and among single either CD4 or CD8 positive cells the helper T-cells dominate over cytotoxic T-cells (41.7% *vs.* 3.3%), as normally observed in young adult BALB/c mice. In comparison the mock (GFP)-transfected embryonic thymic lobe (Fig. 5C) shows a somewhat different ratio for CD4/CD8 expression. There are more double negative thymocytes (34.8% CD4−, CD8−) and less single either CD4 or CD8 positive T-cells (15% and 5.8%, respectively) with equal number of double positive thymocytes (44.4% CD4+, CD8+). Differences compared to young adult figures are likely due to the embryonic context of thymocyte development continued in an *ex vivo* setting. What is more striking,

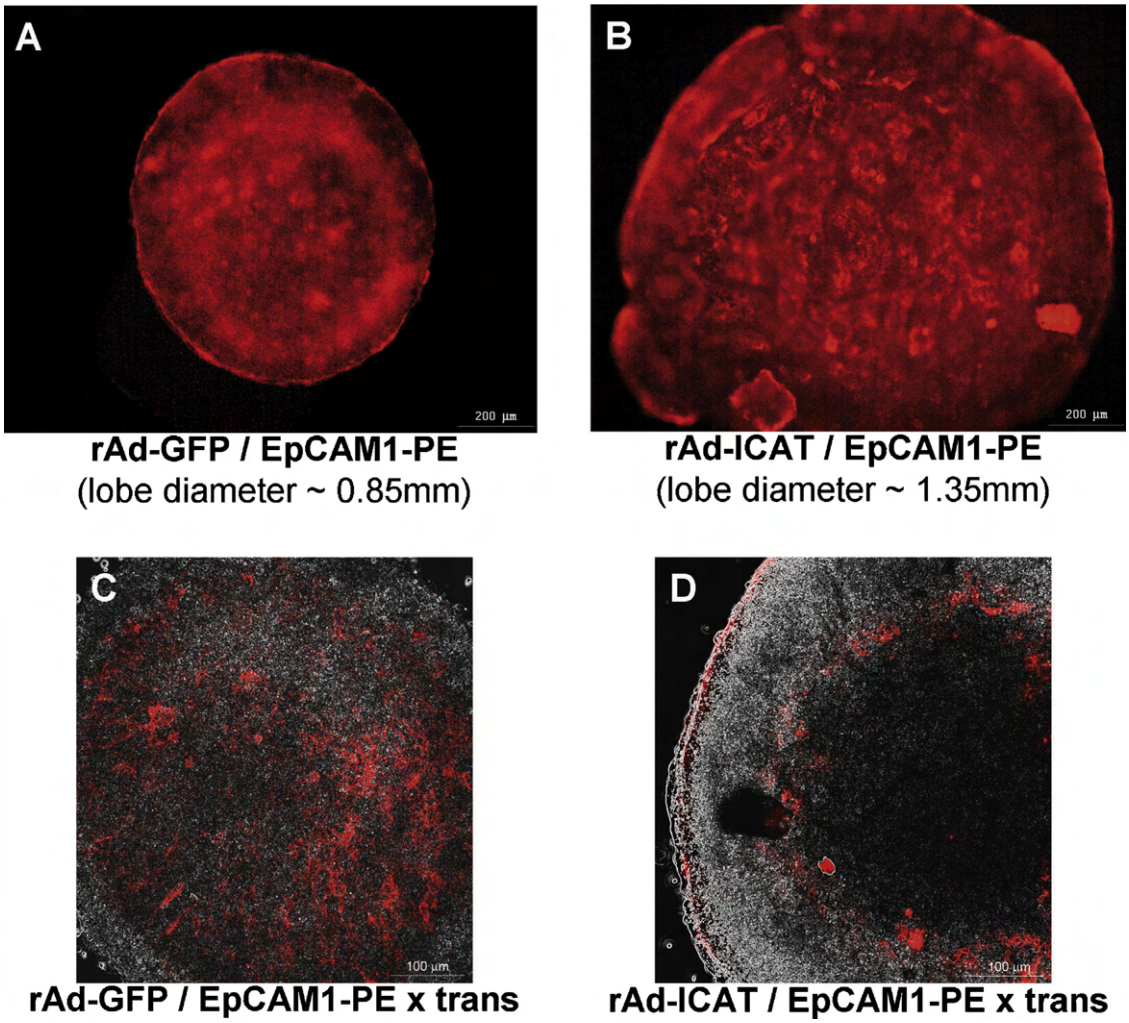

Fig. 4. Figure shows histological level morphological differences of mock and ICAT-transfected embryonic thymic lobes using fluorescent conventional and confocal microscopy. Epithelial cells were stained for their EpCAM1-expression on all four images. (A, B) Obtained with conventional fluorescent microscopy illustrates the size difference of GFP and ICAT-transfected lobes. The applied size marker (lower right corner) allows for approximate determination and comparison of lobe diameters. (C, D) Obtained with confocal microscopy allow for the visualization of internal lobe structure showing EpCAM1-staining cells in the examined plane (staining red) as well as the entire organ (trans-white image layer shown in gray). The lobe is significantly larger following ICAT-transfection as shown by Fig. 3(B and D). However, the lobe is inflated harboring a hollow cavity lined by epithelial cells following ICAT-transfection as shown by Fig. 3D. Occasional cysts are also observed (Fig. 3D).

however, is the degree of difference in CD4/CD8 ratio observed among thymocytes following ICAT-transfection (see Fig. 5D). There is a dominance of double negative thymocytes (80.9% CD4−, CD8−) with very few double positive thymocytes (8% CD4+, CD8+) and even less single either CD4 or CD8 positive T-cells (4.2% and 7%, respectively). The difference in CD4/8 ratio is striking not only compared to young adult, but also compared to mock-transfected E15 thymic lobes. Differences compared to mock-transfection can only be attributed to selective inhibition of Wnt/beta-catenin signaling through ICAT in mouse embryonic thymic epithelial cells selectively transfected by rAd vectors providing an altered niche for murine thymocyte development.

Discussion

Comparative histology

Human (W15) and mouse (E15) embryonic thymic sections were examined at the level of histology. The presence of characteristic cell surface markers (EpCAM-1, Ly-51, cytokeratin8) as well as a secreted protein and its ligand (Wnt4, Fz4) was assessed (Gill et al. 2002; Bennett et al. 2002; Klug et al. 2002). Both human and mouse sections stained positive for all the examined proteins. The thymic epithelial compartments of the medulla and the cortex showed signs of segregation in both the W15 human and the E15 mouse thymic sections. Staining patterns obtained with cytokeratin8 and Fz4 in particular showed differences between human and mouse. This, however, is not surprising as the examined embryonic stages (W15 for human and E15 for mouse) do not match exactly in terms of thymic developmental stage. Nevertheless it is reassuring that the same characteristic cell surface markers, secreted proteins and ligands are equally present during human and murine embryonic development emphasizing the human relevance of murine test systems therefore subsequent experiments were performed on murine cells.

Changes in gene expression related to Wnt/beta-catenin signaling

Reciprocal input signals were provided to murine embryonic thymic epithelial cells in terms of the Wnt/beta-catenin signaling pathway. Increased non-canonical Wnt-effect was modeled through providing additional Wnt4 in the form of supernatant. The opposite effect was achieved through rAd-mediated transfection of the ICAT transgene that inhibits the Wnt/beta-catenin signaling

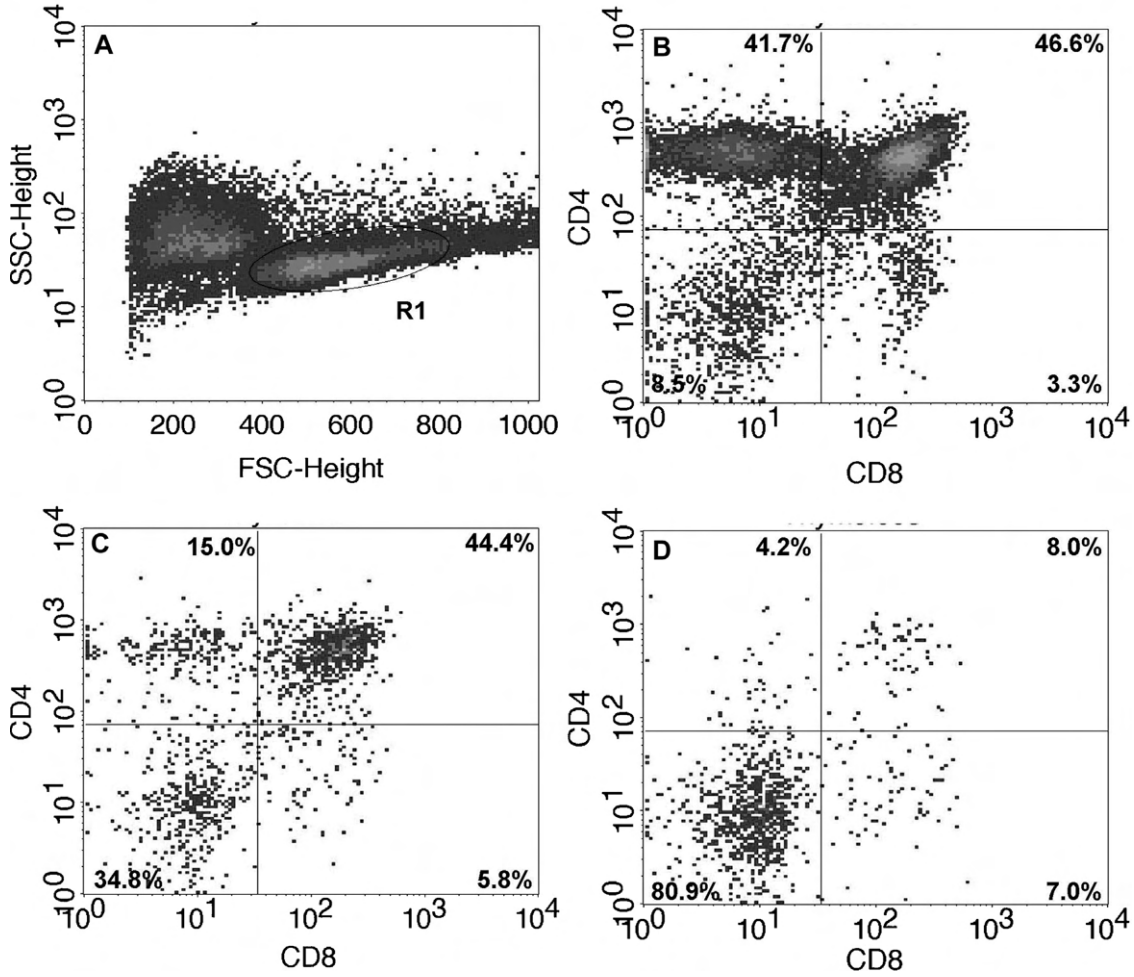

Fig. 5. Figure demonstrates flow-cytometric evaluation of epithelial functionality shown by thymocyte maturation. The thymic lobes were mechanically dispersed liberating the thymocytes. Viable cells were gated (R1) by morphology (A). Thymocytes were stained with CD4-PE and CD8-FITC. The ratio of CD4/CD8 expression is shown in viable thymocytes from young adult (B) control, and GFP-transfected (C) or ICAT-transfected (D) E15 thymic lobes after 7 days of *ex vivo* culture. Percentages of flow-cytometric statistics are shown in the corresponding quadrants. Representative flow-cytometric figures are shown. The young adult sample and the GFP(mock)-transfected sample show similarity in terms of thymocyte subpopulations. The CD4/CD8 double positive group shows equal representation, while double negative cells are more frequent and single positive cells are less frequent in the mock-transfected scenario compared to the young adult control, likely due continued *ex vivo* development in an embryonic setting. However, thymocyte subpopulation distribution is rather different following ICAT-transfection as there is a severe block in development shown by the accumulation of double negative cells and the loss of double positive and single positive cell groups.

pathway. Gene expression analysis of surface (MHCII), intracellular (FoxN1) and secreted (IL7) molecules, conventionally associated with epithelial phenotype and function in the context of the thymus showed that additional Wnt4 exposure could significantly increase the transcription of all three examined genes. It is of note that our data obtained *ex vivo* are in harmony with literature data suggesting that FoxN1 is a direct target gene of Wnt4 (Gill et al. 2002). In contrast, the over-expression of ICAT could consequently, though moderately down-regulate the transcription of all three examined genes.

The fact that decrease in gene expression achieved through ICAT-transfection was moderate is due to several factors. The Wnt4 supernatant affects all cells of the experimental system through a cell non-autonomous effect. In contrast, ICAT could only inhibit the Wnt/beta-catenin signaling pathway in transfected thymic epithelial cells due to its intracellular/cell-autonomous route of action. Also, gene expressional change following ICAT-mediated inhibition was compared to mock-transfection corresponding to basal level Wnt4 secretion that is low compared to additional Wnt4 supernatant. Currently there is no way in our experimental system for quantitative, balanced reciprocal Wnt4/ICAT treatment to affect epithelial cells with opposing signals of equal intensity.

Changes in morphology related to Wnt/beta-catenin signaling

We have performed mock-transfection and ICAT-transfection of E12 mouse embryonic thymic lobes followed by staining for EpCAM-1 and visualization in whole. Conventional fluorescent microscopy shows that the thymic lobes become significantly larger in diameter following ICAT-transfection compared to mock-transfection. However, confocal fluorescent microscopy (especially if combined with trans-white conventional image) shows that the ICAT-transfected lobe is rather empty compared to the mock-transfected thymic lobe containing a hollow cavity without cells. Also the overall number of epithelial cells appears to be lower and restricted to a spherical area surrounding the hollow cavity in this aberrant developmental scenario.

Changes in functionality related to Wnt/beta-catenin signaling

The indirect effect of Wnt4 on thymocyte development has already been thoroughly investigated by other groups (Heinonen et al. 2011). Therefore we focused on examining the indirect effect of selective Wnt/beta-catenin inhibition in murine thymic epithelial cells, thus altering the niche in which thymocytes develop.

At later stages (from E13 onwards) the mouse embryonic thymus contains thymocyte precursors that can undergo maturation processes *ex vivo*. We have performed mock (GFP)-transfection and ICAT-transfection of E15 mouse embryonic thymic lobes followed by flow-cytometric analysis of viable thymocytes for CD4/8 expression to demonstrate changes in the functionality of epithelial cells to support thymocyte maturation. During physiological maturation the developing thymocytes are first double negative (CD4−, CD8−) and then turn on the expression of both CD4 and CD8 to become double positive (CD4+, CD8+). This is followed by the single positive stage where either CD4 or CD8 expression is spared, while the other becomes muted, normally resulting in the dominance of helper T-cells (see Fig. 5B in young adult mouse).

The normal route of thymocyte development is somewhat slowed down in the mock (GFP)-transfected embryonic *ex vivo* cultured setting where we observe less single positive and more double negative thymocytes compared to the young adult mouse (see Fig. 5C). This is not surprising as we compare thymocyte maturation *ex vivo* in embryonic thymic lobes *vs.* thymocyte maturation *in vivo* in physiological young adult thymus. However, differences are much more striking following selective inhibition of Wnt/beta-catenin signaling in thymic epithelial cells by ICAT-encoding rAd vectors as shown by the dominance of the double negative maturation stage and the scarceness of single positive cells (see Fig. 5D). It is also observed that among the few single positive cells there are more CD8+ than CD4+ cells due to the fact that these two cell surface markers are not fully synchronized during transition from double negative to double positive stage, but CD4 up-regulation is a little delayed compared to CD8 (Jimenez et al. 2001; Pearse 2006).

Conclusion

Our data obtained in an *ex vivo* murine test system with human relevance prove that if the Wnt/beta-catenin signaling pathway is blocked in epithelial cells during crucial stages of thymic embryonic development, it seriously impairs normal developmental program resulting in the formation of aberrant thymic lobe morphology. This is also supported by changes recorded at the molecular level as we have observed the consequent, though moderate down-regulation of the examined characteristic genes encoding surface (MHCII), intracellular (FoxN1) and secreted (IL7) molecules. This is in contrast with the significant increase in expression level of the same genes following treatment with additional Wnt4.

Our results obtained during *ex vivo* experiments confirm that the Wnt/beta-catenin signaling pathway is a key player responsible for the proper differentiation and maintenance of thymic epithelial cells during embryonic development and potentially in postnatal life. Literature data also suggest that if *in vivo* the Wnt/b-catenin signaling pathway is either chronically suppressed or hyper-activated both may lead to abnormal tissue homeostasis due to insufficient proliferation signals of tissue stem cells (Wnt-suppression) or due to hyper-proliferating and thus exhausted tissue stem cell pools (Wnt-hyper-activation) (DeCarolis et al. 2008; Miller 2007; Liu et al. 2007). This proposes that the Wnt/b-catenin signaling pathway has a major role not only in development but also in tissue homeostasis.

It is also clearly indicated by our data that active Wnt/beta-catenin signaling is also required for normal embryonic thymic epithelial functionality and not only morphology as demonstrated by the severely impaired capacity to support thymocyte maturation following selective ICAT-transfection into thymic epithelial cells *ex vivo*. The simultaneously observed thymic cyst formation is an exciting phenomenon. It has been reported that following K14-restricted loss of FoxN1 expression, the development of the thymic structure is seriously impaired resulting in distant alveolar-like cystic structures suggesting potential trans-differentiation (Guo et al. 2011). Further studies, however, are required to study the exact mechanisms underlying the alternative developmental scenario resulting aberrant lobe morphology following the selective inhibition of the Wnt/beta-catenin pathway in thymic epithelial cells.

Acknowledgements

Research was supported by the following grants: 'Science Please' Research Team on Innovation grant No.: SROP-4.2.2/08/1/2008-0011 (grant holder: J.E.P.) and OTKA (Hungarian Scientific Research Fund) type: PD (post-doctoral) grant No.: 78310 (grant-holder: K.K.). The funders had no role in study design, data collection and analysis, decision to publish, or preparation of the manuscript. The authors are grateful to Bela Veszpremi MD, PhD (Department of Obstetrics and Gynecology) for providing us access to human embryonic samples and Gergely Berta MD (Department of Medical Biology) for the invaluable help provided during confocal microscopy imaging (confocal image station was purchased from grant no. GVOP-3.2.1-2004-04-0172/3.0). The authors claim that there is no conflict of interest for any of the authors.

References

Anderson, G., Pongracz, J., Parnell, S., Jenkinson, E.J., 2001. Notch ligand-bearing thymic epithelial cells initiate and sustain Notch signaling in thymocytes independently of T cell receptor signaling. Eur. J. Immunol. 31, 3349–3354.

Balciunaite, G., Keller, M., Balciunaite, E., Piali, L., Zuklys, S., Mathieu, Y.D., Gill, J., Boyd, R., Sussman, D.J., Holländer, G.A., 2002. Wnt glycoproteins regulate the expression of FoxN1, the gene defective in nude mice. Nat. Immunol. 3, 1102–1108.

Beardsley, T.R., Pierschbacher, M., Wetzel, G.D., Hays, E.F., 1983. Induction of T-cell maturation by a cloned line of thymic epithelium (TEPI). Proc. Natl. Acad. Sci. U.S.A. 80 (October (19)), 6005–6009.

Bennett, A.R., Farley, A., Blair, N.F., Gordon, J., Sharp, L., Blackburn, C.C., 2002. Identification and characterization of thymic epithelial progenitor cells. Immunity 16, 803–814.

Bleul, C., Boehm, T., 2005. BMP signaling is required for normal thymus development. J. Immunol. 175, 5213–5221.

DeCarolis, N.A., Wharton Jr., K.A., Eisch, A.J., 2008. Which way does the Wnt blow? Exploring the duality of canonical Wnt signaling on cellular aging. Bioessays 30 (February (2)), 102–106.

Gill, J., Malin, M., Hollander, G.A., Boyd, R., 2002. Generation of a complete thymic microenvironment by MTS24(+) thymic epithelial cells. Nat. Immunol. 3, 635–642.

Gordon, M.D., Nusse, R., 2006. Wnt signaling: multiple pathways, multiple receptors, and multiple transcription factors. J. Biol. Chem. 281, 22429–22433.

Guo, J., Rahman, M., Cheng, L., Zhang, S., Tvinnereim, A., Su, D.M., 2011. Morphogenesis and maintenance of the 3D thymic medulla and prevention of nude skin phenotype require FoxN1 in pre- and post-natal K14 epithelium. J. Mol. Med. (Berl.) 89 (March (3)), 263–277.

Hare, K., Pongracz, J., Jenkinson, E., Anderson, G., 2003. Modeling TCR signaling complex formation in positive selection. J. Immunol. 171 (6), 2825–2831.

Hayward, A.R., Ezer, G., 1974. Development of lymphocyte populations in the human foetal thymus and spleen. Clin. Exp. Immunol. 17 (May (1)), 169–178.

Heinonen, K.M., Vanegas, J.R., Brochu, S., Shan, J., Vainio, S.J., Perreault, C., 2011. Wnt4 regulates thymic cellularity through the expansion of thymic epithelial cells and early thymic progenitors. Blood 118 (19), 5163–5173.

Jimenez, E., Vicente, A., Sacedon, R., Muñoz, J.J., Weinmaster, G., Zapata, A.G., Varas, A., 2001. Distinct mechanisms contribute to generate and change the CD4:CD8 cell ratio during thymus development: a role for the Notch ligand, Jagged1. J. Immunol. 166, 5898–5908.

Klug, D.B., Carter, C., Gimenez-Conti, I.B., Richie, E.R., 2002. Cutting edge: thymocyte-independent and thymocyte-dependent phases of epithelial patterning in the fetal thymus. J. Immunol. 169, 2842–2845.

Kvell, K., Pongracz, J.E., 2011. Central immune senescence, reversal potentials. In: Nagata, T. (Ed.), Senescence. Publisher: INTECH, ISBN 978-953-308-28-6.

Kvell, K., Varecza, Z., Bartis, D., Hesse, S., Parnell, S., Anderson, G., Jenkinson, E.J., Pongracz, J.E., 2010. Wnt4 and LAP2alpha as pacemakers of thymic epithelial senescence. PLoS ONE 5 (5), e10701.

Liu, H., Fergusson, M.M., Castilho, R.M., Liu, J., et al., 2007. Augmented Wnt signaling in a mammalian model of accelerated aging. Science 317 (August (5839)), 803–806.

Lobach, D.F., Haynes, B.F., 1987. Ontogeny of the human thymus during fetal development. J. Clin. Immunol. 7 (March (2)), 81–97.

Mikels, A.J., Nusse, R., 2006. Wnts as ligands: processing, secretion and reception. Oncogene 25, 7461–7468.

Miller, R., 2007. Of aging mice and men. Science 318 (October (5849)), 390.

Osada, M., Ito, E., Fermin, H., Vazquez-Cintron, E., Venkatesh, T., Friedel, R.H., Pezzano, 2006. The Wnt signaling antagonist Kremen1 is required for development of thymic architecture. Clin. Dev. Immunol. 13, 299–319.

Pearse, G., 2006. Normal structure, function and histology of the thymus. Toxicol. Pathol. 34, 504–514.

Pongracz, J., Hare, K., Harman, B., Anderson, G., Jenkinson, E.J., 2003. Thymic epithelial cells provide Wnt signals. Eur. J. Immunol. 33, 1949–1956.

Pongracz, J.E., Parnell, S.M., Jones, T., Anderson, G., Jenkinson, E.J., 2006. Overexpression of ICAT highlights a role for catenin-mediated canonical Wnt signalling in early T cell development. Eur. J. Immunol. 36, 2376–2383.

Rezzani, R., Bonomini, F., Rodella, L.F., 2008. Histochemical and molecular overview of the thymus as site for T-cells development. Prog. Histochem. Cytochem. 43 (2), 73–120.

Schweizer, L., Varmus, H., 2003. Wnt/Wingless signaling through beta-catenin requires the function of both LRP/Arrow and frizzled classes of receptors. BMC Cell. Biol. 4, 4.

Varecza, Z., Kvell, K., Talaber, G., Miskei, G., Csongei, V., Bartis, D., Anderson, G., Jenkinson, E.J., Pongracz, J.E., 2011. Multiple suppression pathways of canonical Wnt signalling control thymic epithelial senescence. Mech. Ageing Dev. 132 (May (5)), 249–256.

frontiers in Physiology

ORIGINAL RESEARCH
published: 02 August 2021
doi: 10.3389/fphys.2021.658218

Physical Activity as a Preventive Lifestyle Intervention Acts Through Specific Exosomal miRNA Species—Evidence From Human Short- and Long-Term Pilot Studies

*Kitti Garai[1,2], Zoltan Adam[1,2], Robert Herczeg[3], Krisztina Banfai[1,2], Adam Gyebrovszki[4], Attila Gyenesei[3], Judit E. Pongracz[1,2], Marta Wilhelm[4] and Krisztian Kvell[1,2]**

[1] Department of Pharmaceutical Biotechnology, Faculty of Pharmacy, University of Pécs, Pécs, Hungary, [2] Wnt-Signaling Research Group, Szentagothai Research Center, University of Pécs, Pécs, Hungary, [3] Bioinformatics Research Group, Szentagothai Research Center, University of Pécs, Pécs, Hungary, [4] Faculty of Science, Institute of Sport Sciences and Physical Education, University of Pécs, Pécs, Hungary

Exercise initiates systemic adaptation to promote health and prevent various lifestyle-related chronic diseases. Emerging evidence suggests that circulating exosomes mediate some of the beneficial effects of exercise via the transfer of microRNAs between tissues. Yet to date, a comprehensive profile of the exosomal miRNA (exomiR) content released following short-term (0.5 year in this study) and long-term (25 + years in this study) regular bouts of exercise is still lacking. However, a better understanding of these miRNA species would assist in clarifying the role of regular exercise at the molecular level in the prevention of chronic diseases. In the present pilot studies we analyzed serum exomiR expression in healthy young, sedentary participants (n = 14; age: 23 ± 2 years) at baseline and following a half year-long moderate-intensity regular exercise training. We also analyzed serum exomiR expression in older, healthy trained participants (seniors, n = 11; age: 62 ± 6 years) who engaged in endurance activities for at least 25 years. Following the isolation and enrichment of serum exosomes using Total Exosome Isolation Reagent (TEI) their exomiR levels were determined using the amplification-free Nanostring platform. Hierarchical cluster analysis revealed that the majority of exomiRs overlap for short-term (0.5 year in this study) and long-term (25 + years in this study) regular bouts of exercise. The top 12 significantly altered exomiRs (let-7a-5p; let-7g-5p; miR-130a-3p; miR-142-3p; miR-150-5p; miR-15a-5p; miR-15b-5p; miR-199a-3p; miR-199b-3p; miR-223-3p; miR-23a-3p, and miR-451a-3p) were used for further evaluation. According to KEGG pathway analysis a large portion of the exomiRs target chronic diseases including cancer, neurodegenerative and metabolic diseases, and viral infections. Our results provide evidence that exosomal miRNA modulation is the molecular mechanism through which regular exercise prevents various chronic diseases. The possibility of using such exomiRs to target diseases is of great interest. While further validation is needed, our comprehensive exomiR study presents, for the first time, the disease-preventive molecular pattern of both short and long-term regular exercise.

Keywords: regular exercise, exosome, miRNA, chronic disease, prevention

OPEN ACCESS

Edited by:
Martin Burtscher,
University of Innsbruck, Austria

Reviewed by:
Shamila D. Alipoor,
National Institute for Genetic Engineering and Biotechnology, Iran
Sigrun Lange,
University of Westminster, United Kingdom

***Correspondence:**
Krisztian Kvell
kvell.krisztian@pte.hu

Specialty section:
This article was submitted to Exercise Physiology, a section of the journal Frontiers in Physiology

Received: *25 January 2021*
Accepted: *12 July 2021*
Published: *02 August 2021*

Citation:
Garai K, Adam Z, Herczeg R, Banfai K, Gyebrovszki A, Gyenesei A, Pongracz JE, Wilhelm M and Kvell K (2021) Physical Activity as a Preventive Lifestyle Intervention Acts Through Specific Exosomal miRNA Species—Evidence From Human Short- and Long-Term Pilot Studies. Front. Physiol. 12:658218. doi: 10.3389/fphys.2021.658218

INTRODUCTION

Regular exercise has been known as a major intervention tool not only to attenuate the risk of a multitude of disorders from metabolic disease and neurodegenerative disorders to cancer, but also to delay the occurrence of numerous age-related diseases (Brahmer et al., 2019). While most molecular mechanisms mediating the long-term beneficial effects of exercise remain unexplored, growing evidence suggests the involvement of tissue crosstalk via the release of exosomes following exercise (Frühbeis et al., 2015; Estébanez et al., 2021). Exosomes are small extracellular vesicles (sEVs) (30–150 nm) that are secreted by fusion of multivesicular bodies to the plasma membrane (Brennan et al., 2020). These vesicles transport a large variety of cargo molecules including miRNAs, DNA and proteins that may be taken up by distant cell types and alter the phenotype of these recipients (Kowal et al., 2014). Since miRNA species are well recognized for playing important roles in many physiological and pathological processes, they could also be involved in exercise-related benefits of disease prevention. Deciphering the contribution of miRNAs present in exercise-derived exosomes and their downstream targets is crucial for the better comprehension of how preventive lifestyle actually acts at the molecular level. According to a study, the expression of certain circulating miRNA species increases with age in plasma microvesicles (Rani et al., 2017). Of notable example, hsa-miR-223-3p, hsa-miR-23a-3p, hsa-let-7g-5p, hsa-miR-199a-5p, hsa-miR-15a-5p, and has-miR-142-3p show positive correlation with age and the development of specific chronic diseases (Rani et al., 2017). Recently it has been shown that healthy aging is also reflected by the profile of circulating exosomes, and exercise−induced beneficial effects may be related with the modulation of these exosomes (Bertoldi et al., 2018). There are reports indicating the changes of various miRNA species in exosomes following an acute of exercise (D'souza et al., 2018; Yin et al., 2019), however only a small number of studies examine exosomes in response to long-term training (Nederveen et al., 2021). Of note, in a mammalian study the levels of miR−19b, miR−148a, miR−150, miR−221, miR−361, and miR−486 were up-regulated during the first month of exercise, but returned to baseline by completion of a 4−month study period (Muroya et al., 2015). Regarding long-term human experiments, a significant increase in exosome release was shown after a single bout of flywheel exercise (Annibalini et al., 2019), whereas no change was found after a full year of rowing training (Hou et al., 2019). These conflicting results could potentially be attributed to the adaptation process that occurs with time. Additional research is crucial with various training modalities and durations to further understand the role of exosomes and their miRNA content in the prevention of chronic diseases induced by long-term exercise. In the present study first we investigated the effect of a 0.5 year-long, moderate intensity, personal trainer-supervised, concurrent resistance and aerobic training program on the overall circulating exomiRs expression profile of healthy, young, previously sedentary individuals. We also assessed whether exomiRs differentially expressed after a 0.5 year regular exercise in young adults were similarly present in healthy senior trained participants who have engaged in regular exercise activities for at least 25 years. The effect of short- and long-term regular exercise on the miRNA profile was determined by comparing baseline vs. 0.5 year, and baseline vs. 25 + years miRNA levels. As anticipated we found that the levels of the exomiRs are fairly consistent in comparison of the 0.5 year (short-term adaptation) and the 25 + years (long-term adaptation) active groups. Twelve exomiRs showed overlap for both study periods (baseline vs. 0.5 year and baseline vs. 25 + years). Of note, all of them were significantly down-regulated. Bioinformatics analysis was used to evaluate the interplay between biological signaling pathways offering insight into mechanisms linking exercise and chronic disease prevention. Our results prove that full miRNome analysis might be a useful tool to identify exomiRs acting on particular pathways that prevent the development of specific chronic diseases.

MATERIALS AND METHODS

Participants and Applied Training Protocol

Healthy young, sedentary (n = 14; age: 23 ± 2 years) and senior trained (n = 11; age: 62 ± 6 years) individuals were recruited. Participants were in good general health, defined as having no chronic diseases (e.g., metabolic disorders, cardiovascular disease, cancer, etc.). Main characteristics of the subjects are summarized in **Table 1** (see **Supplementary Material** for further details). Healthy, young sedentary individuals completed moderate-intensity, concurrent resistance and aerobic exercises regular exercise training three times a week for half a year (Garai et al., 2019). Our exercise bouts consisted of four parts: warm-up, resistance training, aerobic exercises and cool-down with stretching. The heart rate of the participants was measured continuously during exercise with a heart rate monitor (Polar Team System, Polar Electro, Finland). Age-predicted maximum heart rates were estimated with the following calculation: 220—age (years). Every trainings began with standardized, active warm-up protocol applying mobility and stability exercises, gymnastic exercises and moderate stretching. After warming-up resistance training was performed. During this part the heart rate of the subjects was allowed to reach 85% of individual heart rate maximum. Aerobic exercises included walking and jogging, if the subject's heart rate was lower than 65% of the individual heart rate maximum. The cool-down protocol included 2 min of slow walking and 8 min of static stretching exercises of all major muscle groups. Participants were asked to keep their diet and daily activity level unchanged during the 6 month-long lifestyle program. Training diary was prepared during the 6 months and compliance was calculated accordingly.

Senior trained subjects were engaged in regular exercise activities for at least 25 years. The exercise behavior of senior participants was assessed with the use of a general lifestyle questionnaire as well as with the International Physical Activity Questionnaire (IPAQ) (Craig et al., 2003). We obtained information on smoking-, alcohol consumption status and physical activity (frequency, type, duration). Senior trained

participants also performed both types of exercise (endurance and resistance training), including running, swimming, weightlifting, cycling, skating, adrenaline sports, walking, hiking and spinning. Over half (54%) of the senior participants performed physical activity on a daily basis, while the rest performed physical activity at least twice a week. For details please check the **Supplementary Material Section**. Each participant gave written informed consent before completing any data collection. The study was conducted according to the Declaration of Helsinki principles and approved by the Regional and Local Ethics Committee of Clinical Center, University of Pecs (ref. no.: 6439/2016 and 7755/2019).

Collection and Preparation of Human Serum Samples

Human blood samples were collected around 7:00 a.m. after a 12 h fasting in blood collection tubes (BD Vacutainer, SST: BD SST Tubes with Silica Clot Activator and Polymer Gel, Franklin Lakes, NJ, United States) at two time-points: at baseline and after the 0.5 year long training program from the young individuals and at one time-point from seniors. Participants were asked to avoid excessive exercise the day before each testing condition. Blood samples were clotted for approximately 30 min at room temperature. Samples were then centrifuged at 1,500 g for 10 min at room temperature. Serum samples were stored at −80°C until further analysis. The same procedure was carried out with the samples of seniors.

Exosome Isolation

In order for their samples to be processed participants had to show min. 85% compliance with regular exercise mandated by the program. Before exosome isolation, equal volumes of serum (100 μl each) from 14 healthy young participants and 11 seniors were pooled, separately (**Figure 1**). Prior to pooling we have carefully evaluated the participants for potential outliers based on the assessment of physiological and blood parameters. Only those participants' samples were pooled who constituted a homogenous population for the evaluated physiological and blood parameters (baseline, 0.5 year, 25 + years). Then, exosomes were isolated from the three pooled serum samples (baseline; n = 1, 0.5 year; n = 1 and 25 + years; n = 1 pooled samples) using TEI (from serum) (Invitrogen, Thermo Fisher Scientific, Waltham, MA, United States) following the manufacturer's protocol. TEI reagents contain volume-excluding polymers (e.g., polyethylene glycol, dextrans, or polyvinyls). According to Andreu et al. (2016) and Banfai et al. (2019), the use of precipitation reagents provide good reproducibility and are suitable for an easy and cost-efficient enrichment of serum exosomes for miRNA analyses. As a result TEI was chosen for studying exosomal miRNA content in our study.

NTA Measurement With Nanosight NS300

NTA Protocol

Exosome-enriched preparations were measured and quantified using Nanosight NS300 instrument (Malvern Panalytical Ltd., Malvern, United Kingdom). The camera level for each sample was manually adjusted to achieve optimal visualization of particles following the manufacturer's instructions. Samples were injected with a syringe pump (infuse = 50). Detection threshold was set for maximum sensitivity with a minimum of background noise. All measurements were performed in five replicates for each sample, collecting 60-s videos. Following capture, the videos were analyzed by the in-built NTA v3.2 software (Gardiner et al., 2013).

Particle Size and Concentration Analysis

The samples of 3 individuals were randomly chosen from each group (baseline, n = 3; 0.5 year, n = 3; and 25 + years, n = 3). All samples were diluted in PBS. Ideal measurement concentrations were achieved by pre-testing the ideal particle per frame value (40–100 particles/frame).

Single EV Direct Immunolabeling and NTA Evaluation

The following monoclonal antibodies were used for immune-labeling: anti-human-CD63-FITC (MEM-259) (Thermo Fisher Scientific) anti-human-CD81-PE/Cy7 (TAPA-1) (Sony Biotechnology). Particle concentrations were established for unlabeled EV sample prior to immune-labeling. The

TABLE 1 | Subject characteristics.

	Baseline	0.5 years	*p*	25 + years
Age (years)	23 ± 2	23.5 ± 2		62 ± 6
BMI	21.64 ± 1.57	21.46 ± 1.44	0.382	27.92 ± 2.95
Body weight (kg)	60.39 ± 5.42	59.55 ± 5.74	0.166	75.16 ± 7.18
Body fat percentage (%)	31.79 ± 3.39	31.49 ± 3.47	0.61	21.23 ± 6.03
VO_2 max (ml/kg/min)	36.41 ± 6.67	39.81 ± 6.20*	0.047	32.9 ± 6.99
LDL (mmol/L)	2.35 ± 0.9	2.44 ± 0.83	0.481	3.63 ± 1.19
HDL (mmol/L)	1.81 ± 0.55	2.13 ± 0.61*	0.002	1.68 ± 0.53
Glucose (mmol/L)	4.94 ± 0.39	4.63 ± 0.31 **	<0.001	5.67 ± 0.45
Systolic BP (Hgmm)	114.5 ± 14.18	108.07 ± 8.69	0.55	131.2 ± 19.42
Diastolic BP (Hgmm)	76.07 ± 9.19	72.93 ± 7.92	0.223	87.00 ± 9.25

*Values are expressed as mean ± SD. Paired t-test (*p < 0.05; **p < 0.001); p-values were calculated for baseline vs. 0.5 year as applicable; VO_2 max, maximal oxygen uptake (cardiorespiratory fitness); LDL, Low Density Lipoprotein; HDL, High Density Lipoprotein; BP, Blood Pressure.*

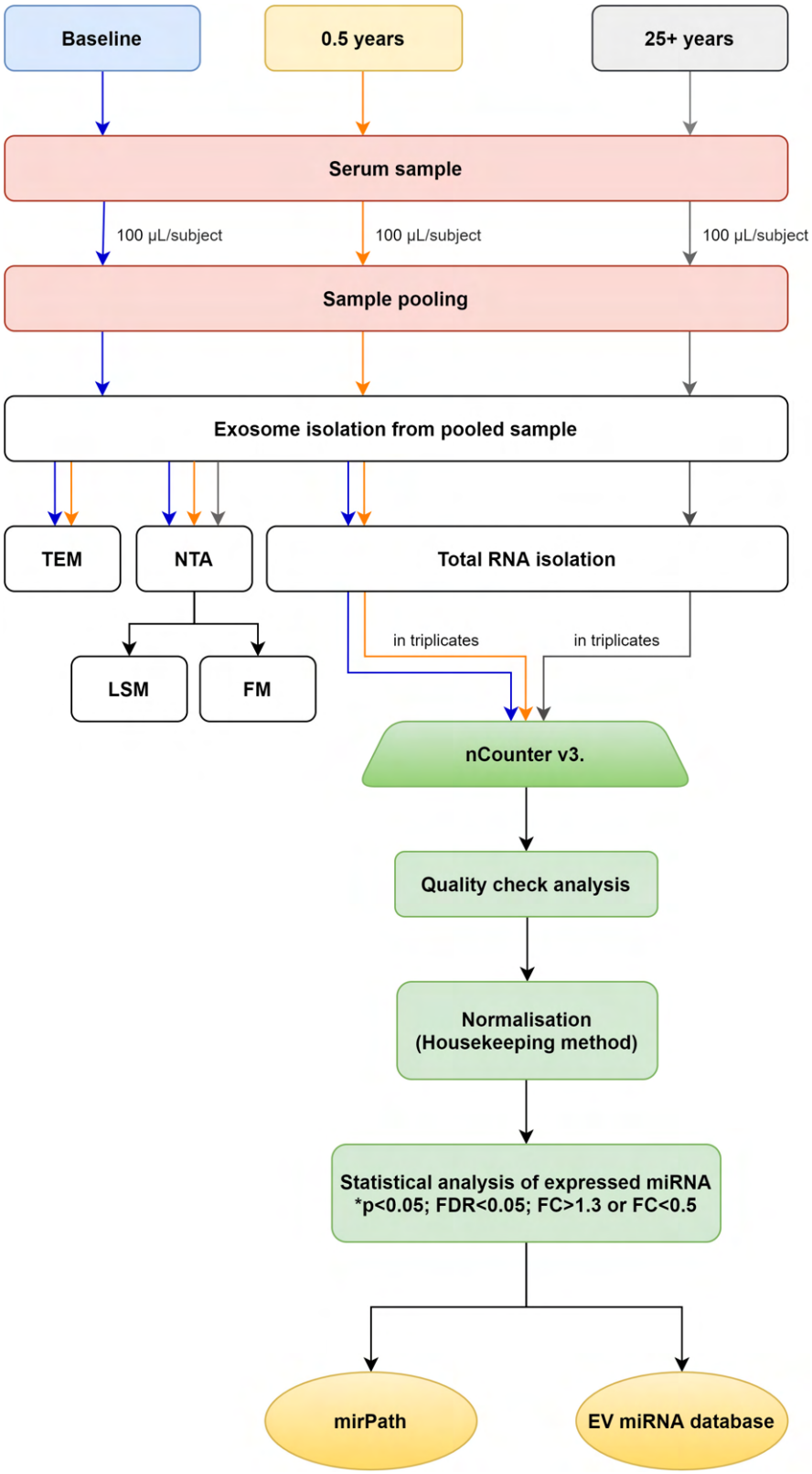

FIGURE 1 | Workflow. Flowchart representing the entire workflow.

concentration of the exosome stock solution was 3.17×10^{10} particles/ml (based on NTA). Sample aliquots were prepared to ensure equal dilution effects for each arm of the experiment. Varying concentration anti-CD63 and anti-CD81 antibodies was added to the 50 μl exosome stock solution to yield a volume of 100 μl and to determine an optimized antibody to exosome ratio for single-vesicle labeling. The samples (anti-CD63 labeled; $n = 1$ and anti-CD81 labeled; $n = 1$) were incubated in the dark for 1 h at room temperature. In order to minimize photobleaching during fluorescence mode (FM), all immune-labeled samples were evaluated first in FM, followed immediately by evaluation in light scatter mode (LSM). Then, the FM/LSM percentage was calculated (Thane et al., 2019).

Transmission Electron Microscopy (TEM)

Exosomes were visualized by transmission electron microscopy. Sample volume of 2.5 μl was placed onto a 300 mesh grid. The grid was left to air dry overnight. Then 5% uranyl-acetate and later 3% sodium-citrate were added to the grid. After 5 min incubation, the grid was allowed to air dry. Twenty four hours later the grid was analyzed using JEOL TEM 1,200 EX. The average diameter of the isolated exosomes was determined using three independent TEM preparations and ImageJ software.

Exosomal Total RNA Purification and Complete miRNome Profiling

Total RNA from exosomes was extracted using Total Exosome RNA and Protein Isolation Kit (Invitrogen, Thermo Fisher Scientific, Waltham, MA, United States) according to the manufacturer's protocol. ExomiR level profiling was performed using the Nanostring platform (NanoString Technologies, Seattle, WA) according to the manufacturer's instructions to analyze 800 human miRNAs. Since the extraction of exosomal miRNA yields low amounts of RNA, but amplification-free methods require high amounts, we adopted the standard method of using pooled samples to yield reproducible reads. Three technical replicates were run per sample (baseline; 0.5 year and 25 + years groups). Quality check confirmed the reliability of the run and also the validity and reproducibility of the miRNA screening protocol. nSolver software was used for data analysis and normalization. Normalization was performed using the Housekeeping method according to nCounter miRNA expression analysis in plasma and serum samples technote instructions. Briefly, NormFinder was used to identify putative housekeeping miRNAs. First, raw data (RCC files) were imported into nSolver and any sample which failed QC was removed. An experiment was built and background subtraction was set to the Mean + 1 SD of the NEG control probes. Of note, we kept normalization options turned off during this process. Data from the completed experiment were exported into an excel file derived from the normalized dataset. Using NormFinder background subtracted data were sorted by average counts across all samples, and all miRNAs expressed below 50 mean counts were deleted when averaged across all samples. NormFinder created a worksheet listing all the genes and a stability value for each of them. With the aid of NormFinder the potential housekeepers with the most stringent stability values were identified. After that we have applied normalization using the geometric mean of five stably expressed miRNAs (hsa-miR-495-3p; hsa-miR-302d-3p; hsa-miR-3144-3p; hsa-miR-612; hsa-miR-548ar-5p) (Andersen et al., 2004). Quality Control fulfilled all the requirements set by the manufacturer.

Statistical Analysis

All statistical analyses were performed with R (R Core Team, 2019). Paired *t*-tests (baseline vs. 0.5 year) and *t*-tests (baseline vs. 25 + years; 0.5 year vs. 25 + years) were used. We adjusted the *P*-values due to the multiple comparisons therefore False Discovery Rate (FDR) correction was also applied. Heatmap was created in R with the help of "heatmap.2" function from g-plots package (Bolker et al., 2020).

miRNA Target Prediction and Pathway Analysis

After identifying a dozen similarly expressed exomiRs in the active young and senior groups, miRNA—mRNA signaling pathway interaction analysis was performed. Briefly, online available software mirPath v.3 was used for this purpose (Vlachos et al., 2015). Human database of the mirPath v.3 and the TarBase v7.0 were used for mRNA target prediction. *P*-value and MicroT thresholds were kept as default, 0.05 and 0.8, respectively. False discovery rate (FDR) correction was applied.

ExomiRs as Biomarkers of Chronic Disease

The exomiR biomarkers related to certain types of chronic diseases were screened through the EVmiRNA database[1] (Liu et al., 2019). Studies were included if they were original research and evaluated the exomiR levels in a specific disease.

RESULTS

Anthropometric and Physiological Parameters

The study comprised 14 healthy, young, previously inactive and 11 senior trained participants. Healthy, young sedentary individuals completed moderate-intensity regular exercise training three times a week for half a year. Senior subjects have done regular exercise for at least 25 years. Participant parameters are listed in **Table 1**. After half a year of regular exercise, the previously inactive young individuals showed significant improvement in cardiorespiratory fitness (VO_2max), glucose and lipid metabolism. All physiological parameters of senior trained participants were within a normal range. For them, the VO_2max values were far better than the age-matched reference range (**Supplementary Material**).

Validation of Isolated Exosomes

Exosomes were isolated from blood serum samples and obtained from study participants, as described in section "Materials and

[1] http://bioinfo.life.hust.edu.cn/EVmiRNA

Methods." The purified exosomes were characterized using TEM, a gold-standard technique for nanoparticle validation (Kestens et al., 2017). Our TEM analysis showed typical exosomal round morphology (**Figure 2A**). Nanoparticle Tracking Analysis (NTA) allowed us to obtain the size distribution of EVs and estimate particle concentration. The mean size of particles (n = 9) was 143.2 ± 16.43 nm, which falls into the size range of exosomes (Brennan et al., 2020), confirming that the purified EVs contained exosomes (**Figure 2B**; see **Supplementary Material** for further details). Exosome concentrations in our preparations (n = 9) ranged from 1.97×10^{10} to 3.75×10^{10} particles/ml. For details please see the **Supplementary Material section**. Immune-labeled EV sample was evaluated using NTA in FM and LSM modes. The FM:LSM percentage was 83.87% for of CD63. With the CD81-labeled sample, the FM:LSM percentage was 76.95% (**Figure 2C**; please also refer **Supplementary Videos**).

The Expression Patterns of exomiRs After 0.5 Year of Regular Exercise

In order to study regular exercise-related changes in serum exomiR expression, we used amplification-free Nanostring technology. The effect of regular exercise on circulating exomiRs was assessed by comparing baseline (inactive status) and active status (after 0.5 year of regular exercise) expression levels. After analyzing and normalizing raw data, we identified 54 exomiRs (**Figure 3**). Then, we applied filtering criteria to differentiate baseline vs. 0.5 year results ($^*p < 0.05$; #FDR < 0.05; FC > 1.3 or FC < 0.5). Through this analysis, we have observed significant differences in exomiR abundance for several exomiRs (let-7a-5p, $p < 0.05$; let-7g-5p, $p < 0.05$; miR-130a-3p, FDR < 0.05; miR-142-3p, $p < 0.05$; miR-150-5p, $p < 0.05$; miR-15a-5p, $p < 0.05$; miR-15b-5p, FDR < 0.05; miR-199a-3p, FDR < 0.05; miR-199b-3p, FDR < 0.05; miR-223-3p, FDR < 0.05; miR-23a-3p, FDR < 0.05; miR-451a-3p, FDR < 0.05; miR-126-3p, $p < 0.05$; miR-199a-5p, $p < 0.05$; miR-21-5p, FDR < 0.05; miR-25-3p, $p < 0.05$; miR-374a-5p, $p < 0.05$) (for further details please refer to **Supplementary Material**) (ArrayExpress accession number: **E-MTAB-10067**).

ExomiR Overlap of the 0.5 Year- and the 25 + Years of Exercise Groups

Going further we then wished to assess whether exomiRs differentially expressed after 0.5 year of regular exercise were similarly expressed in healthy senior trained participants who engaged in endurance activities for at least 25 years. Therefore, using Nanostring technology we examined the miRNA copy numbers in 11 trained senior individuals focusing on the levels of serum exomiRs. Then, we utilized a hierarchical clustering method to compare circulating exomiR profiles at baseline, after 0.5 year and 25 + years of exercise. As shown by **Figure 3**, the 0.5 year and 25 + years group share an exomiR expression profile that is completely different from that of the sedentary group. In contrast, the 0.5 year and 25 + years active groups showed a highly similar exomiR expression pattern. In addition, 12 exomiRs (let-7a-5p; let-7g-5p; miR-130a-3p; miR-142-3p; miR-150-5p; miR-15a-5p; miR-15b-5p; miR-199a-3p; miR-199b-3p; miR-223-3p; miR-23a-3p, and miR-451a-3p) showed overlap between the two tested signatures (baseline vs. 0.5 year and baseline vs. 25 + years) (**Supplementary Material**). Notably, all 12 exomiRs were significantly down-regulated both in the 0.5 year and the 25 + years trained groups as compared to the sedentary group. Having performed a detailed comparison of the 0.5 year vs. 25 + years trained group profiles, miR-411-5p ($p < 0.05$; FC = 0.879) and miR-144-3p (FC = 1.322)

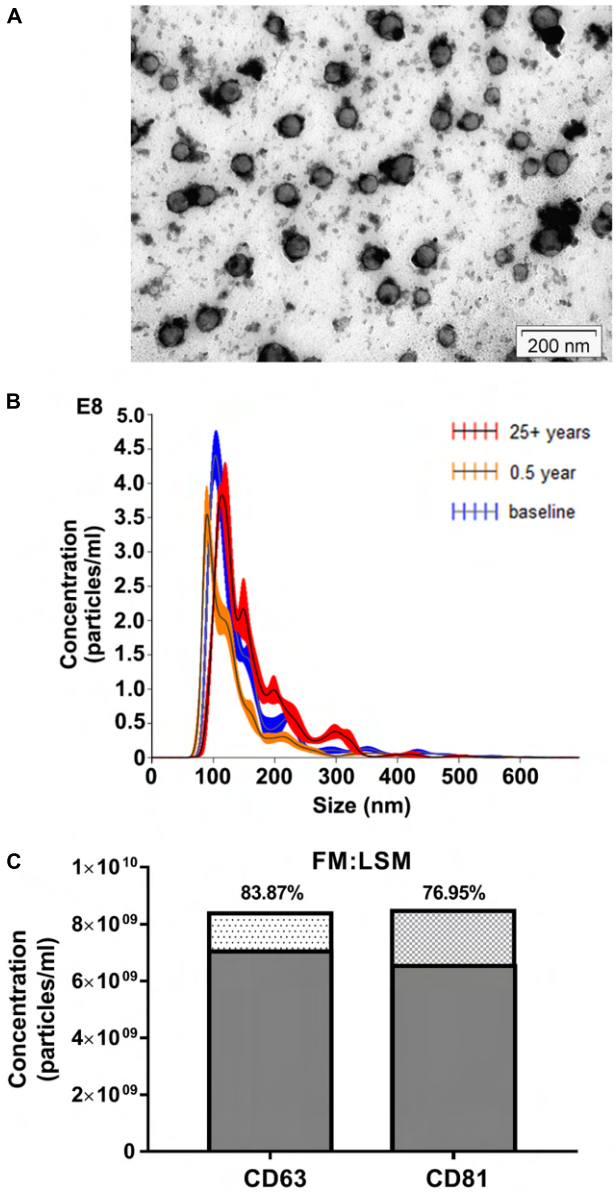

FIGURE 2 | Characterization of exosome-enriched preparations isolated from human serum. **(A)** Transmission electron microscope (TEM) image of exosomes purified from human serum samples (Scale bar: 200 nm). **(B)** Analysis of EV size distribution and concentration in exosome-enriched preparations using a NanoSight NS300 instrument. **(C)** Evaluation of CD63 and CD81 surface expression abundance in exosome-enriched preparations using a NanoSight NS300 instrument.

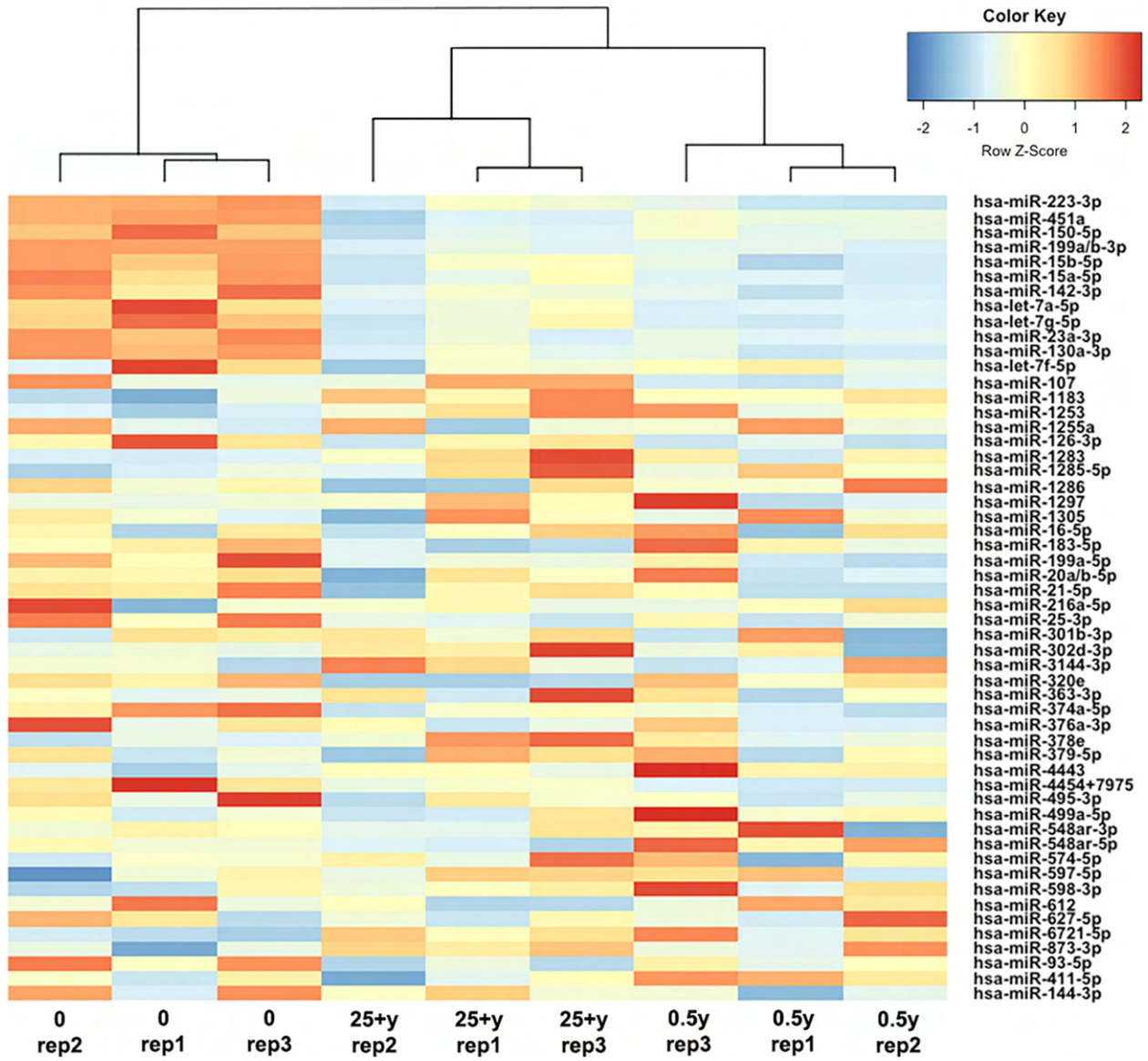

FIGURE 3 | Differential expression of circulating exomiRs. Heatmap with dendrogram shows clustering results for 54 exomiRs at baseline (0), after 0.5 year and 25 + years of regular exercise. Colors represent the level of exomiR expression; red: high expression; blue: low expression.

showed remarkably different expression. Specifically, miR-411-5p was significantly down-regulated, while miR-144-3p was up-regulated in the 25 + years trained group.

Pathway Analysis

To better understand how these exomiRs may contribute to the health benefits of exercise, we examined the mRNA targets of the 12 similarly expressed exomiRs of the 0.5 year and 25 + year trained groups. Then, to reveal the top targeted pathways associated with each exomiRs, KEGG database analysis was used. We found that 38 KEGG signaling pathways were significantly affected by the 12 selected exomiRs (**Figure 4B**). Of these Pathways in cancer (hsa05200) had the largest number of targeted mRNAs (148 genes) (**Figure 4A**). The 148 genes were targeted by four differentially expressed exomiRs (let-7a-5p; let-7g-5p; miR-15b-5p; miR-23a-3p). These findings are consistent with the fact that regular exercise is associated with reduced risk of cancer development. Going further, most exomiRs targeted proteoglycans in cancer pathways (nine exomiRs) and let-7g-5p appeared to affect the most pathways (26 pathways) (for details see **Supplementary Material 2**).

ExomiRs as Biomarkers of Chronic Diseases

exomiR biomarkers related to specific diseases were evaluated using an EVmiRNA database. It is the first concise database

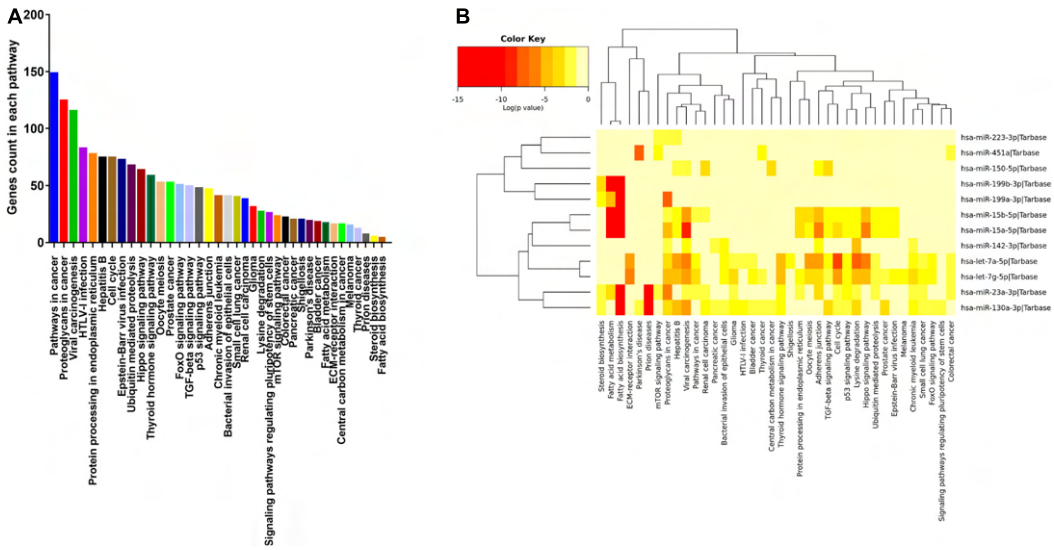

FIGURE 4 | Pathways targeted by the 12 similarly expressed exomiRs in the active young and active senior group. **(A)** Number of genes targeted within each pathways ranked based on high to low. **(B)** The 12 similarly expressed exomiRs in the active young and active senior group regulate 38 signaling pathways in total.

focusing on miRNA expression profiles in EVs (Liu et al., 2019). Several studies have reported the aberrant expression of the 12 identified exomiRs in various chronic diseases (as summarized by **Table 2**).

DISCUSSION

Regular exercise has a beneficial role in preventing a number of chronic diseases. This is primarily due to the fact that regular exercise acts at a systemic level (Anderson and Durstine, 2019). However, a gap remains between identifying in detail the molecular mechanisms induced by exercise and the observed potential benefits in health (Sanford et al., 2020). A better understanding of these biological processes and pathways could allow for the development of targeted exercise intervention and also provide basis for developing exercise-mimetic molecular level interventions (Sanford et al., 2020).

Therefore, in the present study we examined, for the first time, the effect of short-term (0.5 year in this study) and long-term (25 + years in this study) regular exercise on global circulating exomiR profile. To the best of our knowledge, this is the first study to use an amplification-free platform (Nanostring) to determine the miRNA expression profile of exercise-derived exosomes as most studies of the field evaluate specific miRNA species by amplification-based RT-qPCR (Estébanez et al., 2021). The technology applied in the current study is not only amplification-free, but also a sensitive, robust and reproducible state-of-the-art method (Hong et al., 2021). Exosomal miRNA analysis showed a significant number of differentially expressed exosomal miRNAs in all group comparisons. Comparing the miRNAs enriched or depleted in both groups (0.5 year and 25 + years), we have identified 12 similarly regulated exomiRs in the young and senior trained groups as compared to the sedentary group as shown by **Figure 3** (for details please refer to **Supplementary Material**). The KEGG pathway analysis of similarly expressed serum-derived exomiRs confirmed their involvement in pathways related to cancer development affecting TGF-beta, p53 and mTOR signaling. In support of our observations, physical activity has been shown to be associated with lower cancer risks (Li et al., 2020). Moreover, the overall cancer incidence is lower in athletes than in the general population (Sormunen et al., 2014). Recently, a number of studies have indicated that certain exosomal miRNA species (**Table 2**), can be used as biomarkers of cancer and other chronic diseases (references of the studies are listed in **Table 2**).

An elevated expression level of miR-23a has been identified in the serum of various types of human cancer, including breast, gastric, pancreatic, and esophageal squamous cell carcinoma (Wang et al., 2019). Further analysis showed that miR-23a travels as exosomal cargo, and circulating exosomal miR-23a is up-regulated in the serum of early stage colorectal cancer patients (Yong et al., 2013). As a robust cellular regulator of gene expression, miR-23a targets a broad range of mRNA species in cancer cells by directly binding to their three prime untranslated regions (3'-UTR), which in turn suppresses gene expression (Wang et al., 2019). For example, the up-regulation of miR-23a in gastric cancer promotes cell proliferation and inhibits apoptosis (Hua et al., 2018). Zhu et al. (2010) suggested that miR-23a can target IL6R in gastric adenocarcinoma thus encouraging the proliferation of tumor cells. Based on literature data, the inhibition of miR-23a by antisense oligonucleotide inhibits proliferation and promotes the apoptosis of gastric adenocarcinoma cells (Liu et al., 2014). Its biological functions encompass drug resistance, metastasis formation and cancer

TABLE 2 | Summary of exomiR biomarkers related to certain diseases according to EVmiRNA database.

miRNA species	Affected age-related chronic disease, autoimmune condition or infection	References
hsa-let-7a-5p	Colorectal-, renal-, prostate-, ovarian-, breast-, lung-, pancreas-, gastric-, esophageal-, thyriod cancer, Ewing's and Kaposi's sarcoma, glioblastoma, AML and MML; metastasis formation; cell cycle control; inflammation; diabetes; cardiovascular disease; hepatitis B infection	Iliopoulos et al., 2009; Trang et al., 2010; Lee et al., 2011
hsa-let-7g-5p	Breast-, esophageal-, lung cancer, glioblastoma, AML and CML; graft-vs.-host disease; inflammation; autoimmune thyroid disease; cell cycle control; diabetes; cardiovascular disease; metabolic syndrome; hepatitis B and influenza A infection	Arora et al., 2011; Wang et al., 2013; Biamonte et al., 2019
hsa-miR-130a-3p	Lung-, liver-, prostate-, ovarian-, breast-, cervical-, nasopharyngeal-, prostate cancer, myeloma, CML and glioblastoma; cardiovascular disease; fibrosis; inflammation; autophagy; diabetes; Crohn's disease; hepatitis C infection; cardiac arrhythmia; renal GBM disease; UV damage	Osbourne et al., 2014; Huang et al., 2015; Eichelmann et al., 2018
hsa-miR-142-3p	Liver-, lung-, colorectal-, breast-, cervical-, esophageal cancer, osteosarcoma, prolactinoma, ALL, AML, CLL and MALT lymphoma; graft rejection; Hashimoto's thyroiditis; multiple sclerosis; cardiovascular disease; inflammation; rotavirus infection; Alzheimer's disease; fibrosis	Ma et al., 2016; Sukma Dewi et al., 2017; Wang et al., 2017
hsa-miR-150-5p	Colorectal-, lung-, liver-, prostate-, cervical-, pancreas-, breast-, ovarian-, esophageal cancer, osteosarcoma, glioblastoma, melanoma; Burkitt lymphoma, ALL and MML; inflammation; cardiovascular disease; fibrosis; irritable bowel syndrome; myasthenia; diabetes; SLE; psoriasis	Roderburg et al., 2013; Qu et al., 2014; Yu et al., 2015
hsa-miR-15a-5p	Gastric-, colorectal-, lung-, breast-, liver-, ovarian-, prostate cancer, melanoma, osteosarcoma, neuroblastoma, pheochromocytoma, AML, CLL and multiple myeloma; inflammation; cell cycle control; apoptosis induction; autophagy; multiple sclerosis; hepatitis B infection; fibrosis; diabetes	Xia et al., 2008; Bandi et al., 2009; Sun et al., 2013
hsa-miR-15b-5p	Liver-, gastric-, lung-, liver-, pancreas-, ovarian-, squamous cell cancer, glioblastoma, melanoma, CLL and thymoma; apoptosis induction; metastasis formation; angiogenesis; fibrosis; bipolar disorder; insulin-resistance; skin photoaging; multiple sclerosis; diabetes	Zhang et al., 2015; Li et al., 2016; MacLean et al., 2016
hsa-miR-199a/b-3p	Liver-, gastric-, lung-, renal cell-, ovarian-, pancreas-, colorectal, liver-, breast-, testicular germ cell-, thyroid-, colorectal cancer, endometriosis, glioblastoma, CLL, melanoma, chondrosarcoma and osteosarcoma; osteoarthritis; COPD; autophagy; angiogenesis; HCV infection; inflammation	Li et al., 2015
hsa-miR-223-3p	Ovarian-, gastric-, colorectal-, prostate-, pancreas-, lung-, liver cancer, CLL, AML, ALL, glioblastoma and osteosarcoma; metastasis formation graft rejection; inflammation; osteoarthritis; lipid metabolism; obesity; rheumatoid arthritis; psoriasis; cardiovascular disease; diabetes; COPD; Alzheimer's disease	Wong et al., 2008; Filková et al., 2014; Lunavat et al., 2015
hsa-miR-23a-3p	Gastric-, colorectal-, esophageal-, liver-, renal-, breast-, prostate-, pancreas-, lung-, laryngeal-, lung cancer, CML, AML, Burkitt lymhoma, melanoma, osteosarcoma and endometriosis; retinal degeneration; UV damage; apoptosis induction; autophagy; progeria; osteoarthritis; obesity	Wang et al., 2014; Yang et al., 2014; Zheng et al., 2014
hsa-miR-451a	Lung-, colorectal-, breast-, skin-, bladder-, gastric-, renal-, esophageal-, thyroid-, liver cancer, T-ALL, AML, CML, multiple myeloma, endometriosis, prolactinoma, osteosarcoma and glioblastoma; drug transporters; cell cycle; metastasis formation; angiogenesis; rheumatoid arthritis; cardiomyopathy	Lopotová et al., 2011; Song et al., 2014; Riquelme et al., 2016

progression, suggesting its potential role as an emerging targetable entity in cancer treatment (Wang et al., 2019). Of note, miR23a shows natural correlation with age, partly explaining the correlation of the above cancers with senior age (Rani et al., 2017).

Exosomal miR-451a was highly expressed in non-small-cell lung carcinoma patients (NSCLC) compared to healthy individuals. This miRNA was strongly associated with tumor progression, recurrence, and poor prognosis in NSCLC patients. According to literature data, it may serve as a potential predictive biomarker for NSCLC (Kanaoka et al., 2018). Zhu et al. (2014) also found that miR-451 levels were consistently elevated in the plasma of patients with gastric cancer providing high diagnostic accuracy for early stage gastric adenocarcinoma. To date, numerous genes have been confirmed as actual targets of miR-451, covering multiple biological signaling pathways including apoptosis, cell invasion and migration, cell proliferation and angiogenesis. Taken together, an accumulating body of evidence indicates that miR-451 is a potential biomarker for cancer diagnosis and prognosis, possibly a treatment target in combination with established drugs (Bai and Wu, 2019).

Exosomal miR-223-3p level in the serum of patients with breast cancer was significantly higher in comparison with healthy controls (Yoshikawa et al., 2018). Its expression was tightly associated with the malignancy of breast cancer, suggesting that exosomal miR-223-3p might be a useful biomarker for the early detection of invasive breast cancer. Of further note, miR223-3p also shows correlation with the advance of age, and these cancers are known to emerge at senior age (Rani et al., 2017).

Elevated expression of miR-150-5p has been shown in breast cancer (BC), described as a good prognostic biomarker for patients with HER2-positive BC (Ozawa et al., 2020).

Exercise was shown to modulate the expression of several miRNA species that in turn are protective against cancer (Li et al., 2020; Pulliero et al., 2020). In our report we demonstrate this modulation observed after both short-term (0.5 year) and long-term (25 + years) regular exercise since our miR-23a, 451a, 223-3p, and miR-150-5p were all suppressed emphasizing the role of exercise in the prevention of several cancer entities. Nevertheless, data on exercise-derived exosomal miRNA species in modulating cancer prevention is still in its infancy (Pulliero et al., 2020). Therefore, elaborate research effort

is required to reveal the role of exosomal miRNA species in this particular field.

The deregulation of miRNA species described in conjunction with other chronic diseases has also been observed in our study. According to our results, regular exercise altered the levels of miR-15a and miR-142 in the opposite direction as observed in patients with diabetes and neurodegenerative disease, supporting that regular exercise (either short- or long-term) reduces the risk of developing such chronic diseases. In more detail, miR-15a was shown to be elevated in the plasma of diabetic patients also showing correlation with disease severity (Kamalden et al., 2017). Xiong et al. (2020) demonstrated that miR-15a-3p is up-regulated in exosomes of diabetic patients, and impairs wound healing. When miR-15a-3p was knocked down and such exosomes were utilized later on, their negative effects on the metabolism and wound healing in particular were partially reversed both *in vitro* and *in vivo* (Xiong et al., 2020).

Barbagallo et al. (2020) isolated exosomal miRNA from the serum of 30 Parkinson disease (PD) patients and compared it with that of 30 healthy controls. The expression levels of ex-miR-23a; ex-miR-142-3p were significantly elevated in the serum of PD patients, unlike in our study where miR-142 showed a decrease in expression compared to healthy, but sedentary state (Barbagallo et al., 2020). Previous studies have also reported the benefits of physical exercise in improving the symptoms in individuals with PD (Da Silva et al., 2021). Taken together these reports suggest the protective role of miR-142-3p in PD, though further studies are required.

Taken together, the miRNAs that we have observed to be modulated by both short and long-term exercise are mostly involved in cancer prevention mechanisms including tumor suppression (miR-223-3p; miR-451a; miR-15a/b-5p; let-7a/7g-5p) (Wang et al., 2016; Gao et al., 2011), aging (miR-223-3p; miR-451a; miR-15a/b-5p; miR-23a-3p) (Mercken et al., 2013; Teteloshvili et al., 2015), induction of apoptosis (miR-150-5p; miR-15a/b-5p; miR-130a-3p) (Xu et al., 2014; Wang et al., 2015) and reduction of inflammation (miR-199a/b-3p; miR-142-3p) (Cai et al., 2012). In addition, the inverse deregulation of miR-15a characteristic to diabetes, and miR-142 featured in Parkinson's disease has also been recorded in our study. Potential applications target these miRNA species to prevent the development of cancer, diabetes and neurodegenerative disease or to be used as adjuvant therapy in established diseases. However, to date no such experiments exist supporting that exercise-derived exomiRs could prevent or treat chronic diseases.

So, beyond the utility of serum-derived exomiRs as potential biomarkers of physical fitness or chronic diseases, our work suggests their key role in essential pathways, potentially preventing the development of multiple chronic diseases. In the future the evaluation of physical activity level may be used to predict the risk of developing various chronic diseases. Furthermore, this study is important as a starting point to understand the global pattern of regular exercise-related exomiRs and their target pathways in health and disease. However, the present study must be seen as an exploratory study. Our current pilot-study is limited by the number of biological replicates. Therefore, further studies are required with larger sample size to comprehensively examine the effect of regular exercise on circulating exomiR profile.

CONCLUSION

Both short- (0.5 year) and long-term (25 + years) regular exercise significantly alters the serum miRNA profile in healthy individuals, potentially reducing the risk of a number of malignant, metabolic and neurodegenerative diseases. Combining an amplification-free miRNome profiling platform and bioinformatics analysis, our study revealed that numerous disease-associated exomiRs show differential expression toward a more beneficial pattern. Physiological relevance is also supported by the large number of genes targeted by these miRNAs. Future work lies ahead in determining the exact mechanism of action and the potential use of exomiRs as therapeutic tools to efficiently prevent or successfully treat age-related diseases.

DATA AVAILABILITY STATEMENT

The datasets presented in this study can be found in online repositories. The names of the repository/repositories and accession number(s) can be found below: EBI ArrayExpress, accession no: E-MTAB-10067.

ETHICS STATEMENT

The studies involving human participants were reviewed and approved by the Regional and Local Ethics Committee of Clinical Centre, University of Pecs (ref. no.: 6439/2016 and 7755/2019). The patients/participants provided their written informed consent to participate in this study.

AUTHOR CONTRIBUTIONS

KG, KK, and MW designed the study. KG, ZA, KB, and AdG recruited participants, collected samples and performed the experiments. RH and AtG analyzed the data. KG and ZA interpreted data and drafted the manuscript. JP, MW, and KK critically revised the manuscript. All authors contributed to the article and approved the submitted version.

FUNDING

The project was supported by the ÚNKP-19-3-I 2019/2020 new national excellence program of the ministry for innovation and technology to KG and KB. Scientific research support was provided by GINOP -2.3.2.-15-2016-00047 to MW. The Janos Bolyai Scholarship of the Hungarian Academy of Sciences and Bolyai + 2019/2020 (UNKP-19-4 or 2019/2020 new national excellence program of the ministry of human capacities) also

supported KK. JP was supported by the EFOP-3.6.1-16-2016-00004; 2020-4.1.1/TKP2020 'Biomedical Engineering', and GINOP-2.3.2.-15-2016-00022. The publication process has been supported by PTE Internal grant PoC to KK.

ACKNOWLEDGMENTS

We wish to thank Prof. Hajnalka Abraham MD, Ph.D. (Central Electron Microscope Laboratory, University of Pecs, Hungary) for the technical aid in taking transmission electron microscope images. The research was performed in collaboration with the Genomics and Bioinformatics Core Facility at the Szentágothai Research Center of the University of Pecs. We are also grateful for Prof. Mary Keen (Faculty of Pharmacy, University of Birmingham, United Kingdom) having performed careful and critical revision on key parts of the manuscript as a native English speaker.

SUPPLEMENTARY MATERIAL

The Supplementary Material for this article can be found online at: https://www.frontiersin.org/articles/10.3389/fphys.2021.658218/full#supplementary-material

REFERENCES

Andersen, C. L., Jensen, J. L., and Ørntoft, T. F. (2004). Normalization of real-time quantitative reverse transcription-PCR data: A model-based variance estimation approach to identify genes suited for normalization, applied to bladder and colon cancer data sets. *Cancer Res.* 64, 5245–5250. doi: 10.1158/0008-5472.CAN-04-0496

Anderson, E., and Durstine, J. L. (2019). Physical activity, exercise, and chronic diseases: A brief review. *Sports Med. Health Sci.* 1, 3–10. doi: 10.1016/j.smhs.2019.08.006

Andreu, Z., Rivas, E., Sanguino-Pascual, A., Lamana, A., Marazuela, M., González-Alvaro, I., et al. (2016). Comparative analysis of EV isolation procedures for miRNAs detection in serum samples. *J. Extracell. Vesicl.* 5, 1–10. doi: 10.3402/jev.v5.31655

Annibalini, G., Contarelli, S., Lucertini, F., Guescini, M., Maggio, S., Ceccaroli, P., et al. (2019). Muscle and systemic molecular responses to a single flywheel based iso-inertial training session in resistance-trained men. *Front. Physiol.* 10:1–10. doi: 10.3389/fphys.2019.00554

Arora, H., Qureshi, R., Jin, S., Park, A. K., and Park, W. Y. (2011). MiR-9 and let-7g enhance the sensitivity to ionizing radiation by suppression of NFκB1. *Exp. Mol. Med.* 43, 298–304. doi: 10.3858/emm.2011.43.5.031

Bai, H., and Wu, S. (2019). Mir-451: A novel biomarker and potential therapeutic target for cancer. *OncoTargets Ther.* 12, 11069–11082. doi: 10.2147/OTT.S230963

Bandi, N., Zbinden, S., Gugger, M., Arnold, M., Kocher, V., Hasan, L., et al. (2009). miR-15a and miR-16 are implicated in cell cycle regulation in a Rb-dependent manner and are frequently deleted or down-regulated in non-small cell lung cancer. *Cancer Res.* 2009:4277. doi: 10.1158/0008-5472.CAN-08-4277

Banfai, K., Garai, K., Ernszt, D., Pongracz, J. E., and Kvell, K. (2019). Transgenic exosomes for thymus regeneration. *Front. Immunol.* 10:1–9. doi: 10.3389/fimmu.2019.00862

Barbagallo, C., Mostile, G., Baglieri, G., Giunta, F., Luca, A., Raciti, L., et al. (2020). Specific Signatures of Serum miRNAs as Potential Biomarkers to Discriminate Clinically Similar Neurodegenerative and Vascular-Related Diseases. *Cell. Mol. Neurobiol.* 40, 531–546. doi: 10.1007/s10571-019-00751-y

Bertoldi, K., Cechinel, L. R., Schallenberger, B., Corssac, G. B., Davies, S., Guerreiro, I. C. K., et al. (2018). Circulating extracellular vesicles in the aging process: impact of aerobic exercise. *Mol. Cell. Biochem.* 440, 115–125. doi: 10.1007/s11010-017-3160-4

Biamonte, F., Santamaria, G., Sacco, A., Perrone, F. M., Di Cello, A., Battaglia, A. M., et al. (2019). MicroRNA let-7g acts as tumor suppressor and predictive biomarker for chemoresistance in human epithelial ovarian cancer. *Sci. Rep.* 9:5668. doi: 10.1038/s41598-019-42221-x

Bolker, B., Huber, W., Lumley, T., Maechler, M., Magnusson, A., and Moeller, S. (2020). *Package 'gplots' R topics documented*. Vienna: R Core Team.

Brahmer, A., Neuberger, E., Esch-Heisser, L., Haller, N., Jorgensen, M. M., Baek, R., et al. (2019). Platelets, endothelial cells and leukocytes contribute to the exercise-triggered release of extracellular vesicles into the circulation. *J. Extracell. Vesicl.* 8:1615820. doi: 10.1080/20013078.2019.1615820

Brennan, K., Martin, K., FitzGerald, S. P., O'Sullivan, J., Wu, Y., Blanco, A., et al. (2020). A comparison of methods for the isolation and separation of extracellular vesicles from protein and lipid particles in human serum. *Sci. Rep.* 10, 1–13. doi: 10.1038/s41598-020-57497-7

Cai, Z. G., Zhang, S. M., Zhang, Y., Zhou, Y. Y., Wu, H. B., and Xu, X. P. (2012). MicroRNAs are dynamically regulated and play an important role in LPS-induced lung injury. *Canad. J. Physiol. Pharmacol.* 90, 37–43. doi: 10.1139/Y11-095

Craig, C. L., Marshall, A. L., Sjöström, M., Bauman, A. E., Booth, M. L., Ainsworth, B. E., et al. (2003). International physical activity questionnaire: 12-Country reliability and validity. *Med. Sci. Sports Exerc.* 35, 1381–1395. doi: 10.1249/01.MSS.0000078924.61453.FB

D'souza, R. F., Woodhead, J. S. T., Zeng, N., Blenkiron, C., Merry, T. L., Cameron-Smith, D., et al. (2018). Circulatory exosomal miRNA following intense exercise is unrelated to muscle and plasma miRNA abundances. *Am. J. Physiol. Endocrinol. Metabol.* 315, E723–E733. doi: 10.1152/ajpendo.00138.2018

Da Silva, F., Rode, M., Vietta, G., Iop, R., Creczynski-Pasa, T., Martin, A., et al. (2021). Expression levels of specific microRNAs are increased after exercise and are associated with cognitive improvement in Parkinson's disease. *Mol. Med. Rep.* 24, 1–10. doi: 10.3892/mmr.2021.12257

Eichelmann, A. K., Matuszcak, C., Lindner, K., Haier, J., Hussey, D. J., and Hummel, R. (2018). Complex role of miR-130a-3p and miR-148a-3p balance on drug resistance and tumor biology in esophageal squamous cell carcinoma. *Sci. Rep.* 8:17553. doi: 10.1038/s41598-018-35799-1

Estébanez, B., Jiménez-Pavón, D., Huang, C. J., Cuevas, M. J., and González-Gallego, J. (2021). Effects of exercise on exosome release and cargo in in vivo and ex vivo models: A systematic review. *J. Cell. Physiol.* 236, 3336–3353. doi: 10.1002/jcp.30094

Filková, M., Aradi, B., Šenolt, L., Ospelt, C., Vettori, S., Mann, H., et al. (2014). Association of circulating miR-223 and miR-16 with disease activity in patients with early rheumatoid arthritis. *Ann. Rheumat. Dis.* 2014:202815. doi: 10.1136/annrheumdis-2012-202815

Frühbeis, C., Helmig, S., Tug, S., Simon, P., and Krämer-Albers, E. M. (2015). Physical exercise induces rapid release of small extracellular vesicles into the circulation. *J. Extracell. Vesicl.* 4, 1–11. doi: 10.3402/jev.v4.28239

Gao, S. M., Xing, C. Y., Chen, C. Q., Lin, S. S., Dong, P. H., and Yu, F. J. (2011). MiR-15a and miR-16-1 inhibit the proliferation of leukemic cells by down-regulating WT1 protein level. *J. Exp. Clin. Cancer Res.* 30, 1–9. doi: 10.1186/1756-9966-30-110

Garai, K., Adam, Z., Herczeg, R., Katai, E., Nagy, T., Pal, S., et al. (2019). Artificial Neural Network Correlation and Biostatistics Evaluation of Physiological and Molecular Parameters in Healthy Young Individuals Performing Regular Exercise. *Front. Physiol.* 10:01242. doi: 10.3389/fphys.2019.01242

Gardiner, C., Ferreira, Y. J., Dragovic, R. A., Redman, C. W. G., and Sargent, I. L. (2013). Extracellular vesicle sizing and enumeration by nanoparticle tracking analysis. *J. Extracell. Vesicl.* 2:19671. doi: 10.3402/jev.v2i0.19671

Hong, L. Z., Zhou, L., Zou, R., Khoo, C. M., Chew, A. L. S., Chin, C. L., et al. (2021). Systematic evaluation of multiple qPCR platforms, NanoString and miRNA-Seq for microRNA biomarker discovery in human biofluids. *Sci. Rep.* 11, 1–11. doi: 10.1038/s41598-021-83365-z

Hou, Z., Qin, X., Hu, Y., Zhang, X., Li, G., Wu, J., et al. (2019). Longterm Exercise-Derived Exosomal miR-342-5p: A Novel Exerkine for Cardioprotection. *Circulat. Res.* 124, 1386–1400. doi: 10.1161/CIRCRESAHA.118.314635

Hua, K., Chen, Y. T., Chen, C. F., Tang, Y. S., Huang, T. T., Lin, Y. C., et al. (2018). Microrna-23a/27a/24-2 cluster promotes gastric cancer cell proliferation synergistically. *Oncol. Lett.* 16, 2319–2325. doi: 10.3892/ol.2018.8924

Huang, J. Y., Chou, S. F., Lee, J. W., Chen, H. L., Chen, C. M., Tao, M. H., et al. (2015). MicroRNA-130a can inhibit hepatitis B virus replication via targeting PGC1α and PPARγ. *RNA* 2015, 114. doi: 10.1261/rna.048744.114

Iliopoulos, D., Hirsch, H. A., and Struhl, K. (2009). An Epigenetic Switch Involving NF-κB, Lin28, Let-7 MicroRNA, and IL6 Links Inflammation to Cell Transformation. *Cell* 2009:014. doi: 10.1016/j.cell.2009.10.014

Kamalden, T. A., Macgregor-Das, A. M., Kannan, S. M., Dunkerly-Eyring, B., Khaliddin, N., Xu, Z., et al. (2017). Exosomal MicroRNA-15a Transfer from the Pancreas Augments Diabetic Complications by Inducing Oxidative Stress. *Antioxid. Redox Signal.* 27, 913–930. doi: 10.1089/ars.2016.6844

Kanaoka, R., Iinuma, H., Dejima, H., Sakai, T., Uehara, H., Matsutani, N., et al. (2018). Usefulness of Plasma Exosomal MicroRNA-451a as a Noninvasive Biomarker for Early Prediction of Recurrence and Prognosis of Non-Small Cell Lung Cancer. *Oncology* 94, 311–323. doi: 10.1159/000487006

Kestens, V., Bozatzidis, V., De Temmerman, P. J., Ramaye, Y., and Roebben, G. (2017). Validation of a particle tracking analysis method for the size determination of nano- and microparticles. *J. Nanopart. Res.* 19:271. doi: 10.1007/s11051-017-3966-8

Kowal, J., Tkach, M., and Théry, C. (2014). Biogenesis and secretion of exosomes. *Curr. Opin. Cell Biol.* 29, 116–125. doi: 10.1016/j.ceb.2014.05.004

Lee, S. T., Chu, K., Oh, H. J., Im, W. S., Lim, J. Y., Kim, S. K., et al. (2011). Let-7 microRNA inhibits the proliferation of human glioblastoma cells. *J. Neuro Oncol.* 102, 19–24. doi: 10.1007/s11060-010-0286-6

Li, F., Bai, M., Xu, J., Zhu, L., Liu, C., and Duan, R. (2020). Long-Term Exercise Alters the Profiles of Circulating Micro-RNAs in the Plasma of Young Women. *Front. Physiol.* 11:1–10. doi: 10.3389/fphys.2020.00372

Li, J., Chen, Y., Guo, X., Zhou, L., Jia, Z., Tang, Y., et al. (2016). Inhibition of miR-15b decreases cell migration and metastasis in colorectal cancer. *Tumor Biol.* 2016, 8765–8773. doi: 10.1007/s13277-015-4396-9

Li, S. Q., Wang, Z. H., Mi, X. G., Liu, L., and Tan, Y. (2015). MiR-199a/b-3p suppresses migration and invasion of breast cancer cells by downregulating PAK4/MEK/ERK signaling pathway. *IUBMB Life* 2015:1433. doi: 10.1002/iub.1433

Liu, T., Zhang, Q., Zhang, J., Li, C., Miao, Y. R., Lei, Q., et al. (2019). EVmiRNA: A database of miRNA profiling in extracellular vesicles. *Nucleic Acids Res.* 47, D89–D93. doi: 10.1093/nar/gky985

Liu, X., Liu, Q., Fan, Y., Wang, S., Liu, X., Zhu, L., et al. (2014). Downregulation of PPP2R5E expression by miR-23a suppresses apoptosis to facilitate the growth of gastric cancer cells. *FEBS Lett.* 588, 3160–3169. doi: 10.1016/j.febslet.2014.05.068

Lopotová, T., Žáèková, M., Klamová, H., and Moravcová, J. (2011). MicroRNA-451 in chronic myeloid leukemia: MiR-451-BCR-ABL regulatory loop? *Leukemia Res.* 2011:029. doi: 10.1016/j.leukres.2011.03.029

Lunavat, T. R., Cheng, L., Kim, D. K., Bhadury, J., Jang, S. C., Lässer, C., et al. (2015). Small RNA deep sequencing discriminates subsets of extracellular vesicles released by melanoma cells – Evidence of unique microRNA cargos. *RNA Biol.* 2015:1056975. doi: 10.1080/15476286.2015.1056975

Ma, Z., Liu, T., Huang, W., Liu, H., Zhang, H. M., Li, Q., et al. (2016). MicroRNA regulatory pathway analysis identifies miR-142-5p as a negative regulator of TGF-ß pathway via targeting SMAD3. *Oncotarget* 2016:12229. doi: 10.18632/oncotarget.12229

MacLean, J. A., King, M. L., Okuda, H., and Hayashi, K. (2016). WNT7A regulation by miR-15b in ovarian cancer. *PLoS One* 2016:0156109. doi: 10.1371/journal.pone.0156109

Mercken, E. M., Majounie, E., Ding, J., Guo, R., Kim, J., Bernier, M., et al. (2013). Age-associated miRNA alterations in skeletal muscle from rhesus monkeys reversed by caloric restriction. *Aging* 5, 692–703. doi: 10.18632/aging.100598

Muroya, S., Ogasawara, H., and Hojito, M. (2015). Grazing affects exosomal Circulating microRNAs in cattle. *PLoS One* 10:1–19. doi: 10.1371/journal.pone.0136475

Nederveen, J. P., Warnier, G., Di Carlo, A., Nilsson, M. I., and Tarnopolsky, M. A. (2021). Extracellular Vesicles and Exosomes: Insights From Exercise Science. *Front. Physiol.* 11:604274. doi: 10.3389/fphys.2020.604274

Osbourne, A., Calway, T., Broman, M., McSharry, S., Earley, J., and Kim, G. H. (2014). Downregulation of connexin43 by microRNA-130a in cardiomyocytes results in cardiac arrhythmias. *J. Mol. Cell. Cardiol.* 2014:024. doi: 10.1016/j.yjmcc.2014.04.024

Ozawa, P. M. M., Vieira, E., Lemos, D. S., Souza, I. L. M., Zanata, S. M., Pankievicz, V. C., et al. (2020). Identification of miRNAs enriched in extracellular vesicles derived from serum samples of breast cancer patients. *Biomolecules* 10:biom10010150. doi: 10.3390/biom10010150

Pulliero, A., You, M., Chaluvally-Raghavan, P., Marengo, B., Domenicotti, C., Banelli, B., et al. (2020). Anticancer effect of physical activity is mediated by modulation of extracellular microRNA in blood. *Oncotarget* 11, 2106–2119. doi: 10.18632/oncotarget.27609

Qu, Z., Li, W., and Fu, B. (2014). MicroRNAs in autoimmune diseases. *BioMed Res. Int.* 2014:527895. doi: 10.1155/2014/527895

R Core Team (2019). *A Language and Environment for Statistical Computing*. Vienna: R Foundation for Statistical Computing.

Rani, A., O'Shea, A., Ianov, L., Cohen, R. A., Woods, A. J., and Foster, T. C. (2017). miRNA in circulating microvesicles as biomarkers for age-related cognitive decline. *Front. Aging Neurosci.* 9:1–10. doi: 10.3389/fnagi.2017.00323

Riquelme, I., Tapia, O., Leal, P., Sandoval, A., Varga, M. G., Letelier, P., et al. (2016). miR-101-2, miR-125b-2 and miR-451a act as potential tumor suppressors in gastric cancer through regulation of the PI3K/AKT/mTOR pathway. *Cell. Oncol.* 39, 23–33. doi: 10.1007/s13402-015-0247-3

Roderburg, C., Luedde, M., Vargas Cardenas, D., Vucur, M., Scholten, D., Frey, N., et al. (2013). Circulating MicroRNA-150 Serum Levels Predict Survival in Patients with Critical Illness and Sepsis. *PLoS One* 2013:0054612. doi: 10.1371/journal.pone.0054612

Sanford, J. A., Nogiec, C. D., Lindholm, M. E., Adkins, J. N., Amar, D., Dasari, S., et al. (2020). Molecular Transducers of Physical Activity Consortium (MoTrPAC): Mapping the Dynamic Responses to Exercise. *Cell* 181, 1464–1474. doi: 10.1016/j.cell.2020.06.004

Song, L., Su, M., Wang, S., Zou, Y., Wang, X., Wang, Y., et al. (2014). MiR-451 is decreased in hypertrophic cardiomyopathy and regulates autophagy by targeting TSC1. *J. Cell. Mol. Med.* 2014:12380. doi: 10.1111/jcmm.12380

Sormunen, J., Bäckmand, H. M., Sarna, S., Kujala, U. M., Kaprio, J., Dyba, T., et al. (2014). Lifetime physical activity and cancer incidence-A cohort study of male former elite athletes in Finland. *J. Sci. Med. Sport* 17, 479–484. doi: 10.1016/j.jsams.2013.10.239

Sukma Dewi, I., Hollander, Z., Lam, K. K., McManus, J. W., Tebbutt, S. J., Ng, R. T., et al. (2017). Association of serum MiR-142-3p and MiR-101-3p levels with acute cellular rejection after heart transplantation. *PLoS One* 2017:0170842. doi: 10.1371/journal.pone.0170842

Sun, C. Y., She, X. M., Qin, Y., Chu, Z. B., Chen, L., Ai, L. S., et al. (2013). miR-15a and miR-16 affect the angiogenesis of multiple myeloma by targeting VEGF. *Carcinogenesis* 2013:bgs333. doi: 10.1093/carcin/bgs333

Teteloshvili, N., Kluiver, J., Van Der Geest, K. S. M., Van Der Lei, R. J., Jellema, P., Pawelec, G., et al. (2015). Age-associated differences in MiRNA signatures are restricted to CD45RO negative T cells and are associated with changes in the cellular composition, activation and cellular ageing. *PLoS One* 10:1–13. doi: 10.1371/journal.pone.0137556

Thane, K. E., Davis, A. M., and Hoffman, A. M. (2019). Improved methods for fluorescent labeling and detection of single extracellular vesicles using nanoparticle tracking analysis. *Sci. Rep.* 9, 1–13. doi: 10.1038/s41598-019-48181-6

Trang, P., Medina, P. P., Wiggins, J. F., Ruffino, L., Kelnar, K., Omotola, M., et al. (2010). Regression of murine lung tumors by the let-7 microRNA. *Oncogene* 2010:445. doi: 10.1038/onc.2009.445

Vlachos, I. S., Zagganas, K., Paraskevopoulou, M. D., Georgakilas, G., Karagkouni, D., Vergoulis, T., et al. (2015). DIANA-miRPath v3.0: Deciphering microRNA function with experimental support. *Nucleic Acids Res.* 43, W460–W466. doi: 10.1093/nar/gkv403

Wang, F., Ren, X., and Zhang, X. (2015). Role of microRNA-150 in solid tumors (review). *Oncol. Lett.* 10, 11–16. doi: 10.3892/ol.2015.3170

Wang, J., Zhao, X., Shi, J., Pan, Y., Chen, Q., Leng, P., et al. (2016). MIR 451 suppresses bladder cancer cell migration and invasion via

directly targeting c-Myc. *Oncol. Rep.* 36, 2049–2058. doi: 10.3892/or.2016.5040

Wang, N., Tan, H. Y., Feng, Y. G., Zhang, C., Chen, F., and Feng, Y. (2019). microRNA-23a in human cancer: Its roles, mechanisms and therapeutic relevance. *Cancers* 11, 1–22. doi: 10.3390/cancers11010007

Wang, W. L., Yang, C., Han, X. L., Wang, R., Huang, Y., Zi, Y. M., et al. (2014). MicroRNA-23a expression in paraffin-embedded specimen correlates with overall survival of diffuse large B-cell lymphoma. *Med. Oncol.* 31:919. doi: 10.1007/s12032-014-0919-2

Wang, Y. T., Tsai, P. C., Liao, Y. C., Hsu, C. Y., and Juo, S. H. H. (2013). Circulating microRNAs have a sex-specific association with metabolic syndrome. *J. Biomed. Sci.* 2013:72. doi: 10.1186/1423-0127-20-72

Wang, Z., Liu, Z., Fang, X., and Yang, H. (2017). MiR-142-5p Suppresses Tumorigenesis by Targeting PIK3CA in Non-Small Cell Lung Cancer. *Cell. Physiol. Biochem.* 2017:000484459. doi: 10.1159/000484459

Wong, Q. W. L., Lung, R. W. M., Law, P. T. Y., Lai, P. B. S., Chan, K. Y. Y., To, K. F., et al. (2008). MicroRNA-223 Is Commonly Repressed in Hepatocellular Carcinoma and Potentiates Expression of Stathmin1. *Gastroenterology* 2008:003. doi: 10.1053/j.gastro.2008.04.003

Xia, L., Zhang, D., Du, R., Pan, Y., Zhao, L., Sun, S., et al. (2008). miR-15b and miR-16 modulate multidrug resistance by targeting BCL2 in human gastric cancer cells. *Int. J. Cancer* 2008:23501. doi: 10.1002/ijc.23501

Xiong, Y., Chen, L., Yu, T., Yan, C., Zhou, W., Cao, F., et al. (2020). Inhibition of circulating exosomal microRNA-15a-3p accelerates diabetic wound repair. *Aging* 12, 8968–8986. doi: 10.18632/aging.103143

Xu, Q., Meng, S., Liu, B., Li, M. Q., Li, Y., Fang, L., et al. (2014). MicroRNA-130a regulates autophagy of endothelial progenitor cells through Runx3. *Clin. Exp. Pharmacol. Physiol.* 41, 351–357. doi: 10.1111/1440-1681.12227

Yang, Z., Chen, H., Si, H., Li, X., Ding, X., Sheng, Q., et al. (2014). Serum miR-23a, a potential biomarker for diagnosis of pre-diabetes and type 2 diabetes. *Acta Diabetol.* 51, 823–831. doi: 10.1007/s00592-014-0617-8

Yin, X., Zhao, Y., Zheng, Y. L., Wang, J. Z., Li, W., Lu, Q. J., et al. (2019). Time-Course Responses of Muscle-Specific MicroRNAs Following Acute Uphill or Downhill Exercise in Sprague-Dawley Rats. *Front. Physiol.* 10:01275. doi: 10.3389/fphys.2019.01275

Yong, F. L., Law, C. W., and Wang, C. W. (2013). Potentiality of a triple microRNA classifier: MiR-193a-3p, miR-23a and miR-338-5p for early detection of colorectal cancer. *BMC Cancer* 13:280. doi: 10.1186/1471-2407-13-280

Yoshikawa, M., Iinuma, H., Umemoto, Y., Yanagisawa, T., Matsumoto, A., and Jinno, H. (2018). Exosome-encapsulated microRNA-223-3p as a minimally invasive biomarker for the early detection of invasive breast cancer. *Oncol. Lett.* 15, 9584–9592. doi: 10.3892/ol.2018.8457

Yu, F., Lu, Z., Chen, B., Dong, P., and Zheng, J. (2015). microRNA-150: A promising novel biomarker for hepatitis B virus-related hepatocellular carcinoma. *Diagnost. Pathol.* 10:129. doi: 10.1186/s13000-015-0369-y

Zhang, Y., Huang, F., Wang, J., Peng, L., and Luo, H. (2015). MiR-15b mediates liver cancer cells proliferation through targeting BCL-2. *Int. J. Clin. Exp. Pathol.* 8, 15677–15683.

Zheng, H., Li, W., Wang, Y., Xie, T., Cai, Y., Wang, Z., et al. (2014). miR-23a inhibits E-cadherin expression and is regulated by AP-1 and NFAT4 complex during Fas-induced EMT in gastrointestinal cancer. *Carcinogenesis* 2014:bgt274. doi: 10.1093/carcin/bgt274

Zhu, C., Ren, C., Han, J., Ding, Y., Du, J., Dai, N., et al. (2014). A five-microRNA panel in plasma was identified as potential biomarker for early detection of gastric cancer. *Br. J. Cancer* 110, 2291–2299. doi: 10.1038/bjc.2014.119

Zhu, L. H., Liu, T., Tang, H., Tian, R. Q., Su, C., Liu, M., et al. (2010). MicroRNA-23a promotes the growth of gastric adenocarcinoma cell line MGC803 and downregulates interleukin-6 receptor. *FEBS J.* 277, 3726–3734. doi: 10.1111/j.1742-4658.2010.07773.x

Conflict of Interest: The authors declare that the research was conducted in the absence of any commercial or financial relationships that could be construed as a potential conflict of interest.

Publisher's Note: All claims expressed in this article are solely those of the authors and do not necessarily represent those of their affiliated organizations, or those of the publisher, the editors and the reviewers. Any product that may be evaluated in this article, or claim that may be made by its manufacturer, is not guaranteed or endorsed by the publisher.

Transgenic Res (2010) 19:105–112
DOI 10.1007/s11248-009-9288-6

BRIEF COMMUNICATION

Characterisation of eGFP-transgenic BALB/c mouse strain established by lentiviral transgenesis

Krisztián Kvell · Tamás Czömpöly · László Hiripi · Péter Balogh · József Kóbor · Lilla Bodrogi · Judit E. Pongrácz · William A. Ritchie · Zsuzsanna Bősze

Received: 23 February 2009 / Accepted: 19 May 2009 / Published online: 31 May 2009

Abstract Lentiviral technology is a powerful tool for the creation of stable transgenic animals. However, uncertainties have remained whether constitutive promoters resist long-term silencing. We used concentrated HIV-1 based lentiviral vectors to create stable transgenic BALB/c mice by perivitelline injection. In our vectors eGFP expression was driven by the human EF1α promoter. The established transgenic animals were analyzed for eGFP expression by in vivo fluorescence imaging, PCR, histology and flow-cytometry. eGFP expression showed even distribution without mosaicism; however, tissue-dependent differences of eGFP expression were observed. Up to the sixth generation only one newborn showed eGFP inactivation. eGFP + transgenic bone marrow cells efficiently provided long-term haemopoietic repopulation in radiation chimeras, regenerating all bone marrow-derived lineages with eGFP + cells with distinct eGFP expression profiles. The established eGFP + BALB/c mouse strain is expected to be extremely useful in various immunological experiments.

Keywords Balb/c · eGFP · Lentiviral transgenesis · Bone-marrow chimeric mouse

K. Kvell · T. Czömpöly · P. Balogh · J. E. Pongrácz
Department of Immunology and Biotechnology, University of Pecs, Pecs, Hungary

L. Hiripi · L. Bodrogi · Z. Bősze (✉)
Genetic Modification Program Group, Agricultural Biotechnology Center, P. O. Box 411, 2100 Gödöllő, Hungary
e-mail: bosze@abc.hu

J. Kóbor
Department of Oncotherapy, University of Pecs, Pecs, Hungary

W. A. Ritchie
Roslin Embryology Limited, Edinburgh, Scotland, UK

Introduction

Lentiviral transgenesis has become an important and efficient new tool for the establishment of transgenic animals. The transgenic sequence most often used for 'proof-of-principle'-type experiments is eGFP (enhanced green fluorescent protein). Concentrated lentiviral vectors efficiently transfect zygotes following perivitelline injection. With this method the nucleus of the zygote is not affected directly, and higher volumes may be injected with less sophisticated machinery. With lentiviral vectors the efficiency of stable, active transgenesis is significantly higher than with standard pronuclear injection, reaching 8–50% (Park 2007).

In the field of immunology a massive body of experimental evidence is derived from studies performed in mice with BALB/c genetic background (Bleul et al. 2006; Ivanov et al. 2006; Odegaard et al.

2007; Suzuki et al. 2006; Tezuka et al. 2007; Wing et al. 2008). However, BALB/c mice are difficult to manipulate by pronuclear injection, unlike the FVB/n strain which is characterized by vigorous reproductive performance, consistently large litters and prominent pronuclei facilitating the microinjection of DNA (Taketo et al. 1991). Consequently a widely used approach is to generate genetically modified mice on a genetic background which facilitates micromanipulation, and backcross the offsprings to BALB/c background for at least ten generations. To address this issue we sought to generate eGFP transgenic mice directly on BALB/c background by lentiviral transgenesis. Though eGFP is considered as a functionally inert intracellular protein with minimal tendency to interfere with physiological processes both in vitro and in vivo, we wished to examine in our system whether the presence of eGFP in the BALB/c mouse strain interferes with immunological processes in either central or peripheral immune organs. To investigate integration stability and transgene activity following lentiviral transgenesis as well as possible eGFP-triggered interference with immunological processes we also performed long-term in vivo experiments involving haemopoietic stem cell (HSC) transfer.

Results and discussion

Efficiency and transgene inheritance following lentiviral transduction

Purified, concentrated lentiviral supernatant was used for perivitelline injection in both BALB/c and FVB/n mice. Toxicity of viral supernatant was low as high percentages of injected and transferred embryos were born with both mouse strains (60% or 12/20 with BALB/c vs. 66% or 27/41 with FVB/n). Visual observation of newborns for identifying eGFP + transgenic BALB/c mice revealed uniform eGFP expression, lacking traits of mosaicism (Fig. 1a). The presence of integrated transgenic sequence was verified by eGFP PCR performed on genomic DNA and yielded similar efficiencies with both mouse strains among newborn animals (58% or 7/12 with BALB/c vs. 48% or 13/27 with FVB/n). The overall efficiency of active transgenesis (ratio of visually eGFP positive animals and initially injected zygotes) was equally high in both mouse strains examined (20% or 4/20 with BALB/c vs. 22% or 9/41 with FVB/n). An eGFP expressing male BALB/c founder was used to establish the transgenic line through mating with wild type BALB/c females. Southern analysis (Fig. 1b) and the ratio of transgenic animals in the F1 litters indicated one transgene integration site.

The presence of eGFP as a transgenic protein did not abrogate either the macroscopic development of transgenic BALB/c mice or their reproductive abilities; litter sizes were similar to control BALB/c mice (6–7 pups). Long-term transgene stability was remarkable as up to six generations only one single offspring showed loss of detectable eGFP fluorescence. (It has not been tested whether transgene loss or inactivation was responsible for this event). Calculating with 6 pups as average litter size this means that the loss of transgene/transgene activity has occurred at a very low frequency at approx. 3% (1/36). This solid heredity may partly be due to the rigorous flow-cytometric screening performed from blood samples of the F1 generation members, following which only those transgenic animals were further bred that showed unambiguously uniform eGFP expression in peripheral blood mononuclear cells (data not shown). Such stability of transgene inheritance and activity is especially impressive with the notion of utilizing a short, constitutively active promoter (human EF1α). Our results on stable transgene inheritance line up with earlier data obtained with EF1α-eGFP transgenic rats obtained by the lentiviral transduction of spermatogonial stem cells (Ryu et al. 2007).

Analysis of transgene expression in eGFP + BALB/c mice

Tissue samples of eGFP + BALB/c mice were analyzed from several samples by histology and flow-cytometry. Figure 1c–f summarizes representative histological results of cryostat sections of muscle, intestine, spleen and lymph node. eGFP expression is present within the cytoplasm of all nucleated cells. There were significant differences of fluorescence intensity among various tissue and cell types. In lymphoid organs, the mesenchymal-reticular cells and vasculature appeared to express eGFP more heavily than the surrounding lymphocytes. This phenomenon may be the consequence of the promoter sequence used. Although EF1α is ubiquitously active non-viral

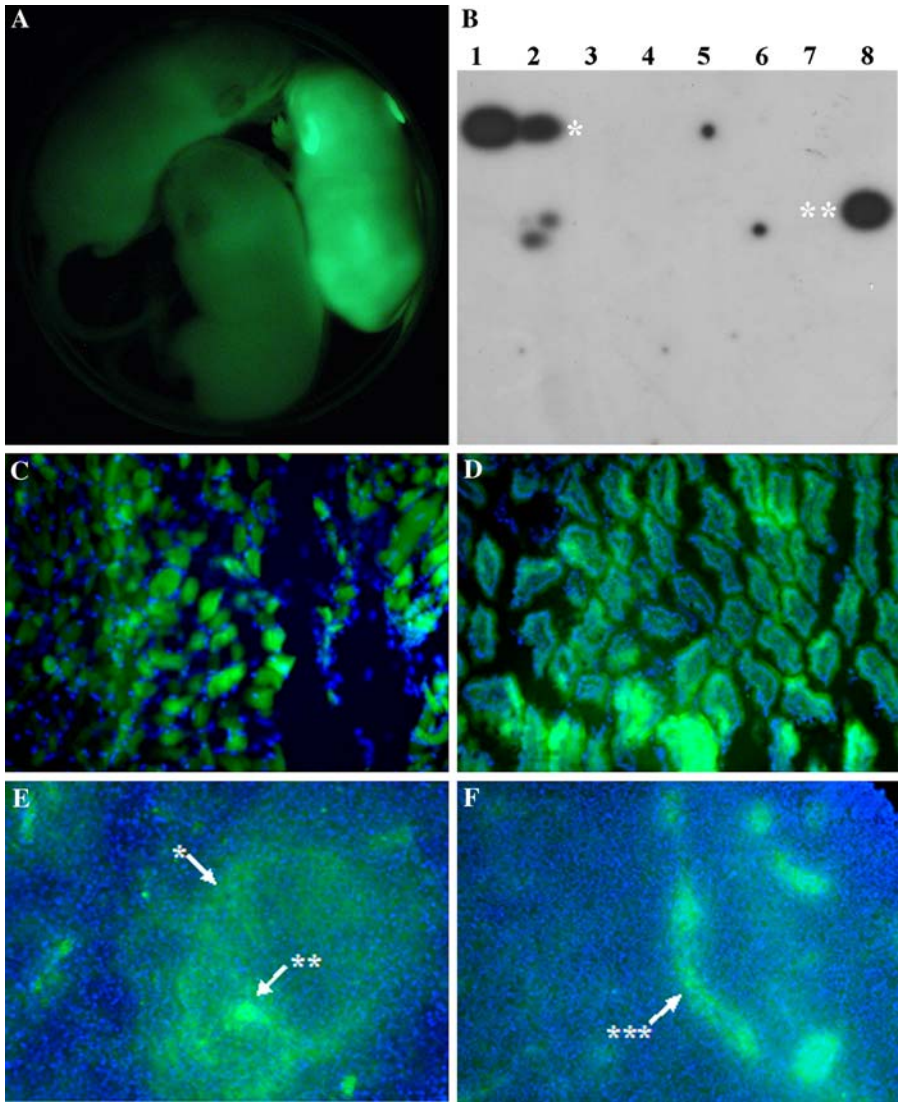

Fig. 1 Macroscopic identification, Southern and histological analysis of eGFP + BALB/c mice. **a** Shows an eGFP + newborn BALB/c mouse (*top right*) under fluorescent light among control littermates. **b** Shows Southern analysis to determine integrated transgene copy number. *Lanes 1 and 2*: eGFP + Balb/c mice. *Lanes 3, 4, and 5*: non-transgenic Balb/c mice. *Lanes 6 and 7*: no DNA added and negative plasmid DNA, *lane 8*: the LTR-cPPT-EF1α-GFP-WPRE-LTR transfer vector. Fragment sizes * >10 kb; ** 7.0 kb. **c–f** show eGFP expression in cryostat sections of muscle (**c**), intestine (**d**), spleen (**e**) and lymph node (**f**) counterstained with DAPI. Intense eGFP fluorescence is associated with stromal-fibroblastic scaffolding of white pulp (*) and vascular elements, including splenic central arteriole (**) and high endothelial venule in lymph node (***)

promoter, there may be significant differences for activity depending on the actual context of gene expression. Alternatively, cells with larger cytoplasmic volume may contain more eGFP molecules, rendering these cells more fluorescent, similar to differences observed during flow-cytometric analyses below.

Figure 2 summarizes the results of flow-cytometric characterization of peripheral blood, thymus and lymph node. The difference of eGFP fluorescence intensity was also obvious by the flow-cytometric analysis of peripheral blood leukocytes. Figure 2a shows peripheral blood leukocytes distinguished by morphology following the lysis of erythrocytes (left figure of Fig. 2a). Three distinct peaks of eGFP fluorescence intensity are seen on the FL1 histogram (middle figure of Fig. 2a), defined by gates R1 (low-), R2 (mid-) and R3 (high intensity). Following backward morphological representation using these gates (right figure of Fig. 2a) cells of weak fluorescence (R1 gate, light gray), medium fluorescence (R2 gate, medium gray) and high fluorescence (R3 gate, high fluorescence) are identified. It appeared that eGFP fluorescence strongly correlated with cell size (FSC scatter) in peripheral blood leukocytes. In the thymus, surface staining was performed to differentiate developing thymocyte subpopulations. Similarly, mature lymphocytes in the lymph node were identified by

CD4/CD8 double staining (Fig. 2b–e), and compared to wild-type BALB/c controls. Mosaicism was not observed by either histology or flow-cytometry. Our results show near identical distribution profiles of developing thymocytes in the thymus and mature lymphocytes in the lymph node. Recent data shown preferential expression of the GFP in the exocrine cells of transgenic pigs, where the GFP transgene was placed under the strong cytomegalovirus (CMV) enhancer-promoter (Vasey et al. 2009).

Analysis of eGFP expression in bone-marrow (BM) chimeric BALB/c mice

To determine whether eGFP-expressing transgenic BALB/c mice are suitable donors for haemopoietic reconstitution experiments, wild-type BALB/c mice were irradiated and repopulated with bone marrow cells from eGFP + BALB/c donors. The degree of chimerism and eGFP-expression pattern was analyzed 6 weeks after bone marrow transplantation. Figure 3 summarizes the results of flow-cytometric characterization of bone marrow, peripheral blood and lymph node samples from BM-chimeric mice. Histogram plot of Fig. 3b shows the efficacy of eGFP + HSCs for reconstituting the haemopoietic system (over 90% of BM cells fall positive in gate M1). Mosaicism among peripheral blood leukocytes was not detected following haemopoietic reconstitution. We also determined the ratio of different peripheral blood leukocytes by flow-cytometry following the lysis of erythrocytes (see Fig. 3c and d). Region statistics of wild-type and eGFP-chimeric BALB/c mice show similar distribution pattern and ratio of major leukocyte groups differentiated by morphological representation. Surface staining for CD4/CD8 antigens was performed to differentiate mature lymphocytes in the lymph node of control and BM chimeric BALB/c mice. Our results show indistinguishable distribution profiles of mature lymphocytes in the lymph nodes of control and BM chimeric BALB/c mice (see Fig. 3e and f). These data indicate that the presence of eGFP in BALB/c HSCs does not impair their capacity to restore haemopoiesis.

In summary, lentiviral transgenesis is a powerful tool for the creation of stable transgenic lines with mouse strains that are challenging for standard pronuclear injection, like the BALB/c in our case. Major immunological parameters of the established eGFP + BALB/c mouse strain were elaborately characterized and found to be equal to that of control BALB/c mice. In the future we plan to use this transgenic strain and take advantage of marker gene-harboring murine cells to investigate i.e. tumor formation, tumor-cell dissemination, lymphocyte homing and recirculation and several other applications.

Materials and methods

Plasmid constructs

Late second generation lentiviral sequences are divided into three plasmid constructs. The envelope construct pMD.G encodes the viral envelope protein pseudotyped with VSV-G (vesicular stomatitis virus G-protein). The packaging construct R8.91 encodes enzymatic and structural elements required for the assembly of recombinant retroviral vectors. The transfer construct pWPTS carries the transgene of interest in an LTR (long terminal repeat) frame. This construct also has cPPT (central polypurine tract) for increased nuclear transport, WPRE (Woodchuck-hepatitis virus post-transcriptional responsive element) for prolonged mRNA half-life and SIN (self-inactivating) mutation in the LTR frame. The HIV-1 derived lentiviral system was kindly provided by Prof. Didier Trono (CMU, Geneva, Switzerland).

Lentivirus production, purification, concentration, titration

Lentiviral particles were produced as described previously (Bovia et al. 2003; Kvell et al. 2005). Briefly, the three plasmid constructs were co-transfected into 293T cells using the calcium–phosphate method. Viral supernatant was harvested after incubation for 48 h at 37°C, 5% CO_2. Purification steps included centrifugation (2,000 rpm, 10 min, 4°C) and filtration (PVDF-coated 0.45 μm filters). For concentration the supernatant was layered on 20% sucrose for ultra-centrifugation (26,000 rpm, 90 min, 4°C). Viral particles were re-suspended in DMEM. Biological titration was performed with HeLa cells. Viral particles were concentrated 1,000-fold in volume; biological titers reached and exceeded 10^8 TU/ml.

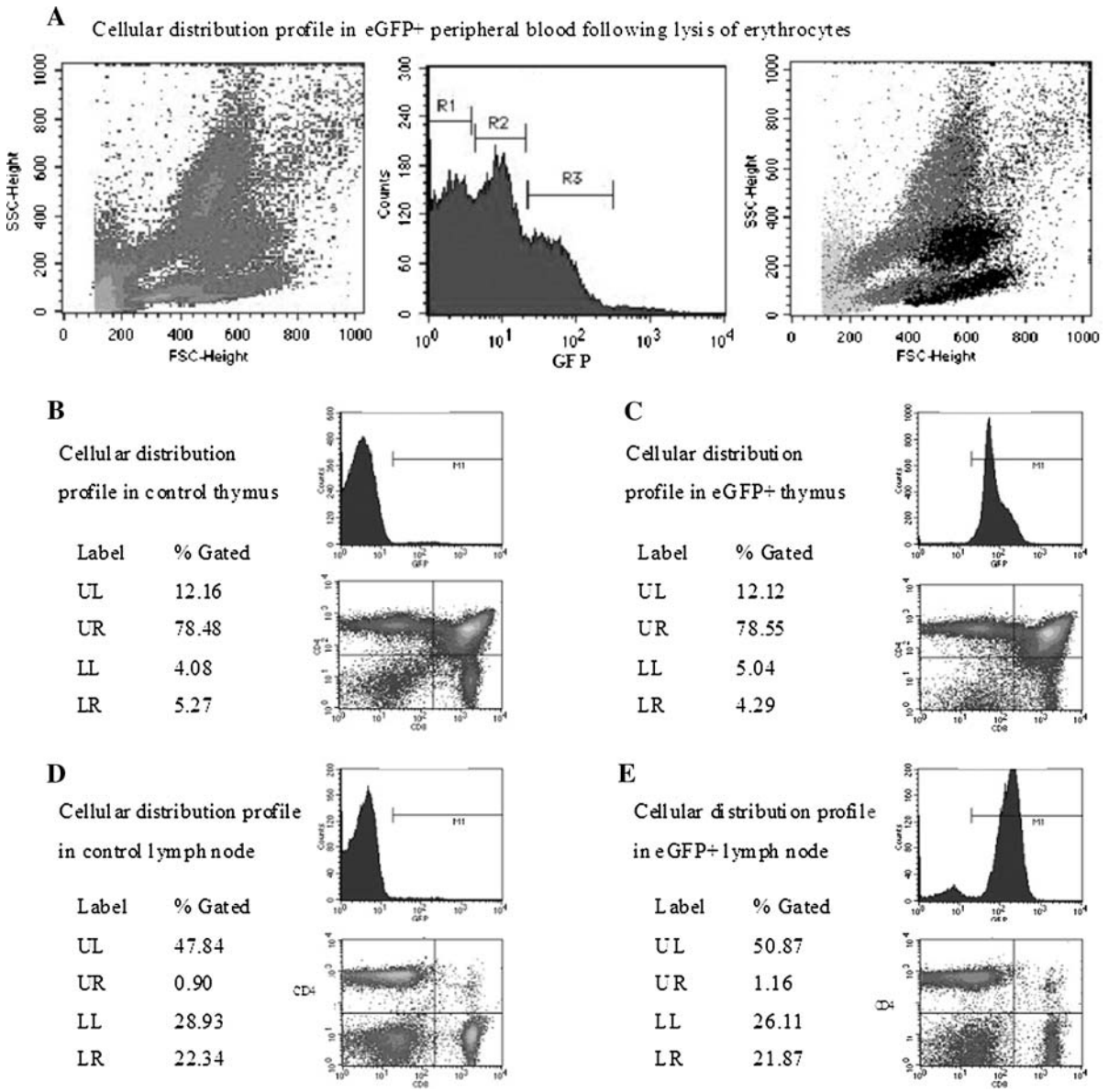

Fig. 2 Flow-cytometric characterization of eGFP + BALB/c mice. **a** Shows cellular distribution profile of eGFP fluorescence intensity in peripheral blood following erythrocyte lysis. *Left* density plot figure shows cell groups distinguished by morphology. *Middle* figure shows eGFP fluorescence intensity distribution profile as FL1 fluorescence histogram. Three distinct cell groups are differentiated by fluorescence intensity defined by gates R1 (low-), R2 (mid-) and R3 (high intensity). Dot plot figure on the *right* shows backward morphological representation. This identifies cells falling into gates R1 (*light gray*), R2 (*mid-gray*) and R3 (*dark gray*). **b** and **c** Show the cellular distribution profile (density plot) of thymocyte subgroups in thymi of control and eGFP + BALB/c mice, respectively. **d** and **e** Show the cellular distribution profile (density plot) of lymphocyte subgroups in lymph node control and eGFP + BALB/c mice, respectively. For comparison, quadrant statistics are enclosed to the figures

Zygote isolation, perivitelline injection, implantation

All strains (control and transgenic) of BALB/c and FVB/n mice were kept in conventional animal house. Lentiviral vector injection was performed based on the modified perivitelline space injection method to produce transgenic mice from low titer lentiviral vector (Ritchie et al. 2007). Approximately 300–500 pl of low titer (10^6–10^8 infectious units per ml)

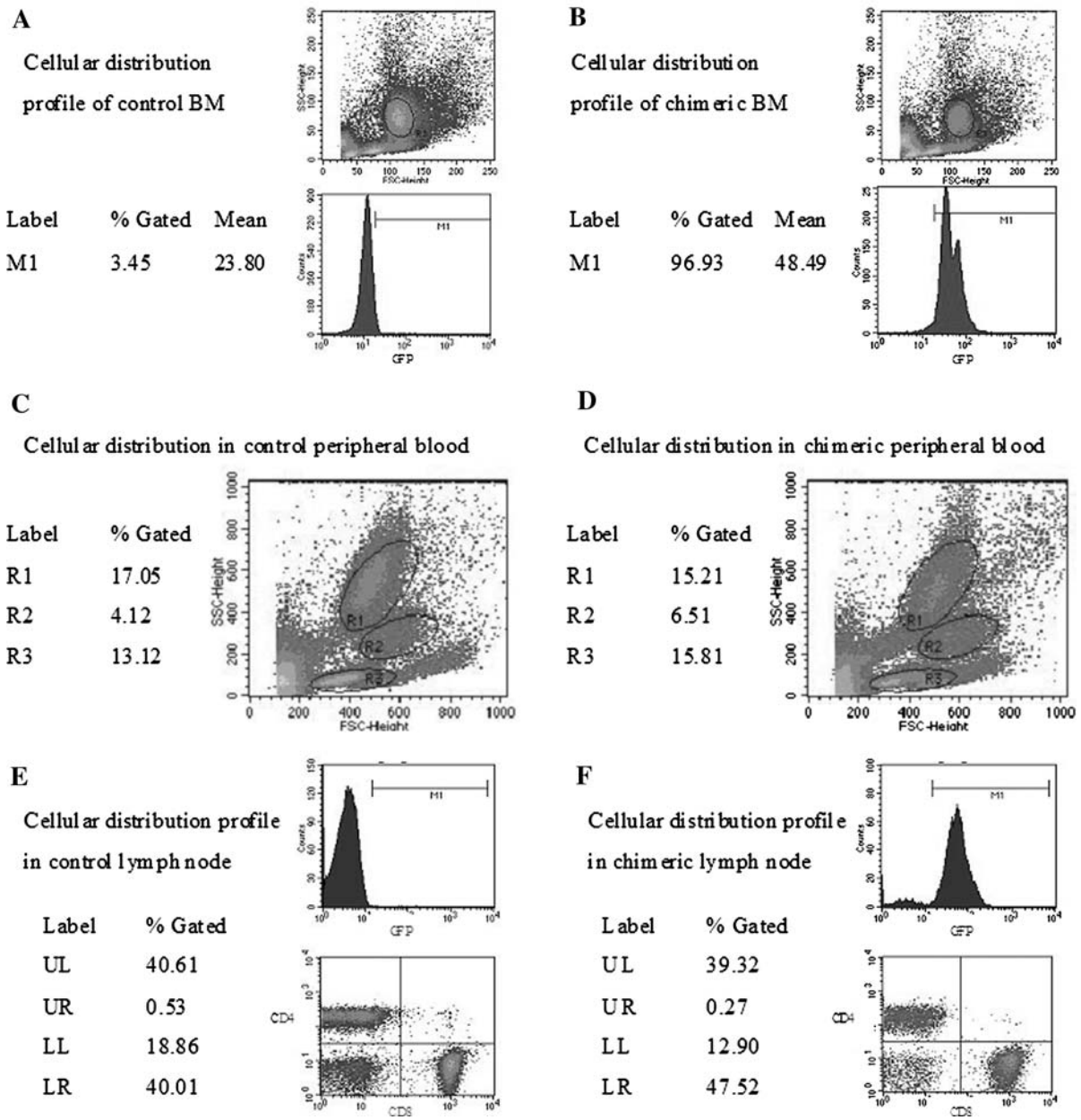

Fig. 3 Flow-cytometric characterization of BM chimeric BALB/c mice. **a** and **b** Show the cellular distribution profile (morphological and histogram plots) of bone marrow (BM) cells of control and BM chimeric BALB/c mice, respectively. For comparison, histogram statistics are shown. **c** and **d** Show cellular distribution (density plots) in peripheral blood from control and BM chimeric animal, respectively. For comparison, region statistics are shown. **e** and **f** Show the cellular distribution profile (histogram and density plots) of lymph node lymphocytes of control and BM chimeric BALB/c mice, respectively. For comparison, quadrant statistics are enclosed to both figures

lentiviral vector was repeatedly injected into the perivitelline space of single cell embryo. Superovulation of donor females, embryo isolation and transfer into surrogate mothers was performed according to standard laboratory protocols.

Bone-marrow chimeric mice were provided with ciprofloxacin during the initial 4 weeks following bone marrow transplantation.

Experiments were approved by the Animal Care and Ethics Committee of the Agricultural Biotechnology

Center and complied with the Hungarian Code of Practice for the Care and Use of Animals for Scientific Purposes, including conditions for animal welfare and handling prior to slaughter.

In vivo fluorescence imaging

eGFP and auto-fluorescence was assayed using blue light illumination (GFP excitation frequency 455–495 nm with a barrier filter cut of below 500 nm). For newborn and adult mice this was performed with a GFSP-5 headset (Biological Laboratory Instruments, Budapest).

Detection of transgene integration

Lentiviral transgene integration number was determined by Southern blot analysis of DNA from tail biopsy. 20 μg of DNA was digested with BamHI, separated on a 1% agarose gel, blotted to a nylon membrane and probed with a 282 bp-long PCR amplified eGFP fragment using primers GFP-forward 5′-CTCGTGACCACCCTGACCTAC-3′ and GFP-reverse 5′-CATGATATAGACGTTGTGGCTGTT-3′.

Detection of eGFP by histology

10 μm thick cryostat sections were prepared from various snap frozen tissues of eGFP + BALB/c mice, including muscle, intestine, spleen and lymph node, and fixed in 4% buffered paraformaldehyde to preserve native eGFP fluorescence. Nuclei were counterstained with DAPI. The specimens were viewed under an Olympus BX61 fluorescent microscope. The digital pictures were acquired with a CCD camera using the analySIS® software.

Detection of eGFP by flow-cytometry

Cells were obtained from bone marrow, thymus, lymph node and blood and peripheral blood. The lymphoid tissues were mechanically dissociated, single cell suspensions were prepared and were stained for CD4 and CD8 (BD, clones: H129.9 (a-CD4) and 53-6.7 (a-CD8)) in PBS containing 0.1% BSA and Na-azide). Stained cells were fixed with paraformaldehyde, measured by FACSCalibur flow-cytometer and analyzed by CellQuest Pro (Becton Dickinson). Cell populations were differentiated by morphology gates.

Protocol of bone marrow transplantation

About 6–8 weeks old BALB/c mice were irradiated with 10 Gy in a single bolus calculated at midline level using a Co^{60}-source. 6 h later irradiated mice were injected intravenously with 200 μl cell suspension of bone marrow cells isolated from eGFP + BALB/c adjusted to 10^7 viable cells/ml. Six weeks after haemopoietic reconstitution cells were obtained, stained and measured as above.

Acknowledgments This work was supported by OTKA T 049034 and OMFB-00118/2008 to BZS, OTKA PD 78310 to KK. TC is a recipient of the Bolyai János Postdoctoral Fellowship of the Hungarian Academy of Sciences. The authors thank G. Takács for the artwork.

References

Bleul CC, Corbeaux T, Reuter A, Fisch P, Monting JS, Boehm T (2006) Formation of a functional thymus initiated by a postnatal epithelial progenitor cell. Nature 441:992–996. doi:10.1038/nature04850

Bovia F, Salmon P, Matthes T, Kvell K, Nguyen TH, Werner-Favre C, Barnet M, Nagy M, Leuba F, Arrighi JF, Piguet V, Trono D, Zubler RH (2003) Efficient transduction of primary human B lymphocytes and nondividing myeloma B cells with HIV-1-derived lentiviral vectors. Blood 101:1727–1733. doi:10.1182/blood-2001-12-0249

Ivanov II, McKenzie BS, Zhou L, Tadokoro CE, Lepelley A, Lafaille JJ, Cua DJ, Littman DR (2006) The orphan nuclear receptor RORgammat directs the differentiation program of proinflammatory IL-17 + T helper cells. Cell 126:1121–1133. doi:10.1016/j.cell.2006.07.035

Kvell K, Nguyen TH, Salmon P, Glauser F, Werner-Favre C, Barnet M, Schneider P, Trono D, Zubler RH (2005) Transduction of CpG DNA-stimulated primary human B cells with bicistronic lentivectors. Mol Ther 12:892–899. doi:10.1016/j.ymthe.2005.05.010

Odegaard JI, Ricardo-Gonzalez RR, Goforth MH, Morel CR, Subramanian V, Mukundan L, Eagle AR, Vats D, Brombacher F, Ferrante AW, Chawla A (2007) Macrophage-specific PPARgamma controls alternative activation and improves insulin resistance. Nature 447:1116–1120. doi:10.1038/nature05894

Park F (2007) Lentiviral vectors: are they the future of animal transgenesis? Physiol Genomics 31:159–173. doi:10.1152/physiolgenomics.00069.2007

Ritchie WA, Neil C, King T, Whitelaw CB (2007) Transgenic embryos and mice produced from low titre lentiviral vectors. Transgenic Res 16:661–664. doi:10.1007/s11248-007-9102-2

Ryu BY, Orwig KE, Oatley JM, Lin CC, Chang LJ, Avarbock MR, Brinster RL (2007) Efficient generation of transgenic rats through the male germline using lentiviral transduction and transplantation of spermatogonial stem cells. J Androl 28:353–360. doi:10.2164/jandrol.106.001511

Suzuki N, Suzuki S, Millar DG, Unno M, Hara H, Calzascia T, Yamasaki S, Yokosuka T, Chen NJ, Elford AR, Suzuki J, Takeuchi A, Mirtsos C, Bouchard D, Ohashi PS, Yeh WC, Saito T (2006) A critical role for the innate immune signaling molecule IRAK-4 in T cell activation. Science 311:1927–1932. doi:10.1126/science.1124256

Taketo M, Schroeder AC, Mobraaten LE, Gunning KB, Hanten G, Fox RR, Roderick TH, Stewart CL, Lilly F, Hansen CT et al (1991) FVB/N: an inbred mouse strain preferable for transgenic analyses. Proc Natl Acad Sci USA 88:2065–2069. doi:10.1073/pnas.88.6.2065

Tezuka H, Abe Y, Iwata M, Takeuchi H, Ishikawa H, Matsushita M, Shiohara T, Akira S, Ohteki T (2007) Regulation of IgA production by naturally occurring TNF/iNOS-producing dendritic cells. Nature 448:929–933. doi:10.1038/nature06033

Vasey DB, Lillico SG, Sang HM, King TJ, Whitelaw CB (2009) CMV enhancer-promoter is preferentially active in exocrine cells in vivo. Transgenic Res 18:309–314. doi:10.1007/s11248-008-9235-y

Wing K, Onishi Y, Prieto-Martin P, Yamaguchi T, Miyara M, Fehervari Z, Nomura T, Sakaguchi S (2008) CTLA-4 control over Foxp3 + regulatory T cell function. Science 322:271–275. doi:10.1126/science.1160062

ARTICLE

doi:10.1016/j.ymthe.2005.05.010

Transduction of CpG DNA-Stimulated Primary Human B Cells with Bicistronic Lentivectors

Krisztian Kvell,[1] Tuan H. Nguyen,[2] Patrick Salmon,[2] Frédéric Glauser,[1] Christiane Werner-Favre,[1] Marc Barnet,[1] Pascal Schneider,[3] Didier Trono,[2] and Rudolf H. Zubler[1,*]

[1]*Division of Hematology, Department of Internal Medicine, and* [2]*Department of Genetics and Microbiology, University Hospitals, 1211 Geneva-14, Switzerland*

[3]*Department of Biochemistry, University of Lausanne, 1066 Epalinges, Switzerland*

**To whom correspondence and reprint requests should be addressed. Fax: 41 22 372 72 88. E-mail: rudolf.zubler@hcuge.ch.*

Available online 11 July 2005

Recently, using HIV-1-derived lentivectors, we obtained efficient transduction of primary human B lymphocytes cocultured with murine EL-4 B5 thymoma cells, but not of isolated B cells activated by CD40 ligation. Coculture with a cell line is problematic for gene therapy applications or study of gene functions. We have now found that transduction of B cells in a system using CpG DNA was comparable to that in the EL-4 B5 system. A monocistronic vector with a CMV promoter gave 32 ± 4.7% green fluorescent protein (GFP)$^+$ cells. A bicistronic vector, encoding IL-4 and GFP in the first and second cistrons, respectively, gave 14.2 ± 2.1% GFP$^+$ cells and IL-4 secretion of 1.3 ± 0.2 ng/10^5 B cells/24 h. This was similar to results obtained in CD34$^+$ cells using the elongation factor-1α promoter. Activated memory and naive B cells were transducible. After transduction with a bicistronic vector encoding a viral FLIP molecule, vFLIP was detectable by FACS or Western blot in GFP$^+$, but not in GFP$^-$, B cells, and 57% of sorted GFP$^+$ B cells were protected against Fas ligand-induced cell death. This system should be useful for gene function research in primary B cells and development of gene therapies.

Key Words: HIV-1-derived lentivectors, bicistronic vectors, human primary B lymphocytes, CpG DNA, viral FLIP

INTRODUCTION

Optimization of methods for gene delivery into primary human cells is important for research on gene functions and development of gene therapies [1]. Gene transfer into primary human B lymphocytes has been notoriously difficult. Successful applications of nonviral methods to functional assays of transgenes have not been reported for these cells. Epstein–Barr virus vectors so far have been tested only in B cell lines [2]. Murine oncoretroviral vectors gave low transduction efficiency (of up to about 4%) in primary human B cells; they could be utilized to study effects detectable by very sensitive methods, such as immunoglobulin (Ig) class-switch recombination detectable by PCR [3]. HIV-1-derived lentivectors gave efficient transduction of various immature and mature human hematopoietic cells [4–6]. Transgene expression restricted to B lymphocytes was obtained by grafting lentivector-transduced CD34$^+$ progenitors into NOD/SCID mice [7]. T lymphocytes could be transduced after activation, at least from the G0 to the G1 stage of the cell cycle [5,6]. But primary human B cells activated into proliferation by crosslinking of CD40 in the presence of various cytokines were very poorly transducible [8,9]. Recently with such vectors we obtained efficient transduction of primary B cells cocultured with irradiated murine EL-4 B5 thymoma cells; monocistronic vectors with the human cytomegalovirus (CMV) or elongation factor-1α (EF-1α) internal promoter gave 27 ± 12% green fluorescent protein (GFP)$^+$ cells [9].

For gene therapy applications, however, a cell line potentially adds risks, such as generation of recombinant viruses. For studies of gene functions a handicap is that the functions of the thymoma cells have not yet been molecularly characterized. The first aim of this study was to find a culture system for transduction with HIV vectors of isolated B cells activated by defined stimuli. The LPS receptor, Toll-like receptor-4 (TLR4), is lacking in human B cells. But TLR9, the endosomal receptor for bacterial DNA (short single-stranded DNA containing nonmethylated CpG motifs; CpG DNA), is constitutively expressed in memory human B cells and rapidly upregulated by anti-Ig antibody—which mimics an antigen signal—in

1525-0016/$30.00

naïve B cells [10,11]. We report here efficient lentiviral transduction of B cells cultured with CpG DNA, anti-Ig, IL-2, and IL-10.

The second aim was to test bicistronic HIV vectors encoding the transgene in the first cistron and GFP in the second cistron, downstream of the internal ribosomal entry site (IRES). The vectors contained the woodchuck hepatitis virus posttranscriptional regulatory element (WPRE) [12]. First, we tested a cytokine gene; this allows quantitation of secreted protein. IL-4 was chosen because it was produced neither by B cells nor in our $CD34^+$ cell-derived cultures. $CD34^+$ hematopoietic cells were utilized as a primary cell control known to be transducible with various HIV vector constructs [13,14]. As shown below, with the IL-4 vector using the CMV promoter the cytokine secretion rate of B cells was comparable to that of $CD34^+$-derived cells transduced by this vector with the EF-1α promoter. Second, we tested a viral FLIP gene. Viral FLIP proteins, like the short isoform of cellular FLIP, competitively replace the caspase in the proximal signaling complex that forms after the ligation of death receptors, such as Fas [15]. Thus, transduction should produce a positive (survival enhancing) effect rather than a loss of function readout only. Such an effect was obtained in Fas ligand (FasL)-exposed B cells.

Results and Discussion

B Cell Transduction in a Culture System Using CpG DNA

We found that peripheral blood B cells stimulated by CpG DNA, anti-Ig antibody, and the cytokines IL-2 and IL-10, according to Bernasconi *et al.* [10], were efficiently transduced by HIV vectors. For monocistronic (GFP) and bicistronic (IL-4–IRES–GFP) vectors, the mean fluorescence intensity (MFI) of GFP^+ B cells was always higher (2.5-fold or more) with the CMV than with the EF-1α internal promoter (Fig. 1), confirming our previous findings with monocistronic vectors [9]. As expected, the percentages of GFP^+ cells were lower with the bicistronic compared to the monocistronic vectors (3- or 2.3-fold by the mean, respectively, for the EF-1α or CMV promoter; for the CMV promoter, mean data are shown in Fig. 2, CpG).

The CG-rich oligonucleotides C274 (21 bases) and 2006 (24 bases), which caused optimal B cell proliferation in the study by Marshall *et al.* [16], both allowed for efficient transduction, whereas oligonucleotide C661, with all CG inverted to GC, gave 20-fold lower proliferation and transduction. Vectors had to be added to the B cell cultures on day 2 or later. At a multiplicity of infection of 20 HeLa cell-transducing units per B cell (m.o.i. of 20) the numbers of GFP^+ cells were 1.2-fold higher by the mean than at an m.o.i. of 10, but at an m.o.i. of 30 or higher the numbers progressively decreased. We also found this both with vector particles added to culture plates by low-speed centrifugation at 1000*g* and with the particles left in the supernatant, whereas virus-free supernatant of the virus-producer cells showed no toxicity. In B cells, exposure to vector caused increase in annexin V^+ cells (on day 4, from 13% in control culture to 28% in culture with virus added on day 3 at an m.o.i. of 80), indicating that apoptosis was involved. Our vectors were not toxic for T cells and

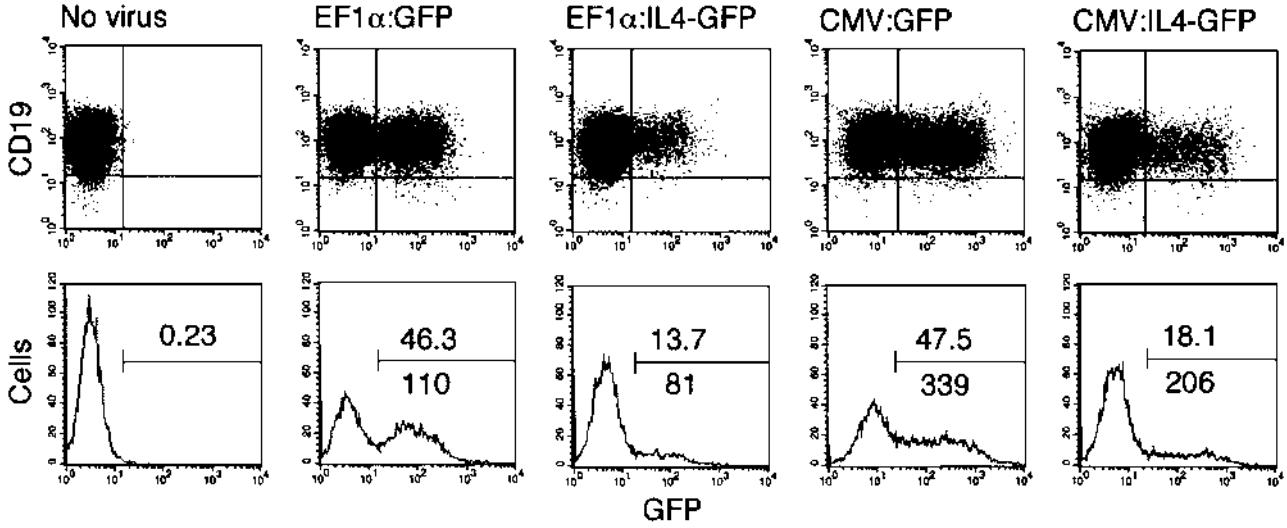

FIG. 1. GFP MFI in B cells transduced with monocistronic or bicistronic HIV vectors was higher with the CMV than with the EF-1α internal promoter. B cells were cultured in the CpG DNA system. Virus particles for the indicated vectors were added to parallel cultures on day 3 at an m.o.i. of 10. FACS analysis was done in viable cells on day 6. 2-D plots show staining with PE-anti-CD19 mAb on the *y* axis (isotype controls gave <0.5% background). Percentages of GFP^+ cells and MFI of these cells are indicated by upper and lower numbers, respectively, in the histograms.

doi:10.1016/j.ymthe.2005.05.010

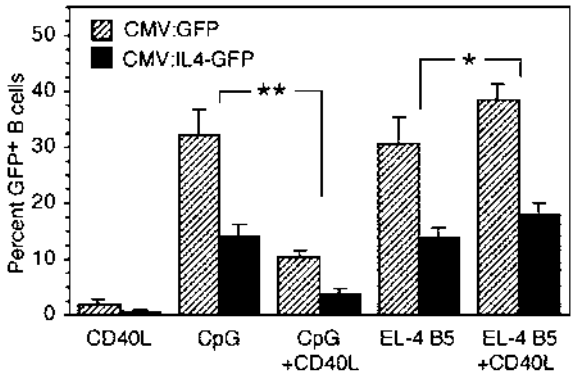

FIG. 2. Differences in B cell transducibility by HIV vectors under various culture conditions. Vectors CMV:GFP or CMV:IL4-GFP were added on day 3 (m.o.i. of 10) to the CD40L system (CD40L), CpG DNA system (CpG), CpG DNA system in the presence of CD40L (CpG + CD40L), EL-4 B5 system (EL-4 B5), or EL-4 B5 system in the presence of CD40L (EL-4 B5 + CD40L). FACS analysis was done in viable cells on day 6 or 7. Shown are means ± 1 SEM for percentages of GFP$^+$ B cells from nine independent experiments for each culture condition. Transduction in CpG versus CpG + CD40L, and in EL-4 B5 versus EL-4 B5 + CD40L, was compared in parallel experiments. Significant, opposite effects of CD40L on transducibility were found with both vectors (**$P < 0.001$; *$P < 0.05$; by two-sided t test).

CD34$^+$ cells. This may reflect the fact that, in general, B cells are more prone to apoptosis in culture than many other cells.

Comparison of Different B Cell Culture Systems

Viable cell expansion in the CpG DNA system set up with total peripheral blood B cells was fivefold by the mean in 10 days. Individual B cells proliferate very heterogeneously in this system [10]. At least fivefold higher B cell expansion was obtained in the system using EL-4 B5 murine thymoma cells as helper T cells [9,17]. But the percentages of transduced B cells among the viable cells analyzed on day 6 or 7 were very similar in both systems (Fig. 2, CpG and EL-4 B5; there were about 30 and 14% GFP$^+$ cells, respectively, for vectors CMV:GFP and CMV:IL4-GFP). Since activated B cells proliferated and outnumbered nonproliferating cells, this means that proliferating B cells were similarly transduced in both systems. Various cell types, e.g., T cells [5,6], after some activation become transducible with lentivectors even if they do not divide. So far this could not be studied with B cells, because—unlike T cells—B cell populations could not be maintained in an activated, nondividing state.

In agreement with our previous data [9], however, transducibility was very low in B cells proliferating in response to soluble CD40 ligand, IL-2, and IL-10 (CD40L, Fig. 2). Moreover, when we added CD40L to the CpG DNA system (CpG + CD40L), thymidine incorporation was enhanced 2-fold compared to the standard CpG DNA system, but the transducibility became 3.2-fold lower by the mean ($P < 0.001$ by two-sided t test; nine independent, paired experiments). By contrast, adding CD40L to the EL-5 B5 system (EL-4 B5 + CD40L) gave not only slightly increased thymidine incorporation compared to the standard EL-4 B5 system, but also 1.3-fold higher B cell transducibility ($P < 0.05$; also nine independent, paired experiments). In those experiments in which the B response in the EL-4 B5 system was relatively weak, addition of CD40L could double the percentage of GFP$^+$ B cells. In addition we found that CD40L enhanced B transduction in total peripheral blood lymphocytes stimulated with pokeweed mitogen. Anti-Ig did not enhance transducibility in the CD40L system, but B cells stimulated with CpG DNA only were transducible (about 15% GFP$^+$ cells with monocistronic vector).

Thus, it appeared that, in particular, B cells stimulated via CD40 in the absence of other T cell signals (an artificial condition) somehow resisted transduction by HIV vectors. The vectors did not cause more annexin V expression in CD40L-stimulated than in CpG DNA-stimulated B cells. Serafini *et al.* [18] found that in B cells activated via CD40 the transduction was blocked at an early stage. It is possible that innate cellular defenses, such as mechanisms involving TRIM5 or APOBEC3 antiretroviral factors [19,20], are involved; they might be triggered under certain (abnormal?) cell activation conditions *in vivo*.

Transduction of Naive and Memory B Cells

In accordance with published data [10,11], anti-Ig enhanced the proliferation of naïve (CD27$^-$), but not of memory (CD27$^+$), B cells in the CpG DNA system (2.9-fold by the mean; Fig. 3A). Even with anti-Ig, proliferation was 2.1-fold lower in naive than in memory B cultures. However, after 7 days of culture the majority of naive B cells expressed CD27, and in cultures with vector these cells expressed GFP very similar to memory B cells (Fig. 3B shows data representative of two other independent experiments). CD27 is an activation marker for naive B cells [21]. The naive B cells that remained CD27$^-$ were not transduced. On the other hand, cultures set up with memory B cells always contained some CD27$^-$ cells after culture, but these cells were transduced. Since some B cells express CD27 ligand [21], these may have been cells with ligand-modulated CD27. In any case, the data show that activated naive and memory B cells were transducible in the CpG DNA system.

IL-4 Secretion by Transduced B Cells

B cells transduced with IL-4 vectors, after cell wash, released IL-4 during secondary culture. We studied whether pseudotransduction (PTD) played a role, i.e., any viral integration-independent effects, including passive transfer of transgene proteins by the virus particles (cells become exposed to numerous defective particles) [9]. Therefore, we tested viruses produced using a pack-

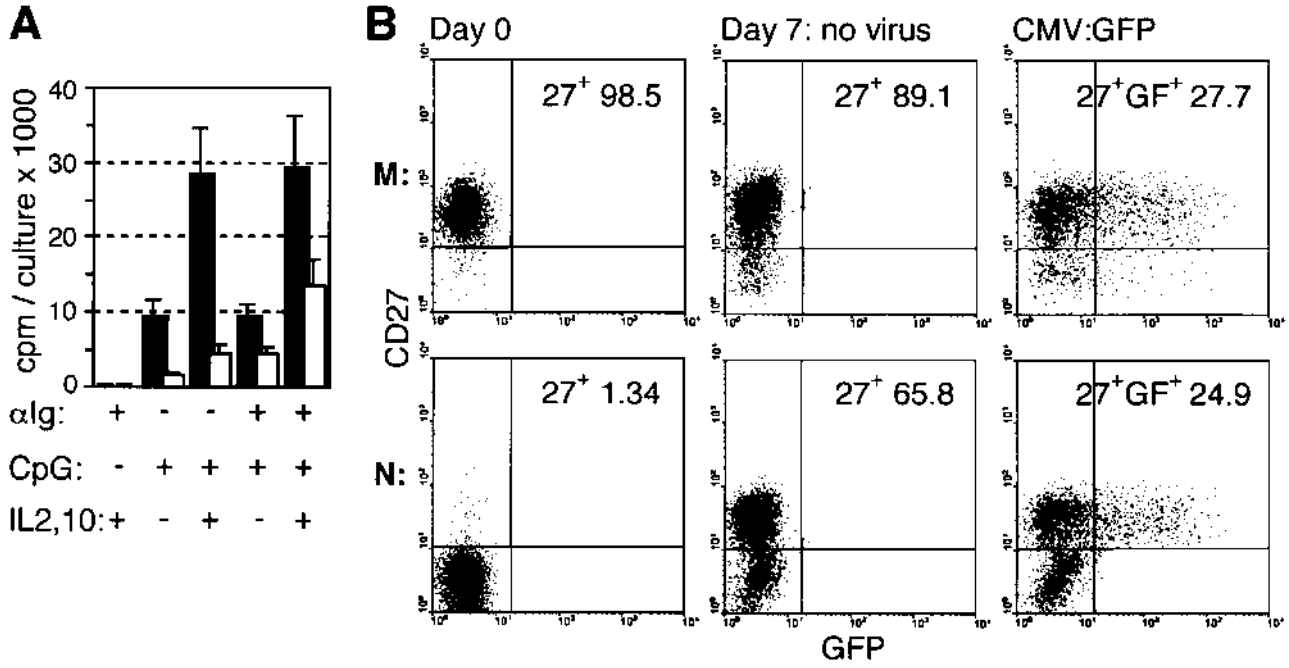

FIG. 3. Naive and memory B cells proliferated and were transducible in the CpG DNA system. (A) Anti-Ig antibody (αIg) enhanced thymidine incorporation by naive ($CD27^-$, white columns), but not by memory ($CD27^+$, black columns), B cells in the presence of CpG DNA, with or without IL-2 and IL-10 (means ± 1 SEM of counts per minute (cpm) from three independent experiments). (B) The 2-D plots show CD27 expression and FL1 fluorescence in sorted memory and naive B cells before (Day 0) and after culture in the CpG DNA system (Day 7), with no virus or with vector CMV:GFP added on day 3 an m.o.i. of 10. Percentages of $CD27^+$ cells (27^+) and of GFP^+ cells among the $CD27^+$ cells (27^+GF^+) are indicated (experiment representative for three independent experiments). Only those naive B cells that became $CD27^+$ were transduced.

aging construct with a loss-of-function mutant integrase or a vector plasmid (CMV:IL4-GFP) lacking the central polypurine tract (cPPT) involved in nuclear translocation [22]. We added control virus at an m.o.i. of 10 and the others, produced in parallel, at concentrations equalized for IL-4 concentrations in the 293T culture supernatant. Control vector gave 13.9% GFP^+ B cells (Fig. 4A) and an IL-4 release of 1.1 ng IL-4/10^5 B cells/24 h (Fig. 4B). The virus lacking integrase activity gave 0.87% GFP^+ cells, but no bright GFP^+ cells, i.e., this was weak PTD that occurs with GFP [9]. The IL-4 release was low, indicating that about 5% of the IL-4 release obtained with the positive control may have been due to PTD. The virus lacking the cPPT gave 1.92% GFP^+ cells, including about 1% bright cells. The IL-4 release (6.7-fold lower than control) was close to what one would expect for this number of bright GFP^+ cells plus PTD as estimated above. Thus, PTD played a negligible role.

Comparison of IL-4 Secretion by B Cells and $CD34^+$ Cells

We used $CD34^+$ cells as a reference for work with lentivectors. After transduction with the IL-4 vector with the EF-1α promoter, which is optimal in these cells [13], the GFP expression in $CD34^+$ cell-derived cultures (Fig. 5A; the upper histograms) was similar to that obtained in B cells with vector CMV:IL4-GFP. In $CD34^+$-derived cells, intracytoplasmic IL-4 was detectable by FACS and correlated with GFP expression among individual transduced cells (lower histograms in Fig. 5A). Although B cells do not produce IL-4 [23], a strong nonspecific staining by the anti-IL-4 antibody in transduced and nontransduced B cells made such detection impossible. IL-4 secretion was also similar in B cells and $CD34^+$-derived cells (Fig. 5B; about 1.2 ng IL-4/10^5 cells/24 h). In B cells, IL-4 secretion with the EF-1α promoter was 3.4-fold lower than with the CMV promoter. In FACS-sorted GFP^+ B cells, the IL-4 secretion increased in parallel with their enrichment (not shown). Thus, transducibility with bicistronic vector was similar for B and $CD34^+$ cells. That many B cells become secretory cells (plasma cells) was apparently not relevant for the cytokine secretion rate. However, a considerably lower cytokine secretion rate was reported for primary B leukemia cells transduced with a bicistronic HIV vector lacking the WPRE [24]. This element enhances mRNA stability [12].

GFP expression and IL-4 secretion were stable in B cells between days 3 and 8 after exposure to vector and in $CD34^+$-derived cells when followed up for 21 days. On day 8 after exposure to vectors with the respective optimal promoters, at an m.o.i. of 10, quantitative PCR revealed multiple copies of GFP DNA per diploid genome

doi:10.1016/j.ymthe.2005.05.010

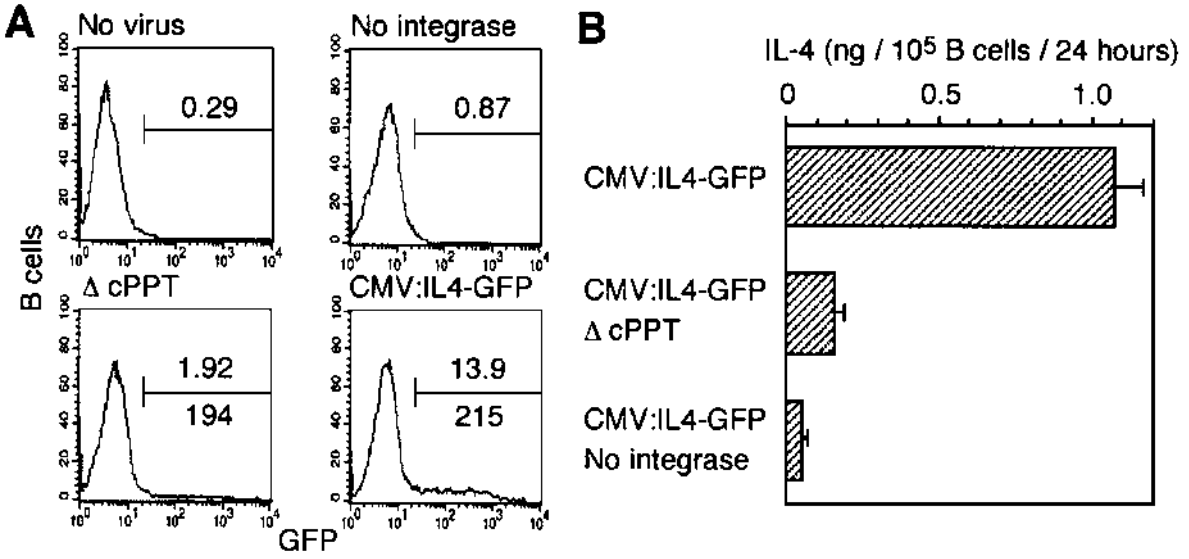

FIG. 4. Correlation between IL-4 secretion and GFP expression in B cells exposed to different vector particles: positive control vector (CMV:IL4-GFP), vector plasmid deleted of the cPPT element (Δ cPPT), and virus made using a packaging construct with an inactive mutant integrase (No integrase). (A) GFP expression. All three types of vector particles were produced in parallel. Control vector CMV:IL4-GFP was added at an m.o.i. of 10. The other vector particles were added at concentrations equalized for the amounts of IL-4 measured in the supernatants of the virus-producer cells. Upper and lower numbers represent percentages of GFP^+ cells and MFI, respectively. (B) IL-4 secretion rates measured in this representative experiment (means ± 1 SEM of triplicate cultures).

in $CD34^+$-derived GFP^+ cells (4.5 ± 0.3), as expected [25], and also in $CD19^+GFP^+$ B cells (4.8 ± 0.4; means ± 1 SEM, $n = 4$, i.e., two transduction experiments with mono- and two with bicistronic vectors for each cell type and for B cells one of each experiment in the CpG and B5 systems). We obtained overlapping results with mono- and bicistronic vectors. We found at least 10-fold lower PCR signals in GFP^- cells, showing low contamination by DNA plasmids. Since vector-derived episomal DNA is short-lived in various cells, including B cells [18], these

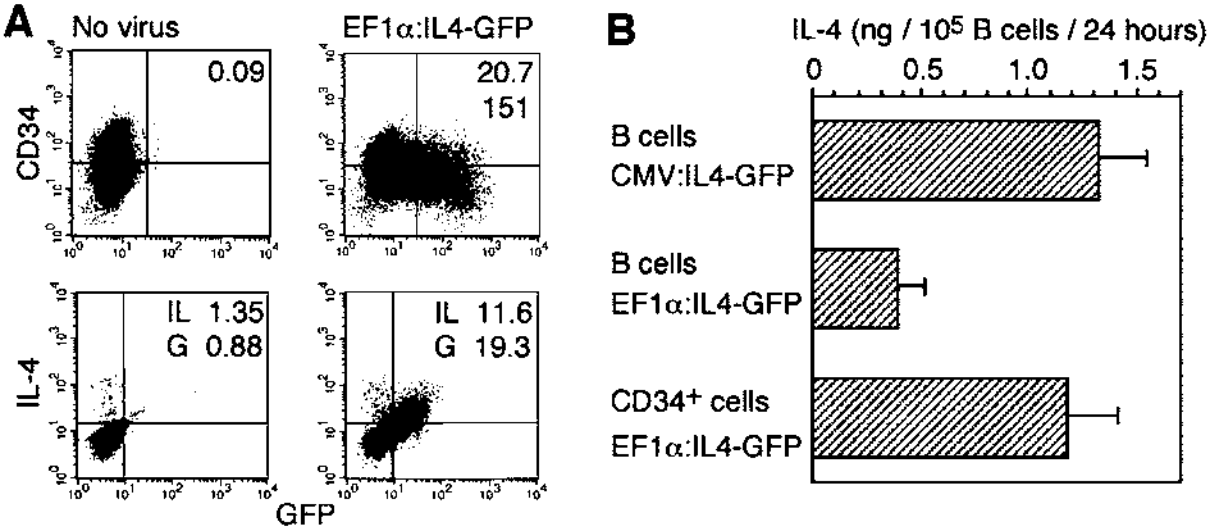

FIG. 5. GFP expression and IL-4 secretion by B cells transduced with vector CMV:IL4-GFP were similar to those found in cell cultures derived from cord blood $CD34^+$ cells transduced with vector EF1α:IL4-GFP. (A) The upper plots show GFP expression in cell culture derived from 97% pure cord blood $CD34^+$ cells from a representative experiment. EF1α:IL4-GFP was added on day 1 at an m.o.i. of 20; cells were analyzed on day 5. Upper and lower numbers represent percentages of GFP^+ cells and MFI, respectively. The lower plots show a staining with PE–anti-IL-4 mAb on the *y* axis and GFP fluorescence on the *x* axis on day 5. Percentages of cells stained by anti-IL-4 ("IL"),and of GFP^+ cells ("G") are indicated. (B) IL-4 secretion rates measured in B cells and $CD34^+$ cell-derived cultures transduced with the indicated vectors at an m.o.i. of 10 (means ± 1 SEM from six independent experiments).

data indicate multiple vector integration in both cell types.

Effects of Bicistronic Vector Expressing Viral FLIP

We then tested a bicistronic vector expressing FLAG-tagged vFLIP of molluscum contagiosum virus [15]. We added this vector (CMV:vFLIP-GFP) or control vector (CMV:GFP) to B cells in the CpG DNA system on day 2 and sorted GFP$^+$ cells on day 5 (Fig. 6A). We recultured the cells in the presence or absence of soluble FasL. In two experiments, transduction of vFLIP caused a 1.8- to 2.4-fold reduction in the number of FasL-induced annexin V$^+$ apoptotic cells after 20 h (without and with FasL, respectively, there were 32 ± 3.9 and 79 ± 5.6% annexin V$^+$ cells for control vector versus 35 ± 4.4 and 57 ± 1.5 for vFLIP vector). In three other experiments, we measured thymidine incorporation after 48 h to detect cell survival (Fig. 6B). Only 14 ± 4% of B cells transduced with control vector, but 63 ± 12% of B cells transduced with vFLIP vector, resisted killing by FasL. Thus, among those cells that could be killed by FasL, 57% (range 45 to 71%) were protected by vFLIP.

In B cells transduced in the EL-4 B5 system, intracellular vFLIP was detectable with anti-FLAG mAb by FACS and its expression correlated with GFP expression in individual cells (Fig. 6C). Viral FLIP was also detectable with this antibody by Western blot in sorted GFP$^+$, but not in GFP$^-$, B cells (Fig. 6D).

In conclusion, with an HIV-1-derived bicistronic vector we obtained proof of principle for the testing of

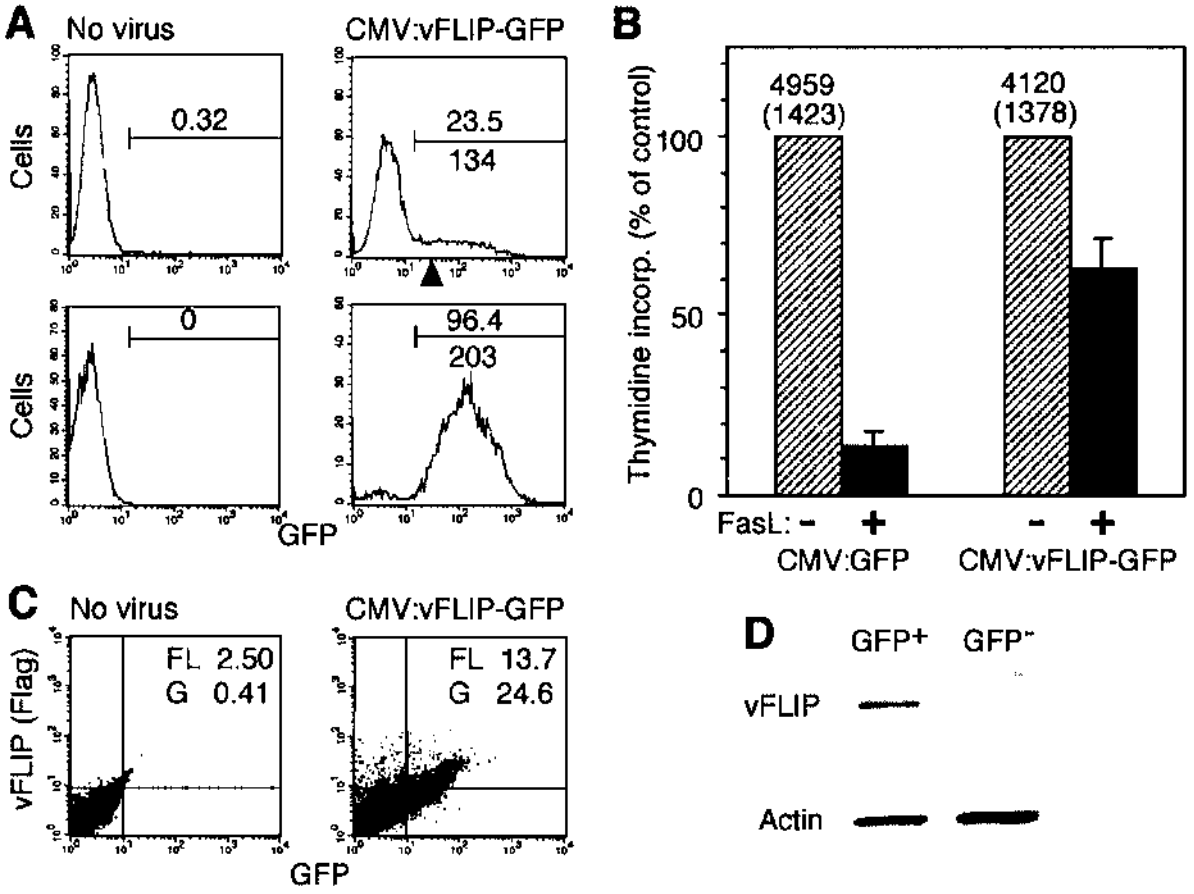

FIG. 6. Detection of viral FLIP protein and of protection from FasL-induced cell death in B cells transduced with vector CMV:vFLIP-GFP. (A) GFP expression in B cells transduced in the CpG DNA system with CMV:vFLIP-GFP at an m.o.i. of 10, before and after sorting of GFP$^+$ B cells. Upper and lower numbers represent percentages of GFP$^+$ cells and MFI, respectively. The gating for the FACS sorting is shown by the arrowhead. (B) Thymidine incorporation by sorted GFP$^+$ B cells transduced with CMV:vFLIP-GFP, or control vector CMV:GFP, after reculture in the presence or absence of FasL. The black columns represent percentages of counts per minute (cpm) relative to no-FasL controls (means ± 1 SEM from three independent experiments). Mean cpm in cultures with no FasL are indicated (SEM in parentheses). (C) Detection of intracellular viral FLIP with anti-FLAG mAb (*y* axis) and GFP fluorescence (*x* axis) in B cells transduced with CMV:vFLIP-GFP in the EL-4 B5 system. Vector was added on day 3 at an m.o.i. of 10 and cells were analyzed on day 8, after 46-fold cell expansion. Percentages of cells stained by anti-FLAG ("FL") and of GFP$^+$ cells ("G") are indicated. (D) Western blot of sorted GFP$^+$ and GFP$^-$ B (CD19$^+$) cells transduced as above in the EL-4 B5 system, performed with protein equivalents of 3×10^5 B cells. Stainings with anti-FLAG mAb or anti-actin antibodies are shown. Viral FLIP was detected as a band of 34 kDa.

doi:10.1016/j.ymthe.2005.05.010

a gene function in primary human B cells. The CpG DNA culture system should be useful for such studies.

MATERIALS AND METHODS

HIV-1-Derived Vectors

A second-generation packaging system and self-inactivating HIV-1 vectors [26] with the pLoxP site in the 3′LTR [27] were utilized. The monocistronic vector with the EF-1α internal promoter (called vector EF1α:GFP in this study) was plasmid pWPT-GFP for which the map and sequence are available at http://www.tronolab.unige.ch. This plasmid carries, in the 5′ to 3′ direction, the cPPT element [22], the intronless ("short") EF-1α promoter, the expression cassette, and the WPRE [12]. Vector CMV:GFP was made by replacing the promoter with the human CMV promoter [13] between the *Cla*I and the *Bam*HI restriction sites. In the bicistronic vectors, which were derived from the above vectors, the first cistron was the transgene of interest, between the *Bam*HI and the *Sal*I restriction sites, followed by the encephalomyocarditis virus IRES [27] and GFP encoded downstream of the IRES. In the vectors EF1α:IL4-GFP and CMV:IL4-GFP the transgene was the complete human IL-4 cDNA sequence (a kind gift from Dr. J.-F. Gauchat, formerly at the Institut Pierre Fabre, St. Julien, France). In vector CMV:vFLIP-GFP the transgene was the FLAG-tagged viral FLIP of human molluscum contagiosum virus (open reading frame 159L), kindly provided by Dr. Margot Thome of the Department of Biochemistry, University of Lausanne [15]. In some experiments we used a vector plasmid as above, except that it lacked the cPPT element, or a packaging construct [9] with a loss-of-function mutant integrase (mutation D64V) [28].

Virus particles pseudotyped with vesicular stomatitis virus G glycoprotein were produced, concentrated 100-fold by ultracentrifugation, and titrated on HeLa cells by measurement of GFP^+ cells by FACS to establish HeLa transducing units per milliliter (usually 0.5 to 2×10^8), as described [9]. Viral stocks were suspended in B cell culture medium and stored at −70°C.

Cell Cultures and Transduction

Approval for research on human cells was obtained from the Ethics Committee of the Geneva University Hospitals. Written consent was provided for all cell samples. B cells were isolated to more than 99% purity from buffy coats of virus-screened blood donations obtained from the Geneva Transfusion Center using Ficoll–Hypaque centrifugation and anti-CD19 magnetic beads (Dynal) [29]. All B cell cultures were grown in RPMI 1640 medium supplemented with 10% fetal calf serum, 2-mercaptoethanol, Hepes buffer, and antibiotics as described [29].

CpG DNA system. B cells (25,000 cells/200 μl culture; flat-bottom 96-well plates) were stimulated with CpG DNA (2.5 μg/ml), anti-Ig antibody (2 μg/ml), IL-2 (50 ng/ml), and IL-10 (10 ng/ml). CpG oligonucleotides of the published sequences C274, 2006, and C661 [16] were obtained as complete phosphorothioates synthesized to our order by Microsynth (Balgach, Switzerland). Anti-Ig was goat $F(ab')_2$ anti-human IgA + IgG + IgM (H+L) (Jackson ImmunoResearch). The cytokines were from PeproTech. FACS sorting of $CD27^+/CD27^-$ cells was done as described [29].

CD40L system. B cells (50,000 cells/200 μl) were stimulated with a soluble oligomeric CD40L (300 ng/ml), IL-2 (50 ng/ml), and IL-10 (10 ng/ml) as described [29]. When CD40L was added to the CpG DNA system or the EL-4 B5 system, its concentration was also 300 ng/ml.

EL-4 B5 system. B cells (3000 cells/200 μl) were stimulated with 50,000 irradiated EL-4 B5 murine thymoma cells and a mixture of human cytokines acting on the EL-4 B5 cells (IL-1β) or the B cells (TNF-α, IL-2, and IL-10), as described [9].

To transduce B cell cultures at different times, the big cell clusters, which formed in all culture systems, were dispersed by gentle pipetting (five times aspiration of the culture using 200-μl tips). Virus particles were then added to the cultures in a volume of 2 to 4 μl, at the indicated m.o.i. according to cell counts by microscope (B cells or B plus EL-4 B5 cells), without further manipulations or cell wash. We found that centrifugation of virus particles in new culture plates (spinoculation) with cell transfer did not give better results.

$CD34^+$ cell culture and transduction. Umbilical cord blood $CD34^+$ cells were isolated to >95% purity with anti-CD34 magnetic beads (Dynal), cultured, and transduced as described [13]. Briefly, the cells (10^5/200 μl) were first cultured and transduced on day 1 in the presence of thrombopoietin (TPO). After 48 h, the cells were recultured in Iscove's modified Dulbecco's medium supplemented with 10% fetal calf serum, antibiotics, TPO, Flt3-ligand, and stem cell factor; the cells were recultured every 6 days.

Sorting and FACS Analysis of Transduced Cells

Various GFP^+ cell populations were sorted on a FACStar sorter, and analyses of GFP^+ cells were performed on a FACScan analyzer using CellQuest software (Becton–Dickinson), at the cytofluorometry laboratory of the Geneva Medical Center. Cells were pretreated with polyclonal mouse Ig before staining with phycoerythrin (PE)-coupled anti-CD19 [9], anti-CD27 [29], or anti-CD34 [13] mAb, and viable (7-amino-actinomycin-D low) cells were gated for analysis of GFP expression [9]. For analysis of cytoplasmic IL-4, cells were cultured with brefeldin A (Sigma), 2.5 μg/ml, for 3 h. For analysis of cytoplasmic IL-4 or viral FLIP, cells were treated with Cytofix/Cytoperm and Perm/Wash solutions, followed by AB^+ serum, and then stained, respectively, with PE-coupled anti-IL-4 mAb (Pharmingen) or anti-FLAG-M2 mAb (Sigma), which we coupled to biotin, followed by PE-coupled streptavin (Jackson ImmunoResearch). The isotype control was mouse IgG1. Apoptosis was assessed using the Annexin V–PE Apoptosis Detection Kit I (Becton–Dickinson).

Other Analyses of Transduced Cells

IL-4 secretion rate. On day 2 or 3 after addition of viral particles, B cells or $CD34^+$ cells were harvested and washed twice in culture medium in Eppendorf tubes, and viable, trypan blue-excluding cells were counted. The cells were recultured as before, and after 24 h soluble IL-4 was measured in culture supernatants by Quantikine Human IL-4 Immunoassay (R&D Systems).

Real-time quantitative PCR. The LightCycler system, High Pure PCR Template Preparation Kit, and LightCycler FastStart DNA Master^{PLUS} SYBR Green I kit (all from Roche) were utilized. Cells were transduced with vectors treated with DNase I before ultracentrifugation [7]. PCR was performed in separate assays for genomic DNA, using intron-binding primers for β2-microglobulin (5′-GGCACTGCTGAGATACTGAT-3′, reverse 5′-GCTAGGACAGCAGGACTTA-3′; 215-bp product) and for vector DNA, using GFP primers (5′-GGCAAGCTGACCCTGAAGTT-3′, 5′-GCATGGCGGACTTGAAGAAGT-3′; 149-bp product); respective plasmid standards were utilized.

FasL assay. GFP^+ cells were sorted 3 days after exposure to vector and recultured (20,000 trypan blue-excluding cells/200 μl, triplicate cultures) in the CpG DNA system (without anti-Ig) in the presence of soluble oligomeric FasL (200 ng/ml) prepared as described [30]. Thymidine incorporation was measured after 48 h including the pulsing during the last 12 h [29] with 1 μCi (0.037 MBq) [*methyl*-^{3}H]thymidine (Amersham Pharmacia Biotech).

Western blot for viral FLIP. This was done with the ECL Western blotting analysis system (Amersham) using 0.45-μm nitrocellulose membranes (Bio-Rad) and Biomax chemiluminescence films (Kodak). The antibodies were IgG1 mouse anti-FLAG-M2 mAb (Sigma) or polyclonal goat IgG anti-actin (Santa Cruz Biotechnologies) in conjunction with horseradish peroxidase-coupled anti-mouse or anti-goat antibodies, respectively (Santa Cruz Biotechnologies).

ACKNOWLEDGMENTS

These studies were supported by grants from the Swiss National Science Foundation (to D.T. and R.Z.), the European Community, and the Institut Clayton pour la Recherche (to D.T.). K. Kvell is a member of the M.D.–Ph.D. Program of the University of Pécs, Hungary.

RECEIVED FOR PUBLICATION JANUARY 25, 2005; REVISED APRIL 13, 2005; ACCEPTED MAY 2, 2005.

REFERENCES

1. Somia, N., and Verma, I. M. (2000). Gene therapy: trials and tribulations. *Nat. Rev. Genet.* **1:** 91–99.
2. Basu, U., and Banerjee, S. (2004). An engineered EBV vector expressing human factor VIII and von Willebrand factor in cultured B cells. *J. Gene Med.* **6:** 760–768.
3. Ballantyne, J., *et al.* (1998). Efficient recombination of a switch substrate retrovector in CD40-activated B lymphocytes: implications for the control of CH gene switch recombination. *J. Immunol.* **161:** 1336–1337.
4. Zufferey, R., *et al.* (1997). Multiply attenuated lentiviral vector achieves efficient gene delivery in vivo. *Nat. Biotechnol.* **15:** 871–875.
5. Unutmaz, D., *et al.* (1999). Cytokine signals are sufficient for HIV-1-infection of resting human T lymphocytes. *J. Exp. Med.* **189:** 1735–1746.
6. Ducrey-Rundquist, O., Guyader, M., and Trono, D. (2002). Modalities of interleukin-7-induced human immunodeficiency virus permissiveness in quiescent T lymphocytes. *J. Virol.* **76:** 9103–9111.
7. Moreau, T., Bardin, F., Imbert, J., Chabannon, C., and Tonnelle, C. (2004). Restriction of a transgene expression to the B-lymphoid progeny of human lentivirally transduced $CD34^+$ cells. *Mol. Ther.* **10:** 45–56.
8. Janssens, W., *et al.* (2003). Efficiency of onco-retroviral and lentiviral gene transfer into primary mouse and human B-lymphocytes is pseudotype dependent. *Hum. Gene Ther.* **14:** 263–276.
9. Bovia, F., *et al.* (2003). Efficient transduction of primary human B lymphocytes and nondividing myeloma B cells with HIV-1-derived lentiviral vectors. *Blood* **101:** 1727–1733.
10. Bernasconi, N. L., Onai, N., and Lanzavecchia, A. (2003). A role for Toll-like receptors in acquired immunity: up-regulation of TLR9 by BCR triggering in naïve B cells and constitutive expression in memory B cells. *Blood* **101:** 4500–4504.
11. Bourke, E., *et al.* (2003). The toll-like receptor repertoire of human B lymphocytes: inducible and selective expression of TLR9 and TLR10 in normal and transformed cells. *Blood* **102:** 956–963.
12. Zufferey, R., Donello, J. E., Trono, D., and Hope, T. J. (1999). Woodchuck hepatitis virus posttranscriptional regulatory element enhances expression of transgenes delivered by retroviral vectors. *J. Virol.* **73:** 2886–2892.
13. Salmon, P., *et al.* (2000). High-level transgene expression in human hematopoietic progenitors and differentiated blood lineages after transduction with improved lentiviral vectors. *Blood* **96:** 3392–3398.
14. Schomber, T., Kalberer, C. P., Wodnar-Filipowicz, A., and Skoda, R. C. (2004). Gene silencing by lentivirus-mediated delivery of siRNA in human $CD34^+$ cells. *Blood* **103:** 4511–4513.
15. Thome, M., *et al.* (1997). Viral FLICE-inhibitory proteins (FLIPs) prevent apoptosis induced by death receptors. *Nature* **386:** 517–521.
16. Marshall, J. D., *et al.* (2003). Identification of a novel CpG DNA class and motif that optimally stimulate B cell and plasmocytoid dendritic cell functions. *J. Leucocyte Biol.* **73:** 781–792.
17. Grimaître, M., Werner-Favre, C., Kindler, V., and Zubler, R. H. (1997). Human naive B cells cultured with EL-4 T cells mimic a germinal center-related B cell stage: concordant changes in Bcl-2 protein and messenger RNA levels. *Eur. J. Immunol.* **27:** 199–205.
18. Serafini, M., Naldini, L., and Introna, M. (2004). Molecular evidence of inefficient transduction of proliferating human B lymphocytes by VSV-pseudotyped HIV-1-derived lentivectors. *Virology* **325:** 413–424.
19. Bieniasz, P. D. (2004). Intrinsic immunity: a front-line defense against viral attack. *Nat. Immunol.* **5:** 1109–1115.
20. Turelli, P., and Trono, D. (2005). Editing at the crossroads of innate and adaptive immunity. *Science* **307:** 1061–1065.
21. Lens, S. M. A., Tesselaar, K., van Oers, M. H. J., and van Lier, R. A. W. (1998). Control of lymphocyte function through CD27–CD70 interactions. *Semin. Immunol.* **10:** 491–499.
22. Zennou, V., Petit, C., Guetard, D., Nehrbass, U., Mantagnier, L., and Charneau, P. (2000). HIV-1 genome nuclear import is mediated by a central DNA flap. *Cell* **101:** 173–185.
23. Matthes, T., *et al.* (1993). Cytokine mRNA expression during an in vitro response of human B lymphocytes: kinetics of B cell tumor necrosis factor α, interleukin (IL) 6, IL-10 and transforming growth factor β1 mRNAs. *J. Exp. Med.* **178:** 512–528.
24. Stripecke, R., *et al.* (2000). Lentiviral vectors for efficient delivery of CD80 and granulocyte–macrophage-colony-stimulating factor in human acute lymphoblastic leukemia and acute myeloid leukemia cells to induce antileukemic immune responses. *Blood* **96:** 1317–1326.
25. Woods, N. B., *et al.* (2003). Lentiviral vector transduction of NOD/SCID repopulating cells results in multiple vector integrations per transduced cell: risk of insertional mutagenesis. *Blood* **101:** 1284–1289.
26. Zufferey, R., *et al.* (1998). Self-inactivating lentivirus vector for safe and efficient in vivo gene delivery. *J. Virol.* **72:** 9873–9880.
27. Salmon, P., *et al.* (2000). Reversible immortalization of human primary cells by lentivector-mediated transfer of specific genes. *Mol. Ther.* **2:** 404–414.
28. Leavitt, A. D., Robles, G., Alesandro, N., and Varmus, H. E. (1996). Human immunodeficiency virus type 1 integrase mutants retain in vitro integrase activity yet fail to integrate viral DNA efficiently during infection. *J. Virol.* **70:** 721–728.
29. Werner-Favre, C., *et al.* (2001). IgG subclass-switch capacity is low in switched and in IgM-only, but high in IgD^+IgM^+, post-germinal center ($CD27^+$) human B cells. *Eur. J. Immunol.* **31:** 243–249.
30. Holler, N., *et al.* (2003). Two adjacent trimeric Fas ligands are required for Fas signaling and formation of a death-inducing signaling complex. *Mol. Cell. Biol.* **23:** 1428–1440.

frontiers in Immunology

ORIGINAL RESEARCH
published: 06 November 2017
doi: 10.3389/fimmu.2017.01515

PPARgamma Deficiency Counteracts Thymic Senescence

*David Ernszt[1,2], Krisztina Banfai[1,2], Zoltan Kellermayer[3], Attila Pap[4], Janet M. Lord[5], Judit E. Pongracz[1,2] and Krisztian Kvell[1,2]**

[1] Faculty of Pharmacy, Department of Pharmaceutical Biotechnology, University of Pecs, Pecs, Hungary, [2] Szentagothai Research Center, University of Pecs, Pecs, Hungary, [3] Faculty of Medicine, Department of Immunology and Biotechnology, University of Pecs, Pecs, Hungary, [4] Faculty of Medicine, Department of Biochemistry and Molecular Biology, University of Debrecen, Debrecen, Hungary, [5] College of Medical and Dental Sciences, Institute of Inflammation and Aging, University of Birmingham, Birmingham, United Kingdom

Thymic senescence contributes to increased incidence of infection, cancer and autoimmunity at senior ages. This process manifests as adipose involution. As with other adipose tissues, thymic adipose involution is also controlled by PPARgamma. This is supported by observations reporting that systemic PPARgamma activation accelerates thymic adipose involution. Therefore, we hypothesized that decreased PPARgamma activity could prevent thymic adipose involution, although it may trigger metabolic adverse effects. We have confirmed that both human and murine thymic sections show marked staining for PPARgamma at senior ages. We have also tested the thymic lobes of PPARgamma haplo-insufficient and null mice. Supporting our working hypothesis both adult PPARgamma haplo-insufficient and null mice show delayed thymic senescence by thymus histology, thymocyte mouse T-cell recombination excision circle qPCR and peripheral blood naive T-cell ratio by flow-cytometry. Delayed senescence showed dose–response with respect to PPARgamma deficiency. Functional immune parameters were also evaluated at senior ages in PPARgamma haplo-insufficient mice (null mice do not reach senior ages due to metabolic adverse affects). As expected, sustained and elevated T-cell production conferred oral tolerance and enhanced vaccination efficiency in senior PPARgamma haplo-insufficient, but not in senior wild-type littermates according to ELISA IgG measurements. Of note, humans also show increased oral intolerance issues and decreased protection by vaccines at senior ages. Moreover, PPARgamma haplo-insufficiency also exists in human known as a rare disease (FPLD3) causing metabolic adverse effects, similar to the mouse. When compared to age- and metabolic disorder-matched other patient samples (FPLD2 not affecting PPARgamma activity), FPLD3 patients showed increased human Trec (hTrec) values by qPCR (within healthy human range) suggesting delayed thymic senescence, in accordance with mouse results and supporting our working hypothesis. In summary, our experiments prove that systemic decrease of PPARgamma activity prevents thymic senescence, albeit with metabolic drawbacks. However, thymic tissue-specific PPARgamma antagonism would likely solve the issue.

Keywords: PPARgamma, thymus, immunity, senescence, rejuvenation

OPEN ACCESS

Edited by:
Duncan Howie, University of Oxford, United Kingdom

Reviewed by:
Susan Mariola Schlenner, KU Leuven, Belgium
Juei-Tang Cheng, Chang Jung Christian University, Taiwan

****Correspondence:***
Krisztian Kvell
kvell.krisztian@pte.hu

Specialty section:
This article was submitted to Immunological Tolerance and Regulation, a section of the journal Frontiers in Immunology

Received: *28 July 2017*
Accepted: *26 October 2017*
Published: *06 November 2017*

Citation:
Ernszt D, Banfai K, Kellermayer Z, Pap A, Lord JM, Pongracz JE and Kvell K (2017) PPARgamma Deficiency Counteracts Thymic Senescence. Front. Immunol. 8:1515. doi: 10.3389/fimmu.2017.01515

INTRODUCTION

The peroxisome proliferator-activated receptor (PPAR) molecular family is widely studied (1–3). These nuclear receptor proteins possess transcription factor activities and influence multiple cellular events at the molecular level including adipocyte differentiation and metabolism. Among them, PPARgamma is of particular interest being expressed by all adipose tissue subtypes and being indispensable for adipose tissue development and for the homeostasis of physiological metabolism (4–7). As a consequence, in the mouse systemic loss of PPARgamma activity severely impairs glucose and lipid metabolism as characterized by others (8–10). In accordance, PPARgamma null mice are only viable if using conditional knockout strategy (11). Similar to the mouse above, in human PPARgamma haplo-insufficiency leads to the development of a rare metabolic condition known as familial partial lipodystrophy, type 3 (FPLD3, ORPHA 79083) also characterized by diabetes and dyslipidemia (12–15).

In mammals, systemic PPARgamma activity may be increased at multiple levels. Environmental factors including excessive caloric consumption or corticosteroid exposure increase PPARgamma activity systemically (16–18). Pharmacological systemic activation may be achieved through administration of thiazolidinediones previously used as part of oral antidiabetic treatment, but currently neglected due to adverse cardiovascular side effects (19, 20). Genetic engineering-based enhancement of PPARgamma activity in mouse models has also been performed (21). In every case, increased PPARgamma activity promotes adipose tissue development at multiple sites of the body.

Thymic aging is observed as adipose involution during which the functional thymus niche that normally supports T-cell production is gradually lost and replaced by adipose tissue (22). The process starts focally in childhood then spreads and accelerates with puberty due to hormonal changes (23). Diminishing T-cell production results in decreased availability of fresh naive T-cells (24). Consequences include increasing incidence of infection, cancer and autoimmunity observed at senior ages (25, 26). Thymic adipose involution appears to be PPARgamma-dependent: any condition that systemically enhances PPARgamma activity—either environmental, pharmacological, or genetic—accelerates thymic senescence or adipose involution with all its immunological consequences (27–32). However, the opposite phenomenon whether systemically decreased PPARgamma activity can ameliorate long-term functional immune parameters has barely been addressed (33, 34). For this reason, we have set out to characterize the effect of systemic genetic PPARgamma loss of function on long-term immune homeostasis in both mouse and human.

MATERIALS AND METHODS

Human Thymus Samples

Formalin-fixed, paraffin-embedded (FFPE) human thymus samples from age groups 30–40, 50–60, and 70–80 years were obtained from the Department of Pathology (Faculty of Medicine, University of Pecs, Hungary.) Experiments involving human thymus samples were performed with the consent of the Regional and Local Ethics Committee of Clinical Centre, University of Pecs (ref. no.: 6331/2016) according to their guidelines. All subjects gave written informed consent in accordance with the Declaration of Helsinki.

Human Immunohistochemistry

Human thymus lobes were fixed in paraformaldehyde (4% PFA in PBS) then paraffin embedded. 5 μm thick sections were stained using immunohistochemistry (35). First, the slides were rinsed in heated xylene and were washed with a descending series of alcohol to remove paraffin. After deparaffination the slides were rehydrated in distilled water and antigen retrieval was performed by heating the slides in Target Retrieval Solution (pH 6 DAKO) at 97°C for 20–30 min. Subsequently slides were washed in dH_2O and endogenous peroxidase activity was blocked with 3% H_2O_2 containing TBS (pH 7.4) for 15 min. Then slides were washed three times with TBS containing Tween (0.05%, pH 7.4). Pre-blocking was carried out with 3% BSA in TBS for 20 min before overnight incubation with anti-PPARgamma (1:100, rabbit monoclonal antibody clone: C26H12 Cell Signalling Technology) primary antibody at 4°C. Following incubation slides were washed with TBS for three times then incubated with peroxidase conjugated secondary antibody (1:100, Polyclonal Goat Anti-Rabbit IgG, DAKO) for 90 min. Antibody labeling was visualized with the help of liquid DAB Substrate Chromogen System (DAKO). For nuclear counterstaining, hematoxylin staining was performed. Finally, slides were mounted with Faramount Aqueous Mounting Medium (DAKO). Histological evaluation was performed with the help of Panoramic MIDI digital slide scanner (3DHistech). Image analysis was performed using ImageJ software with IHC toolbox plug-in.

Mouse Breeding and Maintenance

For certain experiments, we have used wild-type and PPARgamma heterozygous (haplo-insufficient) or PPARgamma null (KO) mice of C57BL/6J genetic background. The mice were age matched, and both genders were used for the investigation. The design to generate PPARgamma KO mice was described previously (11). Briefly, PPARgamma$^{+/-}$/Sox2Cre^{+} male mice were crossed with PPARgamma fl/fl female mice to generate heterozygous PPARgamm$^{afl/-}$/Sox2Cre^{-} and homozygous PPAR gamma$\Delta^{fl/-}$/Sox2Cre^{+} mice, wherein the floxed allele was recombined resulting a null allele. Mice were housed under minimal disease conditions in the Laboratory Animal Core Facility of University of Debrecen. Animal rooms were ventilated 15 times/h with filtered air, mice received autoclaved pellet diet (Altromin VRF1) and tap water *ad libitum*. The cages contained sterilized bedding. Room lightning was automated with 12 h light and 12 h dark periods. The room temperature was 21 ± 2°C, the relative humidity is between 30 and 60%. Senescent animals developed and aged normally, without any treatment. Permission to perform the described animal experiments was granted to the relevant utilities of the University of Pecs (ref. no.: BA02/2000-46/2016). Permission to generate PPARgamma GM mice was granted to the relevant utilities of the University of Debrecen (ref. no.: TMF/82-10/2015). Permission to perform experimental procedures with PPARgamma GM mice was granted to the relevant utilities of the University of Pecs (ref. no.: TMF/124-11/2017).

Mouse Immunofluorescence

Immunofluorescent staining was performed on 8 μm cryosections of mouse thymus lobes as described previously (35). Briefly, the slides were fixed in cold acetone, then dried and blocked to prevent non-specific staining using 5% BSA in PBS for 20 min before staining with fluorochrome-conjugated or primary antibodies: anti-EpCAM1-FITC (1:100, rat monoclonal antibody clone: G8.8), anti-Ly51-PE (1:100, rat monoclonal antibody clone: 6C3, eBioscience), and anti-PPARgamma (rabbit monoclonal antibody clone: C26H12 Cell Signaling Technology). For secondary antibody, Alexa-555 conjugated a-rabbit goat IgG (1:200, Life Technologies) was used. In certain cases, DAPI (Life Technologies) nuclear counterstain was also applied. Sections were analyzed using a Nikon Eclipse Ti-U microscope equipped with a CCD camera (Andor Zyla 5.5) and NIS-Elements software. The medulla/cortex ratio was calculated using ImageJ software.

Mouse Flow Cytometry

Thymocyte subsets and T-cell subpopulations in blood were investigated by flow-cytometry as published by others (36, 37). Thymocytes and PBMC were isolated from mice and labeled with fluorophore-conjugated antibodies in PBS-BSA (5% BSA diluted in PBS). In every case, 100,000 cells were stained for measurement. Incubation with antibodies was performed at 4°C for 60 min followed by a washing step. FACSCanto II flow-cytometer and FACSDiva software (Becton Dickinson) were used for analysis. In every case, 10,000 events (parent R1 morphological lymphocyte gate) were recorded by flow-cytometry. For thymocyte subset measurement, Alexa-647 conjugated antimouse CD4 (clone: YTS 191) and FITC-conjugated antimouse CD8 (clone: IBL 3/25) antibodies were used (both produced in the Department of Immunology and Biotechnology, University of Pecs, Hungary). For peripheral blood T-cell subpopulation analysis, Pacific Blue-conjugated antimouse CD3 (clone: 17A2), PerCP-conjugated antimouse CD4 (clone: GK1.5), APC/Cy7-conjugated antimouse CD8 (clone: YTS156.7.7), PE-conjugated antimouse CD44 (clone: IM7), APC-conjugated antimouse CD62L (clone: MEL-14) (all purchased form BioLegend), and FITC-conjugated antimouse CD19 (clone: 1D3, produced by the Department of Immunology and Biotechnology, University of Pecs, Hungary) were used.

T-Cell Recombination Excision Circle (TREC) Measurement by Digital qPCR in Mouse and Human

T-cell recombination excision circle by-products of gene-rearrangement in fresh naive T-cells were also assessed. We performed mouse Trec (mTrec) digital qPCR using mouse and human Trec (hTrec) digital qPCR using human samples by adapting methods published by others (38). Briefly, DNA was isolated from mouse thymocytes using the NucleoSpin Tissue kit (Macherey-Nagel) according to the manufacturer's instruction. For human, peripheral-blood samples were processed using the DNA Blood Mini kit (Qiagen) following the manufacturer's guides. Absolute copy numbers were measured by digital PCR on the QuantStudio 3D Digital PCR platform (ThermoFisher) using 30 ng DNA per sample. Taqman primers/probes and digital qPCR reagents were also purchased from ThermoFisher and used as suggested. For age-matched range of healthy human hTrec values, refer to the work of Lynch et al. (38). Permission to perform the described animal experiments was granted to the relevant utilities of the University of Pecs (ref. no.: BA02/2000-46/2016). Experiments involving human blood samples were performed with the consent of the Regional and Local Ethics Committee of Clinical Centre, University or Pecs (ref. no.: 6439/2016) according to their guidelines.

Oral Tolerance Induction in Mouse

Induction and evaluation of oral tolerance was performed as described by others (39–41). Briefly, both wild-type and PPARgamma haplo-insufficient mice received 5 mg/ml ovalbumin (OVA, Sigma-Aldrich) in drinking water for seven days. On day 7, mice were challenged with an intraperitoneal injection of 5 μg ovalbumin in 200 μl of 1:1 of PBS:complete Freund adjuvant. On day 14, mice received an intraperitoneal injection of 5 μg ovalbumin in 200 μl of 1:1 of PBS:incomplete Freund adjuvant. Serum was collected on day 21 and anti-OVA IgG antibodies were measured by ELISA. Briefly, 96-well Microtest Plates (Sarstedt) were coated with OVA and blocked with BSA. Then plates were incubated with serial dilutions of mouse serum samples (1:100–1:3,200). The antibody content was visualized with the help of HRP-conjugated antimouse immunoglobulin antibody (rabbit polyclonal, Dako). Optical density was measured at 492 nm with iEMS Reader MF equipment (Thermo Labsystems).

Influenza Vaccination in Mouse

The efficiency of influenza vaccination was investigated as described elsewhere (42). Briefly, both wild-type and PPARgamma haplo-insufficient mice were injected intramuscular once with 0.1 ml human seasonal influenza vaccine cocktail (3Fluart) to mimic human vaccination at 9 months of age. In order to imitate human exposure pattern serum antibody IgG titer against H1N1 A/California/7/2009 strain (part of 3Fluart) was measured by ELISA three months after initial single vaccination at 12 months of age. For detection, ELISA plates were coated with 0.05 μg HA protein of influenza strain A (Recombinant subtype H1N1 A/California/7/2009 His Tag, Life Technologies). Then plates were incubated with serial dilutions of mouse serum samples (1:5–1:1,600). The antibody content was visualized with the help of HRP conjugated a-mouse immunoglobulin antibody (rabbit polyclonal, Dako). Optical density was measured at 492 nm with iEMS Reader MF equipment (Thermo Labsystems).

Statistical Analysis

All experiments were performed at least on three occasions, representative experiments are shown. Measures were obtained in triplicates, data are presented as mean and +SD as error bars. Graphpad Prism software was used for statistical analysis. Two-tailed Student's *t*-test was applied. Significant differences are shown by asterisks (ns for not significant, * for $p \leq 0.05$, ** for $p \leq 0.01$, *** for $p \leq 0.001$).

RESULTS

PPARgamma Distorts the Ratio of Thymic Epithelial Compartments with Age

Previously reported mouse results showed increasing PPARgamma expression with age in the thymic epithelial compartments, accompanied by thymic adipose involution. We have set out to prove human relevance of previous mouse findings and test whether PPARgamma activity influences the ratio of thymic epithelial compartments.

PPARgamma Expression Increases in the Adult Thymus with Age

Human FFPE thymic sections were analyzed for their PPARgamma expression in several adult age groups from young through middle-aged to senior (**Figures 1A–D**). Our results indicate that PPARgamma expression significantly and progressively increases with age (**Figures 1A–C**). Of note, total cellular areas shrink at senior ages in both human (**Figure 1C**) and mouse (**Figure 1F**). As a result the ratio of PPARgamma-expressing cellular areas shows relative increase with age (**Figure 1D**). Immunofluorescent staining of mouse thymic cryosections at 15 months of age (**Figure 1F**) provides visual support for thymic epithelial to adipose transdifferentiation in harmony with the working hypothesis of cellular transdifferentiation. A portion of stromal cells shows dual staining for epithelial identity and adipose differentiation, a hallmark of thymic adipose involution. This phenomenon is not observed at young adult age (**Figure 1E**).

PPARgamma Skews the Ratio of Epithelial Compartments with Age

Mouse thymic cryosections were differentially stained for medullary and cortical epithelial compartments at several ages

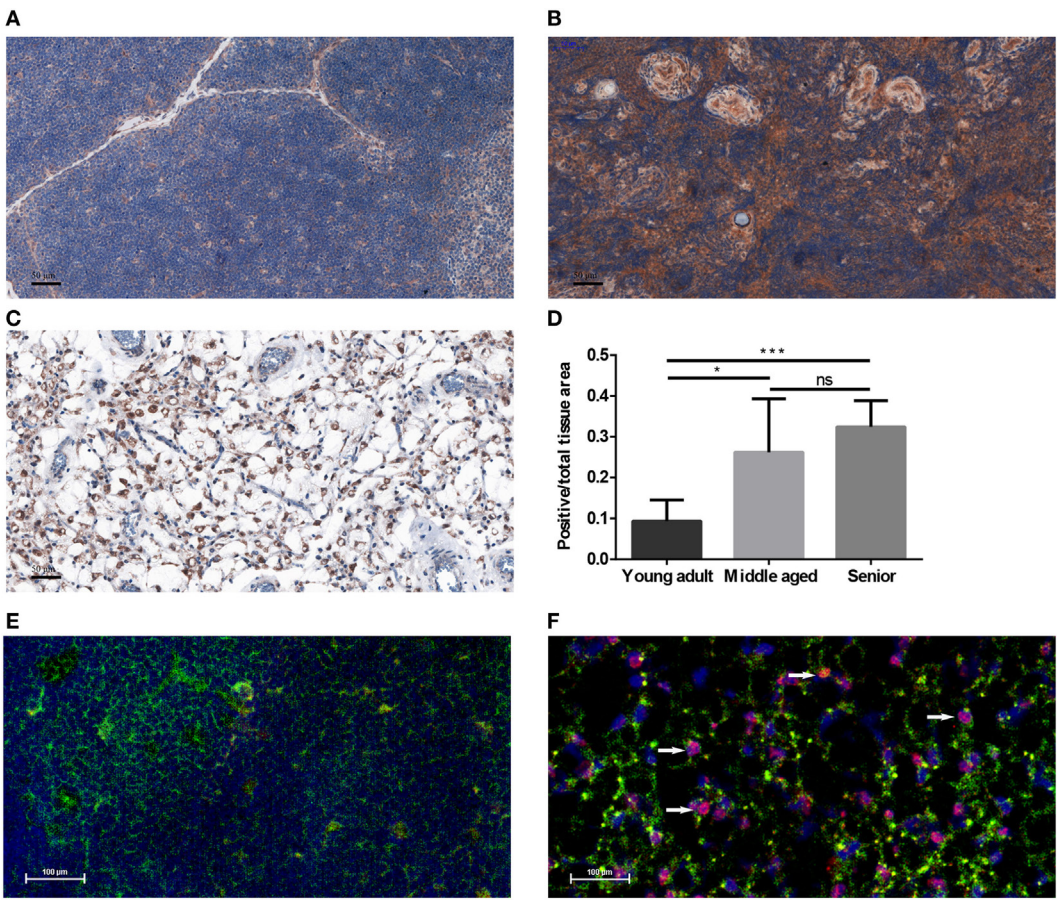

FIGURE 1 | PPARgamma expression in the adult thymus. Human formalin-fixed, paraffin-embedded (FFPE) thymic sections were analyzed for PPARgamma expression by immunohistochemistry in age groups of 20–30 years called young adult **(A)**, 50–60 years called middle-aged **(B)**, and 70–80 years called senior **(C)**. Brown color reaction (DAB) shows PPARgamma expression. Blue color (hematoxylin) shows nuclear counter-stain and defines total cellular areas. The ratio of PPARgamma-expressing cellular areas and total cellular areas is also shown for the different age groups **(D)**. Immunofluorescent staining is also shown for mouse at 1 month of age called young adult and at 15 months of age called senior **(E,F)**. Green color shows epithelial cells (anti-EpCAM1-FITC), red color shows preadipocytes (anti-PPARgamma primary AB with Alexa-555 secondary AB) and blue color defines nuclei (DAPI counter-stain). Note arrowheads pointing at double-staining (EpCAM-1$^+$/PPARgamma$^+$) cells **(F)**. Both stainings show expected patterns: EpCAM-1 staining presents cell surface markers, while PPARgamma-staining shows nuclear localization (observed in magenta color due to overlap with DAPI nuclear counterstain on **Figure 1F**). For exact numerical data, refer to Supplementary Material. Significant differences are shown by asterisks (ns for not significant, * for $p \leq 0.05$, ** for $p \leq 0.01$, *** for $p \leq 0.001$).

and using various genetic backgrounds (**Figures 2A–D**). Our results show that in the wild-type setting the medullary epithelial compartment significantly shrinks with age as reported previously (31). This, however, is not observed in PPARgamma deficient settings. Loss of PPARgamma activity shows protection in a progressive manner presenting dose–response (**Figure 2E**). PPARgamma deficiency efficiently and significantly prevents the erosion of the medullary epithelial compartment, otherwise prone to shrink with senescence.

PPARgamma Affects Thymic T-Cell Production and Peripheral Blood T-Cell Distribution with Age

We have observed changes in thymus architecture in response to PPARgamma status. Consequently, we were interested in whether morphological changes alter thymus function: naive T-cell production. Going beyond, we were eager to see if sustained influence of PPARgamma status on thymocyte function is also reflected in the peripheral blood.

PPARgamma Disturbs Thymic T-Cell Output with Age

Age-related changes in thymocyte levels of mTrec (DNA loop by-product of mouse T-cell receptor gene rearrangement) were evaluated in wild-type and PPARgamma deficient settings using digital qPCR (**Figure 3A**). Our results indicate slight (though not significant) decrease of mTrec and hence fresh-naive T-cell output with age in thymocytes of wild-type mice. PPARgamma deficiency significantly and progressively counteracts the process also showing dose-responsive increase of thymocyte mTrec levels. In further analyses, the percent distribution of thymocyte

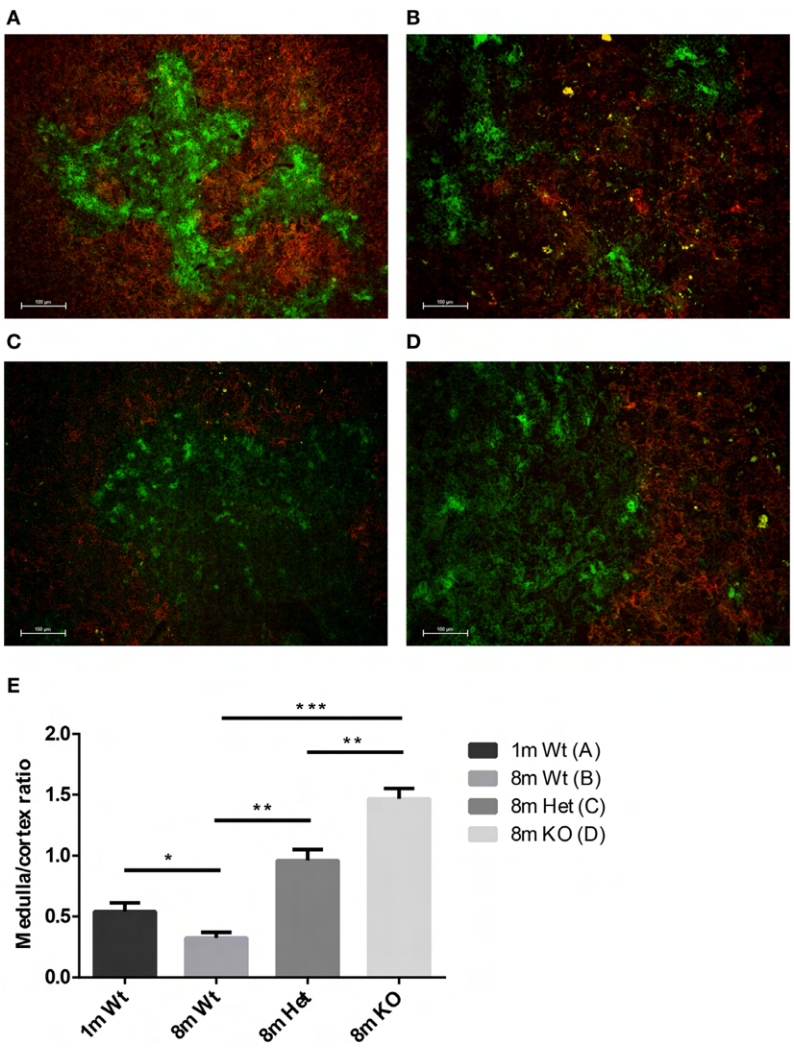

FIGURE 2 | Ratio of epithelial compartments in the adult thymus. Mouse thymic cryosections were stained differentially for medullary (anti-EpCAM1-FITC^{++}, anti-Ly51-PE^{-}) and cortical (anti-Ly51-PE^{++}, anti-EpCAM1-FITC^{+}) epithelial compartments. Wild-type thymus is shown at 1 month **(A)** and 8 months of age **(B)**. PPARgamma heterozygous **(C)** and PPARgamma KO **(D)** animals are shown at 8 months of age. The ratio of medullary and cortical epithelial compartment is also shown **(E)** for both ages and genetic backgrounds. For exact numerical data, refer to Supplementary Material. Significant differences are shown by asterisks (ns for not significant, * for $p \leq 0.05$, ** for $p \leq 0.01$, *** for $p \leq 0.001$).

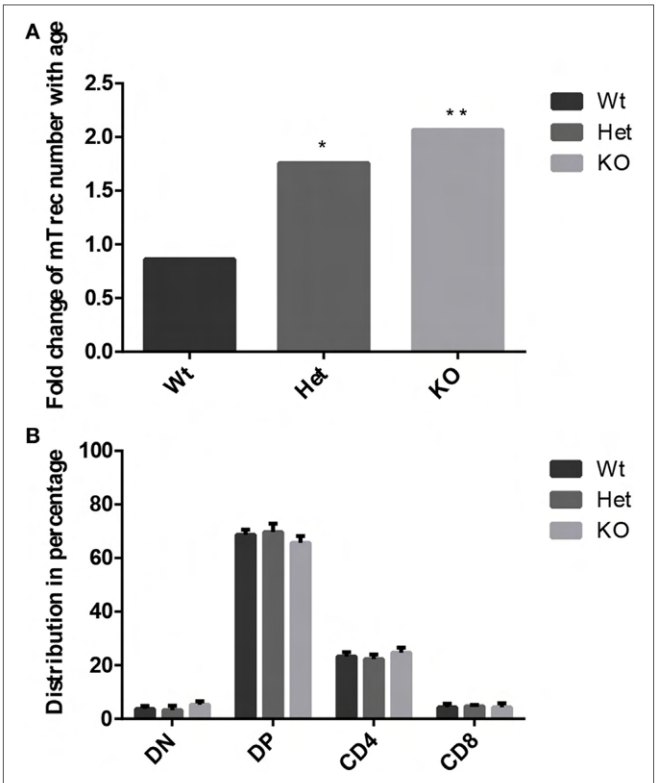

FIGURE 3 | Thymocyte development in the adult thymus. Changes in level of mouse T-cell recombination excision circles (mTrecs) was evaluated by Taqman digital qPCR in wild-type, PPARgamma heterozygous, and PPARgamma KO thymocytes **(A)**. The columns represent mTrec values measured at 8 months divided by those measured at 1 month for every strain. The ratio of thymocyte subpopulations was assessed by flow-cytometry at 8 months of age in wild-type, PPARgamma heterozygous and PPARgamma KO animals **(B)**. Double negative ($CD4^-$, $CD8^-$), double positive ($CD4^+$, $CD8^+$), and single positive ($CD4^+$ or $CD8^+$) subpopulations are shown. For the measurement of every sample, 100,000 cells were stained and 10,000 events (parent R1 morphological lymphocyte gate) were recorded by flow-cytometry. For exact cell numbers, refer to Supplementary Material. Significant differences are shown by asterisks (ns for not significant, * for $p \leq 0.05$, ** for $p \leq 0.01$, *** for $p \leq 0.001$).

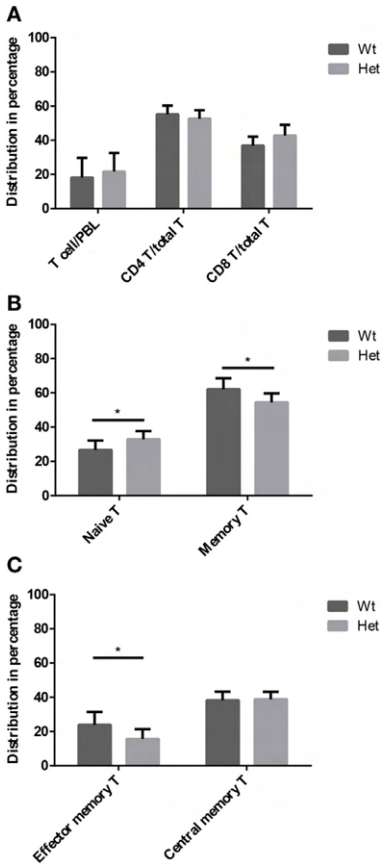

FIGURE 4 | T-cell subpopulations in adult peripheral blood. Peripheral blood T-cell subpopulations were evaluated by flow-cytometry at 12 months of age in wild-type and PPARgamma heterozygous animals (KO animals decease by this age). Percent distribution of T-cells ($CD3^+$), helper T-cells ($CD3^+$, $CD4^+$), and cytotoxic T-cells ($CD3^+$, $CD8^+$) is shown by **(A)**. Also, the percent distribution of naive T-cells ($CD3^+$, $CD44^-$, $CD62L^+$) and memory T-cells ($CD3^+$, $CD44^+$, $CD62L^{+/-}$) was evaluated within the CD3-gate of T-cells **(B)**. Further analysis of memory T-cell subpopulation shows percent distribution of effector memory T-cells ($CD3^+$, $CD44^+$, $CD62L^-$) and central memory T-cells ($CD3^+$, $CD44^+$, $CD62L^+$) within the CD3-gate of T-cells **(C)**. For the measurement of every sample, 100,000 cells were stained and 10,000 events (parent R1 morphological lymphocyte gate) were recorded by flow-cytometry. For exact cell numbers, refer to Supplementary Material. Significant differences are shown by asterisks (ns for not significant, * for $p \leq 0.05$, ** for $p \leq 0.01$, *** for $p \leq 0.001$).

subpopulations was assessed using flow-cytometry in wild-type and PPARgamma deficient mice (**Figure 3B**). All thymocyte subpopulations showed near identical distribution pattern with all genetic backgrounds. Taken together, PPARgamma deficiency progressively enhances thymocyte development in adult age, but without skewing the distribution of thymocyte subpopulations or their differentiation preference.

PPARgamma Influences T-Cell Subpopulation Distribution in Adult Peripheral Blood

Peripheral blood T-cell subpopulations were evaluated by flow-cytometry at 12 months of age in wild-type and PPARgamma deficient animals. Our results do not show differences in the percent distribution of the major T-cell groups of helper T-cells and cytotoxic T-cells (**Figure 4A**) within the CD3-gate of T-cells. However, the evaluation of naive T-cell and memory T-cell ratio reveals significant effect of PPARgamma deficiency (**Figure 4B**). There is significant increase of naive T-cells in the peripheral blood of PPARgamma deficient animals compared to wild-type animals, conversely and significantly decreasing the memory T-cell pool within the CD3-gate of T-cells. Deeper analysis of the memory T-cell pool reveals it is the mobile effector memory T-cell subpopulation that shows significant decrease and not central memory T-cells (**Figure 4C**) within the CD3-gate of T-cells. Sustained and prolonged naive T-cell production due to PPARgamma deficiency in the thymus as suggested by mTrec values above apparently affects peripheral blood T-cell subpopulations as shown here.

Functional Immunological Consequence and Human Relevance

Having seen the far-reaching influence of PPARgamma status on thymus architecture, thymus function and peripheral blood T-cell composition with age, we have set out to test whether these changes have functional immunological relevance. If so, it would be also of high interest to test if our comprehensive mouse results have human relevance.

PPARgamma Modulates Immune Regulation and Immune Response

We have tested the capacity to mount oral tolerance to the foreign protein OVA in wild-type and PPARgamma deficient aged adult mice by measuring OVA-specific IgG titers following oral and/or intraperitoneal OVA challenge (**Figure 5A**). As reported by others, age impairs oral tolerance in wild-type animals (40, 41). As a consequence, there is only moderate, insufficient decrease of OVA-specific IgG titers in case of parallel oral OVA administration and i.p. OVA-injection in senior animals. However, PPARgamma deficiency rescues oral tolerance in the same experimental setting despite age, profoundly and significantly decreasing OVA-specific IgG titers (**Figure 5A**). Consequently, naive T-cell dependent immune regulation (oral tolerance) remains efficient in PPARgamma heterozygous animals despite their age.

The capacity to mount immune reaction to foreign influenza antigens was also tested as human seasonal influenza vaccine was injected into aged adult wild-type and PPARgamma deficient animals. Subsequent analysis of serum IgG titers specific to a vaccine component showed elevated protective antibody production (maximal ELISA OD values) in PPARgamma deficient animals, but not in their wild-type littermates (**Figure 5B**). This tendency is not significant because of individual variation observed due to the applied human vaccination protocol being inferior to standard mouse immunization protocol. Nevertheless, naive T-cell dependent immune response proves to be efficient in aged, PPARgamma heterozygous animals.

Human Evidence of PPARgamma Deficiency Preventing Thymic Senescence

Genetic PPARgamma deficiency is a rare, but existing condition in human called FPLD3 (15). It leads to a metabolic phenotype called lipodystrophy, similar to the mouse (11–15). Other rare human conditions not affecting PPARgamma can also lead to lipodystrophy (12–15). In case of FPLD2 lamin mutations trigger similar metabolic changes (14). Peripheral blood hTrec (DNA loop by-product of human T-cell receptor gene rearrangement) levels were measured using digital qPCR in age-matched patients with FPLD2 condition and FPLD3 condition (**Figure 6**). As expected and in perfect harmony with previous mouse thymocyte results elevated mean hTrec levels were detected in FPLD3 samples compared to FPLD2 samples. The tendency is

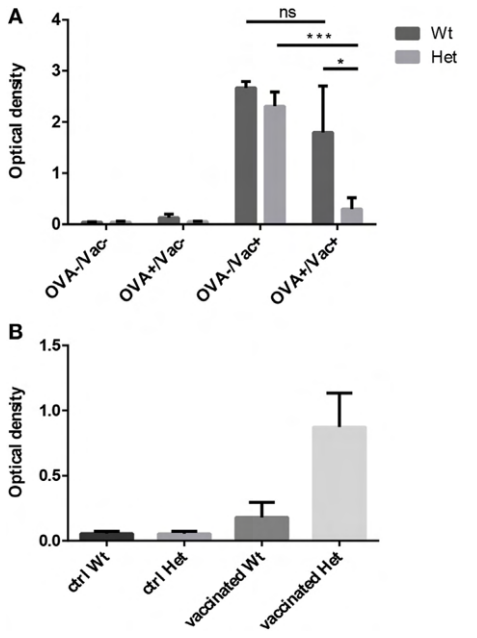

FIGURE 5 | Functional immunological experiments in adult hosts. Oral tolerance induction capacity to ovalbumin (OVA) was assayed in wild-type and PPARgamma heterozygous animals at 12 months of age. Animals received OVA by either drinking water, i.p. injection, both or neither. OVA-specific IgG titers were evaluated 3 weeks later by ELISA method **(A)**. The presented figure was obtained using 1:400 dilution of serum. Mean ELISA OD values are shown for each study group. Human seasonal influenza vaccine (3Fluart) was injected (0.1 ml, 1×, i.m.) into wild-type and PPARgamma heterozygous animals at 9 months of age. Serum IgG titers specific to a vaccine component (H1N1 A/California/7/2009 strain) were tested 3 months later by ELISA method **(B)**. The presented figure was obtained using 1:50 dilution of serum. Maximal ELISA OD values are shown for each study group. For exact numerical data, refer to Supplementary Material. Significant differences are shown by asterisks (ns for not significant, * for $p \leq 0.05$, ** for $p \leq 0.01$, *** for $p \leq 0.001$).

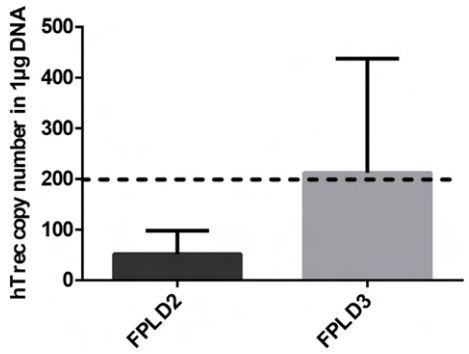

FIGURE 6 | Thymus function in adult FPLD patients. Level of human T-cell recombination excision circle (hTrec) was measured by Taqman digital qPCR in peripheral blood leukocytes of age-matched and disease-matched rare disease patients with FPLD2 condition (lipodystrophy due to LMNA deficiency) and FPLD3 condition (lipodystrophy due to PPARgamma deficiency) (**Figure 6**). Patient sample numbers were $n = 3$ for FPLD2 and $n = 5$ for FPLD3. For exact numerical data, refer to Supplementary Material. For age-matched (approx. 50 years of age) range of healthy human hTrec values, refer to the work of Lynch et al. (38). Accordingly, the lower limit of healthy human hTrec threshold (approximately 200 copies/µg DNA) is represented by dotted line.

not significant due to individual variation within the patient groups. Unfortunately, current patient sample numbers cannot be increased due to the extremely rare nature of these conditions (FPLD2 or ORPHA 2348 has prevalence of ≤1/1,000,000 and FPLD3 or ORPHA 79083 also has prevalence of ≤1/1,000,000) (14, 15). For age-matched range of healthy human hTrec values, refer to the work of Lynch et al. (38). Lower limit of healthy human hTrec threshold (approx. 200 copies/μg DNA) is not reached by FPLD2 (lamin) patient samples, but this is rescued in FPLD3 (PPARgamma) patients despite being age and disease matched.

DISCUSSION

PPARgamma Drives Thymic Epithelial to Adipose Trans-Differentiation with Age

It has been previously suggested based on direct fate-mapping experiments that with senescence thymic adipose tissue develops from the thymic stromal or epithelial compartment (28). Based on indirect evidence others have also supported this concept (29). In further support, we here present visual evidence of epithelial to adipose transdifferentiation in the mouse. This is indicated by the presence by EpCAM-1/PPARgamma double-positive cells shown by histology (**Figure 1D**). These cells still express cell surface markers of their fading thymic epithelial identity (EpCAM-1), but already show early signs of the novel adipocyte differentiation program in their nuclei (PPARgamma). The fact that such double positive cells show rather scattered and not uniform staining pattern at a given time point may provide explanation for gradual thymic adipose involution observed during senescence.

PPARgamma Impairs Naive T-Cell Production with Age

Thymus histology data show that the medullary compartment is rescued from age-related shrinking in case of PPARgamma deficiency (**Figures 2A–D**). Extended survival of this stromal niche ensures permissive environment for sustained thymus function: naive T-cell production. This is indicated by elevated mTrec values showing direct correlation with PPARgamma deficiency (**Figure 3A**). Of extreme importance and highlighting human relevance, peripheral blood leukocyte hTrec values from adult FPLD3 patients (with genetic PPARgamma deficiency) also exceed adult FPLD2 patient values (with unrelated genetic background) despite being age-matched and disease-matched (lipodystrophy, diabetes) (**Figure 6**). Of note, such metabolic disorders are known to impair thymus function indicated by decreased hTrec values as reported by others (43, 44). For exactly, this reason have we used disease-matched controls (FPLD2 vs. FPLD3) to show enhanced thymus function with PPARgamma deficiency despite metabolic disorders. Unlike lower than physiological hTrec values measured in FPLD2 (lamin) patients, those measured in FPLD3 (PPARgamma) patients are within healthy human physiological range (**Figure 6**). Since both mTrec and hTrec DNA loops originate from gene rearrangement during thymocte development this is direct evidence of sustained T-cell development indicating intact thymic niche in PPARgamma deficient animal models and human patients (38). Of note, the distribution of thymocyte subpopulations shows identical pattern irrespective of PPARgamma status proving that sustained, enhanced thymocyte development does not skew differentiation preference, but rather enhances fresh, naive T-cell production of all thymocyte subtypes uniformly (**Figure 3B**). Finally, since sustained thymic naive T-cell production is not restricted to a given time-point, but rather represents a continuous trend, the peripheral blood naive T-cell population shows cumulative differences as it is rescued from age-driven shrinking, against the memory T-cell population—more specifically against the effector memory T-cell pool (**Figures 4B,C**).

PPARgamma Hampers T-Dependent Immune Regulation and Immunity with Age

Oral consumption of foreign T-depended antigen normally initiates immune tolerance inhibiting any eliminative immune response (e.g., serum IgG), despite parallel immunization in young adult individuals with appropriate naive T-cell supply. Unfortunately, the phenomenon is disrupted at senior age due to the lacking naive T-cell pool in the Peyer's patches of the gut (40, 41, 45) This loss of oral tolerance (impaired immune regulation) is a possible link to increasing food intolerance prevalence observed in the aging adult population (46–49). However, the phenomenon may be rescued by PPARgamma deficiency despite age providing evidence that sustained T-cell production is necessary for efficient oral (immune) tolerance (**Figure 5A**).

Senescence-triggered decrease of naive T-cell output also impairs T-dependent immunity. An example in the senior human population is decreased protection from seasonal flu strains despite annual vaccination campaigns (50–52). The phenomenon has well established animal models (53–55). This is caused by low levels of neutralizing antibody titers due to lacking naive T-cells necessary during T-B cooperation to mount adequate innate immune response against T-dependent antigens of the vaccine. This, however, is not the case with PPARgamma deficiency (**Figure 5B**). Single intramuscular vaccination against seasonal flu (mimicking human vaccination campaign) resulted in higher maximal antibody production three months later (a typical delay in human exposure). This confirms that the cause of decreased vaccination efficiency in the senior population is impaired T-dependent immunity due to thymic senescence.

In our experiments, we have focused on the decline of T-dependent immunity since the thymus shows early and dramatic signs of senescence during adipose involution. This, however, is not the case for the B-cell compartment for which aging has been reported to occur later and in a more gradual fashion, lacking such profound histological changes (56).

PPARgamma is an enigmatic transcription factor showing unique expression pattern in both time and space throughout the body (57). PPARgamma affects both hemopoietic and stromal

compartments during development and aging. Further dissection would require to perform, e.g., bone-marrow transplantation experiments between control and PPARgamma deficient animals. However, PPARgamma KO animals develop severe metabolic disorders that hamper such experiments, especially at elevated ages.

Limitations and Perspectives

We here present the long-term thymus- and T-dependent immunity-preserving effect of systemic (genetic) loss of PPARgamma function as observed in PPARgamma deficient mouse models and in a human rare disease (FPLD3). In both cases, there are severe metabolic drawbacks (diabetes, dyslipidemia etc.) due to systemically lacking PPARgamma activity. However, alternative, thymus tissue-restricted suppression of PPARgamma activity would likely solve the issue. Of note, as reported previously, overexpression of Wnt4 glycolipoproteins by thymic epithelial cells can efficiently counteract PPARgamma (31). Also, Wnt4 was described to travel in extracellular vesicles including exosomes and affect thymocyte differentiation (58, 59). Hence, it is conceivable that thymic epithelium-derived, enriched exosomes would efficiently home to the thymus and deliver their Wnt4 cargo locally even when administered systemically. This would, in theory, allow for the natural, tissue-specific, protein-mediated maintenance of thymic epithelial identity and prevent thymic senescence from developing.

Although tissue senescence is ultimately inevitable, there are conditions that accelerate thymic senescence including certain viral infections, intoxications, irradiation, chemotherapy, etc. Outcomes include increased incidence of infection, cancer and autoimmune disorder. In any case, the identification of molecular level targets for potential intervention is highly desired. Therefore, molecular level insight into immune senescence has medical, economical, and personal relevance, all at once.

ETHICS STATEMENT

Experiments involving human thymus samples were performed with the consent of the Regional and Local Ethics Committee of Clinical Centre, University or Pecs (ref. no.: 6331/2016) according to their guidelines. Experiments involving human blood samples were performed with the consent of the Regional and Local Ethics Committee of Clinical Centre, University or Pecs (ref. no.: 6439/2016) according to their guidelines. All subjects gave written informed consent in accordance with the Declaration of Helsinki. Permission to perform the described animal experiments was granted to the relevant utilities of the University of Pecs (ref. no.: BA02/2000-46/2016). Permission to generate PPARgamma GM mice was granted to the relevant utilities of the University of Debrecen (ref. no.: TMF/82-10/2015). Permission to perform experimental procedures with PPARgamma GM mice was granted to the relevant utilities of the University of Pecs (ref. no.: TMF/124-11/2017).

AUTHOR CONTRIBUTIONS

DE performed most histological, molecular biology, and statistics work in the project and was involved in manuscript preparation. KB performed all human IHC work. ZK performed oral immune tolerance experiments. AP was in charge for the breeding, metabolic, and genetic characterization of PPARgamma haploinsufficient and null mice. JL was in charge for planning human experiments, involved in manuscript preparation as well as local supervision of respective department. PE was involved in planning mouse experiments, involved in manuscript preparation as well as local supervision of respective department. KK was involved in histological, molecular biology and statistics work, also in planning experiments and manuscript preparation, and supervised the project.

ACKNOWLEDGMENTS

The authors wish to thank the PPARgamma$^{+/-}$ and PPARgamma$^{fl/fl}$ mice that were obtained from Yaacov Barak PhD (Salk Institute, La Jolla, CA, USA) and also the Sox2Cre mice obtained from Beatrice Desvergne MD, PhD (University of Lausanne, Switzerland). We are grateful for Gregory D. Sempowski MD PhD (Duke Human Vaccine Institute, Duke University, Durham, NC, USA) for providing the Trec primer and probe sequences along with protocols for TaqMan qPCR, and also Peter Balogh MD PhD (Department of Immunology and Biotechnology, University of Pecs, Hungary) for providing test antibodies for mouse CD3, CD4, CD8. The authors wish to thank David B. Savage, MD, PhD (Metabolic Research Laboratories, School of Clinical Medicine, University of Cambridge, Cambridge, United Kingdom) for providing peripheral blood DNA samples from genetically verified FPLD2 and FPLD3 rare disease patients.

FUNDING

Scientific research support was provided by the Hungarian National Science Foundation (no. 78310) and PTE AOK KA-2016-16 to KK. The project was also supported by the University of Pecs in the frame of Pharmaceutical Talent Center program and the Viral Pathogenesis Talent Center program *via* KK. The Janos Bolyai Scholarship of the Hungarian Academy of Sciences also supported KK. JEP was supported by the European Union and he State of Hungary, co-financed by the European Social Fund in the framework of GINOP 2.3.2–15–2016-00022 TAMOP-4.2.2.A-11/1/KON-2012-0024, TAMOP-4.2.4.A/2-11/1-2012-0001 "National Excellence Program," PTE AOK-KA-2013/22 and EFOP-3.6.1-16-2016-00004. The present scientific contribution is also dedicated to the 650th anniversary of the foundation of the University of Pecs, Hungary.

SUPPLEMENTARY MATERIAL

The Supplementary Material for this article can be found online at http://www.frontiersin.org/article/10.3389/fimmu.2017.01515/full#supplementary-material.

REFERENCES

1. Ammazzalorso A, De Filippis B, Giampietro L, Amoroso R. Blocking the peroxisome proliferator-activated receptor (PPAR): an overview. *ChemMedChem* (2013) 8(10):1609–16. doi:10.1002/cmdc.201300250
2. Montagner A, Rando G, Degueurce G, Leuenberger N, Michalik L, Wahli W. New insights into the role of PPARs. *Prostaglandins Leukot Essent Fatty Acids* (2011) 85(5):235–43. doi:10.1016/j.plefa.2011.04.016
3. Christodoulides C, Vidal-Puig A. PPARs and adipocyte function. *Mol Cell Endocrinol* (2010) 318(1–2):61–8. doi:10.1016/j.mce.2009.09.014
4. Janani C, Ranjitha Kumari BD. PPAR gamma gene – a review. *Diabetes Metab Syndr* (2015) 9(1):46–50. doi:10.1016/j.dsx.2014.09.015
5. Lefterova MI, Haakonsson AK, Lazar MA, Mandrup S. PPARγ and the global map of adipogenesis and beyond. *Trends Endocrinol Metab* (2014) 25(6):293–302. doi:10.1016/j.tem.2014.04.001
6. Siersbaek R, Nielsen R, Mandrup S. PPARgamma in adipocyte differentiation and metabolism – novel insights from genome-wide studies. *FEBS Lett* (2010) 584(15):3242–9. doi:10.1016/j.febslet.2010.06.010
7. Tontonoz P, Spiegelman BM. Fat and beyond: the diverse biology of PPARgamma. *Annu Rev Biochem* (2008) 77:289–312. doi:10.1146/annurev.biochem.77.061307.091829
8. Duan SZ, Ivashchenko CY, Whitesall SE, D'Alecy LG, Duquaine DC, Brosius FC III, et al. Hypotension, lipodystrophy, and insulin resistance in generalized PPARgamma-deficient mice rescued from embryonic lethality. *J Clin Invest* (2007) 117(3):812–22. doi:10.1172/JCI28859
9. Duan SZ, Usher MG, Foley EL IV, Milstone DS, Brosius FC III, Mortensen RM. Sex dimorphic actions of rosiglitazone in generalised peroxisome proliferator-activated receptor-gamma (PPAR-gamma)-deficient mice. *Diabetologia* (2010) 53(7):1493–505. doi:10.1007/s00125-010-1748-2
10. O'Donnell PE, Ye XZ, DeChellis MA, Davis VM, Duan SZ, Mortensen RM, et al. Lipodystrophy, diabetes and normal serum insulin in PPARγ-deficient neonatal mice. *PLoS One* (2016) 11(8):e0160636. doi:10.1371/journal.pone.0160636
11. Nadra K, Quignodon L, Sardella C, Joye E, Mucciolo A, Chrast R, et al. PPARgamma in placental angiogenesis. *Endocrinology* (2010) 151(10):4969–81. doi:10.1210/en.2010-0131
12. Hegele RA, Joy TR, Al-Attar SA, Rutt BK. Thematic review series: adipocyte biology. Lipodystrophies: windows on adipose biology and metabolism. *J Lipid Res* (2007) 48(7):1433–44. doi:10.1194/jlr.R700004-JLR200
13. Hegele RA. Familial partial lipodystrophy: a monogenic form of the insulin resistance syndrome. *Mol Genet Metab* (2000) 71(4):539–44. doi:10.1006/mgme.2000.3092
14. ORPHANET. *FPLD2*. Available from: http://www.orpha.net/consor/cgi-bin/OC_Exp.php?Expert=2348
15. ORPHANET. *FPLD3*. Available from: http://www.orpha.net/consor/cgi-bin/OC_Exp.php?Lng=GB&Expert=79083
16. Argmann CA, Cock TA, Auwerx J. Peroxisome proliferator-activated receptor gamma: the more the merrier? *Eur J Clin Invest* (2005) 35(2):82–92. doi:10.1111/j.1365-2362.2005.01456.x
17. Corton JC, Brown-Borg HM. Peroxisome proliferator-activated receptor gamma coactivator 1 in caloric restriction and other models of longevity. *J Gerontol A Biol Sci Med Sci* (2005) 60(12):1494–509. doi:10.1093/gerona/60.12.1494
18. Luconi M, Cantini G, Serio M. Peroxisome proliferator-activated receptor gamma (PPARgamma): is the genomic activity the only answer? *Steroids* (2010) 75(8–9):585–94. doi:10.1016/j.steroids.2009.10.012
19. Choi SS, Park J, Choi JH. Revisiting PPARγ as a target for the treatment of metabolic disorders. *BMB Rep* (2014) 47(11):599–608. doi:10.5483/BMBRep.2014.47.11.174
20. Ahmadian M, Suh JM, Hah N, Liddle C, Atkins AR, Downes M, et al. PPARγ signaling and metabolism: the good, the bad and the future. *Nat Med* (2013) 19(5):557–66. doi:10.1038/nm.3159
21. Youm YH, Yang H, Amin R, Smith SR, Leff T, Dixit VD. Thiazolidinedione treatment and constitutive-PPARgamma activation induces ectopic adipogenesis and promotes age-related thymic involution. *Aging Cell* (2010) 9(4):478–89. doi:10.1111/j.1474-9726.2010.00574.x
22. Steinmann GG. Changes in the human thymus during aging. *Curr Top Pathol* (1986) 75:43–88.6. doi:10.1007/978-3-642-82480-7_2
23. Palmer DB. The effect of age on thymic function. *Front Immunol* (2013) 4:316. doi:10.3389/fimmu.2013.0031
24. Bertho JM, Demarquay C, Moulian N, Van Der Meeren A, Berrih-Aknin S, Gourmelon P. Phenotypic and immunohistological analyses of the human adult thymus: evidence for an active thymus during adult life. *Cell Immunol* (1997) 179(1):30–40. doi:10.1006/cimm.1997.1148
25. Falci C, Gianesin K, Sergi G, Giunco S, De Ronch I, Valpione S, et al. Immune senescence and cancer in elderly patients: results from an exploratory study. *Exp Gerontol* (2013) 48(12):1436–42. doi:10.1016/j.exger.2013.09.011
26. Fletcher AL, Calder A, Hince MN, Boyd RL, Chidgey AP. The contribution of thymic stromal abnormalities to autoimmune disease. *Crit Rev Immunol* (2011) 31(3):171–87. doi:10.1615/CritRevImmunol.v31.i3.10
27. Yang H, Youm YH, Sun Y, Rim JS, Galbán CJ, Vandanmagsar B, et al. Axin expression in thymic stromal cells contributes to an age-related increase in thymic adiposity and is associated with reduced thymopoiesis independently of ghrelin signaling. *J Leukoc Biol* (2009) 85(6):928–38. doi:10.1189/jlb.1008621
28. Youm YH, Yang H, Sun Y, Smith RG, Manley NR, Vandanmagsar B, et al. Deficient ghrelin receptor-mediated signaling compromises thymic stromal cell microenvironment by accelerating thymic adiposity. *J Biol Chem* (2009) 284(11):7068–77. doi:10.1074/jbc.M808302200
29. Kvell K, Varecza Z, Bartis D, Hesse S, Parnell S, Anderson G, et al. Wnt4 and LAP2alpha as pacemakers of thymic epithelial senescence. *PLoS One* (2010) 5(5):e10701. doi:10.1371/journal.pone.0010701
30. Varecza Z, Kvell K, Talabér G, Miskei G, Csongei V, Bartis D, et al. Multiple suppression pathways of canonical Wnt signalling control thymic epithelial senescence. *Mech Ageing Dev* (2011) 132(5):249–56. doi:10.1016/j.mad.2011.04.007
31. Kvell K, Fejes AV, Parnell SM, Pongracz JE. Active Wnt/beta-catenin signaling is required for embryonic thymic epithelial development and functionality ex vivo. *Immunobiology* (2014) 219(8):644–52. doi:10.1016/j.imbio.2014.03.017
32. Kvell K, Pongracz JE. Central immune senescence, reversal potentials. In: Nagata T, editor. *Senescence*. Rijeka, HR: InTech (2012). Chater31 p.
33. Yang H, Youm YH, Dixit VD. Inhibition of thymic adipogenesis by caloric restriction is coupled with reduction in age-related thymic involution. *J Immunol* (2009) 183(5):3040–52. doi:10.4049/jimmunol.0900562
34. Talaber G, Kvell K, Varecza Z, Boldizsar F, Parnell SM, Jenkinson EJ, et al. Wnt-4 protects thymic epithelial cells against dexamethasone-induced senescence. *Rejuvenation Res* (2011) 14(3):241–8. doi:10.1089/rej.2010.1110
35. Meggyes M, Lajko A, Palkovics T, Totsimon A, Illes Z, Szereday L, et al. Feto-maternal immune regulation by TIM-3/galectin-9 pathway and PD-1 molecule in mice at day 14.5 of pregnancy. *Placenta* (2015) 36(10):1153–60. doi:10.1016/j.placenta.2015.07.124
36. Solti I, Kvell K, Talaber G, Veto S, Acs P, Gallyas F Jr, et al. Thymic atrophy and apoptosis of CD4+CD8+ thymocytes in the cuprizone model of multiple sclerosis. *PLoS One* (2015) 10(6):e0129217. doi:10.1371/journal.pone.0129217
37. Sallusto F, Geginat J, Lanzavecchia A. Central memory and effector memory T cell subsets: function, generation, and maintenance. *Annu Rev Immunol* (2004) 22:745–63. doi:10.1146/annurev.immunol.22.012703.104702
38. Lynch HE, Goldberg GL, Chidgey A, Van den Brink MR, Boyd R, Sempowski GD. Thymic involution and immune reconstitution. *Trends Immunol* (2009) 30(7):366–73. doi:10.1016/j.it.2009.04.003
39. Simioni PU, Fernandes LG, Gabriel DL, Tamashiro WM. Induction of systemic tolerance in normal but not in transgenic mice through continuous feeding of ovalbumin. *Scand J Immunol* (2004) 60(3):257–66. doi:10.1111/j.0300-9475.2004.01454.x
40. de Faria AM, Ficker SM, Speziali E, Menezes JS, Stransky B, Silva Rodrigues V, et al. Aging affects oral tolerance induction but not its maintenance in mice. *Mech Ageing Dev* (1998) 102(1):67–80. doi:10.1016/S0047-6374(98)00024-4
41. Kato H, Fujihashi K, Kato R, Dohi T, Fujihashi K, Hagiwara Y, et al. Lack of oral tolerance in aging is due to sequential loss of Peyer's patch cell interactions. *Int Immunol* (2003) 15(2):145–58. doi:10.1093/intimm/dxg011
42. Ramirez A, Co M, Mathew A. CpG improves influenza vaccine efficacy in young adult but not aged mice. *PLoS One* (2016) 11(3):e0150425. doi:10.1371/journal.pone.0150425
43. Hofer J, Hofer S, Zlamy M, Jeller V, Koppelstaetter C, Brandstätter A, et al. Elevated proportions of recent thymic emigrants in children and adolescents with type 1 diabetes. *Rejuvenation Res* (2009) 12(5):311–20. doi:10.1089/rej.2009.0863

44. Iskakova S, Urazayev O, Bekmukhambetov Y, Dworacki G, Dworacka M. [The differences of TREC (T-cell receptor excision circles) concentration in type 2 diabetic patients]. *Georgian Med News* (2015) (244–245):29–36.
45. Song F, Guan Z, Gienapp IE, Shawler T, Benson J, Whitacre CC. The thymus plays a role in oral tolerance in experimental autoimmune encephalomyelitis. *J Immunol* (2006) 177(3):1500–9. doi:10.4049/jimmunol.177.3.1500
46. Galipeau HJ, Verdu EF. Gut microbes and adverse food reactions: focus on gluten related disorders. *Gut Microbes* (2014) 5(5):594–605. doi:10.4161/19490976.2014.969635
47. Marietta EV, Murray JA. Animal models to study gluten sensitivity. *Semin Immunopathol* (2012) 34(4):497–511. doi:10.1007/s00281-012-0315-y
48. MacDonald TT. Evidence for cell-mediated hypersensitivity as an important pathogenetic mechanism in food intolerance. *Clin Exp Allergy* (1995) 25(Suppl 1):10–3. doi:10.1111/j.1365-2222.1995.tb01125.x
49. Ferguson A, Ziegler K, Strobel S. Gluten intolerance (coeliac disease). *Ann Allergy* (1984) 53(6 Pt 2):637–42.
50. Cromer D, van Hoek AJ, Jit M, Edmunds WJ, Fleming D, Miller E. The burden of influenza in England by age and clinical risk group: a statistical analysis to inform vaccine policy. *J Infect* (2014) 68(4):363–71. doi:10.1016/j.jinf.2013.11.013
51. Ang LW, Lim C, Lee VJ, Ma S, Tiong WW, Ooi PL, et al. Influenza-associated hospitalizations, Singapore, 2004-2008 and 2010-2012. *Emerg Infect Dis* (2014) 20(10):1652–60. doi:10.3201/eid2010.131768
52. Haq K, McElhaney JE. Immunosenescence: influenza vaccination and the elderly. *Curr Opin Immunol* (2014) 29:38–42. doi:10.1016/j.coi.2014.03.008
53. Thangavel RR, Bouvier NM. Animal models for influenza virus pathogenesis, transmission, and immunology. *J Immunol Methods* (2014) 410:60–79. doi:10.1016/j.jim.2014.03.023
54. Kim JI, Park S, Lee S, Lee I, Heo J, Hwang MW, et al. DBA/2 mouse as an animal model for anti-influenza drug efficacy evaluation. *J Microbiol* (2013) 51(6):866–71. doi:10.1007/s12275-013-3428-7
55. Kamal RP, Katz JM, York IA. Molecular determinants of influenza virus pathogenesis in mice. *Curr Top Microbiol Immunol* (2014) 385:243–74. doi:10.1007/82_2014_388
56. Shekarabi M, Asgari F. In: Massoud A, Rezaei N, editors. *Immunology of Aging*. Berlin, Heidelberg: Springer Verlag (2014).
57. Greene ME, Pitts J, McCarville MA, Wang XS, Newport JA, Edelstein C, et al. PPARgamma: observations in the hematopoietic system. *Prostaglandins Other Lipid Mediat* (2000) 62(1):45–73. doi:10.1016/S0090-6980(00)00075-7
58. Gross JC, Boutros M. Secretion and extracellular space travel of Wnt proteins. *Curr Opin Genet Dev* (2013) 23(4):385–90. doi:10.1016/j.gde.2013.02.017
59. Lundberg V, Berglund M, Skogberg G, Lindgren S, Lundqvist C, Gudmundsdottir J, et al. Thymic exosomes promote the final maturation of thymocytes. *Sci Rep* (2016) 6:36479. doi:10.1038/srep36479

Conflict of Interest Statement: The authors declare that they have no conflicts of interest with the contents of this article. The research was conducted in the absence of any commercial or financial relationship that could be construed as a potential conflict of interest.

toxins

MDPI

Article

Effect of *Vipera ammodytes ammodytes* Snake Venom on the Human Cytokine Network

Francisc Boda [1], Krisztina Banfai [2,3], Kitti Garai [2,3], Augustin Curticapean [1], Lavinia Berta [1,*], Emese Sipos [4] and Krisztian Kvell [2,3]

1 Department of Fundamental Pharmaceutical Sciences, Faculty of Pharmacy, University of Medicine and Pharmacy of Tirgu Mures, Gheorghe Marinescu Street No. 38, 540139 Tirgu Mures, Romania; boda.francisc@umftgm.ro (F.B.); augustin.curticapean@umftgm.ro (A.C.)

2 Department of Pharmaceutical Biotechnology, Faculty of Pharmacy, University of Pecs, Rokus Street No. 2, 7624 Pecs, Hungary; krisztina.banfai@aok.pte.hu (K.B.); garai.kitti91@gmail.com (K.G.); kvell.krisztian@pte.hu (K.K.)

3 Szentagothai Research Center, University of Pecs, Ifjusag Street No. 20, 7624 Pecs, Hungary

4 Department of Specialty Pharmaceutical Sciences, Faculty of Pharmacy, University of Medicine and Pharmacy of Tirgu Mures, Gheorghe Marinescu Street No. 38, 540139 Tirgu Mures, Romania; emese.sipos@umftgm.ro

* Correspondence: grama.lavinia@umftgm.ro; Tel.: +40-740-694-638

Received: 11 June 2018; Accepted: 21 June 2018; Published: 25 June 2018

Abstract: Local inflammation is a well-known symptom of envenomation by snakes of the family *Viperidae*, attributed primarily to the phospholipase A_2s, metalloproteinases and L-amino acid oxidases contained in their venom. The inflammatory effect of snake venoms has been associated with a marked increase of the cytokines IL-1β, IL-6, IL-8, IL-10 and TNF-α. To determine the impact of *Vipera ammodytes ammodytes* snake venom on the expression of inflammation-related genes, we incubated human U937 monocyte cells with dilutions of snake venom. Gene expression was quantified for 28 different genes using a TaqMan® Array Human Cytokine Network 96-well Plate in a RT-qPCR system. Our results have demonstrated that 1.0 µg/mL *Vipera ammodytes ammodytes* venom solution induces a notable change in the expression of several cytokine network genes. Among the upregulated genes, there were several that encode interleukins, interferons, and tumor necrosis factors. We further report the downregulation of three interleukin-related genes. Our findings come as supportive information for the known complex effect of snake venoms on the human cytokine network. It also provides relevant new information regarding the expression of genes that have not been previously associated with the effect of snake venoms.

Keywords: snake venoms; *Vipera ammodytes*; inflammation-related genes; inflammatory mediators; cytokines; RT-qPCR

Key Contribution: We present a Taqman Array method to simultaneously determine the effect of *Vipera ammodytes ammodytes* snake venom on 28 inflammation-related genes. The results show that the venom alters the expression of several cytokine network genes, including genes not yet associated with the effect of snake venoms.

1. Introduction

The inflammatory process represents a defense mechanism of the body against harmful pathogens, damaged cells, or irritating substances. Inflammation can take an acute or chronic form. In its acute form, five typical signs of inflammation are usually present: heat, pain, redness, swelling, and loss of function of the affected tissues or organs. Chronic inflammatory processes are characterized by a

continuous and simultaneous destruction and healing of affected tissues, which may lead to chronic inflammatory diseases with detrimental effects on health [1,2].

Following the initiation of acute inflammation, the affected tissues present an increased blood flow and increased permeability of blood vessels; monocytes extravasate to the affected regions and are transformed into macrophages. Macrophages are responsible for antigen presentation and phagocytosis and modulate the immune response through induction of cytokine, chemokine, and growth factor production [1,3]. Macrophages form different subsets depending on the activating signals. Lipopolysaccharides (LPS), interferon gamma (IFN-γ), or interleukin 1 beta (IL-1β) activate M1-type macrophages. These macrophages are known to generate reactive oxygen species (ROS) and to produce proinflammatory cytokines, such as interleukin 6 (IL-6), interleukin 12 (IL-12), IFN-γ, and tumor necrosis factor alpha (TNF-α) [4]. M2-type macrophages are activated by interleukin 4 (IL-4), interleukin 10 (IL-10), or interleukin 13 (IL-13). These macrophages participate in the halting of inflammatory processes and promote tissue recovery through the production of anti-inflammatory mediators, including IL-10, transforming growth factor beta (TGF-β), and IL-1 receptor antagonists [5].

Envenomation by snakes of the family *Viperidae* is associated with both local and systemic effects. Local effects include severe tissue damage, necrosis, hemorrhage, and inflammation of the affected area. Systemic effects are related mainly to the action of snake venom proteins on the cardiovascular system and hemostasis [6,7]. The inflammatory response caused by *Viperidae* snake venoms is attributed primarily to phospholipase A_2s (svPLA_2s), snake venom metalloproteinases (SVMPs), and L-amino acid oxidases (LAAOs) contained in the venom. Furthermore, hyaluronidases, nucleases, nucleotidases, phosphomonoesterases, and some nonenzymatic toxins found in snake venoms contribute to the inflammation-inducing effect [8].

Snake venom PLA_2s are proteins that hydrolyze phospholipids at the sn-2 position, generating lysophospholipids and free fatty acids, including arachidonic acid [9,10]. Arachidonic acid functions as substrate for the synthesis of various proinflammatory mediators, such as leukotrienes (LT), thromboxane A_2 (TXA_2), prostacyclin, and prostaglandins (PG). Thus, the inflammatory effect of svPLA_2s can be directly linked to their enzymatic activity [11–13]. However, there are reports of catalytically inactive svPLA_2s capable of inducing inflammation and nociceptive responses, suggesting the existence of other inflammation-inducing mechanisms not related to the arachidonic pathway [14–16].

Snake venom metalloproteinases (SVMPs) are zinc-dependent enzymes responsible for the hemorrhagic, necrotic, and inflammatory effects of snake venoms [17]. Local effects frequently associated with SVMP administration include edema formation, hyperalgesia, leukocyte infiltration, and mast cell degranulation [7,8,18]. SVMP treatment has been associated with the release of various inflammatory mediators, such as IL-1β, IL-6, IL-10, prostaglandin E2 (PGE_2), and TNF-α [12,19,20].

L-amino acid oxidases (LAAOs) are flavoproteins that catalyze the oxidative deamination of L-amino acids to α-keto acids. The oxidative process leads to the formation of hydrogen peroxide and ammonia. The release of hydrogen peroxide is linked to the apoptotic, cytotoxic, hemorrhagic, and edema inducing effect of LAAOs [8,21]. Furthermore, recent studies have demonstrated that administration of purified LAAOs induces the release of several proinflammatory mediators, such as IL-6, IL-8, TNF-α, PGE_2, and leukotriene B4 (LTB_4) [22–24].

European venomous snakes are representatives of the genera *Vipera*. Among this genera, the most venomous species is the *Vipera ammodytes* (nose-horned viper) with its two subspecies, *V. ammodytes ammodytes* and *V. ammodytes meridionalis* [25]. This species is widespread in southern Europe, from central and northern Italy to southern Austria, through the Balkans and southern Romania to north-eastern Turkey and southern Caucasia [26]. The most frequently recorded effects of envenomation by *V. ammodytes* are local tissues damage, local and systemic hemorrhage, and to a smaller extent, neurotoxicity [27]. These effects may lead to permanent sequelae and organ function loss and in severe cases, envenomation might have lethal outcomes. Although the frequency of envenomation by *V. ammodytes* recorded in Europe is less than that of envenomation caused by other

species in tropical countries, these cases still represent a public health concern, mainly in the Balkan countries [27,28]. While there are several studies focused at isolating and characterizing proteins from the venom of *Vipera ammodytes* [25,29–32], reports are scarce on the effects of unfractionated venom—a complex mixture of biologically active proteins—in humans.

Our study aimed to determine the effect of *Vipera ammodytes ammodytes* venom (*VaaV*) on the human cytokine network. Using a TaqMan® Array Plate quantified by RT-qPCR, we assessed the expression of 28 cytokine-associated genes in monocytes treated with *VaaV*.

2. Results and Discussion

2.1. Effect of Treatment

Viability of cells treated with *VaaV* solution was assessed by microscopic evaluation. *VaaV* caused cell death at concentrations of 3.0, 10, 30, and 100 µg/mL. Monocyte cells treated with 1.0 µg/mL *VaaV* solution showed differentiation towards macrophage lineage as suggested by adherent polygonal cellular shape and growth arrest (Supplementary Figure S1). Cells incubated without treatment were assessed as viable and lacking signs of differentiation (Supplementary Figure S2). Total RNA was isolated from cell cultures deemed viable, namely those treated with 1.0 µg/mL *VaaV* and untreated cells.

2.2. Gene Expression in U937 Cells Treated with VaaV

Gene expression was assayed in triplicate using a TaqMan® Array Human Cytokine Network Plate containing 28 genes coding inflammatory mediators and four endogenous control genes. The endogenous control genes (*18S*, *GAPDH*, *HPRT1*, *GUSB*) allowed for the detection of potential variations in RNA loading. Based on the obtained data, mean fold changes and standard errors were calculated if at least two relative quantification (RQ) values could be measured for one individual gene. The mean fold change of genes following treatment of cells with 1.0 µg/mL *VaaV* solution is presented in Figure 1 in a log2 RQ-based scale. A complete list of genes, obtained RQ values, calculated mean RQs, standard errors, and 90% confidence intervals are presented in Supplementary Table S1.

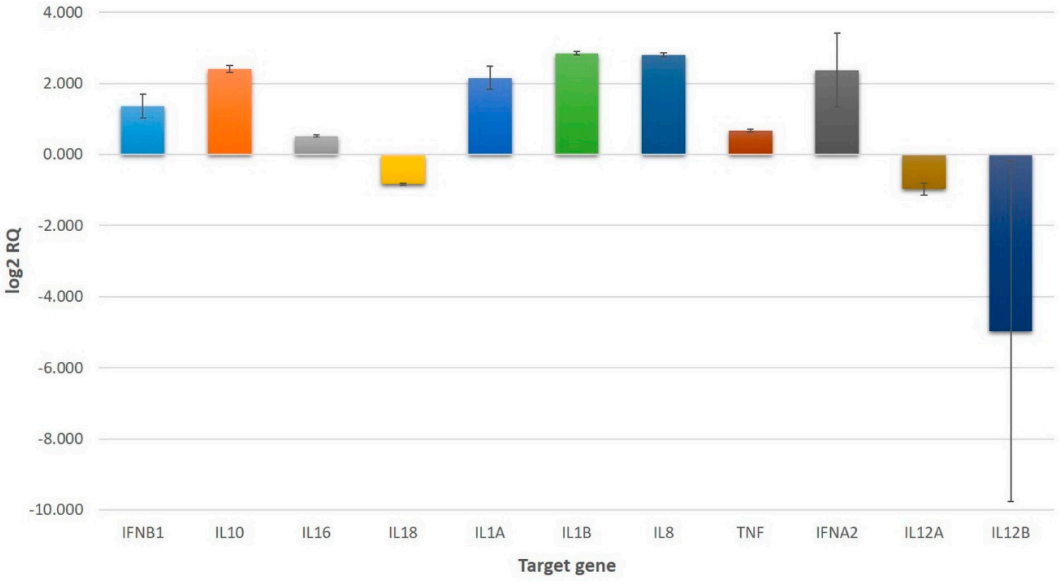

Figure 1. Upregulated and downregulated genes in U937 cells treated with 1.0 µg/mL *VaaV* solution. Values represent mean relative quantification (RQ) error bars represent the standard error on a log2 RQ-based scale. Untreated U937 cells served as reference and are represented by the zero value. The +1 and −1 values represent a two-fold increase or decrease threshold in gene expression.

2.2.1. Upregulation of Interleukin-Related Genes

Our results showed that *IL1A* and *IL1B* genes presented a significant upregulation, with a mean fold change of 4.67 and 7.21, respectively. These genes encode two members of the IL-1 family: interleukin 1 alpha (IL-1α) and beta (IL-1β). The IL-1 family of cytokines has a major role in the initiation and regulation of inflammation. These cytokines possess a pronounced proinflammatory effect and are capable of inducing the expression of several other cytokines and chemokines, including IL-8 [33,34]. Our findings partially correlate with data available in the literature, as increased levels of IL-1β have frequently been reported following administration of snake venoms [35,36], svPLA$_2$s [13,37], or SVMPs [12,20]. However, the expression of IL-1α following envenomation with snake venoms has not yet been the focus of research. Our finding that its gene is similarly upregulated as that of IL-1β suggests that IL-1α might have a pivotal role in the inflammatory process.

IL-10 is an immunosuppressive and anti-inflammatory cytokine that regulates and restrains the inflammatory response by limiting the production of cytokines and chemokines in macrophages and dendritic cells as well as by downregulating the expression of several chemokine receptors [34,38]. Increased IL-10 concentrations have been detected in human patients following envenomation with *Daboia russelii* venom [39] as well as in mice after administration of *Crotalus durissus terrificus* [40] and *Bothrops spp.* venom [41]. Furthermore, several studies have found that administration of SVMPs and svPLA$_2$s isolated from *Bothrops* species leads to a marked increase in IL-10 expression [12,18,19]. The expression of IL-10 provides evidence that snake venoms are capable of modulating the expression of both pro- and anti-inflammatory cytokines. In accordance with these results, we report a significant upregulation of the *IL10* gene (5.32-fold) following treatment with *VaaV*.

We found an approximately 1.4-fold increase in the expression of *IL16*, the gene encoding interleukin 16 (IL-16). IL-16 is a proinflammatory cytokine that functions as a chemoattractant for CD4$^+$ and CD8$^+$ T cells [34,42]. The expression level of *IL16* in our study is a noteworthy finding, considering the increase of IL-16 levels has not been associated with the effects of snake venoms.

2.2.2. Downregulation of Interleukin-Related Genes

Among the studied genes, we observed the downregulation of two interleukin-encoding genes—*IL18* and *IL12A*—responsible for the expression of interleukin 18 (IL-18) and interleukin 12 subunit alpha (IL-12α), respectively. Although statistically not significant, the results also show an indicative trend of downregulation for *IL12B*, the gene responsible for the expression of interleukin 12 subunit beta (IL-12β).

We identified a few cases of increased expression of IL-12 following administration of snake venoms or its components [43–45] but did not find any reports regarding the expression of IL-18. As both IL-12 and IL-18 induce the production of IFN-γ [34], the downregulation of the genes encoding these cytokines supports our findings regarding the lack of expression of *IFNG*, the gene responsible for encoding IFN-γ.

2.2.3. Upregulation of Chemokine-Related Genes

A marked upregulation following treatment of U937 cells with *VaaV* was observed for *IL8* (6.97-fold increase), the gene encoding interleukin 8 (IL-8). The marked increase in *IL8* expression suggests that IL-8 might be a significant mediator of inflammatory processes induced by snake venom.

IL-8, or C-X-C motif chemokine ligand 8 (CXCL8), is a member of the CXC chemokine family. Its main function involves the recruitment of neutrophils to the site of injury or infection but also functions as a potent chemoattractant for other cell types, including basophils, eosinophils, NK cells, and T cells [34,46]. Release of IL-8 from neutrophils has been reported following in vitro treatment of human neutrophils with *Bothrops bilineata* venom [47] and Cr-LAAO, an L-amino acid oxidase isolated from *Calloselasma rhodosthoma* [22].

2.2.4. Upregulation of Interferon-Related Genes

Interferon alpha (IFN-α) and interferon beta (IFN-β) are members of a highly related protein group called type I interferons (IFN-I). The main function of IFN-I consists of the induction of antiviral responses in cells through different mechanisms [48]. One of these mechanisms involves the direct activation of $CD4^+$ and $CD8^+$ T cells and dendritic cells and the subsequent release of various cytokines [49,50].

Our results showed a marked increase in the interferon-related gene *IFNB1* (2.7-fold), the gene responsible for the expression of IFN-β. Although statistically not significant, the results also show an indicative trend of upregulation for *IFNA2* (6.57-fold), the gene responsible for the expression of a variant of IFN-α. To the best of our knowledge, we are the first to report the upregulation of interferon-related genes in connection with snake venoms that may support the antiviral activity of certain snake venom components, as suggested by previous reports in other contexts [51,52].

2.2.5. Upregulation of Tumor Necrosis Factor-Related Genes

The tumor necrosis factor superfamily represents a group of cytokines that play an important role in inflammatory processes, immunity and cell proliferation, differentiation and apoptosis, and the formation of secondary lymphoid organs. Tumor necrosis factor alpha (TNF-α) is secreted by macrophages in the acute phase of an inflammation, while lymphotoxin alpha (LT-α, TNF-β) is produced by activated type 1 T helper (Th1) lymphocytes. Both have a pronounced proinflammatory effect and have a significant role in cell apoptosis and tissue necrosis [53–55]. The latter is also involved in peripheral lymphoid organogenesis [56].

We found that *TNF*, the gene encoding TNF-α, showed an approximately 1.6-fold increase following the treatment of cells with *VaaV*. The increase in *TNF* expression was to be expected, considering high levels of TNF-α have been observed in numerous experiments involving snake venoms. These experiments used either crude snake venoms [11,35,36,40,43] or isolated snake venom proteins, including SVMPs [19,20,57], svPLA$_2$s [13,37,44], or LAAOs [23,58].

2.3. Limitations of the Study

The study design does not allow for the differentiation between the primary effect on gene expression induced directly by *VaaV* and the secondary effect on gene expression caused by the cytokines released following the action of *VaaV* treatment.

Furthermore, the use of unfractionated *VaaV* venom in the study does not allow the determination of the contribution to the overall observed effect by individual components contained in the venom. However, the current study design can be easily adapted to measure the effect of individual proteins on gene expression.

3. Conclusions

We report the influence of *Vipera ammodytes ammodytes* venom on the expression of a large number of inflammation-related genes in monocytes/macrophages. Various authors have reported the increased expression of IL-1β, IL-6, IL-8, IL-10, and TNF-α cytokines as a consequence of administration of snake venoms or the components thereof. We determined that the genes related to these cytokines, except the gene encoding IL-6, were markedly upregulated in our experiment. Thus, our findings come as supportive information for previous observations. Furthermore, we identified other upregulated genes, namely *IL1A*, *IL16*, *IFNA2*, and *IFNB1*. To the best of our knowledge, the cytokines encoded by these genes have not been previously associated with the effect of snake venoms or their components. Additionally, we report the downregulation of several interleukin-related genes, namely *IL12A*, *IL12B*, and *IL18*. Better understanding of the mechanisms and mediators involved in the inflammatory response following envenomation with snake venoms could be of potential use in the development of targeted venom antiserums.

4. Materials and Methods

4.1. Snake Venom

Lyophilized *Vipera ammodytes ammodytes* venom was obtained from the Institute of Immunology, Zagreb, Croatia. A stock solution with a concentration of 10 mg/mL was prepared by dissolving the lyophilized *VaaV* in phosphate buffered saline (PBS) (Lonza, Basel, Switzerland).

4.2. Cell Line

U937 cell line was purchased from the American Type Culture Collection (ATCC CRL-1593.2™) and cultured in RPMI-1640 medium (Lonza, Basel, Switzerland) supplemented with 5 mL L-glutamine (Lonza, Switzerland), 10 mL penicillin/streptomycin (Lonza, Basel, Switzerland), and 50 mL fetal bovine serum (FBS) (EuroClone, Milan, Italy). Cell cultures were maintained in a 5% CO_2 atmosphere at 37 °C for 72 h. Cell viability before treatment was assessed using Olympus CKX41 microscope (Olympus, Tokyo, Japan).

4.3. Treatment of Cells

U937 cell cultures were each treated with 1.0, 3.0, 10, 30, and 100 µg/mL *VaaV* solution for 48 h. Cells incubated without treatment were used as negative control. Following incubation, cell viability was assessed microscopically. Cells deemed viable were collected in RA1 lysis buffer (Macherey-Nagel GmbG, Düren, Germany) and stored at −80 °C until further analysis.

4.4. RNA Isolation and cDNA Construction

To determine the expression of genes associated with the human cytokine network, total RNA was isolated from cell cultures treated with 1.0 µg/mL *VaaV* solution and untreated cell cultures (negative control). Total RNA was isolated using a NucleoSpin RNA II kit (Macherey-Nagel, Düren, Germany) based on the manufacturer's recommended protocol. The obtained RNA concentrations were determined using a Nanodrop 2000 spectrophotometer (Thermo Fischer Scientific, Waltham, MA, USA). The isolated RNA was reverse transcribed to cDNA with a PikoReal 96 Real-Time PCR System (Thermo Scientific, Waltham, MA, USA) using a High-Capacity cDNA Reverse Transcription Kit (Applied Biosystems, Foster City, CA, USA) according to the manufacturer's instructions. The PCR program used for cDNA synthesis consisted of sample incubation for 2 min at 50 °C and 10 min at 95 °C, followed by 40 cycles at 95 °C for 15 s and 60 °C for 60 s.

4.5. RT-qPCR

Gene expression was determined using a TaqMan® Array Human Cytokine Network 96-well Plate (Part No. 4414255, Applied Biosystems, USA). The TaqMan® Array Plate contains 28 assays for genes associated with pro- and anti-inflammatory cytokines and four assays for candidate endogenous control genes.

The quantitative real-time PCR amplification was performed on a 7500 Real-Time PCR System (Applied Biosystems, USA) in a 20 µL volume containing TaqMan Universal PCR Master Mix (Applied Biosystems, USA) and the cDNA samples. The PCR program used consisted of sample incubation for 2 min at 50 °C and 10 min at 95 °C, followed by 40 cycles at 95 °C for 15 s and 60 °C for 1 min. All assays were plated in triplicate. The obtained amplification data was evaluated using the 7500 Software v2.0.6 (Applied Biosystems, USA). Calculations and statistical analysis of the results was performed using Graphpad Prism software (version 6.0), GraphPad Software, La Jolla, CA, USA).

Supplementary Materials: The following are available online at http://www.mdpi.com/2072-6651/10/7/259/s1, Figure S1: Monocyte cells treated with 1.0 µg/mL *VaaV* solution showing differentiation towards macrophage lineage as suggested by adherent polygonal cellular shape and growth arrest. Figure S2: Viable monocytes, lacking signs of differentiation following incubation without treatment, serving as negative control. Table S1: RQ values measured following treatment of U937 cells with 1.0 µg/mL *VaaV*. All assays were plated in triplicate.

Untreated cells served as reference (negative control). Mean RQ, standard error, and 90% confidence interval (using t-distribution for small set of samples) were calculated if at least two values were measured.

Author Contributions: E.S. and K.K. conceived and designed the experiments; F.B., K.B., and K.G. performed the experiments; A.C. analyzed the data; L.B. and F.B. wrote the manuscript; K.K. refined the manuscript for publication. All authors read and approved the final manuscript.

Acknowledgments: F.B. was supported by the Collegium Talentum 2017 Programme of Hungary. K.K. was supported by the Janos Bolyai Scholarship of the Hungarian Academy of Sciences. Scientific research support was also provided by the Pharmaceutical Talent Center program and Viral Pathogenesis Talent Center program of the University of Pecs.

Conflicts of Interest: The authors declare no conflict of interest.

References

1. Hakansson, A.; Molin, G. Gut microbiota and inflammation. *Nutrients* **2011**, *3*, 637–687. [CrossRef] [PubMed]
2. Chan, P.M.; Tan, Y.S.; Chua, K.H.; Sabaratnam, V.; Kuppusamy, U.R. Attenuation of Inflammatory Mediators (TNF-α and Nitric Oxide) and Up-Regulation of IL-10 by Wild and Domesticated Basidiocarps of Amauroderma rugosum (Blume & T. Nees) Torrend in LPS-Stimulated RAW264.7 Cells. *PLoS ONE* **2015**, *10*, e0139593. [CrossRef]
3. Fujiwara, N.; Kobayashi, K. Macrophages in Inflammation. *Curr. Drug Target Inflamm. Allergy* **2005**, *4*, 281–286. [CrossRef]
4. Van Ginderachter, J.A.; Movahedi, K.; Hassanzadeh Ghassabeh, G.; Meerschaut, S.; Beschin, A.; Raes, G.; De Baetselier, P. Classical and alternative activation of mononuclear phagocytes: Picking the best of both worlds for tumor promotion. *Immunobiology* **2006**, *211*, 487–501. [CrossRef] [PubMed]
5. Anderson, C.F.; Mosser, D.M. A novel phenotype for an activated macrophage: The type 2 activated macrophage. *J. Leukoc. Biol.* **2002**, *72*, 101–106. [CrossRef] [PubMed]
6. Menaldo, D.L.; Bernardes, C.P.; Pereira, J.C.; Silveira, D.S.C.; Mamede, C.C.N.; Stanziola, L.; De Oliveira, F.; Pereira-Crott, L.S.; Faccioli, L.H.; Sampaio, S.V. Effects of two serine proteases from Bothrops pirajai snake venom on the complement system and the inflammatory response. *Int. Immunopharmacol.* **2013**, *15*, 764–771. [CrossRef] [PubMed]
7. Teixeira, C.D.F.P.; Fernandes, C.M.; Zuliani, J.P.; Zamuner, S.F. Inflammatory effects of snake venom metalloproteinases. *Mem. Inst. Oswaldo Cruz* **2005**, *100*, 181–184. [CrossRef]
8. Sunitha, K.; Hemshekhar, M.; Thushara, R.M.; Santhosh, M.S.; Sundaram, M.S.; Kemparaju, K.; Girish, K.S. Inflammation and oxidative stress in viper bite: An insight within and beyond. *Toxicon* **2015**, *98*, 89–97. [CrossRef] [PubMed]
9. Teixeira, C.F.P.; Landucci, E.C.T.; Antunes, E.; Chacur, M.; Cury, Y. Inflammatory effects of snake venom myotoxic phospholipases A2. *Toxicon* **2003**, *42*, 947–962. [CrossRef] [PubMed]
10. Costa, S.K.P.; Camargo, E.A.; Antunes, E. Inflammatory Action of Secretory Phospholipases A2 from Snake Venoms. In *Toxins and Drug Discovery*; Gopalakrishnakone, P., Cruz, L., Luo, S., Eds.; Springer: Dordrecht, The Netherlands, 2017; pp. 35–52. ISBN 978-94-007-6451-4.
11. Wanderley, C.W.S.; Silva, C.M.S.; Wong, D.V.T.; Ximenes, R.M.; Morelo, D.F.C.; Cosker, F.; Aragão, K.S.; Fernandes, C.; Palheta-Júnior, R.C.; Havt, A.; et al. Bothrops jararacussu snake venom-induces a local inflammatory response in a prostanoid- and neutrophil-dependent manner. *Toxicon* **2014**, *90*, 134–147. [CrossRef] [PubMed]
12. Menaldo, D.L.; Bernardes, C.P.; Zoccal, K.F.; Jacob-Ferreira, A.L.; Costa, T.R.; Del Lama, M.P.F.M.; Naal, R.M.Z.G.; Frantz, F.G.; Faccioli, L.H.; Sampaio, S.V. Immune cells and mediators involved in the inflammatory responses induced by a P-I metalloprotease and a phospholipase A2 from Bothrops atrox venom. *Mol. Immunol.* **2017**, *85*, 238–247. [CrossRef] [PubMed]
13. Deka, A.; Sharma, M.; Sharma, M.; Mukhopadhyay, R.; Doley, R. Purification and partial characterization of an anticoagulant PLA2 from the venom of Indian Daboia russelii that induces inflammation through upregulation of proinflammatory mediators. *J. Biochem. Mol. Toxicol.* **2017**, *31*. [CrossRef] [PubMed]
14. Gambero, A.; Thomazzi, S.M.; Cintra, A.C.O.; Landucci, E.C.T.; De Nucci, G.; Antunes, E. Signalling pathways regulating human neutrophil migration induced by secretory phospholipases A2. *Toxicon* **2004**, *44*, 473–481. [CrossRef] [PubMed]

15. Kanashiro, M.M.; De Escocard, R.C.M.; Petretski, J.H.; Prates, M.V.; Alves, E.W.; Machado, O.L.T.; Da Silva, W.D.; Kipnis, T.L. Biochemical and biological properties of phospholipases A2 from Bothrops atrox snake venom. *Biochem. Pharmacol.* **2002**, *64*, 1179–1186. [CrossRef]
16. Landucci, E.C.T.; Toyama, M.; Marangoni, S.; Oliveira, B.; Cirino, G.; Antunes, E.; De Nucci, G. Effect of crotapotin and heparin on the rat paw oedema induced by different secretory phospholipases A2. *Toxicon* **2000**, *38*, 199–208. [CrossRef]
17. Markland, F.S.; Swenson, S. Snake venom metalloproteinases. *Toxicon* **2013**, *62*, 3–18. [CrossRef] [PubMed]
18. De Toni, L.G.B.; Menaldo, D.L.; Cintra, A.C.O.; Figueiredo, M.J.; De Souza, A.R.; Maximiano, W.M.A.; Jamur, M.C.; Souza, G.E.P.; Sampaio, S.V. Inflammatory mediators involved in the paw edema and hyperalgesia induced by Batroxase, a metalloproteinase isolated from Bothrops atrox snake venom. *Int. Immunopharmacol.* **2015**, *28*, 199–207. [CrossRef] [PubMed]
19. Bernardes, C.P.; Menaldo, D.L.; Mamede, C.C.N.; Zoccal, K.F.; Cintra, A.C.O.; Faccioli, L.H.; Stanziola, L.; de Oliveira, F.; Sampaio, S.V. Evaluation of the local inflammatory events induced by BpirMP, a metalloproteinase from Bothrops pirajai venom. *Mol. Immunol.* **2015**, *68*, 456–464. [CrossRef] [PubMed]
20. Fernandes, C.M.; Zamuner, S.R.; Zuliani, J.P.; Rucavado, A.; Gutiérrez, J.M.; Teixeira, C.D.F.P. Inflammatory effects of BaP1 a metalloproteinase isolated from Bothrops asper snake venom: Leukocyte recruitment and release of cytokines. *Toxicon* **2006**, *47*, 549–559. [CrossRef] [PubMed]
21. Du, X.Y.; Clemetson, K.J. Snake venom L-amino acid oxidases. *Toxicon* **2002**, *40*, 659–665. [CrossRef]
22. Pontes, A.S.; da Setúbal, S.D.; Nery, N.M.; Da Silva, F.S.; Da Silva, S.D.; Fernandes, C.F.C.; Stábeli, R.G.; Soares, A.M.; Zuliani, J.P. P38 MAPK is involved in human neutrophil chemotaxis induced by L-amino acid oxidase from Calloselasma rhodosthoma. *Toxicon* **2016**, *119*, 106–116. [CrossRef] [PubMed]
23. Machado, A.R.T.; Aissa, A.F.; Ribeiro, D.L.; Hernandes, L.C.; Machado, C.S.; Bianchi, M.L.P.; Sampaio, S.V.; Antunes, L.M.G. The toxin BjussuLAAO-II induces oxidative stress and DNA damage, upregulates the inflammatory cytokine genes TNF and IL6, and downregulates the apoptotic-related genes BAX, BCL2 and RELA in human Caco-2 cells. *Int. J. Biol. Macromol.* **2018**, *109*, 212–219. [CrossRef] [PubMed]
24. Costa, T.R.; Menaldo, D.L.; Zoccal, K.F.; Burin, S.M.; Aissa, A.F.; de Castro, F.A.; Faccioli, L.H.; Greggi Antunes, L.M.; Sampaio, S.V. CR-LAAO, an L-amino acid oxidase from Calloselasma rhodostoma venom, as a potential tool for developing novel immunotherapeutic strategies against cancer. *Sci. Rep.* **2017**, *7*, 42673. [CrossRef] [PubMed]
25. Georgieva, D.N.; Rypniewski, W.; Perbandt, M.; Jain, M.; Genov, N.; Betzel, C. Crystallization and preliminary X-ray diffraction studies of a toxic phospholipase A2from the venom of Vipera ammodytes meridionalis complexed to a synthetic inhibitor. *Biochim. Biophys. Acta Proteins Proteom.* **2003**, *1650*, 1–3. [CrossRef]
26. Tomovic, L. Systematics of the nose-horned viper (Vipera ammodytes, Linnaeus, 1758). *Herpetol. J.* **2006**, *16*, 191–201.
27. Maretić, T.; Cizelj, I.; Čivljak, R. Venomous snakebites and treatment—On the occassion of the acquisition of new venomous snakes at the Zagreb Zoo and private herpetaria. *Infektoloski Glas.* **2013**, *33*, 11–19.
28. Radonić, V.; Budimir, D.; Bradarić, N.; Luksić, B.; Sapunar, D.; Vilović, K. Envenomation by the horned viper (*Vipera ammodytes* L.). *Mil. Med.* **1997**, *162*, 179–182. [CrossRef] [PubMed]
29. Georgieva, D.; Risch, M.; Kardas, A.; Buck, F.; Von Bergen, M.; Betzel, C. Comparative analysis of the venom proteomes of Vipera ammodytes ammodytes and vipera ammodytes meridionalis. *J. Proteome Res.* **2008**, *7*, 866–886. [CrossRef] [PubMed]
30. Leonardi, A.; Sajevic, T.; Kovačič, L.; Pungerčar, J.; Lang Balija, M.; Halassy, B.; Trampuš Bakija, A.; Križaj, I. Hemorrhagin VaH4, a covalent heterodimeric P-III metalloproteinase from Vipera ammodytes ammodytes with a potential antitumour activity. *Toxicon* **2014**, *77*, 141–155. [CrossRef] [PubMed]
31. Kurtović, T.; Brgles, M.; Leonardi, A.; Balija, M.L.; Križaj, I.; Allmaier, G.; Marchetti-Deschmann, M.; Halassy, B. Ammodytagin, a heterodimeric metalloproteinase from Vipera ammodytes ammodytes venom with strong hemorrhagic activity. *Toxicon* **2011**, *58*, 570–582. [CrossRef] [PubMed]
32. Leonardi, A.; Fox, J.W.; Trampuš-Bakija, A.; Križaj, I. Ammodytase, a metalloprotease from Vipera ammodytes ammodytes venom, possesses strong fibrinolytic activity. *Toxicon* **2007**, *49*, 833–842. [CrossRef] [PubMed]
33. Dinarello, C.A. Interleukin-1 in the pathogenesis and treatment of inflammatory diseases. *Blood* **2011**, *117*, 3720–3732. [CrossRef] [PubMed]

34. Akdis, M.; Burgler, S.; Crameri, R.; Eiwegger, T.; Fujita, H.; Gomez, E.; Klunker, S.; Meyer, N.; O'Mahony, L.; Palomares, O.; et al. Interleukins, from 1 to 37, and interferon-γ: Receptors, functions, and roles in diseases. *J. Allergy Clin. Immunol.* **2011**, *127*, 701–721. [CrossRef] [PubMed]
35. Chaves, F.; Teixeira, C.F.P.; Gutiérrez, J.M. Role of TNF-α, IL-1β and IL-6 in the local tissue damage induced by Bothrops asper snake venom: An experimental assessment in mice. *Toxicon* **2005**, *45*, 171–178. [CrossRef] [PubMed]
36. Santhosh, M.S.; Sundaram, M.S.; Sunitha, K.; Kemparaju, K.; Girish, K.S. Viper venom-induced oxidative stress and activation of inflammatory cytokines: A therapeutic approach for overlooked issues of snakebite management. *Inflamm. Res.* **2013**, *62*, 721–731. [CrossRef] [PubMed]
37. Corasolla Carregari, V.; Stuani Floriano, R.; Rodrigues-Simioni, L.; Winck, F.V.; Baldasso, P.A.; Ponce-Soto, L.A.; Marangoni, S. Biochemical, pharmacological, and structural characterization of new basic PLA2 Bbil-TX from Bothriopsis bilineata snake venom. *Biomed. Res. Int.* **2013**, *2013*, 612649. [CrossRef] [PubMed]
38. De Waal Malefyt, R.; Abrams, J.; Bennet, B.; Figdor, C.G.; de Vries, J.E. Interleukin 10(IL-10) inhibits cytokine synthesis by human monocytes: An autoregulatory role of IL-10 produced by monocytes. *J. Exp. Med.* **1991**, *174*, 1209–1220. [CrossRef] [PubMed]
39. Stone, S.F.; Isbister, G.K.; Shahmy, S.; Mohamed, F.; Abeysinghe, C.; Karunathilake, H.; Ariaratnam, A.; Jacoby-Alner, T.E.; Cotterell, C.L.; Brown, S.G.A. Immune Response to Snake Envenoming and Treatment with Antivenom; Complement Activation, Cytokine Production and Mast Cell Degranulation. *PLoS Negl. Trop. Dis.* **2013**, *7*. [CrossRef] [PubMed]
40. Hernández Cruz, A.; Garcia-Jimenez, S.; Zucatelli Mendonça, R.; Petricevich, V.L. Pro- and anti-inflammatory cytokines release in mice injected with Crotalus durissus terrificus venom. *Mediat. Inflamm.* **2008**, *2008*. [CrossRef] [PubMed]
41. Petricevich, V.L.; Teixeira, C.F.P.; Tambourgi, D.V.; Gutiérrez, J.M. Increments in serum cytokine and nitric oxide levels in mice injected with Bothrops asper and Bothrops jararaca snake venoms. *Toxicon* **2000**, *38*, 1253–1266. [CrossRef]
42. McFadden, C.; Morgan, R.; Rahangdale, S.; Green, D.; Yamasaki, H.; Center, D.; Cruikshank, W. Preferential migration of T regulatory cells induced by IL-16. *J. Immunol.* **2007**, *179*, 6439–6445. [CrossRef] [PubMed]
43. Moreira, V.; Dos-Santos, M.C.; Nascimento, N.G.; da Silva, H.B.; Fernandes, C.M.; D'Império Lima, M.R.; Teixeira, C. Local inflammatory events induced by Bothrops atrox snake venom and the release of distinct classes of inflammatory mediators. *Toxicon* **2012**, *60*, 12–20. [CrossRef] [PubMed]
44. Nunes, D.C.O.; Rodrigues, R.S.; Lucena, M.N.; Cologna, C.T.; Oliveira, A.C.S.; Hamaguchi, A.; Homsi-Brandeburgo, M.I.; Arantes, E.C.; Teixeira, D.N.S.; Ueira-Vieira, C.; et al. Isolation and functional characterization of proinflammatory acidic phospholipase A2 from Bothrops leucurus snake venom. *Comp. Biochem. Physiol. C Toxicol. Pharmacol.* **2011**, *154*, 226–233. [CrossRef] [PubMed]
45. Wei, X.L.; Wei, J.F.; Li, T.; Qiao, L.Y.; Liu, Y.L.; Huang, T.; He, S.H. Purification, characterization and potent lung lesion activity of an l-amino acid oxidase from Agkistrodon blomhoffii ussurensis snake venom. *Toxicon* **2007**, *50*, 1126–1139. [CrossRef] [PubMed]
46. Burke, S.M.; Issekutz, T.B.; Mohan, K.; Lee, P.W.K.; Shmulevitz, M.; Marshall, J.S. Human mast cell activation with virus-associated stimuli leads to the selective chemotaxis of natural killer cells by a CXCL8-dependent mechanism. *Blood* **2008**, *111*, 5467–5476. [CrossRef] [PubMed]
47. Da Setubal, S.S.; Pontes, A.S.; Nery, N.M.; Bastos, J.S.F.; Castro, O.B.; Pires, W.L.; Zaqueo, K.D.; de Calderon, L.A.; Stábeli, R.G.; Soares, A.M.; et al. Effect of Bothrops bilineata snake venom on neutrophil function. *Toxicon* **2013**, *76*, 143–149. [CrossRef] [PubMed]
48. Meyer, O. Interferons and autoimmune disorders. *Jt. Bone Spine* **2009**, *76*, 464–473. [CrossRef] [PubMed]
49. Hervas-Stubbs, S.; Perez-Gracia, J.L.; Rouzaut, A.; Sanmamed, M.F.; Le Bon, A.; Melero, I. Direct effects of type I interferons on cells of the immune system. *Clin. Cancer Res.* **2011**, *17*, 2619–2627. [CrossRef] [PubMed]
50. McNab, F.; Mayer-Barber, K.; Sher, A.; Wack, A.; O'Garra, A. Type I interferons in infectious disease. *Nat. Rev. Immunol.* **2015**, *15*, 87–103. [CrossRef] [PubMed]
51. Muller, V.D.M.; Russo, R.R.; Oliveira Cintra, A.C.; Sartim, M.A.; De Melo Alves-Paiva, R.; Figueiredo, L.T.M.; Sampaio, S.V.; Aquino, V.H. Crotoxin and phospholipases A2 from Crotalus durissus terrificus showed antiviral activity against dengue and yellow fever viruses. *Toxicon* **2012**, *59*, 507–515. [CrossRef] [PubMed]

52. Cecilio, A.B.; Caldas, S.; De Oliveira, R.A.; Santos, A.S.B.; Richardson, M.; Naumann, G.B.; Schneider, F.S.; Alvarenga, V.G.; Estevão-Costa, M.I.; Fuly, A.L.; et al. Molecular characterization of Lys49 and Asp49 phospholipases A2 from snake venom and their antiviral activities against Dengue virus. *Toxins* **2013**, *5*, 1780–1798. [CrossRef] [PubMed]
53. Ruddle, N.H. Lymphotoxin and TNF: How it all began—A tribute to the travelers. *Cytokine Growth Factor Rev.* **2014**, *25*, 83–89. [CrossRef] [PubMed]
54. Bauer, J.; Namineni, S.; Reisinger, F.; Zöller, J.; Yuan, D.; Heikenwälder, M. Lymphotoxin, NF-κB, and cancer: The dark side of cytokines. *Dig. Dis.* **2012**, *30*, 453–468. [CrossRef] [PubMed]
55. Aggarwal, B.B.; Gupta, S.C.; Kim, J.H. Historical perspectives on tumor necrosis factor and its superfamily: 25 years later, a golden journey. *Blood* **2012**, *119*, 651–665. [CrossRef] [PubMed]
56. Balogh, P. *Developmental Biology of Peripheral Lymphoid Organs*; Springer: Berlin/Heidelberg, Germany, 2011; ISBN 978-3-642-14428-8.
57. Clissa, P.B.; Laing, G.D.; Theakston, R.D.G.; Mota, I.; Taylor, M.J.; Moura-da-Silva, A.M. The effect of jararhagin, a metalloproteinase from Bothrops jararaca venom, on pro-inflammatory cytokines released by murine peritoneal adherent cells. *Toxicon* **2001**, *39*, 1567–1573. [CrossRef]
58. Pontes, A.S.; da Setúbal, S.S.; Xavier, C.V.; Lacouth-Silva, F.; Kayano, A.M.; Pires, W.L.; Nery, N.M.; De Castro, O.B.; Da Silva, S.D.; Calderon, L.A.; et al. Effect of l-amino acid oxidase from Calloselasma rhodosthoma snake venom on human neutrophils. *Toxicon* **2014**, *80*, 27–37. [CrossRef] [PubMed]

frontiers in Endocrinology

ORIGINAL RESEARCH
published: 18 June 2019
doi: 10.3389/fendo.2019.00369

"Beige" Cross Talk Between the Immune System and Metabolism

*Krisztina Banfai[1,2], David Ernszt[2,3], Attila Pap[4], Peter Bai[5,6,7,8], Kitti Garai[1,2], Djeda Belharazem[9], Judit E. Pongracz[1,2] and Krisztian Kvell[1,2]**

[1] Department of Pharmaceutical Biotechnology, Faculty of Pharmacy, University of Pécs, Pécs, Hungary, [2] Szentagothai Research Center, University of Pécs, Pécs, Hungary, [3] Department of Physiology, Medical School, University of Pécs, Pécs, Hungary, [4] Department of Biochemistry and Molecular Biology, Faculty of Medicine, University of Debrecen, Debrecen, Hungary, [5] Medical Chemistry, Faculty of Medicine, University of Debrecen, Debrecen, Hungary, [6] MTA-DE Cell Biology and Signaling Research Group, Debrecen, Hungary, [7] MTA-DE Lendulet Laboratory of Cellular Metabolism, Debrecen, Hungary, [8] Research Center for Molecular Medicine, University of Debrecen, Debrecen, Hungary, [9] Department of Pathology, University Hospital of Mannheim, Mannheim, Germany

With thymic senescence the epithelial network shrinks to be replaced by adipose tissue. Transcription factor TBX-1 controls thymus organogenesis, however, the same TBX-1 has also been reported to orchestrate beige adipose tissue development. Given these different roles of TBX-1, we have assessed if thymic TBX-1 expression persists and demonstrates this dualism during adulthood. We have also checked whether thymic adipose involution could yield beige adipose tissue. We have used adult mouse and human thymus tissue from various ages to evaluate the kinetics of TBX-1 expression, as well as mouse (TEP1) and human (1889c) thymic epithelial cells (TECs) for our studies. Electron micrographs show multi-locular lipid deposits typical of beige adipose cells. Histology staining shows the accumulation of neutral lipid deposits. qPCR measurements show persistent and/or elevating levels of beige-specific and beige-indicative markers (TBX-1, EAR-2, UCP-1, PPAR-gamma). We have performed miRNome profiling using qPCR-based QuantStudio platform and amplification-free NanoString platform. We have observed characteristic alterations, including increased miR21 level (promoting adipose tissue development) and decreased miR34a level (bias toward beige adipose tissue differentiation). Finally, using the Seahorse metabolic platform we have recorded a metabolic profile (OCR/ECAR ratio) indicative of beige adipose tissue. In summary, our results support that thymic adipose tissue emerging with senescence is *bona fide* beige adipose tissue. Our data show how the borders blur between a key immune tissue (the thymus) and a key metabolic tissue (beige adipose tissue) with senescence. Our work contributes to the understanding of cross talk between the immune system and metabolism.

Keywords: thymus senescence, beige adipose tissue, TBX-1, UCP-1, PPARgamma

OPEN ACCESS

Edited by:
Jie Chen,
Xiamen University, China

Reviewed by:
Lluis Tort,
Autonomous University of Barcelona, Spain
Mark Klitgaard Nøhr,
University of Copenhagen, Denmark

****Correspondence:***
Krisztian Kvell
kvell.krisztian@pte.hu

Specialty section:
This article was submitted to Experimental Endocrinology, a section of the journal Frontiers in Endocrinology

Received: *11 March 2019*
Accepted: *24 May 2019*
Published: *18 June 2019*

Citation:
Banfai K, Ernszt D, Pap A, Bai P, Garai K, Belharazem D, Pongracz JE and Kvell K (2019) "Beige" Cross Talk Between the Immune System and Metabolism. Front. Endocrinol. 10:369. doi: 10.3389/fendo.2019.00369

INTRODUCTION

In human the degenerative process of thymic adipose involution is already detectable in childhood and accelerates with puberty due to hormonal (sex-steroid) induction (1–3). The process shows identical kinetics in mouse. Also, we have developed a model whereby TECs are treated by a steroid (using Dx or dexamethasone) thus both *in vivo* and *in vitro* model systems are readily available (4) As for all adipose tissues subtypes, thymic adipose involution is orchestrated by transcription

factor PPARgamma (5–7). It is estimated that by the age of 50 years in human (approx. 12 months in mouse), the thymus loses approx. Ninety percent of its function: naïve T-cell production (8, 9). The consequences of impaired thymus function are profound: elevated incidence of infections, cancer and autoimmune disorders observed at senior ages (10, 11). This poses a significant burden on health-care and health-insurance systems, while simultaneously lowering the quality of life in the elderly.

Transcription factor TBX-1 is a key molecular player in the formation of the third pharyngeal pouch involved in thymus organogenesis during embryonic development (12). Human patients with 22q11.2DS impairing TBX-1 often have thymus hypoplasia or aplasia. In accordance, Tbx-1^{null} mice develop severe pathologies in tissues derived from the third pharyngeal pouch, including hypoplasia of the thymus (13, 14). In these cases, impaired thymus organogenesis leads to deficient thymocyte development, naive T-cell production, and immune functions (15). However, recently it has also been reported that the role of TBX-1 in thymus organogenesis is more complex. Ectopic expression of TBX-1 may suppress transcription factor FoxN1, the mastermind of thymic epithelial identity (16). The issue was investigated in the embryonic setting, but the potential role of persistent TBX-1 expression during adulthood has not been addressed.

TBX-1 has another pivotal role in the development and function of a recently described subtype of adipose tissue: beige adipose tissue (17–20). White adipose tissue stores energy, brown adipose tissue generates heat (via NST or non-shivering thermogenesis), while beige adipocytes act as intermediates. Beige adipocytes respond to adrenergic stimuli by thermogenesis (21). TBX-1 is considered as a beige-specific marker, but other beige-indicative markers have also been described. Mitochondrial uncoupling proteins (mostly UCP-1) have been reported to be expressed by brown / beige adipose tissue. EAR2 (also known as Nr2f6) was reported to efficiently promote adipose tissue development with beige bias, while CD137 (also known as Tnfrsf9) is an acknowledged beige adipocyte surface marker (22).

The adult thymus expresses TBX-1 and UCP-1 in the stromal compartment, both known to promote beige adipose tissue development. Yet to date thymic adipose tissue that develops with age has not been accurately positioned on this white-beige-brown continuum of adipose tissue subtypes, despite recent cellular analysis from an adipocyte perspective (23–26). For this reason, we have characterized senescence-related thymic adipose tissue using molecular, cellular and histological markers, at structural and ultra-structural levels, using both mouse and human samples. Additionally, we have also performed metabolic profiling and complete miRNome analysis using both PCR-based and amplification-free platforms.

METHODS

Cell Cultures

For *in vitro* experiments primary-derived (BALB/c) thymic epithelial cells were used (TEP1) as reported previously (cell source: Prof. G. Anderson, University of Birmingham, UK) (27). Briefly, the cells were cultured in DMEM (Dulbecco's Modified Eagle's medium Lonza) supplemented with 10% FCS, penicillin, streptomycin and β-mercapto-ethanol. Human thymus-derived 1889c thymic carcinoma cells were cultured in RPMI 1640 (Roswell Park Memorial Institute medium, Lonza) containing 10% FCS, penicillin, streptomycin, L-Glutamine and Hepes (28, 29). Adipose differentiation of TEP1 and 1889c cells was induced by steroid treatment. Briefly, experiments differentiation was induced by dexamethasone alone (Dx) as added to complete DMEM and RPMI medium. Cells were treated with Dx at a final concentration of 1 μM for 1 week.

Animal Samples

Thymus lobes were used from C57BL/6J mice at 1, 6, 8, 12, 14, 18, and 21 months of age. Mice were housed under minimal disease (MD) conditions. Animal rooms were ventilated 15 times/h with filtered air, mice received autoclaved pellet diet (Altromin VRF1) and tap water *ad libitum*. The cages contained sterilized bedding. Room lighting was automated with 12 h light and 12 h dark periods. Room temperature was 21 ± 2°C, relative humidity was between 30 and 60%. Mice were kept in the Laboratory Animal Core Facility of the University. Experimental procedures were carried out according to the "1988/XXVIII act of the Hungarian Parliament on Animal Protection (243/1988)" which complies with recommendations of the Helsinki Declaration. All animal experiments were performed with the consent of the Ethics Committee on Animal Research of the University (ref. no.: #BA02/2000-46/2016).

Enrichment of Primary Cells

Mouse thymic epithelial cells were isolated by MACS cell separation. Briefly, mouse thymic lobes (1 month-old or 12 month-old) were digested with type F collagenase from C. hystolyticum (3mg/ml, Sigma-Aldrich) for 2 h, with stirring in every 20 min, then washed with DMEM. Cell suspensions were then labeled with anti-EpCAM1 antibody (1:100, rat monoclonal antibody clone: G8.8) and washed with MACS-buffer (2% FCS, 1mM EDTA in PBS) followed by incubation with Dynabeads sheep anti-rat IgG-coated beads (Invitrogen) The EpCAM+-cells were separated with EasySep column-free cell isolation platform (Stemcell Technologies) according to the manufacturer's instructions. Isolated cells were used for total RNA isolation and subsequent qPCR analysis.

Human Thymus Samples

Formalin-fixed, paraffin-embedded (FFPE) human thymus samples from 18, 23, 42, 44, and 58 years of age were provided by the Department of Pathology, Faculty of Medicine, University of Pecs, Hungary. Experiments involving human samples were performed with the consent of the Regional and Local Ethics Committee of Clinical Center of the University (ref. no.: 6069/2016) according to their guidelines. All subjects gave written informed consent in accordance with the Declaration of Helsinki.

Transmission Electron Microscopy

Cells were harvested and pelleted then fixed with PBS containing 2.5% glutaraldehyde overnight at 4°C. Following fixation, pellets were mixed in 3% porcine gelatin (Sigma-Aldrich). Hardened small blocks of approximately 1 mm^3 were cut. Blocks were post-fixed in 1% osmium-tetroxide in PBS for 1 h at 4°C and dehydrated with increasing concentration of ethanol. Uranyl-acetate (1%) was added in 70% ethanol to increase contrast. After complete dehydration in ascending ethanol series, blocks were transferred to propylene-oxide twice for 4 min. Then blocks were immersed in the mixture of propylene-oxide and Durcupan resin (Sigma-Aldrich) for 30 min. Later blocks were placed into Durcupan-containing tin-foil boats overnight, and embedded into gelatin capsule filled with Durcupan resin (Sigma-Aldrich). Following polymerization and hardening of the resin at 56 °C for 72 h, semi thin sections were cut with Leica Ultracut ultramicrotom, mounted on glass slides, stained with toluidine-blue and examined with Olympus BX50 light microscope. Then serial ultra-thin sections were cut by ultramicrotom, and mounted on mesh grids. Ultra-thin sections were contrasted by uranyl-acetate and lead-citrate, and examined using JEOL 1200EX-II electron microscope.

Immune-Histochemistry

Human thymus lobes were fixed in paraformaldehyde (4% PFA in PBS) then paraffin embedded. 5μm thick sections were stained with immunohistochemistry method as described earlier (30). First, slides were rinsed in heated xylene then washed with a descending series of alcohol. After deparaffinization slides were rehydrated and antigen retrieval was performed in Target Retrieval Solution (pH 6 DAKO) at 97°C for 20–30 min. Following wash in dH_2O and endogenous peroxidase activity was blocked with 3% H_2O_2 in TBS (pH 7.4) for 15 min. Then slides were washed with TBS containing Tween (0.05%, pH 7.4). Pre-blocking was carried out with 3% BSA in TBS for 20 min followed by overnight incubation with a-TBX-1 (1:100, rabbit polyclonal antibody, Sigma-Aldrich) primary antibody at 4°C. After the incubation slides were washed with TBS then incubated with peroxidase conjugated secondary antibody (1:100, Polyclonal Goat Anti-Rabbit IgG, DAKO) for 90 min. Labeling was visualized with liquid DAB Substrate Chromogen System (DAKO). Hematoxylin served for nuclear counterstaining. Slides were mounted with Faramount Aqueous Mounting Medium (DAKO). Histological evaluation was performed with Panoramic MIDI digital slide scanner (3DHistech) and images were captured with CaseViewer. Image analysis was made with ImageJ / IHC toolbox.

Immune-Fluorescent Staining

Immune-fluorescent staining was performed on 8μm cryostat thymus sections. Cytospin technique was used to spin TEP1 and 1889c cells onto glass slides (4). Slides were fixed in cold acetone, then dried and blocked using 5% BSA in PBS for 20 min before staining with fluorochrome conjugated or primary antibodies: a-EpCAM-FITC (1:100, clone: G8.8,), a-UCP-1 (1:100, rabbit polyclonal antibody, Abcam) a-TBX-1 (1:100, rabbit polyclonal antibody, Sigma-Aldrich), a-PPAR-gamma (1:100, rabbit monoclonal antibody, Cell Signaling Technology). For secondary antibody Alexa-555 conjugated a-rabbit goat IgG (1:200, Life Technologies) was used. Fluorescent lipid staining was performed on paraformaldehyde (4%) fixed TEP1 and 1889c cytospin slides with LipidTOX Red dye (1:200, Invitrogen). For nuclear counterstain DAPI (Life Technologies) was used. Sections were imaged using a Nikon Eclipse Ti-U microscope equipped with a CCD camera (Andor Zyla 5.5) and NIS-Elements software.

Metabolic Profiling

The use of TEP1 cells for Seahorse metabolic profiling was started by pilot experiments for optimal starting cell number, duration of differentiation, differentiation medium etc. Accordingly, 15,000 cells/well were cultured for 9 days using standard MDI differentiation protocol (31). This was followed by the evaluation of their metabolic profile using the Seahorse XF 96 platform (Seahorse Bioscience). Cells were plated into Seahorse cell plates at confluence and were left to attach overnight. The next day, cells were subject to oxymetry measurement. After recording baseline oxygen consumption cells were treated with butyril-cAMP (500 μM), oligomycin (2 μM), and antimycin (10 μM). Antimycin-resistant oxygen consumption was considered as background and was subtracted from all values. Baseline oxygen consumption, membrane leak (OCR, after oligomycin treatment) was calculated. Glycolysis was assessed through the extracellular acidification value (ECAR, before oligomycin treatment) and the ECAR/OCR values were calculated. Negative values were omitted in calculations.

RNA Isolation, cDNA Preparation, qRT-PCR, TaqMan Array

Total RNA of enriched thymic epithelial cells, TEP1 and 1889c cells was isolated with the NucleoSpin RNAII kit (Macherey-Nagel). cDNA was prepared using the High Capacity cDNA Reverse Transcription kit (Applied Biosystems). For qPCR analysis the StepOnePlus (Applied Biosystems) platform was used with SensiFAST SYBR Hi-ROX Mix (Bioline) as well as PikoReal™ Real-Time PCR System (Thermo Fisher Scientific) using Luminaris Color HiGreen qPCR Master Mix (Thermo Fisher Scientific) (for primer list see **Table 1**). Gene expression was normalized to β-actin, GUSB and HPRT1 housekeeping genes. Reverse transcription of 1889c RNA samples for miRNA analysis was completed with Megaplex™ RT Primers specific to human Pool A (Cat. No.: 4399966) and Pool B (Cat. No.: 4444281). MiRNA profiling was performed on Applied Biosystems Quantstudio™ 12K Flex Real-Time PCR System platform using TaqMan™ Array Human MicroRNA A (Applied Biosystems, Cat. No.: 4398965) and B Card (Applied Biosystems, Cat. No.: 4444910) containing 6 housekeeping genes (RNU44, RNU48, ath-miR159a and 4 U6 snRNAs) and 377 human miRNAs. Additionally 600 ng of total RNA was mixed with TaqMan™ Fast Universal PCR Master Mix (2X), no AmpErase™ UNG (Applied Biosystems, Cat. No.: 4364103) for each array

TABLE 1 | List of mouse and human primer sequences.

Gene Name	Mouse primer sequence	Human primer sequence
Actin-for	GGGAGGGTGAGGGACTTCC	GCGCGGCTACAGCTTCA
Actin-rev	TGGGCGCTTTTGACTCAGGA	CTTAATGTCACGCACGATTTCC
GUSB-for	AAATGGAGTGCGTGTTGGGT	GATGCTGTACCCCCAGGA
GUSB-rev	CGGTACCATTGCTGCTCGAA	GTCGGTTGTCAGAGAAGTCG
HPRT-for	TTGCTCGAGATGTCATGAAGGA	CTGGCGTCGTGATTAGTGAT
HPRT-rev	ATGTAATCCAGCAGGTCAGCA	ACATCTCGAGCAAGACGTTC
CD137-for	CGTGCAGAACTCCTGTGATAAC	CCTGAGCTACAAAGAGGACAC
CD137-rev	CTCCACCTATGCTGGAGAAGG	GTGCAGCGCAAGTGAAAC
Ear2-for	CCTGTACCCCAGAACTCCA	GCAAGCATTACGGTGTCTTC
Ear2-rev	CAGATGAGCAAAGGTGCAAA	GATCTGGCAGTCACGGTTG
PPARg-for	TGTCTCACAATGCCATCAGGT	GGTGGCCATCCGCATCT
PPARg-rev	TCTTTCCTGTCAAGATCGCCC	GCTTTTGGCATACTCTGTGATCTC
TBX1-for	GGCAGGCAGACGAATGTTC	CTACGACCACTATCTCGGGG
TBX1-rev	TTGTCATCTACGGGCACAAAG	TGGGGCAATAGTCGTAGGAG
UCP1-for	GGCCTCTACGACTCAGTCCA	ACAATCACCGCTGTGGTAAA
UCP1-rev	TAAGCCGGCTGAGATCTTGT	GTAGAGGCCGATCCTGAGAG

card. Gene expressions were analyzed using Expression Suite Software version 1.1.

NanoString System Assay

One hundred nanogram of total RNA was used to detect up to 800 miRNA targets with nCounter SPRINT Profiler (NanoString Technologies) using nCounter® Human v3 miRNA Expression Assay. Sample preparation was performed with nCounter® CodeSet (NanoString Technologies) following annealing, ligation and purification. Hybridization protocol was completed at 65°C and 12 h long according to the manufacturer's instructions. Quantified data was analyzed using nSolver™ Analysis Software version 4.0. Threshold count was determined using negative controls as background noise. Gene expression changes were visualized on heat map using GraphGad Prism version 7.04.

Statistical Analysis

All experiments were performed at least on three occasions, representative experiments are shown. Measures were obtained in triplicates, data are presented as mean and ±SD as error bars. For statistical analysis GraphPad Prism software and SPSS Statistics version 22.0 was used. To evaluate the kinetics of TBX-1 expression with age in both mouse and human samples normality distribution was tested using Shapiro-Wilk test ($n < 50$). In case of human samples our data met the assumption of homogeneity of variances, so parametric one-way ANOVA with Tukey's honestly significant difference (HSD) *post hoc* test was used. To determine the significant differences of mouse samples non-parametric Kruskal-Wallis test was used. For further cases two-tailed student's *t*-test was applied. Significant differences are shown by asterisks (ns for $p > 0.05$, $^{*}p \leq 0.05$, $^{**}p \leq 0.01$, $^{***}p \leq 0.001$).

RESULTS

Aging and Steroid-Induced TECS Show Beige Adipocyte Markers

Thymic senescence is accompanied by the appearance of adipose tissue. Mediastinal location and local FGF21 production are characteristic to the thymus and both were reported to promote beige adipose tissue development (23–25). For this reason we searched for the up-regulation of beige adipocyte markers in the adult thymus tissue and its model system: steroid-induced TECs.

Aging Up-Regulates key Beige Adipocyte Marker in Human Thymus Tissue

Using a pilot set of human thymic FFPE samples of various adult ages (18, 23, 42, 44, and 58 years) we performed immune-histochemistry staining for beige adipose tissue-specific marker TBX-1 (**Figures 1A–E**). TBX-1 expression (enzyme reaction in brown) appears to persist throughout adulthood. Normalization to hematoxylin nuclear counterstain (in blue) shows that TBX-1 staining intensity transiently decreases at young adult age (23 years) to show rebound at later ages (**Figure 1F**). In other words: TBX-1 expression may present a bimodal nature with elevations at both young and adulthood ages and an in-between transient decrease during young adulthood. The histological appearance of adipocytes is observed from 44 years of age onwards in this series.

Further Beige Adipocyte Markers Are Also Up-Regulated in Steroid-Induced Human TECs

As reported previously molecular level events are similar in the aging thymus and steroid-induced TECs in the mouse setting (4, 6). Accordingly, Dx-treatment significantly up-regulated ($p < 0.01$) pan-adipocyte marker PPAR-gamma expression in the human 1889c TEC line (**Figures 2A,B,I**). We have evaluated 1889c human TECs for the expression of beige-specific and beige-indicative protein markers as well following Dx-treatment. Similar to human thymus sections above, 1889c cells showed persistent and increasing ($p < 0.05$) TBX-1 expression following Dx-treatment (**Figures 2C,D,I**). UCP-1 expression showed only indicative (not significant) increase upon Dx-treatment (**Figures 2E,F,I**). Lipid accumulation was also tested, using a fluorescent dye (LipidTox Red) specific for neutral lipid deposits. The staining showed that Dx-treatment triggers significant ($p < 0.05$) accumulation of neutral lipid deposits (**Figures 2G–I**) in harmony with our previous reports (4, 6).

Aging Up-Regulates key Beige Adipocyte Marker in Mouse Thymus Tissue

Using a pilot set of mouse thymic cryosections of various ages (1, 6, 8, 12, 14, 18, and 21 months) we performed immune-fluorescent staining for beige adipose tissue-specific marker TBX-1 (**Figures 3A–G**). TBX-1 expression (in red) appears to persist throughout adulthood in the mouse similar to human above. EpCAM-1 staining (in green) shows medullary areas to demonstrate histological organization. Normalization

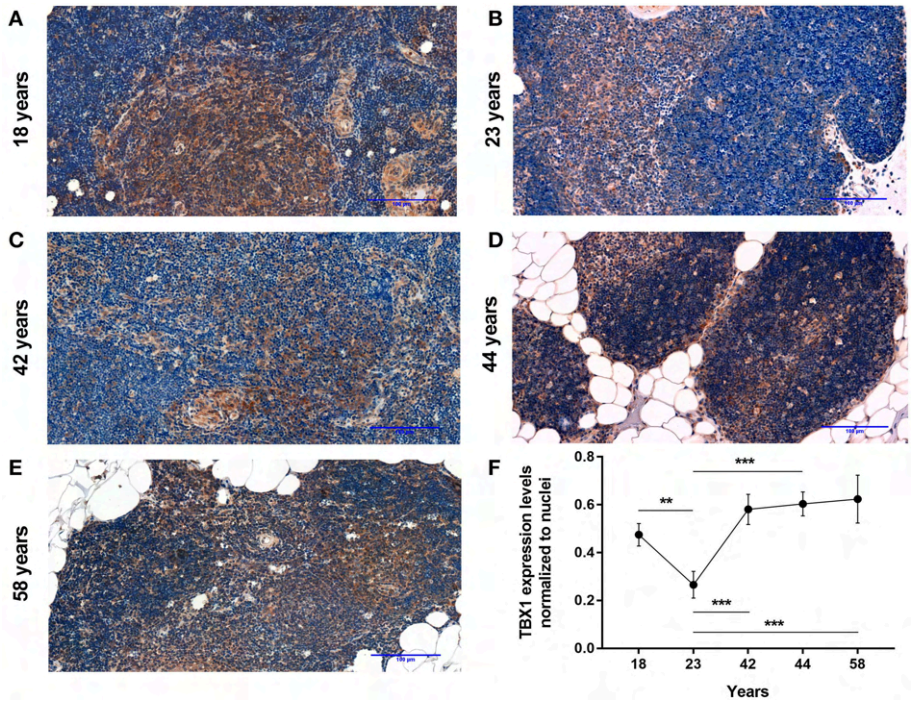

FIGURE 1 | Kinetics of TBX-1 expression in the adult human thymus with age. Human thymic FFPE sections from different ages (18, 23, 42, 44, and 58 years) were evaluated by immune-histochemical staining **(A–E)**, respectively. Brown color reaction (DAB) shows TBX-1 expression along with hematoxylin nuclear counter-staining. Please note signs of adipose degeneration (vacuoles) at elevated ages. TBX-1 staining was normalized to nuclear counter-stain and is shown as relative value **(F)**. Please note that relative TBX-1 expression shows a transient decrease at young adult age (23 years of age). Significant differences are shown by asterisks (**$p \leq 0.01$, ***$p \leq 0.001$). Data were calculated from three slides and representative slide is shown. For exact numerical values and standard error of mean please refer to **Supplementary Data Sheet**.

to DAPI nuclear counterstain (in blue, not shown here) reveals that TBX-1 staining intensity transiently decreases at adult mid-term (12–14 months) to show rebound at senior ages (**Figure 3H**). In other terms: TBX-1 expression potentially appears to be bimodal in the mouse as well showing elevation at both young and senior ages with a transient in-between decrease during adulthood. Murine kinetics of TBX-1 expression resembles the previously shown human kinetics but with higher resolution in time. Please note medullary involution observed from 14 months of age onwards in line with our previous reports (4, 6).

Further Beige Adipocyte Markers Are Also Up-Regulated in Steroid-Induced Mouse TECs

As reported previously focusing on PPARgamma expression molecular level events are similar in the aging thymus and steroid-induced TECs in the mouse setting (4, 6). We have evaluated TEP1 mouse TECs for the expression of beige-specific and beige-indicative protein markers after Dx-treatment. TEP1 cells showed persistent, unchanged TBX-1 expression following Dx-treatment (**Figures 4A,B,I**). UCP-1 expression showed significant ($p < 0.01$) increase following Dx-treatment (**Figures 4C,D,I**). Lipid accumulation was also tested (LipidTox Red as above). The staining showed that Dx-treatment results in significant ($p < 0.05$) accumulation of neutral lipid deposits (**Figures 4E,F,I**) in accordance with our previous reports (4, 6). Ultra-structural imaging by TEM shows the appearance of multi-locular intracellular lipid deposits (indicated by asterisks) upon Dx-treatment, reminiscent of beige adipose tissue (**Figures 4G,H**).

Steroid-Induced TECs Show Beige Adipocyte Metabolic Profile

There is a significant difference between white, brown and beige adipose tissue metabolic traits. In search of further evidence we have characterized the metabolic fingerprint of Dx-induced mouse TECs (TEP1).

The metabolic fingerprint of TEP1 cells treated with Dx (as part of MDI differentiation medium) was assayed using the Seahorse platform (**Figure 5**). MDI cells showed significantly higher basal OCR values compared to control cells ($p < 0.001$) (**Figure 5A**). Of note cAMP-induced OCR was rapid (30 min post-treatment) and lasted shorter than in previous reports (32, 33). In line with elevated UCP-1 expression oligomycin-resistant respiration was significantly higher in MDI cells than in control cells ($p < 0.001$) (**Figure 5B**). Although we have recorded increased glycolysis marked by significantly increased ECAR values ($p < 0.001$) (**Figure 5C**), the significantly increased ratio of basal OCR and ECAR ($p < 0.001$) (**Figure 5D**) in MDI cells suggests their dependence on mitochondrial oxidation.

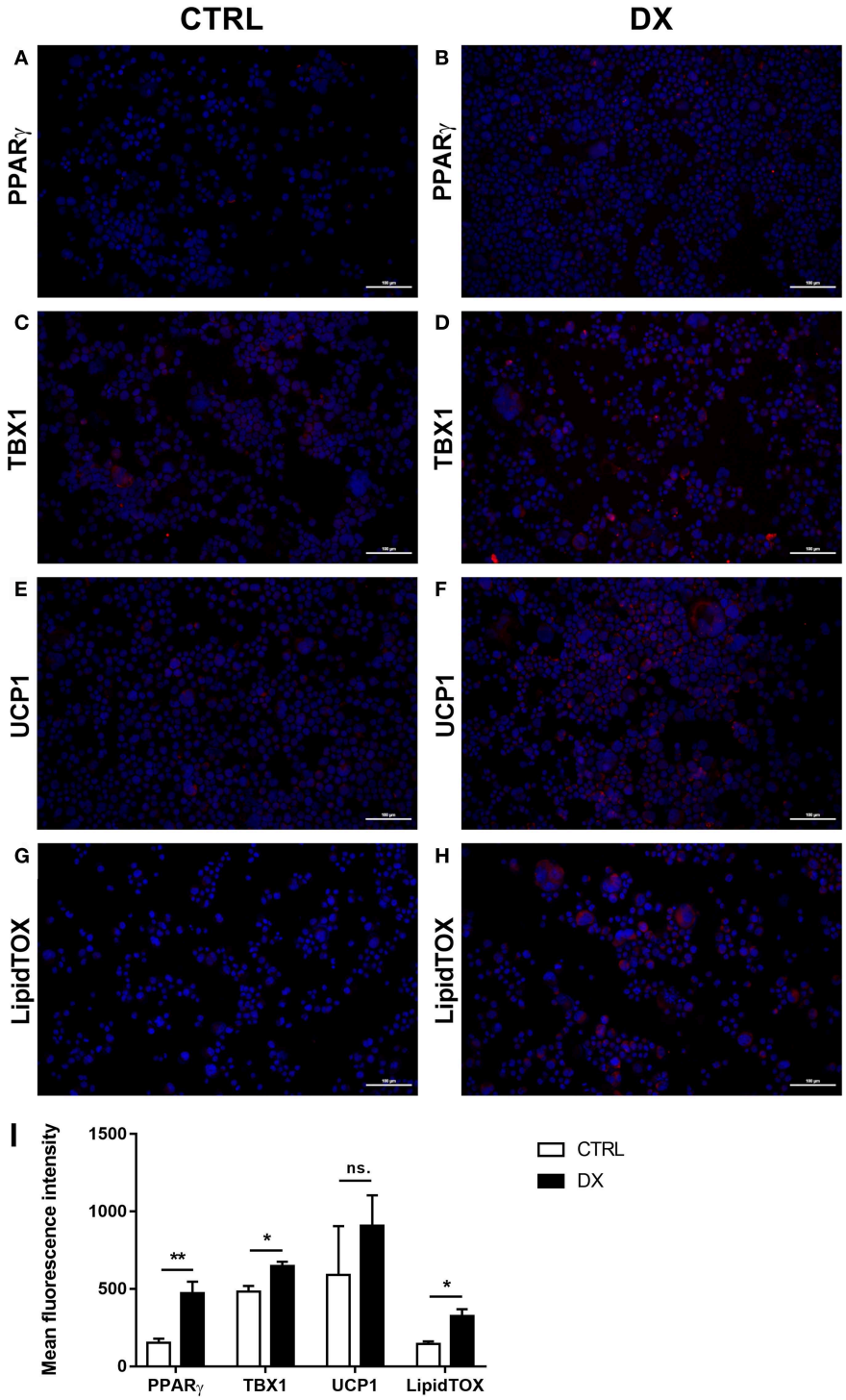

FIGURE 2 | Beige adipocyte marker expression and lipid accumulation in steroid-induced human TECs. Cytospin slides of control (Ctrl) and steroid-induced (Dx) 1889c cells were stained by immune-fluorescence. Adipose tissue mastermind transcription factor PPARgamma **(A,B)**, beige-specific marker TBX-1 **(C,D)** and beige-indicative marker UCP-1 **(E,F)** was evaluated in red (Alexa555). Neutral lipid deposits were stained with LipidTOX Red dye **(G,H)**. DAPI staining was also applied as fluorescent nuclear counter stain in all cases. PPAR-gamma, TBX-1, UCP-1 and LipidTOX staining relative to DAPI staining is also shown by histograms **(I)**. PPAR-gamma and TBX-1 show significant increase, UCP-1 remains unchanged, while neutral lipid deposits show significant increase following Dx-induction. Significant differences are shown by asterisks ($^{*}p \leq 0.05$, $^{**}p \leq 0.01$). Data were calculated from six slides, representative slide is shown. For exact numerical values and standard error of mean please refer to **Supplementary Data Sheet**.

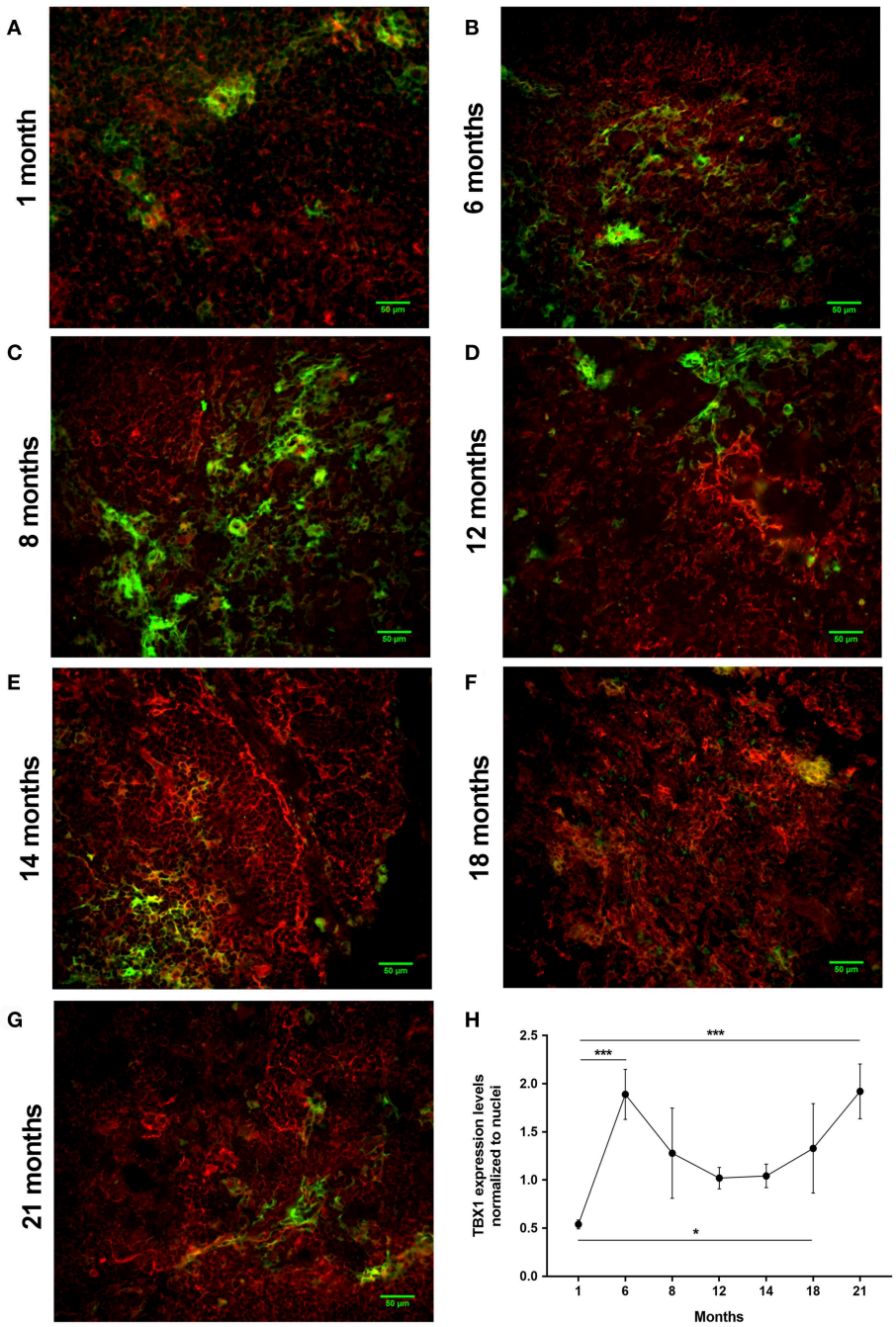

FIGURE 3 | Kinetics of TBX-1 expression in the adult mouse thymus with age. Murine thymic frozen sections from different ages (1, 6, 8, 12, 14, 18, and 21 months) were evaluated by immune-fluorescent staining **(A–G)**, respectively. Epithelial network is shown in green (EpCAM1-FITC) while TBX-1 expression is shown in red (TBX1-Alexa555) fluorescence. Please note signs of degeneration (auto-fluorescence) at elevated ages. Please also note that TBX-1 staining pattern localizes to both nuclear and cytoplasmic bodies in accordance with The Human Protein Atlas: http://www.proteinatlas.org/ENSG00000184058-TBX1/cell. TBX-1 staining was normalized to DAPI nuclear counter-stain (not shown) and is presented as relative value **(H)**. Please note that relative TBX-1 expression shows a transient decrease at adult age (12 months of age). Significant differences are shown by asterisks (*$p \leq 0.05$, ***$p \leq 0.001$). Data were calculated from three slides, representative slide is shown. For exact numerical values and standard error of mean please refer to **Supplementary Data Sheet**.

Taking the observed increase in basal OCR value, OCR/ECAR ratio, cAMP-response, and oligomycin-resistant respiration into consideration, these suggest that MDI-differentiated TECs possess a beige metabolic fingerprint in accordance with the up-regulation of beige-specific and beige-indicative markers shown above.

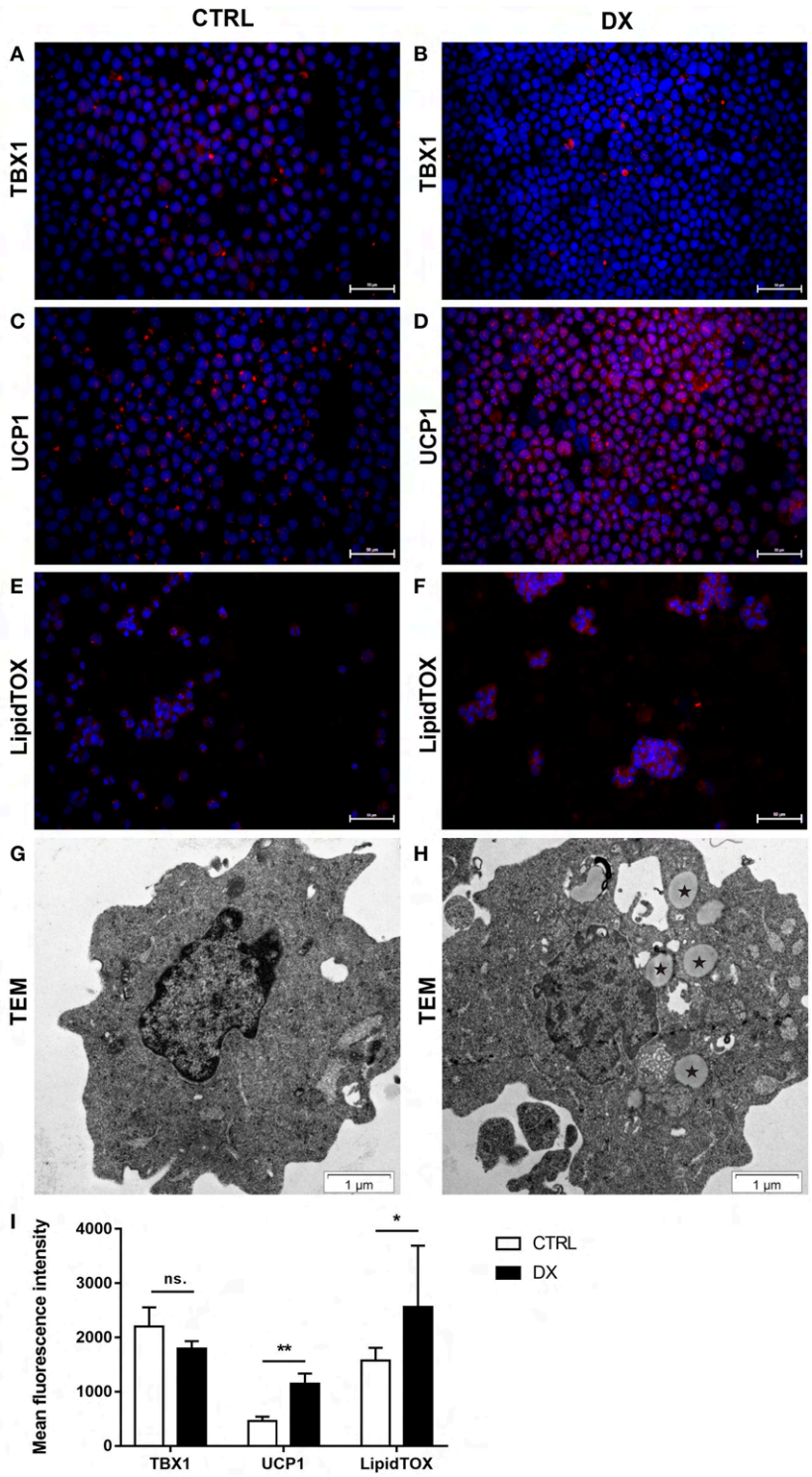

FIGURE 4 | Beige adipocyte marker expression and lipid accumulation in steroid-induced mouse TECs. Cytospin slides of control (Ctrl) and steroid-induced (Dx) TEP1 cells were stained by immune-fluorescence. Beige-specific marker TBX-1 **(A,B)** and beige-indicative marker UCP-1 **(C,D)** was evaluated in red (Alexa555). Neutral lipid deposits were stained with LipidTOX Red dye **(E,F)**. DAPI staining was also applied as nuclear counter-stain. TBX-1, UCP-1, and LipidTOX staining relative to DAPI staining is also shown by histograms **(I)**. TBX-1 shows unaltered expression, while UCP-1 and lipid accumulation show significant increase following Dx-induction. Significant differences are shown by asterisks (*$p \leq 0.05$, **$p \leq 0.01$). Data were calculated from six slides, representative slide is shown. For exact numerical values and standard error of mean please refer to **Supplementary Data Sheet**. Ultrastructure of control (Ctrl) and steroid-induced (Dx) TEP1 cells was also evaluated by transmission electron microscopy (TEM) **(G,H)**, respectively. Asterisks (*) show intracellular multi-locular lipid deposits following Dx-induction.

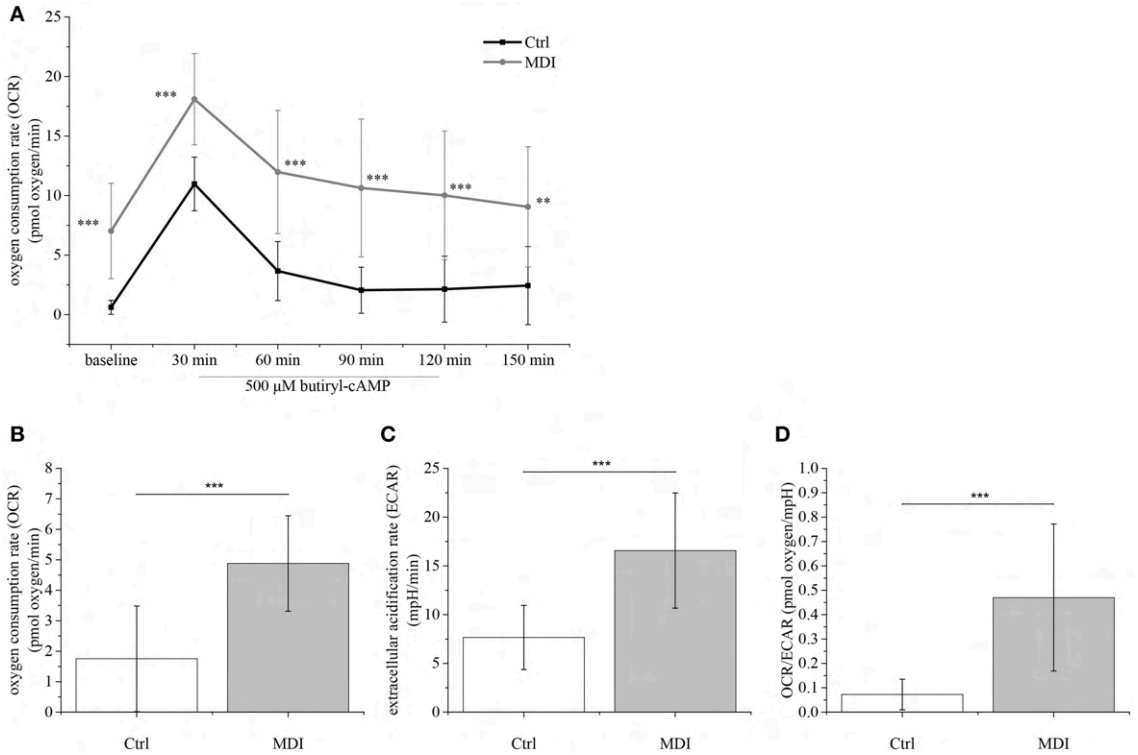

FIGURE 5 | Metabolic parameters of steroid-induced TECs. Following pilot experiments, 15,000 cells / well were cultured for 9 days in MDI (or control) medium prior to Seahorse measurements. Baseline OCR was recorded followed by induction with cAMP (readings every 30 min) **(A)**. Cells were treated with oligomycin to show oligomycin-resistant respiration indicating mitochondrial inner membrane leakage **(B)**. ECAR was also determined **(C)** and the OCR/ECAR ratio was calculated **(D)**. Significant differences are shown by asterisks (**$p \leq 0.01$, ***$p \leq 0.001$). Data were calculated from forty measurements, mean is shown. For exact numerical values and standard error of mean please refer to **Supplementary Data Sheet**.

Aged and Steroid-Induced TECs Show Beige Adipocyte Gene Expression Profile

Adult human and mouse thymus sections showed similar histological changes with age. Likewise, mouse and human steroid-induced TECs were also similar by immune-fluorescent staining. Next, TECs enriched from adult mice or Dx-treated (murine or human) TECs were subjected to gene expression analysis.

Changes in gene expression were further tested at the mRNA level in EpCAM1-enriched primary murine thymic epithelial cells from senior adult age (12 m) and steroid-induced TEP1 or 1889c cells for beige-specific (TBX1) and beige-indicative genes (UCP1, CD137, EAR2) (21–26). Enriched cells showed the up-regulation of both beige-specific and beige-indicative genes with age (1 vs. 12 months) as TBX1, UCP1, and EAR2 all showed significant elevation ($p < 0.05$ for all, **Figure 6A**), while CD137 activity remained unchanged. Gene expression analysis of mouse TEC line following Dx-treatment showed a similar tendency. as significant increase of TBX1 and UCP1 expression was detected ($p < 0.01$ and $p < 0.05$, respectively, **Figure 6B**), while CD137 and EAR2 were not altered. Likewise, the steroid-induced human TEC line showed significantly increased PPAR-gamma expression ($p < 0.01$) as reported previously for mouse TECs (4) and also significant increase of UCP-1 expression ($p < 0.05$) (**Figure 6C**), while CD137 and EAR2 remained identical. Please note the harmony of *in vivo* and *in vitro* data in both mouse and human species supporting our observations.

Steroid-Induced TECs Show Beige Adipocyte miRNA Profile

There is a significant difference between white, brown and beige adipose tissue miRNA profile. Seeking further evidence we have characterized the miRNA profile of Dx-induced human TECs (1889c).

We have elaborated two distinct platforms (**Figure 7**) for complete human miRNome analysis. For both platforms increased copy numbers are shown in red, while decreased copy numbers are shown in green (heat map). QuantStudio miRNA (QS) panels (A and B, **Figures 7A,B**) evaluate 768 miRNA entities, while the NanoString (NS) cartridge measures copy numbers of 880 miRNA entries (**Figure 7C**). Of note QS is amplification- (PCR) based while NS is amplification free. QS provides enhanced sensitivity, NS ensures unmatched signal-to-noise ratio. Accordingly, QS identified more miRNA species with occasional out-of-scale activities (shown in white) while NS recognized less species with a compressed scale of activities relative to QS. An overlap of the recognized miRNA species identified by at least one platform or evaluated by both

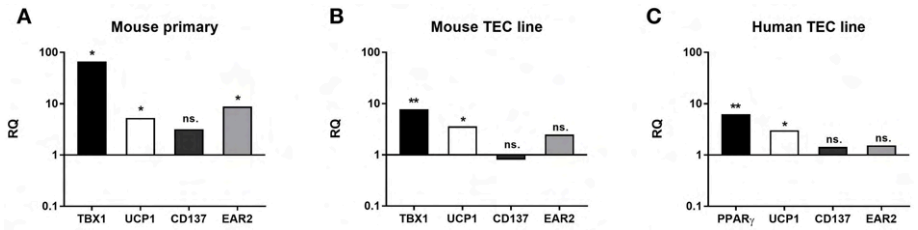

FIGURE 6 | Beige adipocyte marker expression in aged or steroid-induced, mouse, and human TECs. Marker expression was evaluated by qRT-PCR from sorted TECs of mice **(A)**. TBX-1, UCP-1 and EAR-2 showed significant increase with age (1 m vs 12 m). CD137 remained unchanged. Marker expression was evaluated by qRT-PCR in Dx-induced mouse TEP1 cells **(B)** and human 1889c cells **(C)**, respectively. In mouse TEP1 cells TBX-1 and UCP-1 showed significant increase with Dx-induction. CD137 and EAR-2 did not present significant difference. In human 1889c cells PPAR-gamma and UCP-1 showed significant increase with Dx-induction. CD137 and EAR-2 did not present significant difference. Relative quantity values (RQ) are shown where Y = 1 represents young adult **(A)** or control expression levels **(B,C)**, respectively. Significant differences are shown by asterisks (*$p \leq 0.05$, **$p \leq 0.01$). Please not that Y-axis is logarithmic. For exact numerical values and standard error of mean please refer to **Supplementary Data Sheet** containing both RQ and Ct/SD values for all experiments and target genes.

platforms similarly is summarized by **Table 2**. The table connects the identified miRNA species with context-relevant function based on literature search. Of note, several of the recognized species have relevance to thymus senescence with special focus on adipose tissue development, epithelial-to-mesenchymal transition, cell proliferation and senescence.

DISCUSSION

Thymic Tissue Samples and Steroid-Induced TECs Show Beige Adipocyte Markers

TBX-1 has been extensively studied for its role in the thymic context during embryonic organogenesis, but not in the adult thymus undergoing adipose involution (11–15). Using human and mouse thymus sections we show that TBX-1 expression persists throughout adulthood with a transient decrease in expression (23 years of age in human and 12 months of age in mouse) based on our pilot studies. This persistence of thymic TBX-1 expression raises the possibility of an alternative role in adulthood. This hypothesis is supported by reports showing that (1) once the thymus has been formed TBX-1 suppresses FoxN1 (key transcription factor of thymic epithelial identity) and (2) TBX-1 has a key and specific role in beige adipose tissue development (17–21). This plausible connection is supported by our results as further beige-indicative markers (UCP-1, EAR2) show increasing mRNA levels with age. This is in harmony with the fact that the thymus resides in the mediastinum and secretes FGF21, both reported to promote the emergence of beige adipose tissue (25). The *in vitro* model system of aging (Dx-treated mouse TEP1 or human 1889c cells) show similar molecular and cellular changes. Immune-fluorescent histology shows the presence of TBX-1 both in control conditions and following Dx-treatment. UCP-1 protein expression, on the other hand, significantly increases following Dx-treatment. Protein level data are in accordance with mRNA results as both TBX-1 and UCP-1 showed an increase following Dx-treatment (both in mouse and human). The above molecular changes are accompanied by evident phenotypical changes: the appearance of typical intracellular multi-locular neutral lipid deposits (characteristic to brown/beige adipose tissue) as shown by LipidTox staining and transmission electron microscopy. Taken together, these data suggest that thymic adipose tissue emerging with senescence and modeled by steroid-induced TECs show beige adipocyte features.

Steroid-Induced TECs Show Beige Adipocyte Metabolic Profile

There is profound difference between white and brown/beige adipose tissues with respect to metabolic traits (23). Basal respiration (OCR) is significantly lower in white fat cells than in brown/beige fat cells. Also, UCP-mediated uncoupled respiration rate (resistant to inhibition by oligomycin) is characteristic to brown/beige fat cells and not observed in white fat cells (32). Furthermore, in brown/beige fat cells cAMP-induced mitochondrial oxidation is elevated compared to white fat cells (33). Having analyzed these metabolic parameters, our data suggest that adipocyte differentiation in our model system shows beige bias as indicated by elevated basal OCR, increased OCR/ECAR ratio, enhanced cAMP-response and oligomycin-resistant respiration. Our metabolic readouts are in accordance with the recorded beige adipose tissue markers, morphological characteristics and gene expression profiles.

Steroid-Induced TECs Show Beige Adipocyte miRNA Profile

Unbiased dual platform complete miRNome analysis identified a number of context-relevant miRNA copy number alterations. Of note, miR-27a and miR-106b are beige adipose tissue regulators and miR-155 is an inhibitor of brown/beige adipose tissue formation (36, 46, 53). From a broad pan-adipocyte perspective, miR-128a-3p, miR-1825, miR-301a-5p, miR-30d, miR-425-5p, miR-550a, and miR92b-3p also influence adipose tissue formation and show changes in the current experimental setting (40, 43, 48, 49, 54, 55, 62, 66, 67). Furthermore, a cornerstone of thymus adipose involution: epithelial-to-mesenchymal transition (EMT), operates via miR-105-5p, miR-200a-3p, miR-597-5p, miR-888, and miR-99b, all demonstrating

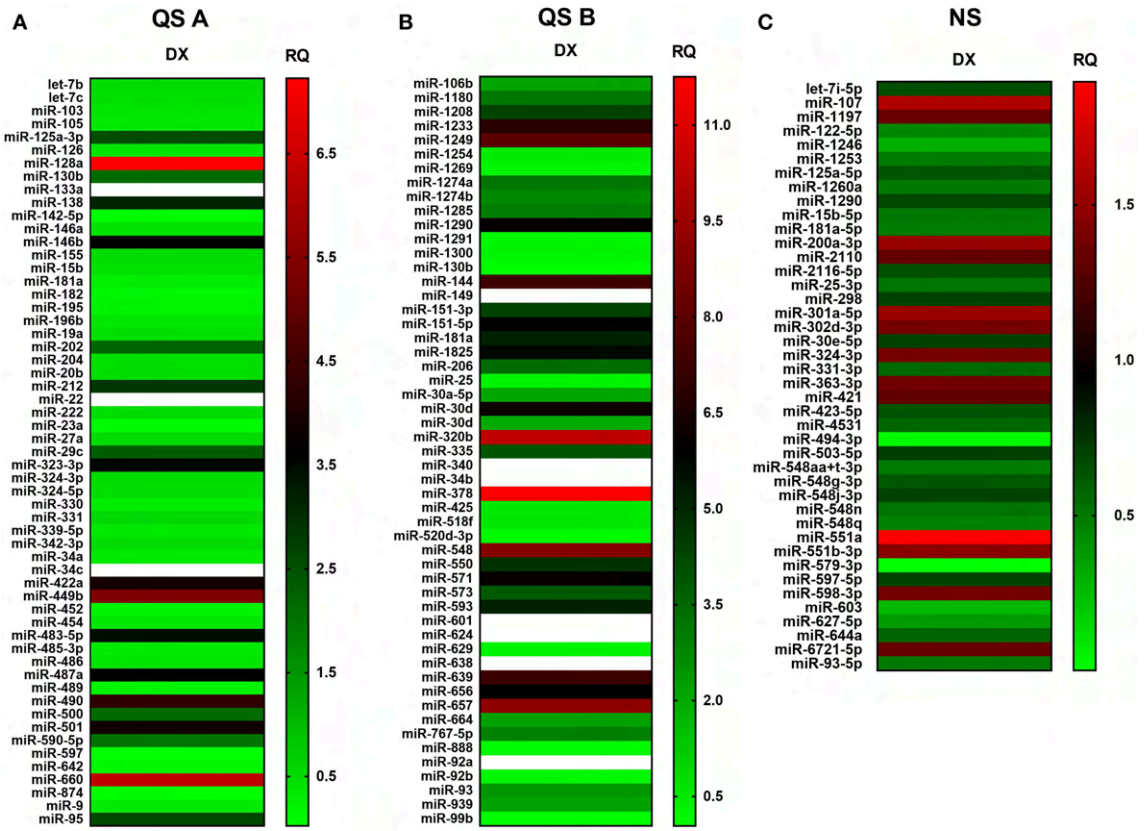

FIGURE 7 | miRNA profile of steroid-induced TECs. miRNA profile of Dx-treated human 1889c cells measured by Quantstudio 12K Flex Pool A **(A)**, Pool B **(B)** and NanoString nCounter SPRINT Profiler **(C)**. Heat-map representation shows miRNA species with most significant changes in copy number. Relative quantity values are presented (ctrl = 1). Up-regulation of miRNA species is shown in red while down-regulation is shown in green. Out-of-scale RQ values are shown in white. Pilot study is shown, for exact numerical values please refer to **Supplementary Data Sheet**.

changes in copy number in steroid-induced TECs (35, 36, 50, 63, 65, 69, 70). Taking a final expansion of interest, from a senescent perspective miR-125a-3p, miR-125a-5p, miR-15b-5p, miR-181a-5p, miR-323-3p, and miR-331-3p affect cellular / tissue level senescence with focus on the thymus and also show significant changes (36, 39, 40, 45, 47, 56–58). In summary, steroid-treatment in TECs affects the same miRNA species that were reported in connection with senescence-related thymus adipose involution that apparently yields beige adipose tissue.

Expanding Overlap Between Metabolism and Immunity

Overlap of metabolism and immunity has already been raised decades ago, and this inter-disciplinary field has recently become a prominent research area. For example, both previous and recent papers discussed overlap between the neuroendocrine and immune systems with regard to melatonin (71–73). Melatonin—mainly produced by the pineal gland, but also expressed by the thymus in small amounts—has been reported to have an immune-modulatory effect, enhancing immune functions with Th1 bias. Accordingly, anti-viral and anti-cancer defense is boosted by melatonin and age-related loss of melatonin production partly explains elevated incidence of infection and cancer observed with senescence. Protection from cancer metastasis development in the central nervous system (CNS) implies proper blood-brain barrier (BBB) function (74–76). BBB function, CNS function and immune status are all controlled by metabolic interplays involving small molecules such as lactate. Local tissue lactate concentration has been reported to have important role in immune regulation, its accumulation promoting autoimmune reactions (77, 78). Intercellular immune modulatory signals triggered by metabolically active small molecules are transmitted in cells through signaling pathways. An important pathway connecting metabolism and immunity utilizes mechanistic target of rapamycin (mTOR). It was shown that mTOR senses certain small nutrients (amino acids) and thus affects immune tolerance through regulatory T-cells (79, 80). Mammalian immunity heavily relies on both the innate and the adaptive branch. Within innate immunity macrophages have an important role in connecting metabolism and immunity. It has also been reported that carbohydrate metabolism significantly affects inflammation via macrophages (81).

Carbohydrates are also basic metabolic fuels. The mammalian immune system is a costly defense system with regard to T-cell

TABLE 2 | Overlap of QS- and NS-based miRNA results with functional and literature annotation.

Name	Up/down regulation	QS/ NS	Function	References
miR-103a-3p		QS A	Inactivation upregulates insulin receptors in adipocytes	(34)
miR-105-5p		QS A, NS	Epithelial to mesenchymal transition	(35)
miR-106b		QS B	Beige adipose tissue regulator	(36)
miR-1208		QS B	Targets TGFB2 (involved in adipose tissue development)	(37)
miR-1246		NS	Promotes cell proliferation	(38)
miR-125a-3p		QS A	Tissue-specific senescence	(39)
miR-125a-5p		QS A, NS	Regulation of epithelial cell differentiation	(40)
miR-126-3p		QS A	Insulin/IGF1 signaling pathway	(41)
miR-1274a		QS B	Potential biomarker for Alzheimer's Disease	(42)
miR-1274b		QS B	Potential biomarker for Alzheimer's Disease	(42)
miR-128a-3p		QS A	Regulatory effect on PPARg	(43)
miR-138-5p		QS A	Negative regulation of apoptosis	(44)
miR-15b-5p		QS A, NS	Characteristic of senescent cell derived EVs	(36, 45)
miR-155		QS A	Induces brown adipocyte differentiation from white adipocytes	(46)
miR-181a-5p		QS A, NS	Stress-related thymic involution	(47)
miR-1825		QS B	Lipid signaling	(48, 49)
miR-200a-3p		NS	Regulates epithelial cell transformation (EMT and MET)	(50)
miR-2110		NS	Cellular development, cell-mediated immune response	(51)
miR-2116-5p		NS	Regulatory function in colorectal cancer	(52)
miR-25-3p		QS A, B, NS	Modulator of the Wnt pathway	(47)
miR-27a		QS A, B	Negative regulator in beige adipose tissue	(36, 53)
miR-301a-5p		NS	Role in adipogenesis	(54)
miR-30d		QS B	Upregulation in adipose tissue	(55)
miR-323-3p		QS A	Regulation of senescence through IGF signaling pathway	(56)
miR-331-3p		NS, QS A	Induces senescence and cell cycle arrest	(57, 58)
miR-421		NS	Upregulation modulates oxidant stress and lipid metabolism	(59)
miR-425-5p		QS A, B	Inhibits differentiation and proliferation of preadipocytes	(40)
miR-4531		NS	Involved in type 1 diabetes mellitus	(60)
miR-520d-3p		NS, QS B	Regulatory function in colorectal cancer	(52)
miR-548q		NS	Possible biomarker of nasopharyngeal carcinoma	(61)
miR-550a		QS B	Adipogenic differentiation	(62)
miR-597-5p		NS, QS A	Drives EMT	(63)
miR-657		QS B	Regulates IL-37/NF-κB signaling	(64)
miR-6721-5p		NS	Unknown	
miR-888		QS B, NS	Downregulates E-cadherin	(65)
miR-92a-3p		QS A, NS	Replicative and organismal human aging	(36)
miR-92b-3p		QS B, NS	Regulation of lipid deposition	(66, 67)
miR-939-5p		QS B, NS	Inhibits cell proliferation	(68)
miR-99b		QS A, B, NS	Regulates epithelial cell differentiation	(36, 69, 70)

development and selection taking place in the thymus, where approx. Ninety-five percent of developing thymocytes are deleted being useless or potentially autoimmune. However, the adaptive branch heavily relies on the constant supply of fresh naïve and scrupulously selected T-cells to prevent infection, cancer and autoimmunity from developing. Severe negative imbalance in energy expenditure (due to fasting or malnutrition) has long been known to hamper thymus function and immunity (82). In contrast, currently, global human population is more threatened by obesity than fasting/malnutrition along with its reported negative effects on thymus function (1, 83). Fashionable countermeasures of obesity include e.g., applying diet to induce ketosis. Ketosis has been reported to enhance FGF21 secretion, known to promote white adipose tissue browning especially in the mediastinal context, where the thymus also resides (25, 84). Further options of white adipose tissue browning include interventions e.g., irisin (exercise hormone) treatment (32). However, since irisin promotes beige adipose tissue development it may also impair thymus function via promoting adipose involution identical to thymus senescence.

Our study highlights another potential intersection of immunity and metabolism via the dual role of TBX-1 during thymus development and senescence. TBX-1 shows bimodal expression (high expression in early and late ages, with a transient decrease in-between) in both mouse and human. It is conceivable that TBX-1 plays a role in thymus organogenesis early on (early "immune" peak) and thymic adipose involution later on (late "metabolic" peak). This dualism may be unique to the thymus due to the observed "beige" adipose involution process.

With senescence the thymus suffers adipose involution. Impaired thymic niche leads to decreased naïve T-cell output. This in turn weakens T cell-mediated anti-viral and anti-cancer defense, and elevates the chances of autoimmune disorders due to dysfunctional T-cell selection. Therefore, thymic adipose tissue emerging with age impairs immune homeostasis and the maintenance of tolerance. Our results indicate that thymic adipose tissue shows "beige" characteristics by molecular, cellular and metabolic profiling. Our research contributes to the breadth of overlap between metabolism and immune homeostasis.

DATA AVAILABILITY

All datasets generated for this study are included in the manuscript and/or the **Supplementary Files**.

ETHICS STATEMENT

Mice were kept in the Laboratory Animal Core Facility of the University. Experimental procedures were carried out according to the 1988/XXVIII act of the Hungarian Parliament on Animal Protection (243/1988) which complies with recommendations of the Helsinki Declaration. All animal experiments were performed with the consent of the Ethics Committee on Animal Research of the University (ref. no.: #BA02/2000-46/2016). Formalin-fixed, paraffin-embedded (FFPE) human thymus samples from 18, 23, 42, 44, and 58 years of age were provided by the Department of Pathology, Faculty of Medicine, University of Pecs, Hungary. Experiments involving human samples were performed with the consent of the Regional and Local Ethics Committee of Clinical Centre of the University (ref. no.: 6069/2016) according to their guidelines. All subjects gave written informed consent in accordance with the Declaration of Helsinki.

AUTHOR CONTRIBUTIONS

KB performed most histological, molecular biology, and statistics work in the project and was involved in manuscript preparation. DE performed all human IHC work. AP and PB were responsible for preparative Seahorse measurements. KG performed statistical analysis. DB was involved in experiments performed on human 1889c cells. JP was involved in planning experiments and manuscript preparation as well as local supervision of respective department. KK was involved in histological, molecular biology, and statistics work, also in planning experiments and manuscript preparation, and supervised the project.

FUNDING

Scientific research support was provided by the Hungarian National Science Foundation (No. 78310) and PTE AOK KA-2016-16 to KK. The project was also supported by the University of Pecs in the frame of Pharmaceutical Talent Center program and the Viral Pathogenesis Talent Center program via KK. The Janos Bolyai Scholarship of the Hungarian Academy of Sciences and Bolyai+ 2018/2019 (UNKP-18-4 2018/2019 new national excellence program of the ministry of human capacities) also supported KK. JP was also supported by the European Union and the State of Hungary, co-financed by the European Social Fund in the framework of, TAMOP-4.2.2. A-11/1/KON-2012-0024 and TAMOP-4.2.4.A/2-11/1-2012-0001 National Excellence Program and PTE AOK-KA-2013/22. Further grant support was provided to PB by NKFIH K108308, C120732, TAMOP-4.2.2.A-11/1/KONV-2012-0025. The project was also supported by the UNKP-18-3 2018/2019 new national excellence program of the ministry of human capacities to KG. Research funding was also provided by University of Pecs Biomedical Engineering Project to JP and KK.

ACKNOWLEDGMENTS

The authors wish to thank Hajnalka Abraham MD, PhD (Central Electron Microscope Laboratory, University of Pecs, Hungary) for the technical aid in taking transmission electron microscope images. The thymic carcinoma cell line 1889c was kindly provided by Prof Ralf J. Riecker (Institute of Pathology, University Hospital, Heidelberg, Germany). The authors wish to thank Ricky Odedra (Humeltis Ltd) and prof. Mary Keen (University of Birmingham, UK) for improving the manuscript using their native speaker skills. The present scientific contribution is dedicated to the 650th anniversary of the foundation of the University of Pecs, Hungary.

SUPPLEMENTARY MATERIAL

The Supplementary Material for this article can be found online at: https://www.frontiersin.org/articles/10.3389/fendo.2019.00369/full#supplementary-material

REFERENCES

1. Yang H, Youm Y-H, Vandanmagsar B, Rood J, Kumar KG, Butler AA, et al. Obesity accelerates thymic aging. *Blood*. (2009) 114:3803–12. doi: 10.1182/blood-2009-03-213595
2. Dixit VD. Thymic fatness and approaches to enhance thymopoietic fitness in aging. *Curr Opin Immunol.* (2010) 22:521–8. doi: 10.1016/j.coi.2010.06.010
3. Yang H, Youm Y-H, Dixit VD. Inhibition of thymic adipogenesis by caloric restriction is coupled with reduction in age-related thymic involution. *J Immunol*. (2009) 183:3040–52. doi: 10.4049/jimmunol.0900562

4. Talaber G, Kvell K, Varecza Z, Boldizsar F, Parnell SM, Jenkinson EJ, et al. Wnt-4 protects thymic epithelial cells against dexamethasone-induced senescence. *Rejuvenation Res*. (2011) 14:241–8. doi: 10.1089/rej.2010.1110
5. Youm Y-H, Yang H, Amin R, Smith SR, Leff T, Dixit VD. Thiazolidinedione treatment and constitutive-PPARgamma activation induces ectopic adipogenesis and promotes age-related thymic involution. *Aging Cell*. (2010) 9:478–89. doi: 10.1111/j.1474-9726.2010.00574.x
6. Kvell K, Varecza Z, Bartis D, Hesse S, Parnell S, Anderson G, et al. Wnt4 and LAP2alpha as pacemakers of thymic epithelial senescence. *PLoS ONE*. (2010) 5:e10701. doi: 10.1371/journal.pone.0010701
7. Ernszt D, Banfai K, Kellermayer Z, Pap A, Lord JM, Pongracz JE, et al. PPARgamma deficiency counteracts thymic senescence. *Front Immunol*. (2017) 8:1515. doi: 10.3389/fimmu.2017.01515
8. Palmer DB. The effect of age on thymic function. *Front Immunol*. (2013) 4:316. doi: 10.3389/fimmu.2013.00316
9. Bertho JM, Demarquay C, Moulian N, Van Der Meeren A, Berrih-Aknin S, Gourmelon P. Phenotypic and immunohistological analyses of the human adult thymus: evidence for an active thymus during adult life. *Cell Immunol*. (1997) 179:30–40. doi: 10.1006/cimm.1997.1148
10. George AJ, Ritter MA. Thymic involution with ageing: obsolescence or good housekeeping? *Immunol Today*. (1996) 17:267–72. doi: 10.1016/0167-5699(96)80543-3
11. Steinmann GG. Changes in the human thymus during aging. *Curr Top Pathol*. (1986) 75:43–88. doi: 10.1007/978-3-642-82480-7_2
12. Gao S, Li X, Amendt BA. Understanding the role of Tbx1 as a candidate gene for 22q11.2 deletion syndrome. *Curr Allergy Asthma Rep*. (2013) 13:613–21. doi: 10.1007/s11882-013-0384-6
13. Farley AM, Morris LX, Vroegindeweij E, Depreter MLG, Vaidya H, Stenhouse FH, et al. Dynamics of thymus organogenesis and colonization in early human development. *Development*. (2013) 140:2015–26. doi: 10.1242/dev.087320
14. Jerome LA, Papaioannou VE. DiGeorge syndrome phenotype in mice mutant for the T-box gene, Tbx1. *Nat Genet*. (2001) 27:286–91. doi: 10.1038/85845
15. Sirianni MC, Businco L, Seminara R, Aiuti F. Severe combined immunodeficiencies, primary T-cell defects and DiGeorge syndrome in humans: characterization by monoclonal antibodies and natural killer cell activity. *Clin Immunol Immunopathol*. (1983) 28:361–70. doi: 10.1016/0090-1229(83)90103-4
16. Reeh KAG, Cardenas KT, Bain VE, Liu Z, Laurent M, Manley NR, et al. Ectopic TBX1 suppresses thymic epithelial cell differentiation and proliferation during thymus organogenesis. *Development*. (2014) 141:2950–8. doi: 10.1242/dev.111641
17. Wu J, Boström P, Sparks LM, Ye L, Choi JH, Giang A-H, et al. Beige adipocytes are a distinct type of thermogenic fat cell in mouse and human. *Cell*. (2012) 150:366–76. doi: 10.1016/j.cell.2012.05.016
18. Giralt M, Villarroya F. White, brown, beige/brite: different adipose cells for different functions? *Endocrinology*. (2013) 154:2992–3000. doi: 10.1210/en.2013-1403
19. Symonds ME. Brown adipose tissue growth and development. *Scientifica*. (2013) 2013:305763. doi: 10.1155/2013/305763
20. Cinti S. Adipocyte differentiation and transdifferentiation: plasticity of the adipose organ. *J Endocrinol Invest*. (2002) 25:823–35. doi: 10.1007/BF03344046
21. Berg JM, Tymoczko JL, Stryer L. *Biochemistry*. 5th ed, section 18.6. New York, NY: WH Freeman and Co (2002).
22. Peláez-García A, Barderas R, Batlle R, Viñas-Castells R, Bartolomé RA, Torres S, et al. A proteomic analysis reveals that Snail regulates the expression of the nuclear orphan receptor nuclear receptor subfamily 2 group F member 6 (Nr2f6) and interleukin 17 (IL-17) to inhibit adipocyte differentiation. *Mol Cell Proteomics*. (2015) 14:303–15. doi: 10.1074/mcp.M114.045328
23. Cereijo R, Giralt M, Villarroya F. Thermogenic brown and beige/brite adipogenesis in humans. *Ann Med*. (2015) 47:169–77. doi: 10.3109/07853890.2014.952328
24. Poher A-L, Altirriba J, Veyrat-Durebex C, Rohner-Jeanrenaud F. Brown adipose tissue activity as a target for the treatment of obesity/insulin resistance. *Front Physiol*. (2015) 6:4. doi: 10.3389/fphys.2015.00004
25. Gaborit B, Venteclef N, Ancel P, Pelloux V, Gariboldi V, Leprince P, et al. Human epicardial adipose tissue has a specific transcriptomic signature depending on its anatomical peri-atrial, peri-ventricular, or peri-coronary location. *Cardiovasc Res*. (2015) 108:62–73. doi: 10.1093/cvr/cvv208
26. Langhi LGP, Andrade LR, Shimabukuro MK, van Ewijk W, Taub DD, Borojevic R, et al. Lipid-laden multilocular cells in the aging thymus are phenotypically heterogeneous. *PLoS ONE*. (2015) 10:e0141516. doi: 10.1371/journal.pone.0141516
27. Beardsley TR, Pierschbacher M, Wetzel GD, Hays EF. Induction of T-cell maturation by a cloned line of thymic epithelium (TEPI). *Proc Natl Acad Sci USA*. (1983) 80:6005–9. doi: 10.1073/pnas.80.19.6005
28. Ehemann V, Kern MA, Breinig M, Schnabel PA, Gunawan B, Schulten H-J, et al. Establishment, characterization and drug sensitivity testing in primary cultures of human thymoma and thymic carcinoma. *Int J cancer*. (2008) 122:2719–25. doi: 10.1002/ijc.23335
29. Belharazem D, Grass A, Paul C, Vitacolonna M, Schalke B, Rieker RJ, et al. Increased cFLIP expression in thymic epithelial tumors blocks autophagy via NF-κB signalling. *Oncotarget*. (2017) 8:89580–94. doi: 10.18632/oncotarget.15929
30. Meggyes M, Lajko A, Palkovics T, Totsimon A, Illes Z, Szereday L, et al. Feto-maternal immune regulation by TIM-3/galectin-9 pathway and PD-1 molecule in mice at day 14.5 of pregnancy. *Placenta*. (2015) 36:1153–60. doi: 10.1016/j.placenta.2015.07.124
31. Gratzner HG, Ahmad PM, Stein J, Ahmad F. Flow cytometric analysis of DNA replication during the differentiation of 3T3-L1 preadipocytes. *Cytometry*. (1985) 6:563–9. doi: 10.1002/cyto.990060610
32. Kristóf E, Doan-Xuan Q-M, Bai P, Bacso Z, Fésüs L. Laser-scanning cytometry can quantify human adipocyte browning and proves effectiveness of irisin. *Sci Rep*. (2015) 5:12540. doi: 10.1038/srep12540
33. Abdul-Rahman O, Kristóf E, Doan-Xuan Q-M, Vida A, Nagy L, Horváth A, et al. AMP-Activated Kinase (AMPK) activation by AICAR in human white adipocytes derived from pericardial white adipose tissue stem cells induces a partial beige-like phenotype. *PLoS ONE*. (2016) 11:e0157644. doi: 10.1371/journal.pone.0157644
34. Trajkovski M, Hausser J, Soutschek J, Bhat B, Akin A, Zavolan M, et al. MicroRNAs 103 and 107 regulate insulin sensitivity. *Nature*. (2011) 474:649–53. doi: 10.1038/nature10112
35. Jin X, Yu Y, Zou Q, Wang M, Cui Y, Xie J, et al. MicroRNA-105 promotes epithelial-mesenchymal transition of nonsmall lung cancer cells through upregulating Mcl-1. *J Cell Biochem*. (2019) 120:5880–8. doi: 10.1002/jcb.27873
36. Goody D, Pfeifer A. MicroRNAs in brown and beige fat. *Biochim Biophys Acta Mol Cell Biol Lipids*. (2019) 1864:29–36. doi: 10.1016/j.bbalip.2018.05.003
37. Kolhe R, Mondal AK, Pundkar C, Periyasamy-Thandavan S, Mendhe B, Hunter M, et al. Modulation of miRNAs by vitamin C in human bone marrow stromal cells. *Nutrients*. (2018) 10:186. doi: 10.3390/nu10020186
38. Li XJ, Ren ZJ, Tang JH, Yu Q. Exosomal MicroRNA MiR-1246 promotes cell proliferation, invasion and drug resistance by targeting CCNG2 in breast cancer. *Cell Physiol Biochem*. (2017) 44:1741–8. doi: 10.1159/000485780
39. Holly AC, Grellscheid S, van de Walle P, Dolan D, Pilling LC, Daniels DJ, et al. Comparison of senescence-associated miRNAs in primary skin and lung fibroblasts. *Biogerontology*. (2015) 16:423–34. doi: 10.1007/s10522-015-9560-5
40. Du J, Xu Y, Zhang P, Zhao X, Gan M, Li Q, et al. MicroRNA-125a-5p affects adipocytes proliferation, differentiation and fatty acid composition of porcine intramuscular fat. *Int J Mol Sci*. (2018) 19:501. doi: 10.3390/ijms19020501
41. Tryggestad JB, Vishwanath A, Jiang S, Mallappa A, Teague AM, Takahashi Y, et al. Influence of gestational diabetes mellitus on human umbilical vein endothelial cell miRNA. *Clin Sci*. (2016) 130:1955–67. doi: 10.1042/CS20160305
42. Kumar S, Reddy PH. Are circulating microRNAs peripheral biomarkers for Alzheimer's disease? *Biochim Biophys Acta*. (2016) 1862:1617–27. doi: 10.1016/j.bbadis.2016.06.001
43. Wotschofsky Z, Gummlich L, Liep J, Stephan C, Kilic E, Jung K, et al. Integrated microRNA and mRNA signature associated with the transition from the locally confined to the metastasized clear cell renal cell carcinoma exemplified by miR-146-5p. *PLoS ONE*. (2016) 11:e0148746. doi: 10.1371/journal.pone.0148746
44. Dhahbi JM, Spindler SR, Atamna H, Yamakawa A, Guerrero N, Boffelli D, et al. Deep sequencing identifies circulating mouse miRNAs that are functionally implicated in manifestations of aging and responsive to calorie restriction. *Aging*. (2013) 5:130–41. doi: 10.18632/aging.100540

45. Terlecki-Zaniewicz L, Lämmermann I, Latreille J, Bobbili MR, Pils V, Schosserer M, et al. Small extracellular vesicles and their miRNA cargo are anti-apoptotic members of the senescence-associated secretory phenotype. *Aging*. (2018) 10:1103–32. doi: 10.18632/aging.101452
46. Chen Y, Siegel F, Kipschull S, Haas B, Fröhlich H, Meister G, et al. miR-155 regulates differentiation of brown and beige adipocytes via a bistable circuit. *Nat Commun*. (2013) 4:1769. doi: 10.1038/ncomms2742
47. Xu M, Zhang X, Hong R, Su D-M, Wang L. MicroRNAs regulate thymic epithelium in age-related thymic involution via down- or upregulation of transcription factors. *J Immunol Res*. (2017) 2017:2528957. doi: 10.1155/2017/2528957
48. Raghavachari N, Liu P, Barb JJ, Yang Y, Wang R, Nguyen QT, et al. Integrated analysis of miRNA and mRNA during differentiation of human CD34+ cells delineates the regulatory roles of microRNA in hematopoiesis. *Exp Hematol*. (2014) 42:14–27.e1–2. doi: 10.1016/j.exphem.2013.10.003
49. Stace CL, Ktistakis NT. Phosphatidic acid- and phosphatidylserine-binding proteins. *Biochim Biophys Acta*. (2006) 1761:913–26. doi: 10.1016/j.bbalip.2006.03.006
50. Becker LE, Takwi AAL, Lu Z, Li Y. The role of miR-200a in mammalian epithelial cell transformation. *Carcinogenesis*. (2015) 36:2–12. doi: 10.1093/carcin/bgu202
51. Chen Y-J, Chang W-A, Huang M-S, Chen C-H, Wang K-Y, Hsu Y-L, et al. Identification of novel genes in aging osteoblasts using next-generation sequencing and bioinformatics. *Oncotarget*. (2017) 8:113598–613. doi: 10.18632/oncotarget.22748
52. http://exocarta.org
53. Kim SY, Kim AY, Lee HW, Son YH, Lee GY, Lee J-W, et al. miR-27a is a negative regulator of adipocyte differentiation via suppressing PPARγ expression. *Biochem Biophys Res Commun*. (2010) 392:323–8. doi: 10.1016/j.bbrc.2010.01.012
54. Nowak WN, Taha H, Kachamakova-Trojanowska N, Stepniewski J, Markiewicz JA, Kusienicka A, et al. Murine bone marrow mesenchymal stromal cells respond efficiently to oxidative stress despite the low level of heme oxygenases 1 and 2. *Antioxid Redox Signal*. (2018) 29:111–27. doi: 10.1089/ars.2017.7097
55. Nunez Lopez YO, Garufi G, Pasarica M, Seyhan AA. Elevated and correlated expressions of miR-24, miR-30d, miR-146a, and SFRP-4 in human abdominal adipose tissue play a role in adiposity and insulin resistance. *Int J Endocrinol*. (2018) 2018:7351902. doi: 10.1155/2018/7351902
56. Nidadavolu LS, Niedernhofer LJ, Khan SA. Identification of microRNAs dysregulated in cellular senescence driven by endogenous genotoxic stress. *Aging*. (2013) 5:460–73. doi: 10.18632/aging.100571
57. Maes OC, Sarojini H, Wang E. Stepwise up-regulation of microRNA expression levels from replicating to reversible and irreversible growth arrest states in WI-38 human fibroblasts. *J Cell Physiol*. (2009) 221:109–19. doi: 10.1002/jcp.21834
58. Morita K, Fujii T, Itami H, Uchiyama T, Nakai T, Hatakeyama K, et al. NACC1, as a target of MicroRNA-331-3p, regulates cell proliferation in urothelial carcinoma cells. *Cancers*. (2018) 10:347. doi: 10.3390/cancers10100347
59. Cheng Y, Mai J, Hou T, Ping J. MicroRNA-421 induces hepatic mitochondrial dysfunction in non-alcoholic fatty liver disease mice by inhibiting sirtuin 3. *Biochem Biophys Res Commun*. (2016) 474:57–63. doi: 10.1016/j.bbrc.2016.04.065
60. de Almeida RC, Chagas VS, Castro MAA, Petzl-Erler ML. Integrative analysis identifies genetic variants associated with autoimmune diseases affecting putative MicroRNA binding sites. *Front Genet*. (2018) 9:139. doi: 10.3389/fgene.2018.00139
61. Zhuo X, Zhou W, Li D, Chang A, Wang Y, Wu Y, et al. Plasma microRNA expression signature involving miR-548q, miR-630 and miR-940 as biomarkers for nasopharyngeal carcinoma detection. *Cancer Biomark*. (2018) 23:579–87. doi: 10.3233/CBM-181852
62. Heilmeier U, Hackl M, Skalicky S, Weilner S, Schroeder F, Vierlinger K, et al. Serum miRNA signatures are indicative of skeletal fractures in postmenopausal women with and without type 2 diabetes and influence osteogenic and adipogenic differentiation of adipose tissue-derived mesenchymal stem cells *in vitro*. *J Bone Miner Res*. (2016) 31:2173–92. doi: 10.1002/jbmr.2897
63. Xie L, Jiang T, Cheng A, Zhang T, Huan P, Li P, et al. MiR-597 targeting 14-3-3σ enhances cellular invasion and EMT in Nasopharyngeal carcinoma cells. *Curr Mol Pharmacol*. (2018) 12:105–114. doi: 10.2174/1874467212666181218113930
64. Wang P, Wang H, Li C, Zhang X, Xiu X, Teng P, et al. Dysregulation of microRNA-657 influences inflammatory response via targeting interleukin-37 in gestational diabetes mellitus. *J Cell Physiol*. (2019) 234:7141–8. doi: 10.1002/jcp.27468
65. Huang S, Cai M, Zheng Y, Zhou L, Wang Q, Chen L. miR-888 in MCF-7 side population sphere cells directly targets E-cadherin. *J Genet Genomics*. (2014) 41:35–42. doi: 10.1016/j.jgg.2013.12.002
66. Maes OC, An J, Sarojini H, Wu H, Wang E. Changes in MicroRNA expression patterns in human fibroblasts after low-LET radiation. *J Cell Biochem*. (2008) 105:824–34. doi: 10.1002/jcb.21878
67. Wang Z, Li Q, Chamba Y, Zhang B, Shang P, Zhang H, et al. Identification of genes related to growth and lipid deposition from transcriptome profiles of pig muscle tissue. *PLoS ONE*. (2015) 10:e0141138. doi: 10.1371/journal.pone.0141138
68. Chen G, Du C, Shen Z, Peng L, Xie H, Zang R, et al. MicroRNA-939 inhibits cell proliferation via targeting LRSAM1 in Hirschsprung's disease. *Aging*. (2017) 9:2471–9. doi: 10.18632/aging.101331
69. Dalmasso G, Thu Nguyen HT, Yan Y, Laroui H, Srinivasan S, Sitaraman SV, et al. MicroRNAs determine human intestinal epithelial cell fate. *Differentiation*. (2010) 80:147–54. doi: 10.1016/j.diff.2010.06.005
70. Li Y-J, Wang Y, Wang Y-Y. MicroRNA-99b suppresses human cervical cancer cell activity by inhibiting the PI3K/AKT/mTOR signaling pathway. *J Cell Physiol*. (2019) 234:9577–91. doi: 10.1002/jcp.27645
71. Mocchegiani E, Malavolta M, Costarelli L, Giacconi R, Piacenza F, Lattanzio F, et al. Is there a possible single mediator in modulating neuroendocrine-thymus interaction in ageing? *Curr Aging Sci*. (2013) 6:99–107. doi: 10.2174/1874609811306010013
72. Srinivasan V, Spence DW, Trakht I, Pandi-Perumal SR, Cardinali DP, Maestroni GJ. Immunomodulation by melatonin: its significance for seasonally occurring diseases. *Neuroimmunomodulation*. (2008) 15:93–101. doi: 10.1159/000148191
73. Espino J, Pariente JA, Rodríguez AB. Oxidative stress and immunosenescence: therapeutic effects of melatonin. *Oxid Med Cell Longev*. (2012) 2012:670294. doi: 10.1155/2012/670294
74. Mauro C, De Rosa V, Marelli-Berg F, Solito E. Metabolic syndrome and the immunological affair with the blood-brain barrier. *Front Immunol*. (2014) 5:677. doi: 10.3389/fimmu.2014.00677
75. Tang C-Y, Mauro C. Similarities in the metabolic reprogramming of immune system and endothelium. *Front Immunol*. (2017) 8:837. doi: 10.3389/fimmu.2017.00837
76. Wang T, Liu G, Wang R. The intercellular metabolic interplay between tumor and immune cells. *Front Immunol*. (2014) 5:358. doi: 10.3389/fimmu.2014.00358
77. Pucino V, Bombardieri M, Pitzalis C, Mauro C. Lactate at the crossroads of metabolism, inflammation, and autoimmunity. *Eur J Immunol*. (2017) 47:14–21. doi: 10.1002/eji.201646477
78. Haas R, Smith J, Rocher-Ros V, Nadkarni S, Montero-Melendez T, D'Acquisto F, et al. Lactate regulates metabolic and pro-inflammatory circuits in control of T cell migration and effector functions. *PLoS Biol*. (2015) 13:e1002202. doi: 10.1371/journal.pbio.1002202
79. Howie D, Waldmann H, Cobbold S. Nutrient sensing via mTOR in T cells maintains a tolerogenic microenvironment. *Front Immunol*. (2014) 5:409. doi: 10.3389/fimmu.2014.00409
80. Cobbold SP, Adams E, Farquhar CA, Nolan KF, Howie D, Lui KO, et al. Infectious tolerance via the consumption of essential amino acids and mTOR signaling. *Proc Natl Acad Sci USA*. (2009) 106:12055–60. doi: 10.1073/pnas.0903919106
81. Nagy C, Haschemi A. Time and demand are two critical dimensions of immunometabolism: the process of macrophage activation and the pentose phosphate pathway. *Front Immunol*. (2015) 6:164. doi: 10.3389/fimmu.2015.00164

82. Faulk WP, Paes RP, Marigo C. The immunological system in health and malnutrition. *Proc Nutr Soc*. (1976) 35:253–61. doi: 10.1079/PNS19760044
83. Castro É, Silva TEO, Festuccia WT. Critical review of beige adipocyte thermogenic activation and contribution to whole-body energy expenditure. *Horm Mol Biol Clin Investig*. (2017) 31. doi: 10.1515/hmbci-2017-0042
84. Ryan KK, Packard AEB, Larson KR, Stout J, Fourman SM, Thompson AMK, et al. Dietary manipulations that induce ketosis activate the HPA axis in male rats and mice: a potential role for fibroblast growth factor-21. *Endocrinology*. (2018) 159:400–13. doi: 10.1210/en.2017-00486

Conflict of Interest Statement: The authors declare that the research was conducted in the absence of any commercial or financial relationships that could be construed as a potential conflict of interest.